AN INVESTIGATION OF THE REACTION

$K^- p \to K^- \pi^+ n$ at $p_{lab} = 2$ GeV/c

Thesis by

David Chu

In Partial Fulfillment of the Requirements

for the degree of

Doctor of Philosophy

California Institute of Technology

Pasadena, California

1972

(Submitted March 20, 1972)

ACKNOWLEDGMENTS

I would like to acknowledge the supervision of my advisor, Dr. R. Gomez, without whose patient guidance, this work would have never been completed.

I would also like to acknowledge the contributions of the other members of the Caltech-UCLA collaboration: Drs. B. Barish, A. Dzierba, and B. Sherwood of Caltech; and Drs. P. Schlein, W. Slater, and T. Trippe of UCLA.

I am indebted to Dr. G. C. Fox and Richard Poster for many useful suggestions and stimulating conversations.

The assistance of Roy Lippmann and the UCLA scanning group is also gratefully acknowledged.

The patience of Della Harris during the typing of the final draft is acknowledged.

I would also like to thank the National Defense Education Administration, the Atomic Energy Commission, and the California Institute of Technology for financial support.

DEDICATION

To my loving parents.

ABSTRACT

The reaction $K^-p \to K^-\pi^+n$ has been studied for incident kaon momenta of 2.0 GeV/c. A sample of 19,881 events was obtained by a measurement of film taken as part of the K-63 experiment in the Berkeley 72 inch bubble chamber.

Based upon our analysis, we have reached four conclusions. (1) The magnitude of the extrapolated $K\pi$ cross section differs by a factor of 2 from the P-wave unitarity prediction and the K^+n results; this is probably due to absorptive effects. (2) Fits to the moments yield precise values for the $K\pi$ S-wave which agree with other recent statistically accurate experiments. (3) An anomalous peak is present in our backward $K^-p \to (\pi^+n)\ K^-$ u-distribution. (4) We find a non-linear enhancement due to interference similiar to the one found by Bland et al. (Bland 1966).

TABLE OF CONTENTS

Chapter I. Introduction

A. Experiment

A large part of our knowledge of the strong interaction in elementary particle physics comes from the study of two body scattering experiments. However, the present need to have a stable particle as the target has restricted experimental study to a small subset of all conceivable reactions. The only truly free stationary targets used have been protons[(i)]. The study of neutron reactions has been possible through the interpretation of experiments conducted with deuterium. Clearly it would be very useful to extend our study to other types of reactions. Of particular interest are meson-meson reactions, because of the fundamental role such particles play in the strong interaction. (In addition for the π or K mesons, their lack of spin removes many problems.) However, because of the short meson lifetimes, it is not presently possible to directly study $\pi\pi$ or $K\pi$ scattering.

(i) The only exceptions to this statement are the various experiments in which an electron acts as the target. Examples of this are the electron-positron colliding beam machines, the π-e experiment at Serpukhov, and Fermi's measurement of the neutron-electron cross section.

It has been conjectured that one might be able to extract information about the pion scattering cross section for various beam particles by looking at their interactions with the virtual pion cloud of a nucleon as depicted in Figure I-1a. This idea was first suggested by Goebel, and Chew and Low (Goebel 1958, Chew 1959). Chew and Low point out the success of the analogous model of the deuteron, in which it is considered as a bound state of a neutron and a proton. However the pion-neutron system is virtual by 140 MeV, while the proton-neutron is virtual by only 2.2 MeV. The sizes of these two binding energies is a measure of the relative degrees of approximation involved. However, in either case, when the beam momentum is greater than 1 GeV/c, the binding energy becomes a small effect and presumably can be neglected, to first approximation. As we shall see in Chapter IV, the greatest failing of this approximation is not the neglect of the binding energy. Rather it is the neglect of other processes of comparable importance such as, for example, the excitation of a pion-nucleon resonance[ii].

Thus reactions such as $\pi^- p \to \pi^- \pi^+ n$ and $K^- p \to K^- \pi^+ n$ become interesting reactions to study as possible sources of

---

[ii] This situation is analogous to nuclear scattering in which the scattering can be described as either the scattering from a single nucleon, or from the entire nucleus depending upon the exact conditions.

Figure I-1. Schematic views of various processes.

a) the Chew-Low hypothesis

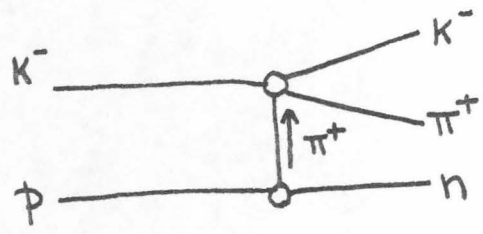

b) the nucleon excitation model

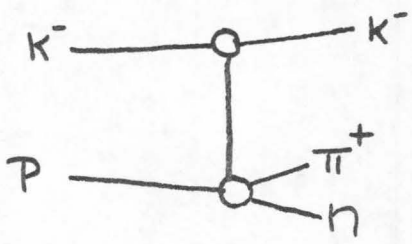

c) OPE model of $pp \to pp\pi^+\pi^-$

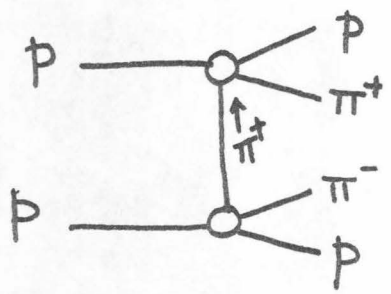

d) the quasi-two-body hypothesis

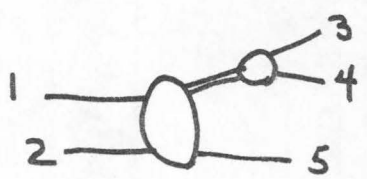

information on meson-meson reactions[iii]. The hypothesis that such reactions are mediated by the exchange of a space-like pion is known as the One Pion Exchange Model (or OPE). It has been extensively developed and tested, and with various modifications has had reasonable success in describing experimental data (Wolf 1969, Gottfried 1964, Fox 1971).

That reactions such as $\pi^- p \to \pi^- \pi^+ n$ or $K^- p \to K^- \pi^+ n$ are dominated by OPE-like mechanisms is indicated by their: (1) s^{-2} dependence of σ_{total} and $\frac{d\sigma}{dt}\Big|_{t=0}$; (2) pole-like behavior of $\frac{d\sigma}{dt}$ as $t \to 0$; (3) lack of shrinkage of $\frac{d\sigma}{dt}$ as a function of s[iv]; and (4) their flat Trieman-Yang angle distribution (Trieman 1961). The one feature of all experiments not reproduced by simple OPE is the quantitative slope of $\frac{d\sigma}{dt}$. The simple model predicts a shape which is flatter than that generally observed. This has led

---

[iii] While reactions such as $\pi^+ p \to \pi^+ \pi^+ n$ or $K^+ p \to K^+ \pi^+ n$ are amenable to study, results of such studies are much more ambiguous due to the lack of an expected strong resonance in the relevant meson-meson channel. However such studies are being undertaken to measure the non-resonant amplitudes.

[iv] Indicative of an $\alpha(t)$=constant behavior in the Regge language. Since this gives, in the Regge formalism, the same behavior as one obtains without Regge corrections, the Regge model is very rarely applied to reactions thought to be dominated by OPE.

to several different, independent prescriptions for adding a faster t dependence. Among these are the absorption model and the Durr-Pilkun kinematic form factors, which will be discussed later[v].

As a quantitative test of the OPE model's validity as a source of meson-meson scattering information, a known cross section can be extracted from a reaction related by the theory. For instance, if we view the process $pp \to pp\pi^+\pi^-$ as in Figure I-1c, then the π^+p and π^-p elastic cross sections and moments can be extracted. This has been done at p_{lab}=6.6 GeV/c (Colton 1968). This experiment is usually cited as conclusive evidence that pole extrapolation and moment analysis will provide information about the analogous meson reactions. However, a careful examination of the results of this experiment leads one to conclude that they are suggestive but certainly not conclusive.

In Figure I-2 the t dependence of the differential cross section from this experiment is plotted along with the prediction (fit) of the Durr-Pilkun theory. Since the cut-off at low t is due to phase space, we can see from the figure that the data are not accurate enough for this to be a stringent test. As we shall see in Chapter V, the large

---

[v] Since these modifications are independently motivated, and give the same numerical results, no model independent picture of the physically meaningful effects emerges.

Figure I-2. The t dependence of $pp \rightarrow p\pi^{-}\Delta^{++}$ at 6.6 GeV/c as determined by E. Colton (1968). In a, c, and e are plotted the t distributions for the data selected on different $\pi^{-}p$ masses. The curve is a Durr-Pilkun fit. The dip at low t is due to the phase space cutoff, so the data do not exhibit a characteristic enough t dependence to make this experiment a very stringent test of the theory.

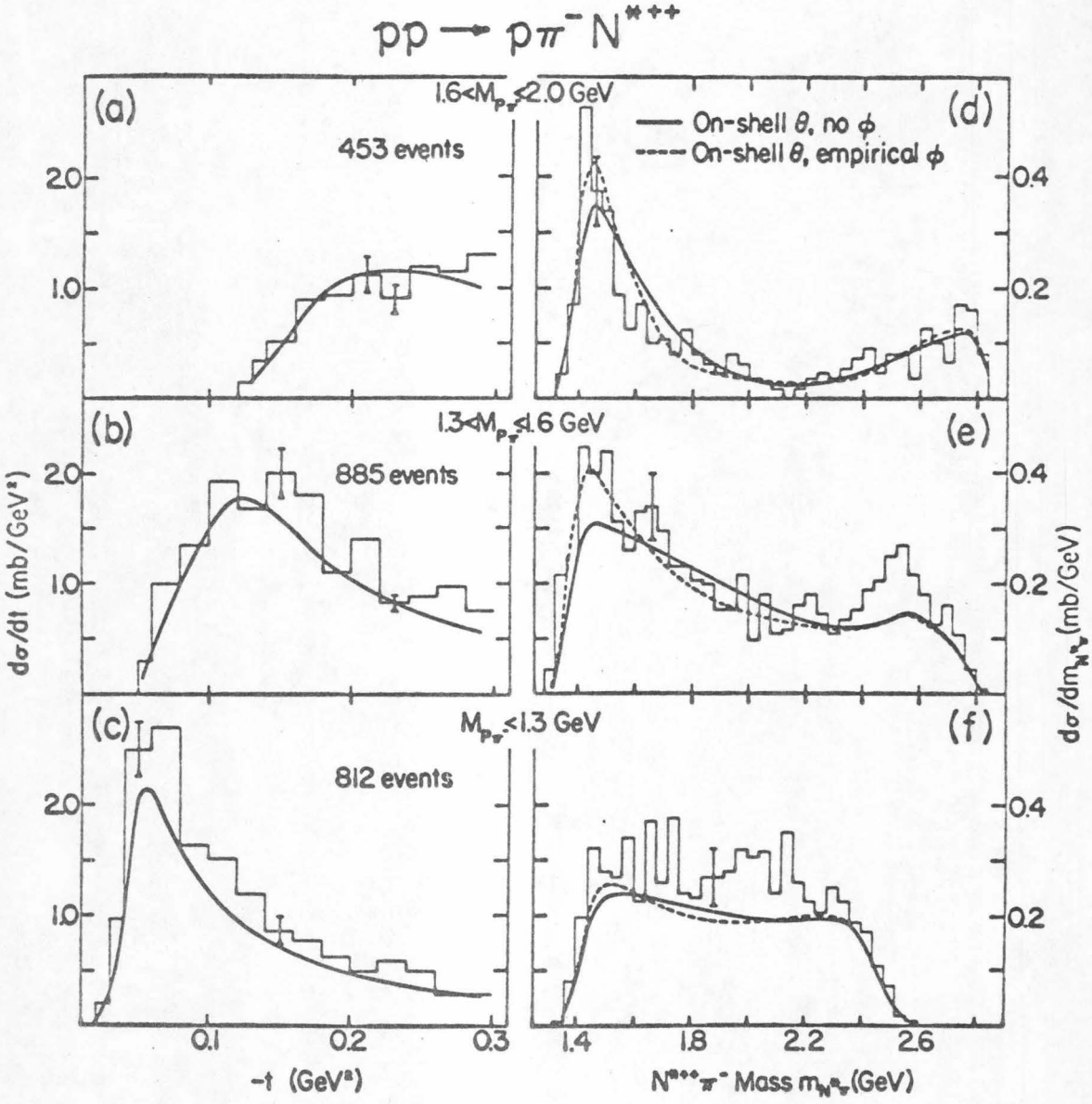
pp → pπ⁻N*⁺⁺
(a)
1.6<M_pπ⁻≤2.0 GeV
453 events
(d)
On-shell θ, no φ
On-shell θ, empirical φ
(b)
1.3<M_pπ⁻≤1.6 GeV
885 events
(e)
(c)
M_pπ⁻<1.3 GeV
812 events
(f)
dσ/dt (mb/GeV²)
dσ/dm_N*⁺⁺π⁻ (mb/GeV)
-t (GeV²)
N*⁺⁺π⁻ Mass m_N*⁺⁺π⁻ (GeV)

number of free parameters in this theory requires a large variety of experiments to both fix and check all these parameters, so this does not comprise a conclusive test of the model.

In Figures I-3 and I-4, the resulting moments (the points) and the on-shell measurements (the curves) for $\pi^- p$ and $\pi^+ p$ elastic scattering are plotted[vi]. The $\pi^- p$ moments show some agreement, but the $\pi^+ p$ results show a glaring discrepancy. In order to justify the Durr-Pilkun model, one must extract the features of both $\pi^- p \to \pi^- p$ and $\pi^+ p \to \pi^+ p$ without ambiguous post hoc modifications. It has been claimed (Colton 1968) that this discrepancy can be cured by either extrapolating the moments in t, or by requiring the other vertex to be a single strong resonance, or by a smaller t cut, etc. However, until this is actually demonstrated for both $\pi^- p$ and $\pi^+ p$, the validity and universality of the method is open to strong doubts.

In spite of such doubts, many people have begun to apply such methods to mesonic reactions. The simplest

---

[vi] Where the differential cross section is expanded as

$$\frac{d\sigma}{d\Omega} = \frac{\sigma}{4\pi} \sum_L \left(\frac{A_L}{A_o}\right) P_L (\cos \theta).$$

Figure I-3. The shape parameters for $\pi^- p$ elastic scattering as determined in $pp \rightarrow pp\pi^+\pi^-$ at 6.6 GeV/c (from Colton 1968). The solid curves are the actual $\pi^- p$ measured values. The experimental moments seem to be in qualitative agreement with the $\pi^- p$ measured values although slight quantitative discrepancies are possibly present.

$p + p \rightarrow N^{**} + p + \pi^-$

Shape parameters for $\pi^- p$ quasi elastic scattering

$1.16 < M(N^*) < 1.30$ GeV $|\cos\theta_{N^*}| > .965$ 2314 combinations

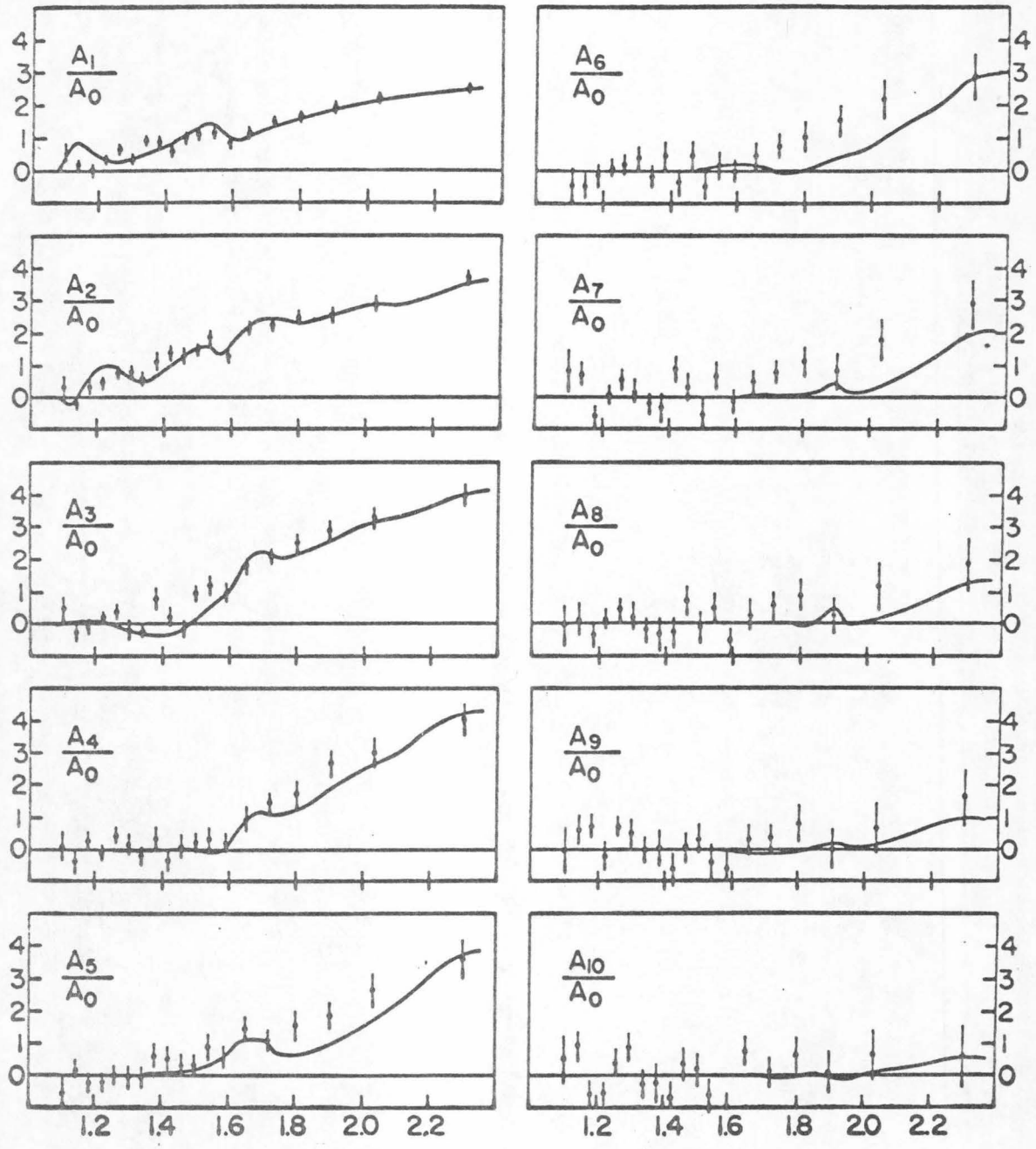

Figure I-4. The shape parameter for π^+p elastic scattering as determined in $pp \rightarrow pp\pi^+\pi^-$. The solid curves are the actual π^+p measured values. There is clearly a glaring discrepancy in A_1/A_0 in these data.

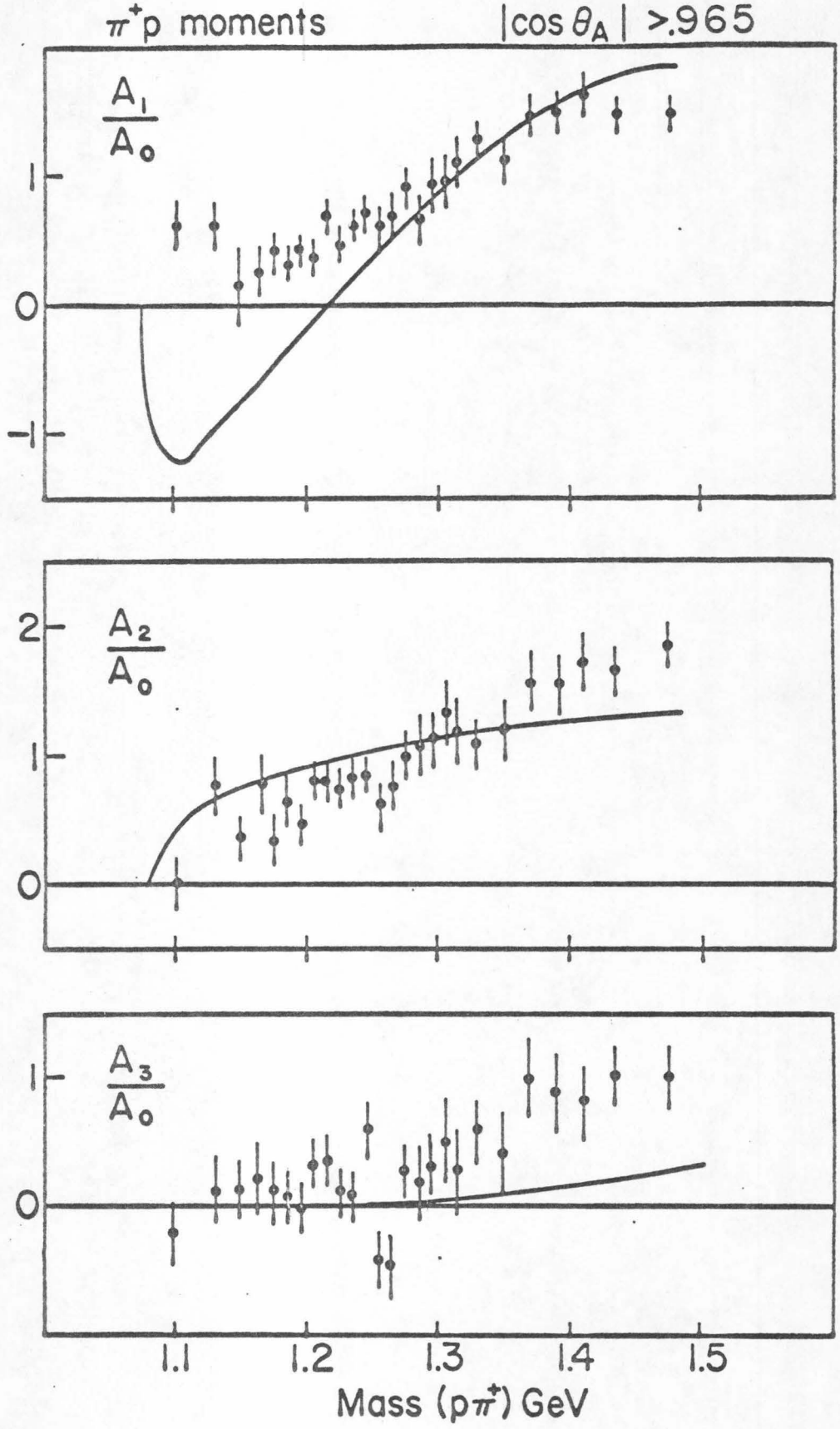
π^+p moments
$|\cos\theta_A| > .965$
$\frac{A_1}{A_0}$
1
0
-1
$\frac{A_2}{A_0}$
2
1
0
$\frac{A_3}{A_0}$
1
0
1.1
1.2
1.3
1.4
1.5
Mass ($p\pi^+$) GeV

reaction to examine is $\pi^- p \to \pi^- \pi^+ n$. Many such experiments have been performed and they seem to yield the features one expects in $\pi\pi$ scattering (Schlein 1967, Malamud 1967). In order to test and extend this hypothesis, several experimenters have begun to examine other reactions. An interesting extension is that of the related pair of reactions $K^- p \to K^- \pi^+ n$ and $K^+ n \to K^+ \pi^- p$, where one can begin to explore the $K\pi$ elastic scattering amplitude. In this case the G-parity constraint which rules out ρ exchange in $\pi^- p \to \pi^- \pi^+ n$ is not present so that these reactions could show deviations not present in the pion induced reactions. Experiments have been completed at 5.5 GeV/c, and 10 GeV/c in $K^- p$ and at 3 GeV/c in $K^+ n$; a comparison of these indicates that this is a more complex system than $\pi^- p \to \pi^- \pi^+ n$ (Fox 1971, ABCLV 1968, Bassompierre 1970).

We have completed a high statistics experiment on the reaction $K^- p \to K^- \pi^+ n$ at p_{lab}=2 GeV/c. The aim of this experiment was to extract the $K^- \pi^+$ elastic cross section. However, as we shall see, this problem is far more ambiguous than was realized at the outset, so that a far more systematic study of several reactions at different energies and with extremely high statistics will be required before we can understand all the extraneous effects, and extract the $K\pi$ cross-section unambiguously.

In Chapter II, the standard experimental methods are discussed and the resulting ambiguous samples summarized.

In Chapter III, the studies which determine the reliability of our data are presented. Also the criteria which define our final data sample are summarized.

In Chapter IV, the data are presented and their qualitative features are discussed. As part of this chapter the evidence indicating an anomalous backward peak is presented and discussed. This backward peak is somewhat surprising since, taken at face value, it violates either SU(3) or the symmetry between s and t channels.

In Chapter V, a quantitative comparison of our data with other experiments is made, and an attempt to extract the $K\pi$ phase shifts is presented. The comparison seems to be surprisingly good but the phase shift analysis seems to yield inconclusive results.

B. Kinematics

In the detailed study of a reaction such as ours, one obtains information from the dependence of the frequency distribution of events upon the various kinematic variables and the association of such dependencies with those of various models. We shall present a brief description of the kinematic variables commonly used in the analysis of a three body final state.

In such a state at fixed beam momentum, there are four kinematic dimensions (neglecting nucleon spins - - see Appendix IX). The particular set of variables we choose is not unique. What we want is a set which is most appropriate for the physics we are describing. In our case the dynamics is dominated by the scattering of the two initial particles into a quasi-two-body final state in which one of the final state particles subsequently decays as depicted in Figure I-1d. This suggests that we choose as our set of kinematic variables the momentum transfer ($t=(\bar{p}_2-\bar{p}_5)^2$); the resonance's mass ($m=\bar{p}_3+\bar{p}_4$); and the resonance's decay distribution (θ,ϕ), and thus treat the reaction $K^-p\to K^-\pi^+n$ as the sum of two processes $K^-p\to\bar{K}^{*o}n$ and $\bar{K}^{*o}\to K^-\pi^+$.

By decomposing the meson-meson center of mass angular distribution into its spherical harmonic moments, we reduce a continuous two dimensional distribution (θ,ϕ) into a discrete set of numerical values which is, in practice,

quite limited in number[vii]. However there does exist one ambiguity in this decomposition which cannot be a priori resolved. There exists the question of what axes to use in defining the relevant angles. The two frames that are commonly used are the helicity (or s-channel helicity) frame, and the Gottfried-Jackson (or t-channel helicity) frame; shown in Figures I-5a and b. In both frames the K^-_{out} - π^+_{out} center of mass is at rest and the y axis is defined as being perpendicular to the production plane. In the helicity frame, the neutron's momentum vector lies along the -z axis; in the Gottfried-Jackson frame the K^-_{in} momentum vector lies along the +z axis. (The azimuthal angle in the Gottfried-Jackson frame is commonly known as the Trieman-Yang angle.) Clearly for any given event the transformation between frames is a well defined rotation. However this rotation is dependent upon both t and $m_{K\pi}$ (for fixed beam momentum).

Naturally the choice of which two particles in a reaction to regard as the decay products of a resonance is ambiguous and must be determined from experiment. For

---

[vii] An exactly equivalent procedure is to decompose the decay distribution by the density matrix formalism. This possesses the advantage of being more closely related to the individual amplitudes, but depends upon the assumption of a maximum spin.

Figure I-5. The two coordinate frames commonly used for decomposing the Kπ decay distribution.

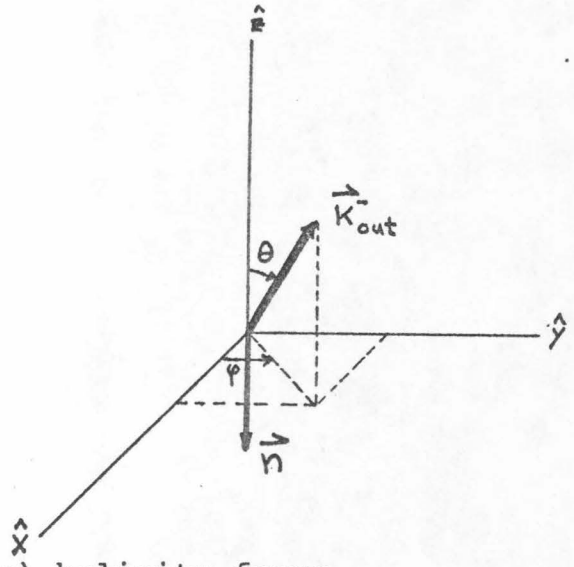

a) helicity frame

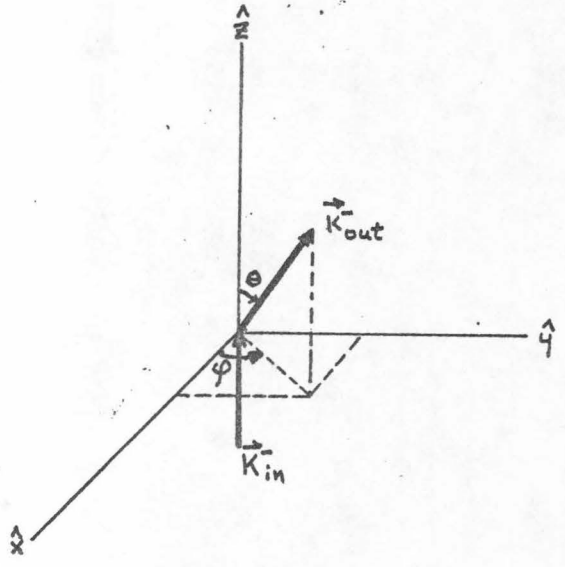

b) Gottfried-Jackson frame

example, the reaction mentioned above can also be regarded as $K^-p \rightarrow K^-N^{*+}$ and $N^{*+} \rightarrow \pi^+ n$. The choice of which model one uses must be empirically determined by finding which view yields the simplest picture of the reaction.

A third, independent choice of variables is that of the Dalitz plot (see Appendix IX). In this scheme, we choose the effective mass squared of two different pairs of final state particles as independent variables. This choice of variables possesses the advantage of yielding a coordinate system in which the phase space in a differential volume is independent of the coordinates (see Appendix IX). Thus any enhancements in a two dimensional frequency distribution must arise in a dynamical manner. Note that since there are only two variables chosen, the dependence of the amplitude upon two dimensions is being suppressed.

Chapter II. Experimental Methods and Data Extraction

A. Beam, Bubble Chamber, And Scanning Measuring Projectors

The 72 inch hydrogen bubble chamber at the Lawrence Radiation Laboratory was exposed in 1964 as part of the K-63 exposure to a beam of 2.0 GeV/c K^- mesons (Hubbard 1964). Figure II-1 shows a schematic diagram of the beam line. The K^- mesons were separated from the π^-'s by two electrostatic separators (S1 and S2) and two mass slits. From measurements and analyses of other event topologies in this film (Dauber 1966, Trippe 1968), the pion contamination in the beam is known to be (1.4 ± 0.3)% and the momentum spread is ±2%.

The chamber was expanded once per Bevatron cycle. Flashtubes and a shutterless camera were used to record three views of each expansion of the chamber on one roll of 46 mm film using the Berkeley film format. Three views are necessary to avoid ambiguities which arise for some spatial configurations when only two views are used. 200,000 expansions were recorded on 315 rolls of film with an average of 7.5 incident K^- mesons per expansion (determined by Dauber and Trippe 1965b). This corresponds to a total track length, in the fiducial volume discussed below in Section III-D, of 6.5 events/μbarn.

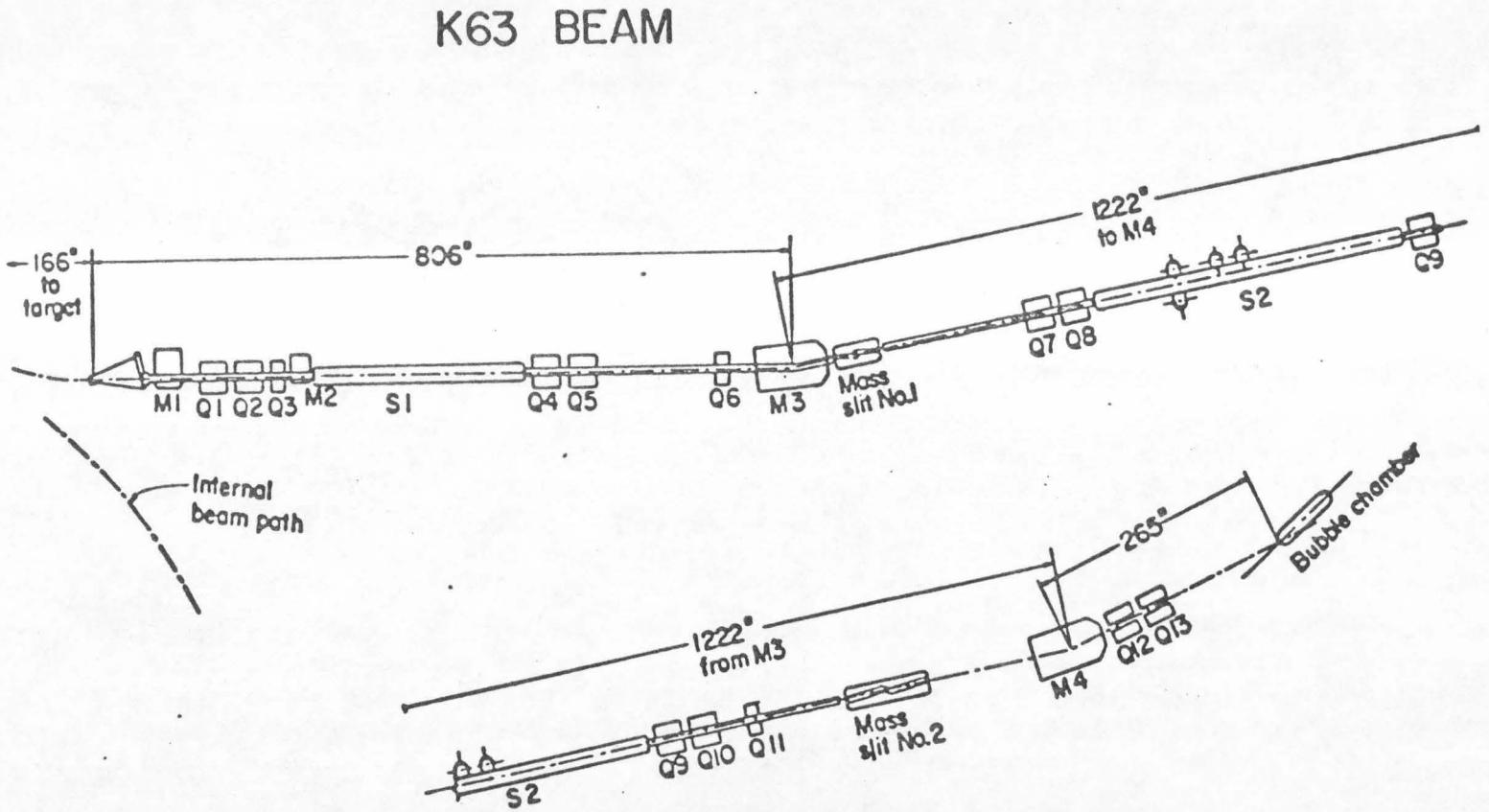

Figure II-1. Schematic diagram of the K-63 beam line. The M's are bending magnets, the Q's are quadrapoles, and the S's are the electrostatic separates.

Figure II-2 is a photograph of a typical event in the 72 inch chamber of the type:

$$K^- p \rightarrow \bar{K}^{*o}(890)\ n \qquad \bar{K}^{*o} \rightarrow K^- \pi^+ \qquad (1)$$

The short horizontal lines numbered 0 through 15 running down the left hand side of the chamber are called the "rakes" and are used for visual approximate location of the events. The "+"'s, positioned at the top glass of the chamber, and the "$\dagger$"'s, positioned on the bottom surface of the chamber, form the fiducial system used for precise definition of the measurement coordinate system.

The origin of the coordinate system used (see inset in Figure II-2) lies on the bottom of the chamber between rakes 7 and 8. The y axis increases in the direction of the incident beam particles and runs the length of the chamber along the bottom, approximately midway between the sides. The x axis is in the horizontal plane, transverse to the beam direction and the z axis is vertical. The azimuthal angle of a vector is the angle made between the vector's projection on the xy plane and the x axis. Its dip angle is the angle between the vector and the xy plane.

Figures II-3 (a-d) display the distributions of x coordinate, z coordinate, azimuthal angle, and dip angle projected to y = 0 for the beam tracks of all events

Figure II-2. The 72" hydrogen bubble chamber.

a) the coordinate system of the 72" chamber

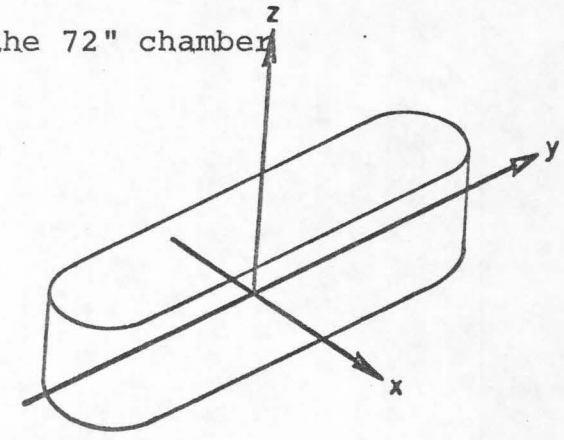

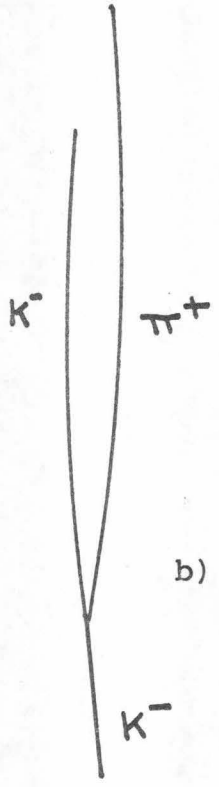

b) photograph of a typical event in the 72" chamber of the type $K^- p \rightarrow K^{*0}(890) n \rightarrow K^- \pi^+ n$.

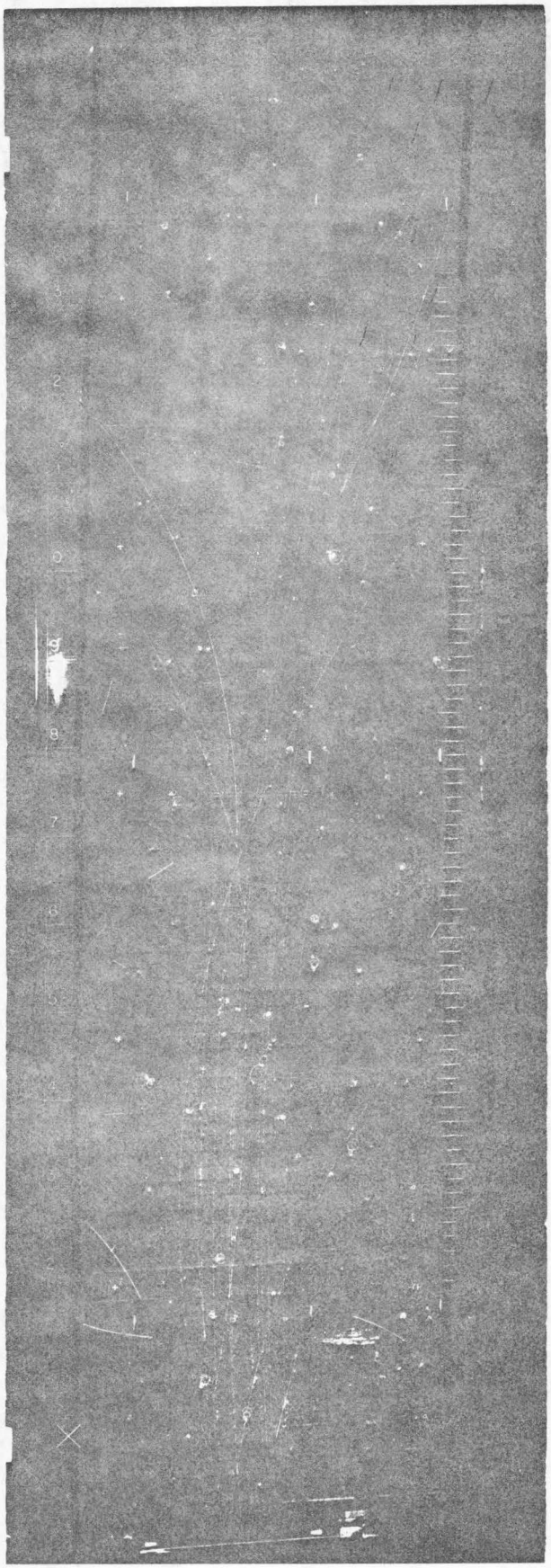

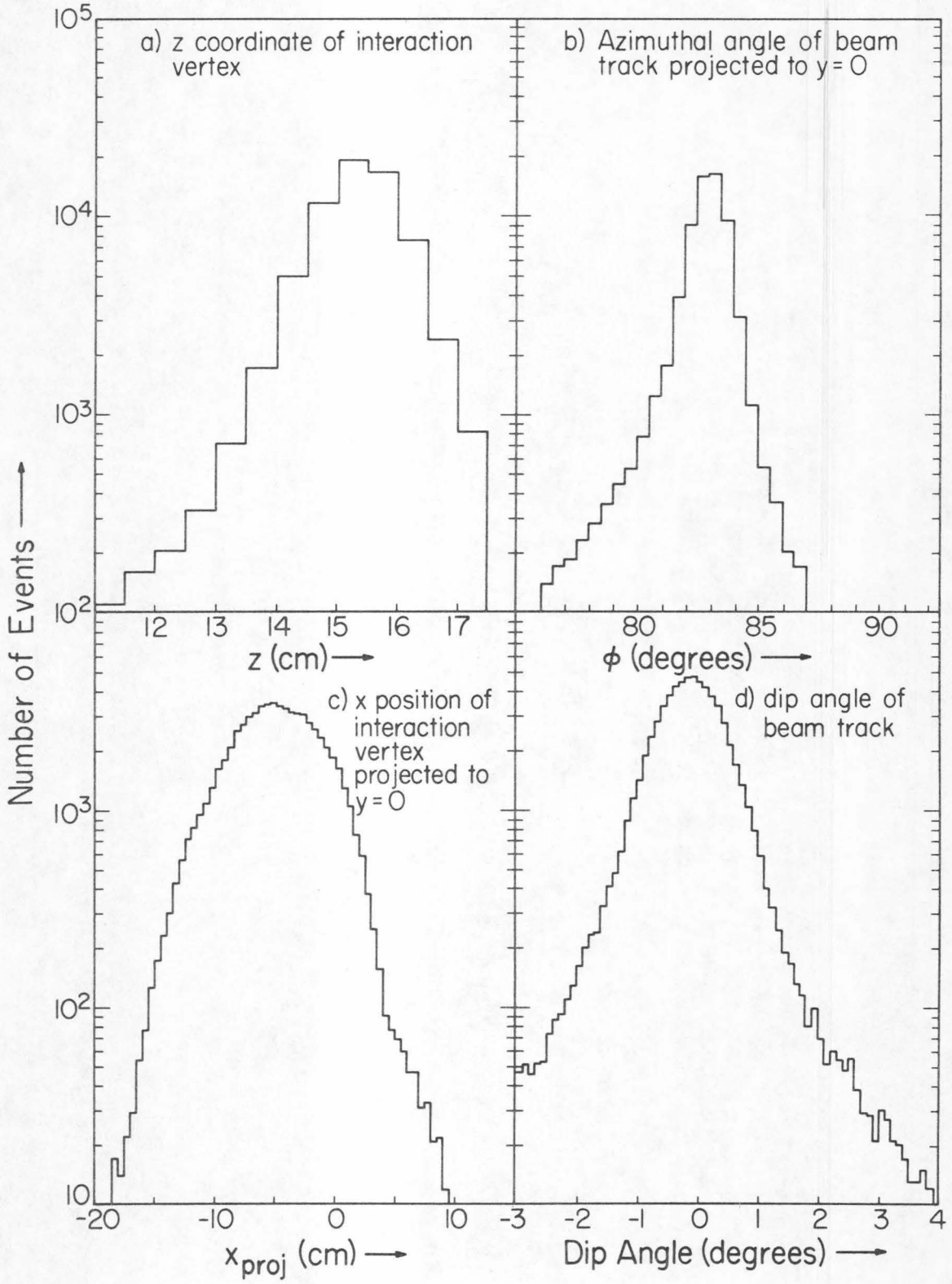

Figure II-3. Dimensions of the beam based upon measured events.

measured in this experiment. The x and z coordinate distributions give the transverse dimensions of the beam as it traverses the chamber. The spread in x aids in separating the interaction points from other beam tracks and facilitates measurement. The magnetic field is vertical with such a sign that negative tracks bend right and positive tracks bend left as viewed on the scanning tables (see Figure II-2).

Figure II-4a is a scatter plot in x and y of the interaction points of all events measured in this experiment and demonstrates the swath of beam as it passes through the chamber. Figure II-4b is a projection of the y position of the interaction vertices and displays the $\sim$20% gradual attenuation of the beam between y = -80 cm and y = 40 cm due to interactions and decays. The sharp drop in the distribution for y > 40 cm was caused by a reduction in the fiducial volume. This reduction was artificially imposed during the measuring process.

The semi-automatic image plane digitizers at UCLA known as Scanning and Measuring Projectors (SMP's) were used to both scan and measure the events of interest in the film according to the criteria discussed below in section II-C. The SMP's (Alvarez 1960, Munson 1963) were designed and constructed at the Lawrence Radiation Laboratory. An on-line IBM 360/40 computer collected, filtered, and tested the SMP measurements. The need for a fast

Figure II-4. Distribution of event vertices in the chamber.

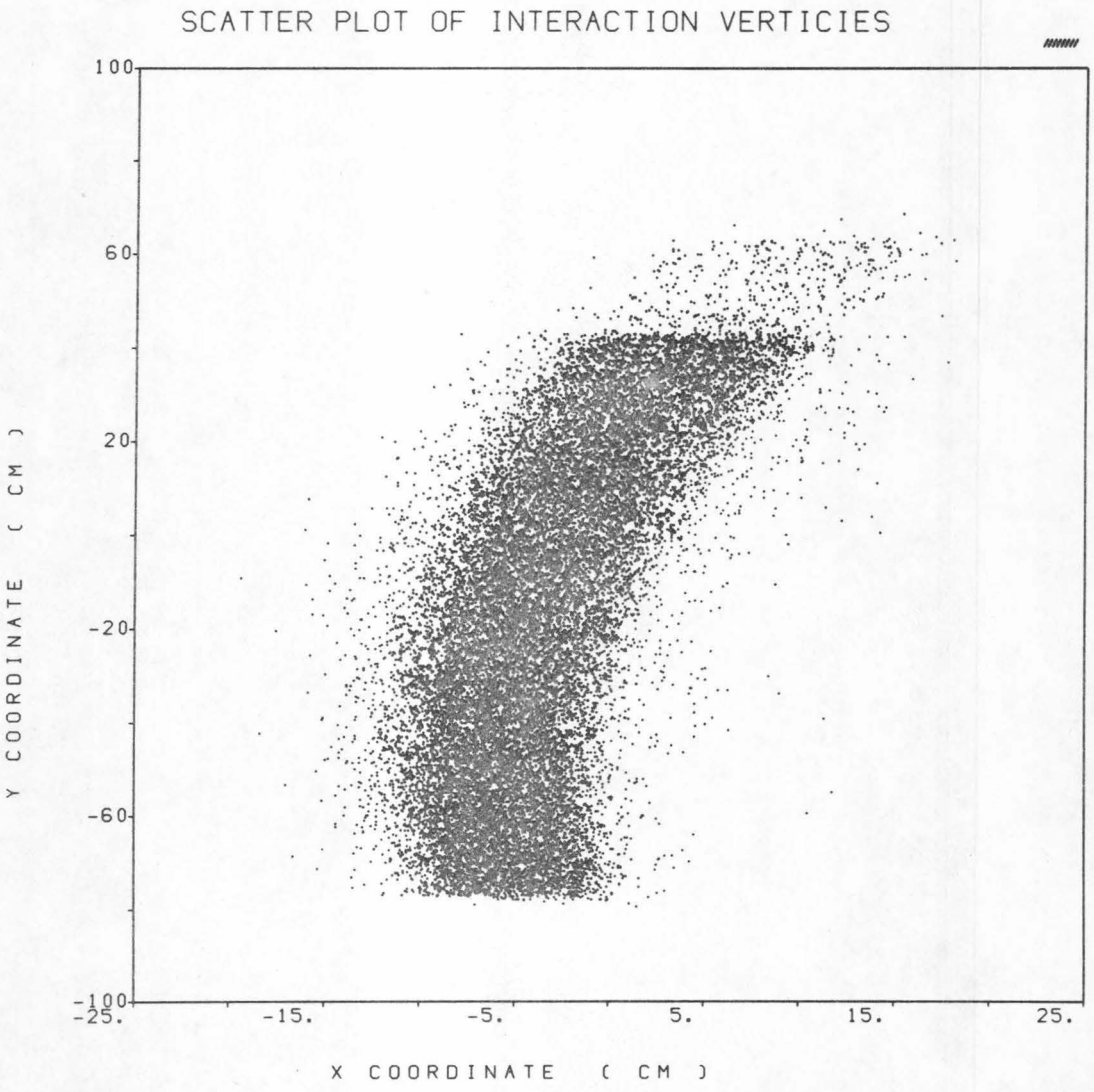

a) x-y scatter plot of the interaction vertices.

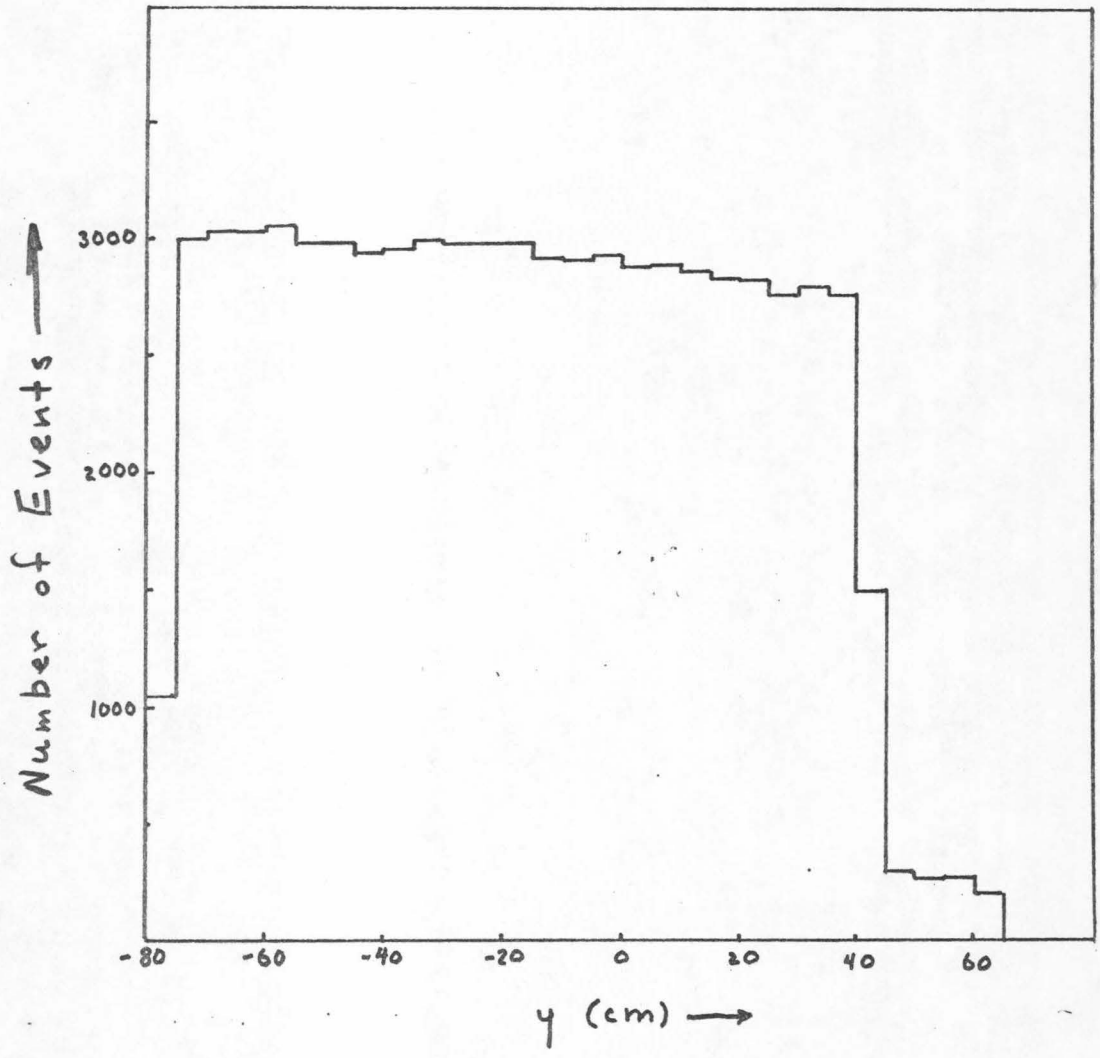

b) the distribution in y of the interaction vertices.

digital computer to pre-process the data is due to the semi-automatic nature of the measuring machines. A SMP digitizes ∿100 points along a track, of which a large fraction (∿30-40%) is unrelated to the track being measured. These data are filtered and averaged to give a maximum of sixteen points per view in the processed output record.

Since the SMP digitizes in the image plane, optical distortion between the film and image planes is corrected for by measuring a grid of known dimensions and performing a least squares polynomial fit to the abberations. The grid, which is scribed on mylar film, was measured on an accurate film plane measuring machine in order to determine its true dimensions. These corrections are applied to the SMP measurements in real time (i.e., as soon as the track measurement is completed) by the 360/40 so that the output record consists of corrected film plane coordinates.

B. Topologies and Expected Event Frequencies

The purpose of this experiment is to study the reaction:

$$K^- p \rightarrow K^- \pi^+ n$$

In a bubble chamber, events of this type with two charged, outgoing particles appear as "two-prong" interactions as depicted in Figure II-5. There are several "background" reactions which also have the two-prong topology, such as $K^- p \rightarrow K^- p$, $K^- p \rightarrow K^- p \pi^0$, and other inelastic channels. Additional sources of background are reactions which contain a Λ^0 or a K^0 which decays via a neutral mode in addition to two charged, outgoing particles. In order to estimate this latter source of background, a sample of two-prong V events (where the Λ^0 or K^0 decays via a charged mode) was also measured. This sample will be discussed in section III-B. These two topologies which are of interest to this experiment, one which contains the signal and one which contains the background, are shown in Figure II-5.

In order to estimate the event yield and background problems of the experiment, we made use of the available cross-section measurements for the significant reaction channels in the $K^- p$ interaction at the nearby momentum of 1.95 GeV/c (Smith 1965). The cross sections of significance to this experiment appear in Table II-1. The expected number of events of each reaction type in the table are

Table II-1. Stable State Cross Sections at 1.95 GeV/c (as determined by Smith 1965).

	Final state	σ(mb)	Expected number of events (in thousands) in this experiment by topology: 2 prong	2 prong V	2 prong kink*
State of interest	$K^-\pi^+n$	2.7±.5	16.5		1.2
States with Λ's	$\pi^-\pi^+\Lambda$	1.47±.09	3.0	6.0	
	$\pi^-\pi^+\Sigma$	0.57±.05	1.2	2.3	
	$\pi^-\pi^+\Lambda\pi^0$	2.11±.14	4.3	8.7	
	$\pi^-\pi^+\Lambda+n\pi^0$ }	0.57±.04	1.2	2.3	
	$\pi^-\pi^+\Sigma^0+n\pi^0$ }				
		4.72±.18	9.7	19.3	
States with K's	$\pi^-p\bar{K}^0$	1.89±.12	7.7	3.8	
	$\pi^-p\bar{K}^0\pi^0$	.65±.06	2.6	1.3	
	$\pi^-\pi^+\bar{K}^0n$	.57±.06	3.8	1.9	
	$\pi^-\pi^+\bar{K}^0n+n\pi^0n\geq1$ }	.03±.01	.4	.2	
	$\pi^-pK^0n+n\pi^0n\geq2$ }				
		3.14±.15	14.5	7.2	
Other States with Protons	K^-p	7.91±.78	47.6		3.7
	$K^-p\pi^0$	1.60±.30	9.7		0.7
		9.51±.84	57.3		4.4

Table II-1 (cont.)

Other States	$\Sigma^-\pi^+$	0.17±.02			1.0
	$\Sigma^+\pi^-$	0.55±.06			(3.4)
	Ξ^-K^+	0.101±.014			.6
	$\Sigma^-\pi^+\pi^0$	0.70±.06			4.3
	$\Sigma^-\pi^++n\pi^0\ (n\geq 2)$	0.20±.05			1.2
	$\Sigma^+\pi^-\pi^0$	0.80±.10			(4.9)
	$\Sigma^+\pi^-+n\pi^0\ (n\geq 2)$	0.42±.10			(2.6)
	$\Xi^-K^+\pi^0$	.026±.007			.2
	$\Xi^-K^0\pi^+$	.057±.009			.3
	$\Xi^0K^+\pi^-$	.062±.010	.1	.2	
			.1	.2	7.6(+9.9)

*Figures in parentheses are events in which the kink is on the positive track.

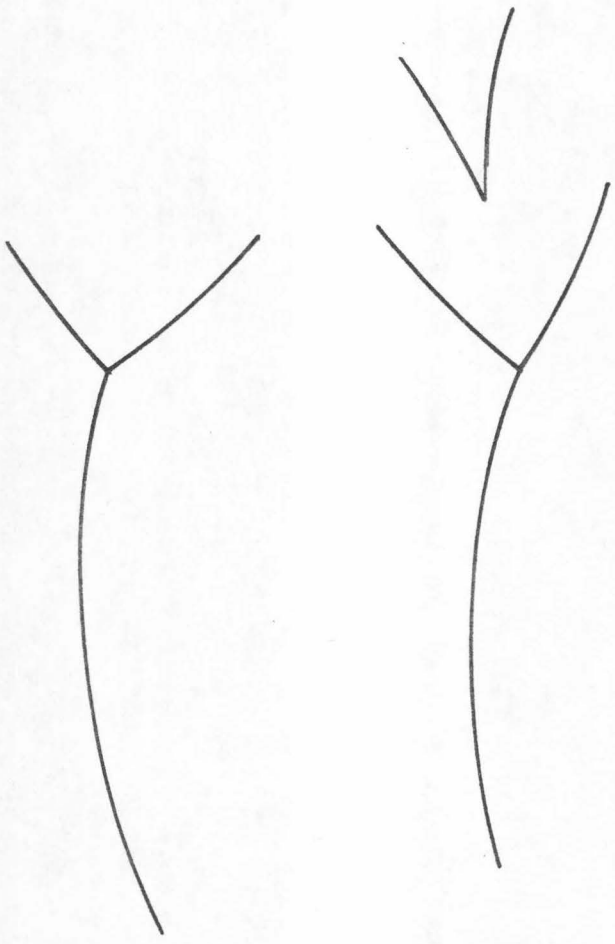

a) two prong b) two prong Vee

Figure II-5. Topologies of interest in this experiment.

based on these cross sections and the known K^- track length in the exposure for the fiducial volume used in our scan (6.5 events/μbarn; see Section II-C).

C. Scanning criteria and Fiducial volume

From Table II-1, it is evident that about five times as many events have the two-prong topology as are really $K^-p \rightarrow K^-\pi^+n$. While a large fraction of these events are kinematically easy to separate, they cause unnecessary measurement time and waste computer time unless removed in scanning.

Most of these two prong background events, about 80%, contain protons which can, under certain circumstances, be distinguished from π^+ mesons. The following scanning criteria were established to reject these events while eliminating a negligible number of real events:

(i) All events in which the positive track stops within the chamber were rejected. Such tracks must be protons since a stopping π^+ decays via the familiar $\pi^+ \rightarrow \mu^+(\nu) \rightarrow e^+(\nu\nu)$ sequence. This selection depends upon the scanner's ability to determine through the use of stereoscopic superposition[i]

---

[i] The method of determining whether a track's endpoint occurs at a surface perpendicular to the camera axis is accomplished through the small angle stereoscopic nature of the camera system. The images of the fiducial marks in two separate views are superimposed by simultaneous projection. If the two images of a track endpoint are then superimposed as well, then the endpoint lies in the same plane as the fiducial marks, which are on the upper and lower surfaces.

whether a track's endpoint lies within the chamber or at the chamber's top or bottom (which would be the case if the track left the chamber before stopping).

(ii) To reject protons which leave the chamber a track bubble density criterion was also employed. This criterion was extremely delicate since any real events rejected because of spuriously dark pion tracks could seriously bias our sample. To be rejected, a positive track had to be long enough and straight enough to pass between two parallel lines 13.5 cm long and 0.42 cm apart (see Figure II-6), and must have less than 1 gap per centimenter of track (a gap is a break in the line of bubble formation). The length criterion insured that the particle had a dip angle less than 45^{o} (since the beam is about 15 cm from both the top and bottom of the chamber), the width criteria determined a maximum sagitta and therefore a minimum momentum (of 300 MeV/c). At this momentum a pion is 1.3x minimum ionizing and a proton is 10x. The density is proportional to the secant of the dip angle and thus the dip angle can increase the density by a factor less than 1.4. In order to meet the $\leq$ 1 gap/cm ionization criterion, a track must have an apparent ionization of $\geq$ 7x. Although our choice may seem too conservative, it was felt that the critical nature of this selection and some of the known bad properties of the chamber's track

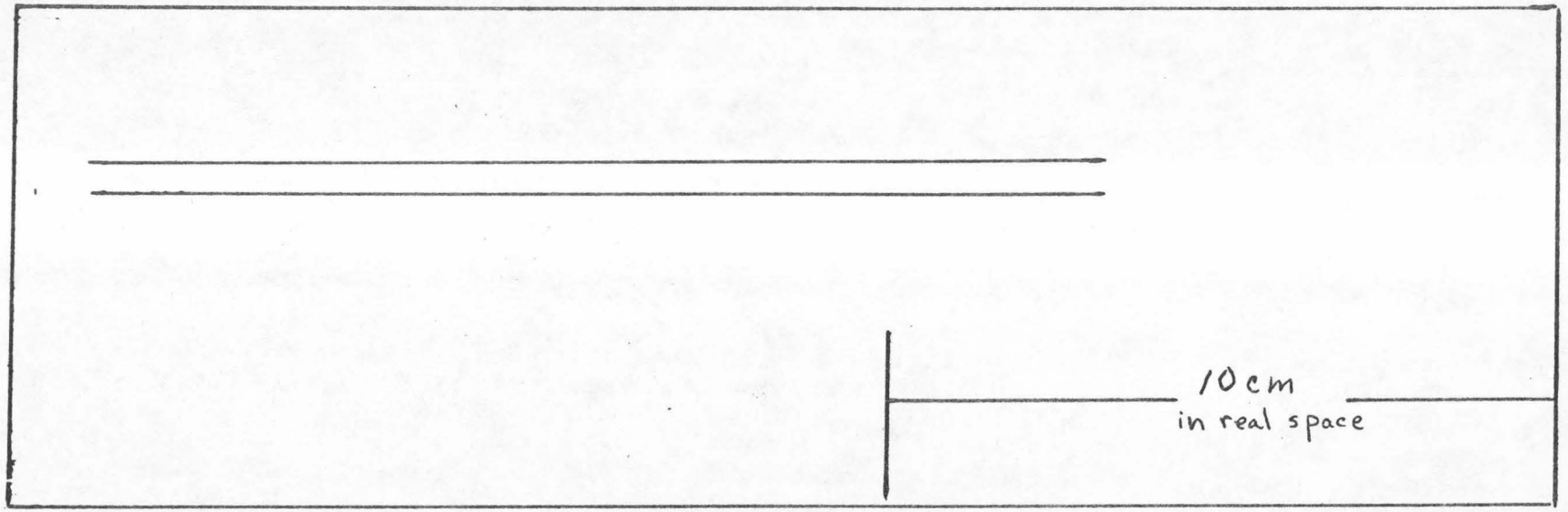

Figure II-6. Template used to reject protons and kinks.

illumination, made it dangerous to attempt a more stringent proton exclusion[ii].

In Figure II-7 is plotted the azimuthal angular distribution of the positive track about the beam direction for elastic events and for the $K^-\pi^+n$ sample. This distribution should be sensitive to scanning loss biases. The observed isotropy of this distribution for the $K^-\pi^+n$ (Figure II-7a) events as contrasted to the elastic events (Figure II-7b) thus implies that the above scanning selections did not bias our results in this way.

Further scanning criteria were established to eliminate the events which contain a Σ^- or a Ξ^-. Since these particles have a very short lifetime, they decay very close to the vertex. Thus by demanding that the negative track should not have a kink (decay) closer than 10 cm from the vertex, they were virtually all eliminated without rejecting a significant number (<1%) of real events in which the K^- decays (see Appendix I). In addition to causing extra measuring effort, such events pose an extremely difficult problem for the kinematics programs if not eliminated. The short tracks always have a poor momentum measurement, since the error in the momentum is inversely

---

[ii] The extent to which ionization can be used as an aid in the resolution of the ambiguities is discussed in Section III-B.

Figure II-7. Rotation angle of the positive track about the beam.

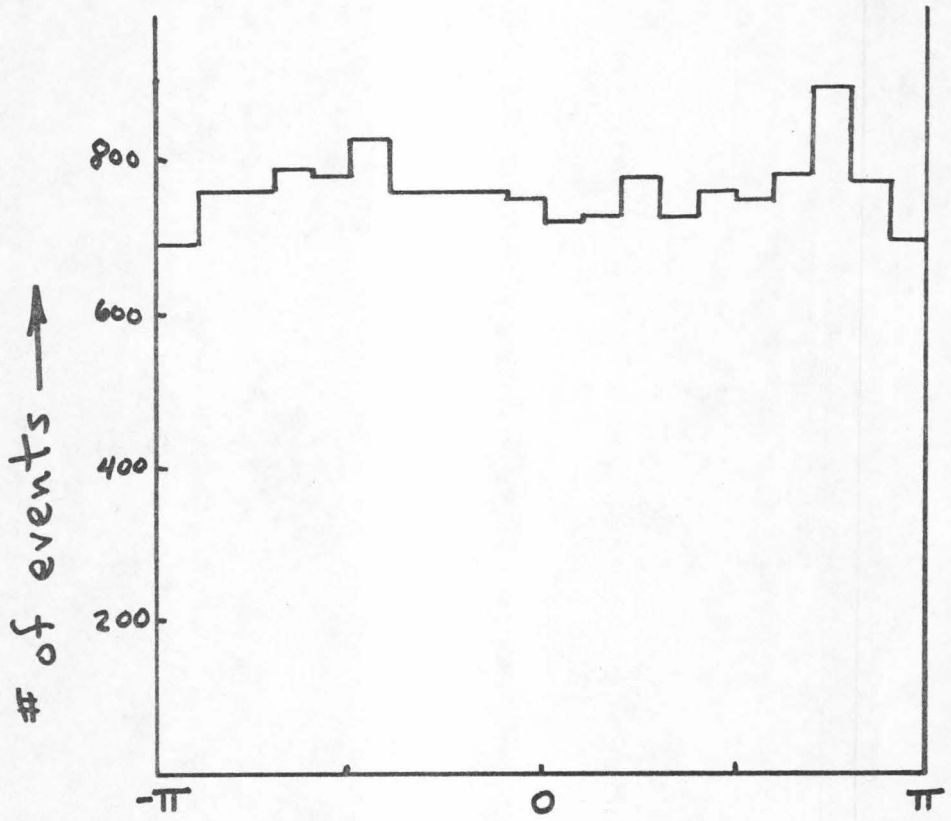

a) events which fit $K^- p \to K^- \pi^+ n$ where $0.84 < m_{K\pi} < 0.94$.

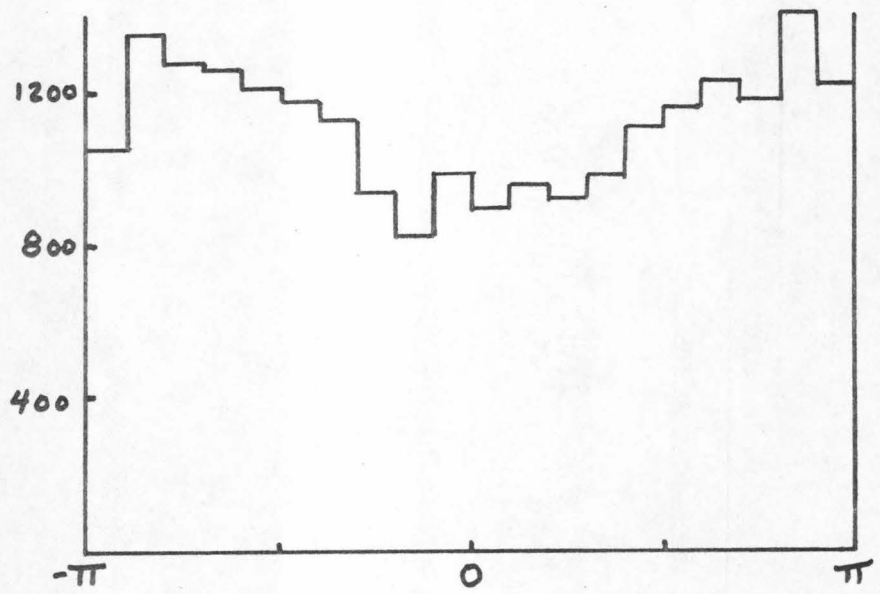

b) coplanar events ($K^- p \to K^- p$ elastic).

proportional to the square of the measured length. Events with one poorly measured momentum will fit almost any one-constraint hypothesis, since one poor measurement is roughly equivalent to losing one constraint.

The scanning fiducial volume[iii] was defined by instructing the operators to reject any event for which the vertex falls below a straight line passing through rake 0 or above a line through rake 11. The scanners were instructed to perform this test only in view 3, since it is sometimes dependent upon which stereo view was used. This did not define a simple fiducial volume in space, but was easy to apply to check scanning efficiencies. In order to compute the absolute cross section, a smaller but well defined fiducial volume, discussed in Section III-D, was used.

[iii] At first a larger fiducial volume was used (< 13). This is the source of the events beyond $y = 40$ cm.

D. Data processing

Once the data are digitized by the SMP machines, they are processed through the TVGP-SQUAW-ARROW[iv] system of computer programs (see Figure II-8) developed at LRL to reduce the events to sets of momentum 4-vectors which satisfy the constraints of energy-momentum conservation. A brief description of these programs is given here:

TVGP reads an SMP output tape and performs spatial reconstruction of each track. A five parameter, three dimensional curve is constructed and projected into each view and a least squares fit is performed to minimize the distance on the film from the measured points to the projected curves. TVGP outputs the azimuth, slope, and inverse projected momentum at the beginning and at the end of each track as well as the correlated errors for these quantities. Film setting errors and Coulomb scattering errors are included in the estimated errors. (The mass of each particle must be assumed at this point in order to compute the effect of energy loss on the track.) TVGP corrects for the optical system by performing a polynomial

---

[iv] The version of TVGP and SQUAW used in this experiment was obtained by splitting the Berkeley SIOUX program (version 4) into its two parts.

Figure II-8. Computer processing steps.

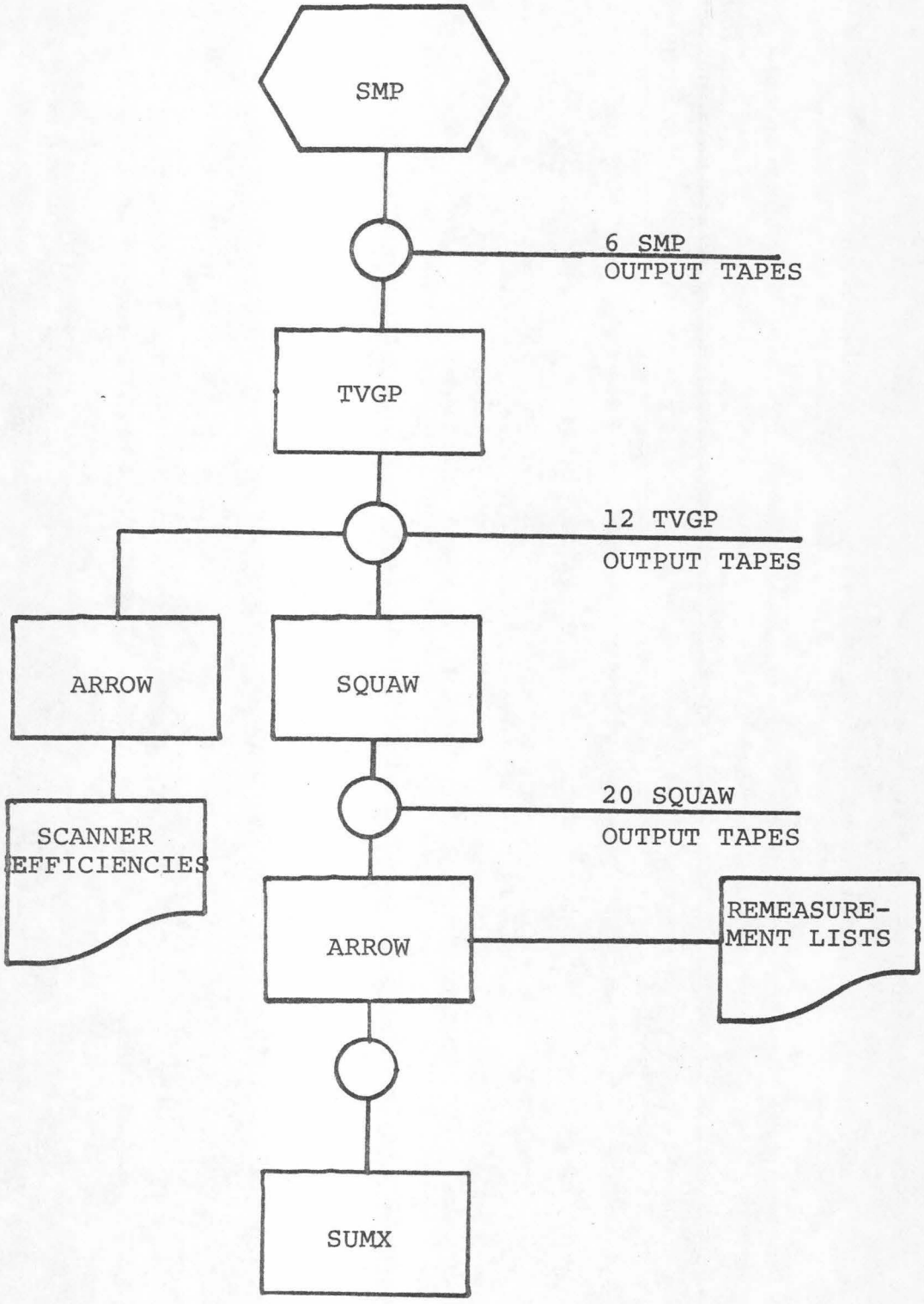

correction to yield ideal camera plane coordinates. For the 72 inch chamber, the distortions are large and not completely understood. This factor accounts for the systematic underestimation of errors which will be discussed in Section II-E.

The magnetic field in the 72 inch chamber varies by 10% in the chamber. This is compensated for in TVGP by a polynomial approximation, and the overall field is scaled by a constant which is adjusted to yield the correct K^o mass in effective mass fits to the V's.

SQUAW inputs a TVGP output tape and fits the measured momenta and angles to kinematic hypotheses. The fit is done by minimizing the chi-square (χ^2) function:

$$\chi^2(x_k) = \sum_{i=1}^{n} \sum_{j=1}^{n} (x_i - x_i^m)\ G_{ij}^{-1}\ (x_j - x_j^m)$$

subject to the analytic constraints appropriate to the hypothesis being tested. The x_i^m and x_i are the measured and fitted values of the azimuth, slope, and inverse projected momentum of each track at the production vertex, and G_{ij}^{-1} is the inverse of the measured error matrix for these quantities. The four energy-momentum conservation equations provide four constraints minus the number of unmeasured variables involved in a given hypothesis. Constraints are introduced by the method of Lagrange multipliers and an iterative search is used to find the point

which minimizes the χ^2. SQUAW outputs the fitted quantities and errors for each hypothesis which achieves a confidence level of better than 10^{-5}.

The two experiment dependent operations in SQUAW are the choice of which kinematic fits to test and the beam averaging. The first of these is straightforward; all possible kinematic fits of interest must be entered into the control subroutine. The beam averaging is a much more controversial operation. In most events the beam track momentum is the least accurately measured quantity, since the beam track has the highest momentum, and thus the least curvature of any track in the event. In order to improve the momentum knowledge of this track in the kinematic fit, it is possible to take advantage of the beam's narrow momentum spectrum to determine an average value, which is then averaged with the measured momentum for each event in TVGP.

The standard technique for computing the nominal beam momentum is to average the fitted beam momentum from a sample of topologically identifiable, kinematically highly over determined events (i.e. events which have many kinks and vees and in which no kinematic variables are unmeasured). For example, the beam momentum in our film had been previously determined by using the reactions $K^-p \rightarrow \Xi^- K^+$, and $K^-p \rightarrow K^+\pi^-\Xi^0$. In our analysis we used the topologically unidentifiable elastic events $K^-p \rightarrow K^-p$; which yielded

the same value with a similiar error - the greater statistics compensating for the possible backgrounds introduced by the topological inseparability. The details of our determination appear in Appendix II.

ARROW reads a TVGP or SQUAW output tape and unpacks it for various special purpose subroutines. These subroutines compute operator and machine efficiencies, list events, and make remeasurement lists. Other versions compute physically interesting quantities and create data summary tapes (DST's) which contain selected, condensed versions of the data on the SQUAW output tape. These condensed tapes can be formatted to make them easy and economical to sort many times.

SUMX is a general purpose histogramming program used to sort our DST's. It is designed to be easily modifiable. This permits us to study the statistical distributions of our data in a rapid, flexible manner.

E. Event statistics and first level kinematic separation.

A total of 71,651 events were recorded in our first pass through the film. Of these, 1709 were rejected by the operators as being unmeasureable, the remaining 69,942 were digitized and processed by TVGP. Of the latter sample, 63,563 events were found by SQUAW to have at least one good kinematic fit to the primary vertex which yields a ratio of events successfully passed through the kinematics programs to events measured of 91%.

The 6379 events which failed to pass the kinematics programs are tabulated in Table II-2. The RC=10005 events correspond to events where the vertex was destroyed by an error in the SMP control program. The RC=10006 events are topologies not covered in this experiment and are due to operator errors. The RC=10007 indicates that the input record contains the wrong number of views or the wrong number of points. This indicates an incompletely measured event.

RC=10004 and 10008 arise from tracks that have too high a chi-square (χ^2). The RC=10004 indicates that TVGP was unable to obtain an initial guess; while RC=10008 indicates a track which could be fitted but whose final chi-square was high enough to indicate a non-smooth curve. Such events usually arise from two sources. There are many events in which the beam track is about half a track width from a

Table II-2. Events Rejected by TVGP and SQUAW Programs

Reject Codes	Number of Such Events	Reason for Reject
TVGP 10004	2059	Some track fitting χ^2 too high in TVGP (see text for explanation)
TVGP 10005	118	Caused by error in SMP control program
TVGP 10006	13	Improper event type (scanner error)
TVGP 10007	1112	Some TVGP fit is pathological (scanner error)
TVGP 10008	2935	High RMS point scatter in TVGP (see text for explanation)
SQUAW 20010	142	No passing fit in SQUAW (see text for explanation)

parallel beam track. The SMP, due to its design, cannot distinguish such tracks and will digitize a randomly mixed set of points from both tracks. Such data cannot be fit with a smooth curve. A second reason for high chi-squares are tracks which have a small angle kink due either to decay or secondary scattering not noticed by the operator and therefore measured beyond the kink.

All failing events were re-examined to determine if they were measureable and remeasured if they were found to be measureable. This was done to determine if the fraction of these events which belong to the real sample is different from the larger sample. It was found that the events in the reject class had generally the same constitution as the good events and differed from them only by the fact that they were of a more difficult class to measure, e.g. other beam tracks too close, secondary pion or kaon decay, etc. Thus they were excluded from the final analysis sample and the cross section was corrected accordingly for this 9% loss (see Section III-C). An uncertain systematic error is introduced by the separation of the track length determination and our measurement. (It is not clear how the track length is defined in terms of nearby beams, bad frames, etc.)

Figure II-9 is the chi-square distribution for the kinematic fit of all events with the hypothesis $K^-p \rightarrow K^-\pi^+n$.

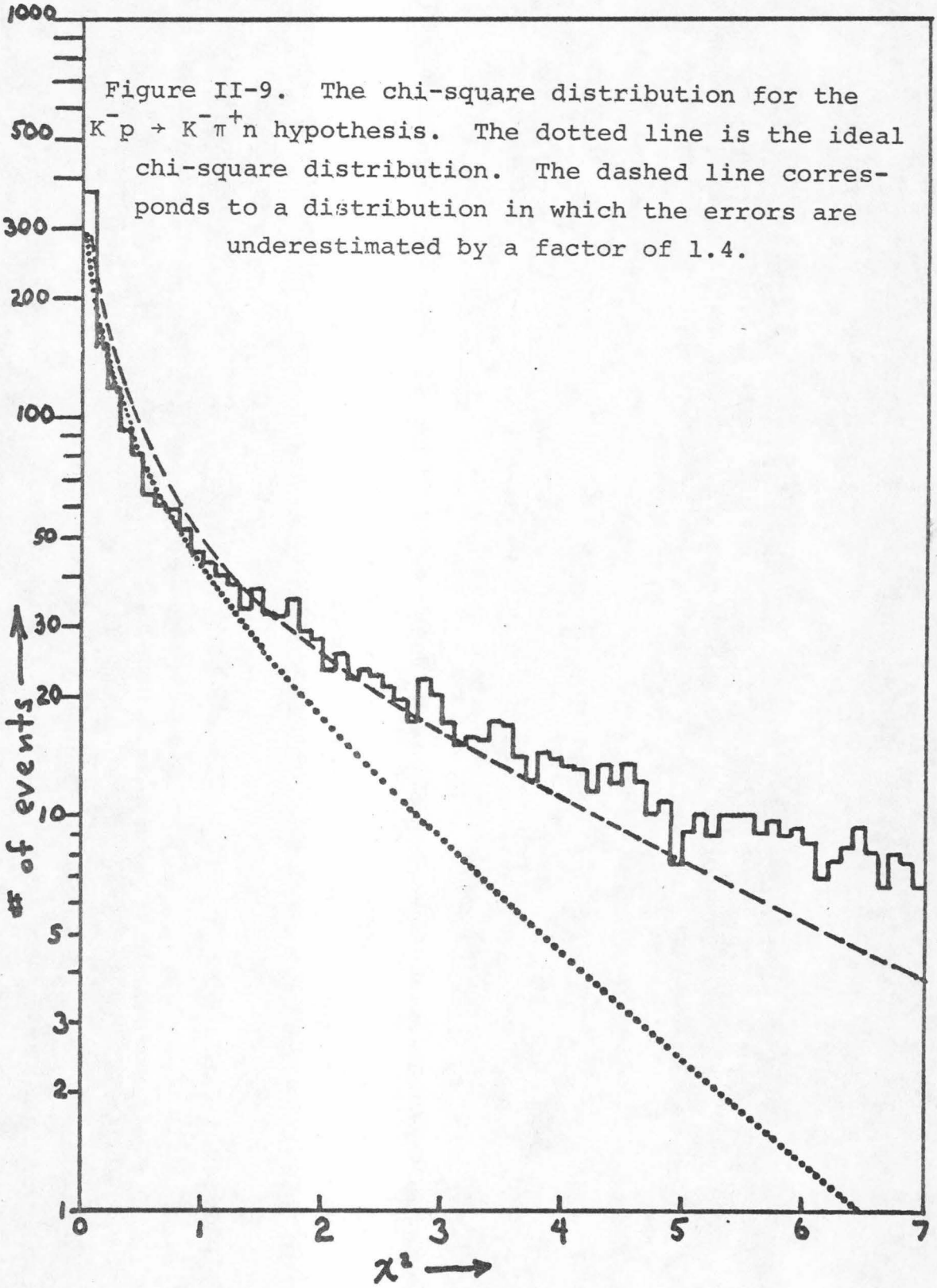

Figure II-9. The chi-square distribution for the $K^-p \to K^-\pi^+n$ hypothesis. The dotted line is the ideal chi-square distribution. The dashed line corresponds to a distribution in which the errors are underestimated by a factor of 1.4.

The solid line is the ideal χ^2 distribution. The discrepancy between this curve and the data implies either that background is present or that the assigned measurement errors are underestimated. The sensitivity of the χ^2 to underestimation of errors is extremely high. The dotted curve is the distribution expected if all errors are underestimated by a factor of 1.4 [v].

The question of whether this discrepancy is due to background or to underestimated measurement errors can be studied by examining samples of differing signal-to-noise ratios. We shall examine such samples through a related function, the confidence level, rather than the chi-square. The confidence level possesses the advantage of yielding a flat distribution in the ideal case, and thus simplifying the comparison of two curves.

The confidence level is a function defined in terms of the χ^2 as

$$CL_n(\chi^2) = \int_{\chi^2}^{\infty} dy \, \frac{1}{2^{n/2}\Gamma(n/2)} \, y^{(n-2)/2} \, e^{-y/2}$$

where n is the number of degrees of freedom. Since this is

---

[v] This is a typical estimate of the underestimation of errors in experiments in the 72 inch bubble chamber.

the probability of having any given χ^2 or higher, the confidence level will be flat for a set of events with an ideal χ^2 distribution.

Figure II-10 displays the confidence level for events in this experiment. The rise at small values (CL $\sim$0.2) is due to the excess of events at χ^2=1-7 in the chi-square distribution. If we examine the same distribution for cleaner samples of data, a rise due to background will diminish but a rise due to measurement error will remain. The lower two sets of points in Figure II-10 are from such samples[vi]. The relative size of the rise does diminish; however, the effect is small. Since the sample for $|t| \leq 0.5$ and $0.84 \leq m_{K\pi} \leq 0.94$ is known to be extremely clean, as will be shown in the next chapter, this behavior implies that underestimated measurement errors are a significant source of the excess of high chi-square events.

In Figure II-11, the normalized integral distribution of events in the K*(890) peak ($840 < m_{K\pi} < 940$ MeV) above background is displayed. Assuming that the chi-square is independent of the Kπ effective mass, we estimate from this curve that for a chi-square cut of <7.0, the number of rejected good events is 4±1%. This is to be compared to the 1% loss for an ideal distribution.

[vi] This will be shown in Chapter III.

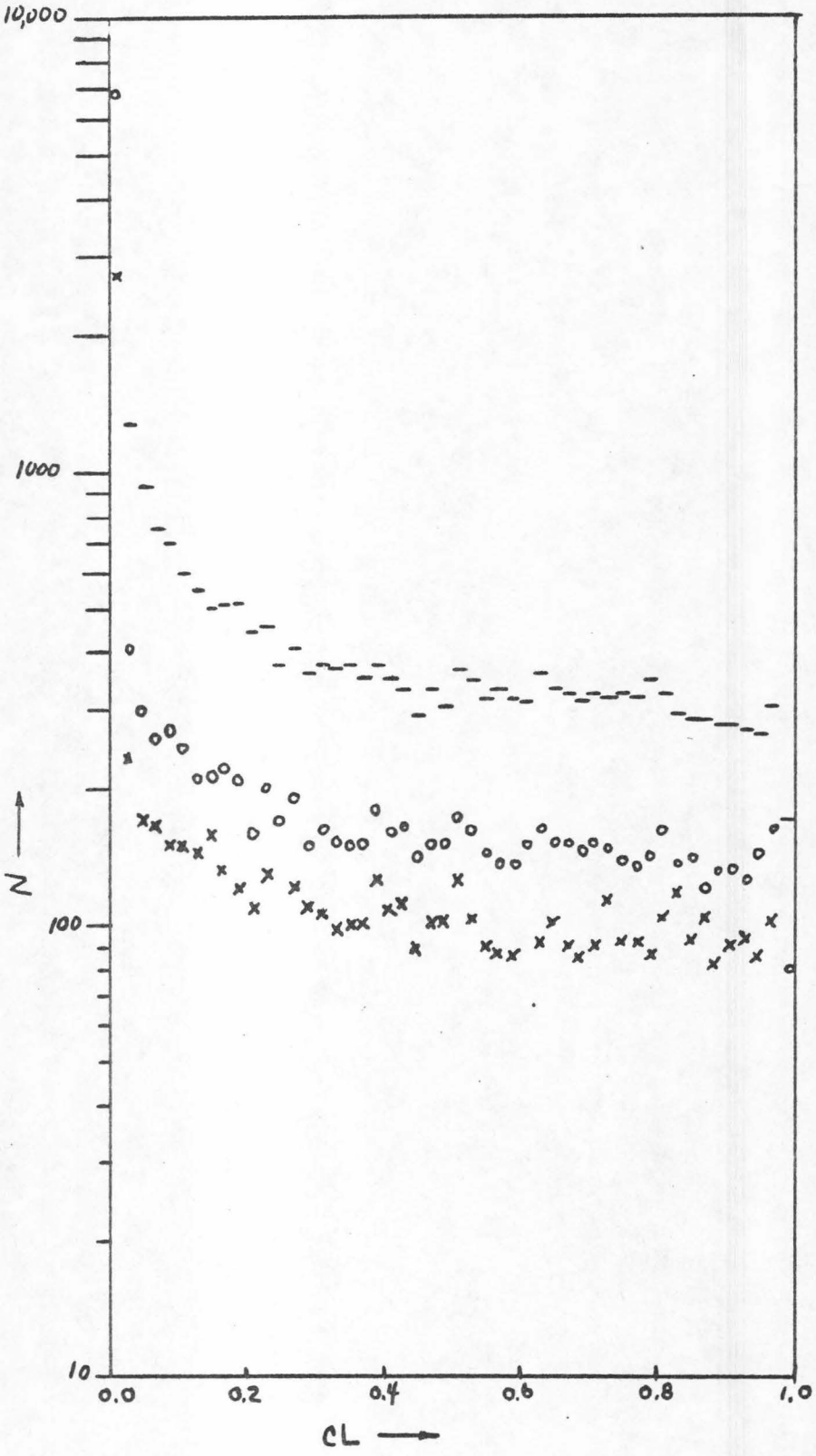

Figure II-10. The confidence level distribution for the one constraint hypothesis $K^- p \to K^- \pi^+ n$. The dashes (-) are all events, the circles (o) are events with $m_{K\pi} = .84$ to .94, and the crosses (x) are events with $m_{K\pi} = .84$ to .94 and $|t| < 0.5$.

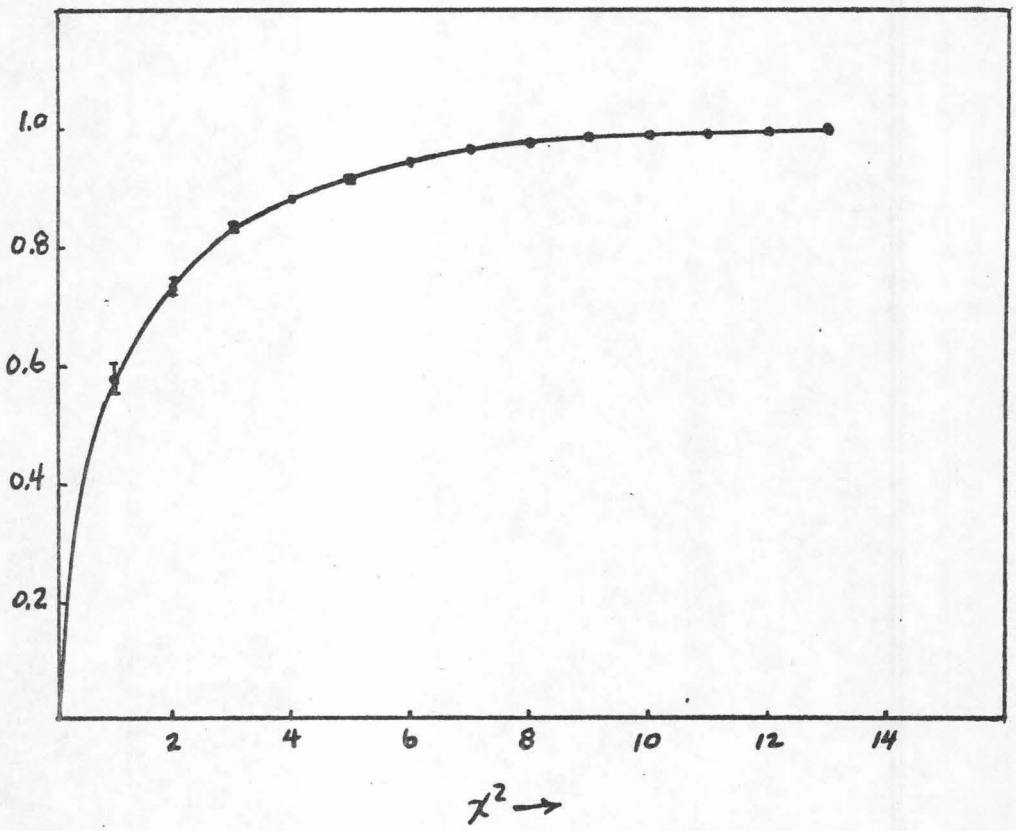

Figure II-11. Integral distribution of the number of events in the $K^*(890)$ peak. (.84 - .94 GeV/c^2) above the background as a function of chi-square.

Choosing such a chi-square as a selection criterion leaves a large number of events which are ambiguous among the one constraint fits. Table II-3 summarizes the level of ambiguity remaining in our data with this selection (A + indicates that the class of events fits the hypothesis in question).

A more direct method of estimating the background which is not subject to the same problems of underestimated errors is discussed in the next chapter.

TABLE II-3. Number of Events Which Fit The Various Combinations of One Constraint Hypotheses with $\chi^2 \leq 7$.

$K^-\pi^+n$	$\pi^-\pi^+\Lambda$	$\pi^-\pi^+\Sigma^0$	$K^-p\pi^0$	π^-pK^0	Number Events	
-	-	-	-	-	28467	
-	-	-	-	+	4315	
-	-	-	+	-	4992	
-	-	-	+	+	3037	
-	-	+	-	-	1385	
-	-	+	-	+	396	
-	-	+	+	-	376	
-	-	+	+	+	216	
-	+	-	-	-	1654	
-	+	-	-	+	464	
-	+	-	+	-	433	
-	+	-	+	+	95	
-	+	+	-	-	1305	
-	+	+	-	+	451	
-	+	+	+	-	402	
-	+	+	+	+	157	
+	-	-	-	-	4476	
+	-	-	-	+	2207	↑
+	-	-	+	-	1284	
+	-	-	+	+	175	
+	-	+	-	-	1185	
+	-	+	-	+	246	
+	-	+	+	-	249	
+	-	+	+	+	94	
+	+	-	-	-	4434	
+	+	-	-	+	1164	
+	+	-	+	-	500	
+	+	-	+	+	509	
+	+	+	-	-	2538	
+	+	+	-	+	589	
+	+	+	+	-	286	
+	+	+	+	+	923	↑ Events In Our Sample

Chapter III. Kinematic Background and Selection of Final Data Sample

A. Studies of Missing Mass Distributions

The measured momentum vectors of all charged tracks emitted from an event vertex, together with a set of hypothesized masses for the charged particles permit the missing mass (mass of the neutral particles) to be calculated. If a single neutral particle has been emitted, a "signal" for this reaction appears superimposed above the smooth background arising from processes with misidentified particles or multi-neutral states. For a one constraint fit, the information contained in this distribution is roughly equivalent to that contained in the chi-square distribution. The information content differs only by not having an estimate of the errors folded into the measurement. Since the estimated errors in our chamber are subject to doubt, such a distribution possesses the clear advantage of being definite.

The nature of our test is to examine the relative number of events in the neutron peak compared to the tails of the distribution. Therefore to study the missing mass distributions it is necessary to examine the distribution of missing masses without a chi-square selection. Therefore all tests

and histograms in this section are done without such a chi-square selection.

Figure III-1a is the distribution of missing mass assuming the charged tracks are a K^- and a π^+ (which will be denoted as $MM/K^-\pi^+$) for all events measured in this experiment. The peak at ∿940MeV corresponds to the neutron mass. If the background were flat under the peak, there would be ∿20% background in the sample selected with $MM/K^-\pi^+$=940±80 MeV. We shall discuss the evidence that the background is not flat, but is probably significantly smaller in the vicinity of the neutron. Note that the sample of low t-K* events ($t<0.5$ GeV^2, $m_{K\pi}$ = .84 - .94 GeV) constitutes an almost background free sample independent of this conclusion (see Figure III-1 b-d).

In Figure III-1, the peaks at $MM/K^-\pi^+$=1.2 GeV/c^2 are due to π^0n production and not to an incorrect mass hypothesis. This is evident from the enhancement of the peak when the K* is selected and its suppression when low t is selected (the physical boundary prohibits $K^-p\to K^{*0}\Delta^0$ from populating the low t region). Therefore these events do not represent a background which continues beneath the neutron peak. On the low side of the neutron mass, the peak in Figure III-1a near m = 0.5 GeV/c^2 is due to $K^-p\to K^-p$ events[(i)]. Proof of this

---

[(i)] The peak appears at 0.5 GeV/c^2 instead of 0. GeV/c^2 because of the particle misidentification.

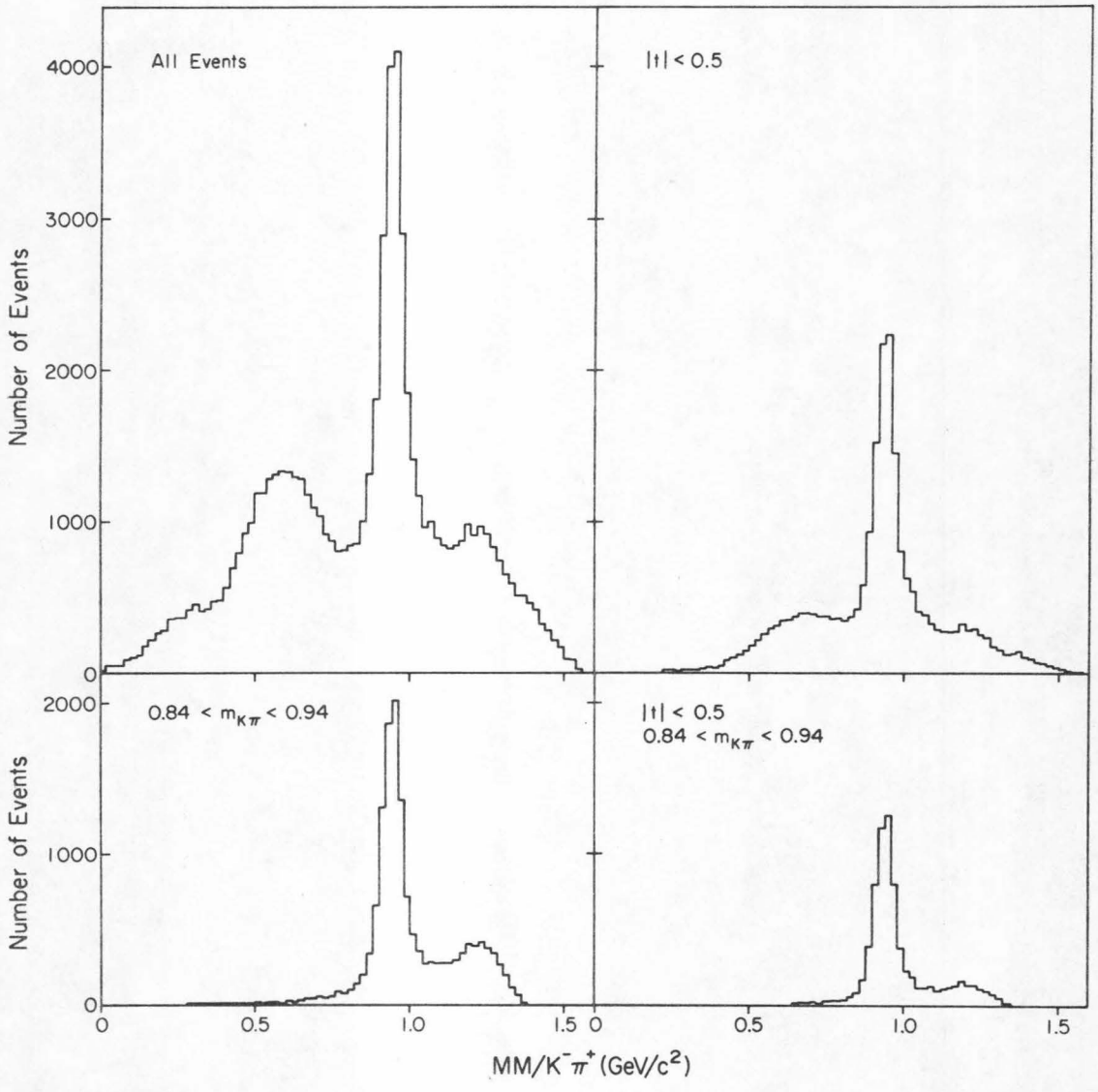

Figure III-1. Missing mass above $K^-\pi^+$ for our total sample and for the selections which define our K^* sample.

appears in Figure III-2, where the missing mass plots are selected on the dihedral angle θ which is the angle between the plane formed by the beam track and the outgoing negative track, and the plane formed by the beam track and the outgoing positive track. The events with $\cos\theta > 0.98$ are coplanar. This condition implies that they are all two body final states. Elastic events comprise the majority of such events.

There are several reactions such as $K^-p \to \pi^-\pi^+\Lambda$, which tend to give peaks near the neutron mass when the tracks are misinterpreted. A further study of such backgrounds appears in Section III-B.

The background remains small throughout this region ($m_{K\pi}$= .84-.94, $t<0.5$). In Figure III-3, this region is divided into smaller t intervals. From this figure, it is evident that the background is not significant even in the highest t bin where the signal becomes quite small relative to the low t bins. This implies that the background will not appreciably affect the shape of the differential cross section for this sample.

In Figure III-4 are displayed the missing mass plots for other $K^-\pi^+$ mass regions. The low $m_{K\pi}$ regions have significant π^0n enhancements which do not contribute to the true background, since the resolution is hwhm = 40 MeV (from the neutron width) and π^0n threshold is at 1080 MeV.

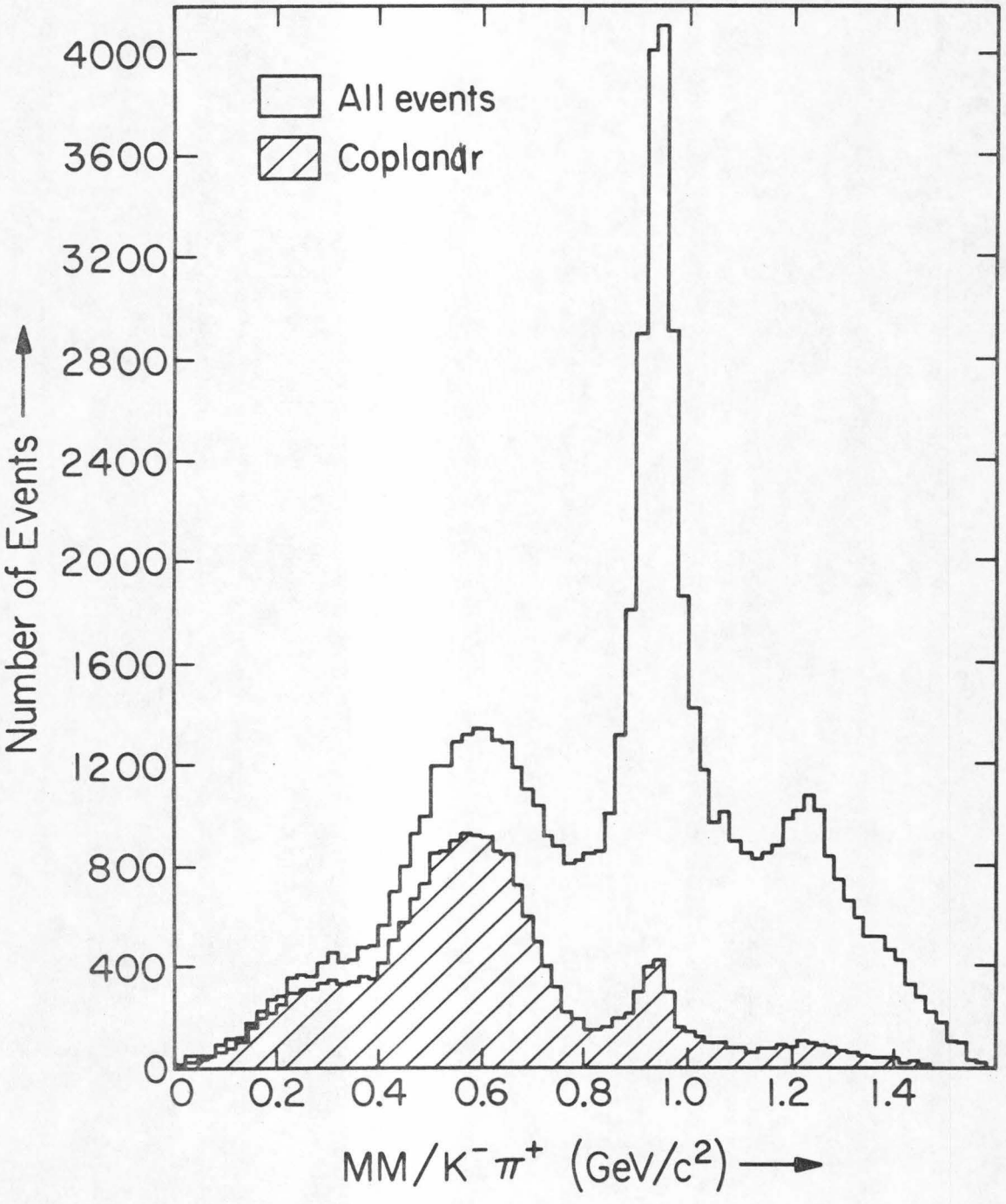

Figure III-2. Missing mass selected on coplanarity.

Figure III-3. Missing mass above $K^-\pi^+$ for the K^* sample with fine t bins.

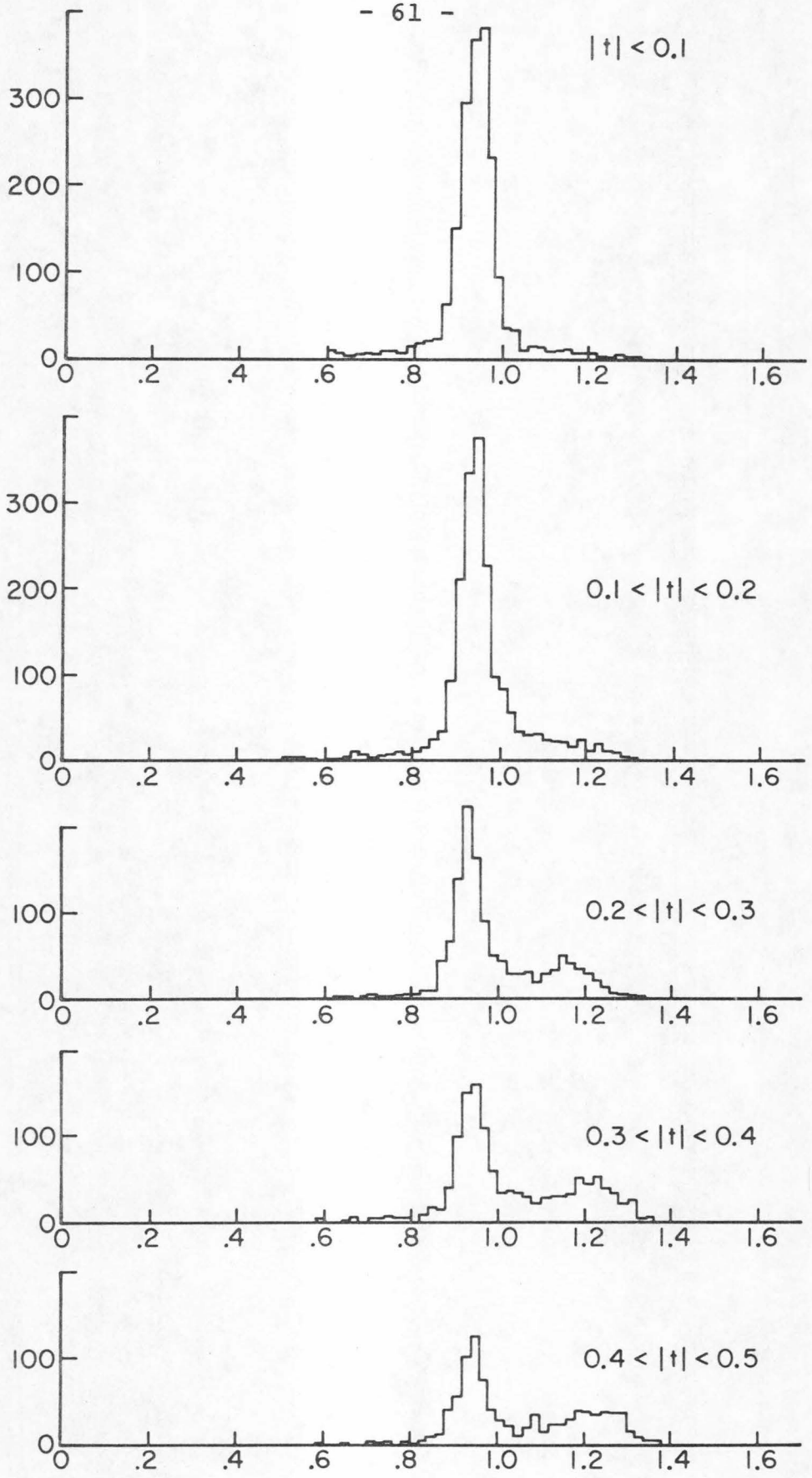
|t| < 0.1
0.1 < |t| < 0.2
0.2 < |t| < 0.3
0.3 < |t| < 0.4
0.4 < |t| < 0.5
300
200
100
0
.2
.4
.6
.8
1.0
1.2
1.4
1.6

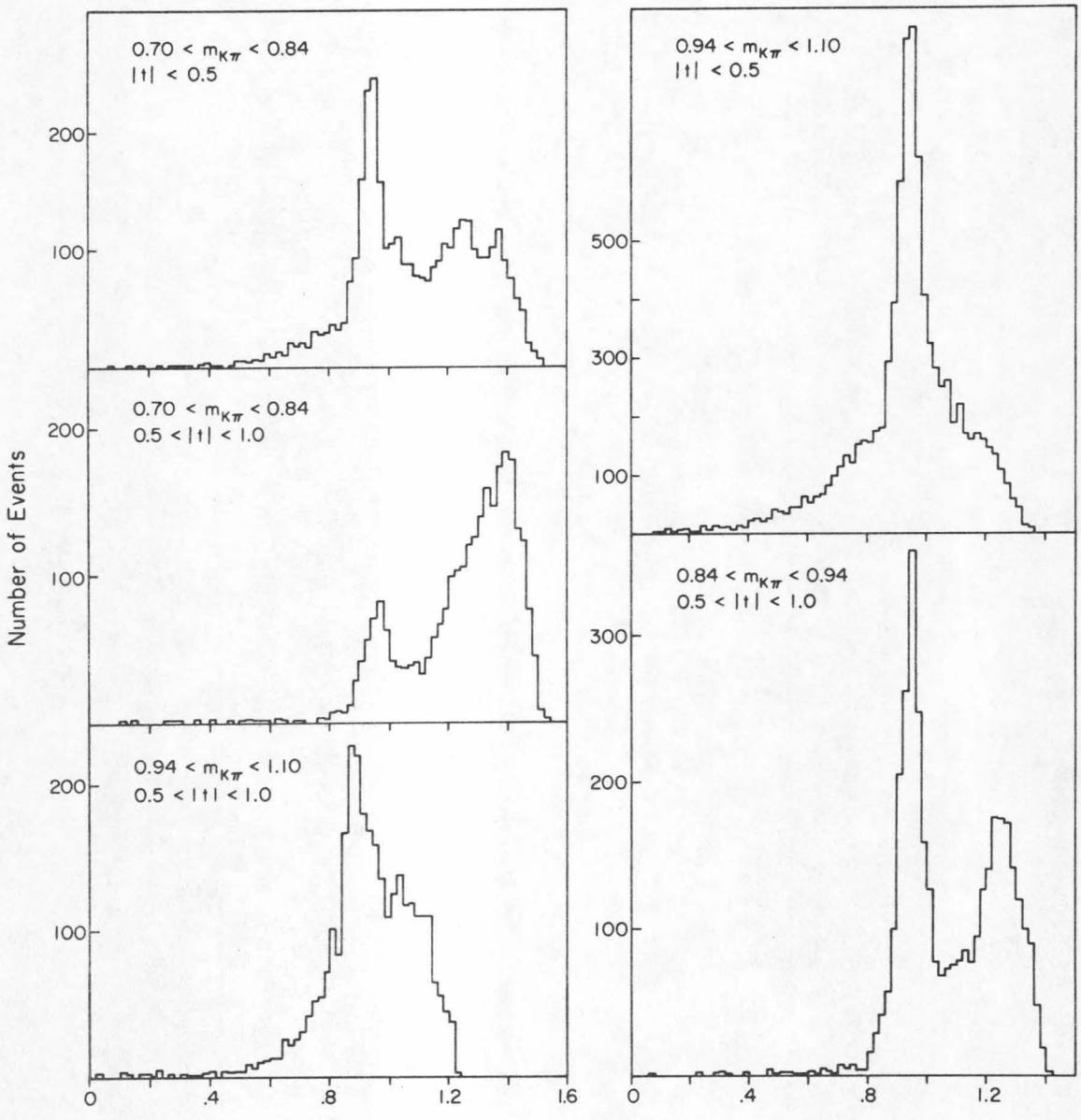

Figure III-4. Missing mass above $K^-\pi^*$ for the other $m_{K\pi}$ - t regions.

This can be seen in Table III-1 where the percentage backgrounds are summarized, with and without taking the π^0n contribution into account. The high $m_{K\pi}$ regions are contaminated by other backgrounds and therefore do not significantly improve when the π^0n events are removed.

From Table III-1b, we conclude that the data with $m_{K\pi}<0.94$ are useable for quantitative physics analysis, and that the K* region is exceptionally free of background. The large $m_{K\pi}$ region is highly contaminated so that although fits will be made to these data, no reliable conclusions can be drawn from this sample. Although the high t bins are quite clean, no use will be made of these data for lack of a relevant theory.

In Figure III-5, the missing mass distribution for the events in the K* - low t region with and without the $\chi^2 < 7$ selection is plotted. As one can see, the primary effect of the $\chi^2 < 7$ selection is to remove the π^0n events and the elastics.

Table III-1. Percentage Background in Various Regions of $M_{K\pi}$ - t

a) Assuming a uniform background

$M_{K\pi}$ (Gev) \ t (Gev^2)	0.0 - 0.5	0.5 - 1.0
0.70 - 0.84	0.32 ± 0.08	0.37 ± 0.14
0.84 - 0.94	0.16 ± 0.08	0.25 ± 0.08
0.94 - 1.10	0.39 ± 0.07	0.55 ± 0.06

b) Assuming a uniform background and a Δ^0 peak

$M_{K\pi}$ (Gev) \ t (Gev^2)	0.0 - 0.5	0.5 - 1.0
0.70 - 0.84	0.20 ± 0.04	0.18 ± 0.04
0.84 - 0.94	0.08 ± 0.02	0.14 ± 0.03
0.94 - 1.10	0.39 ± 0.07	0.55 ± 0.06

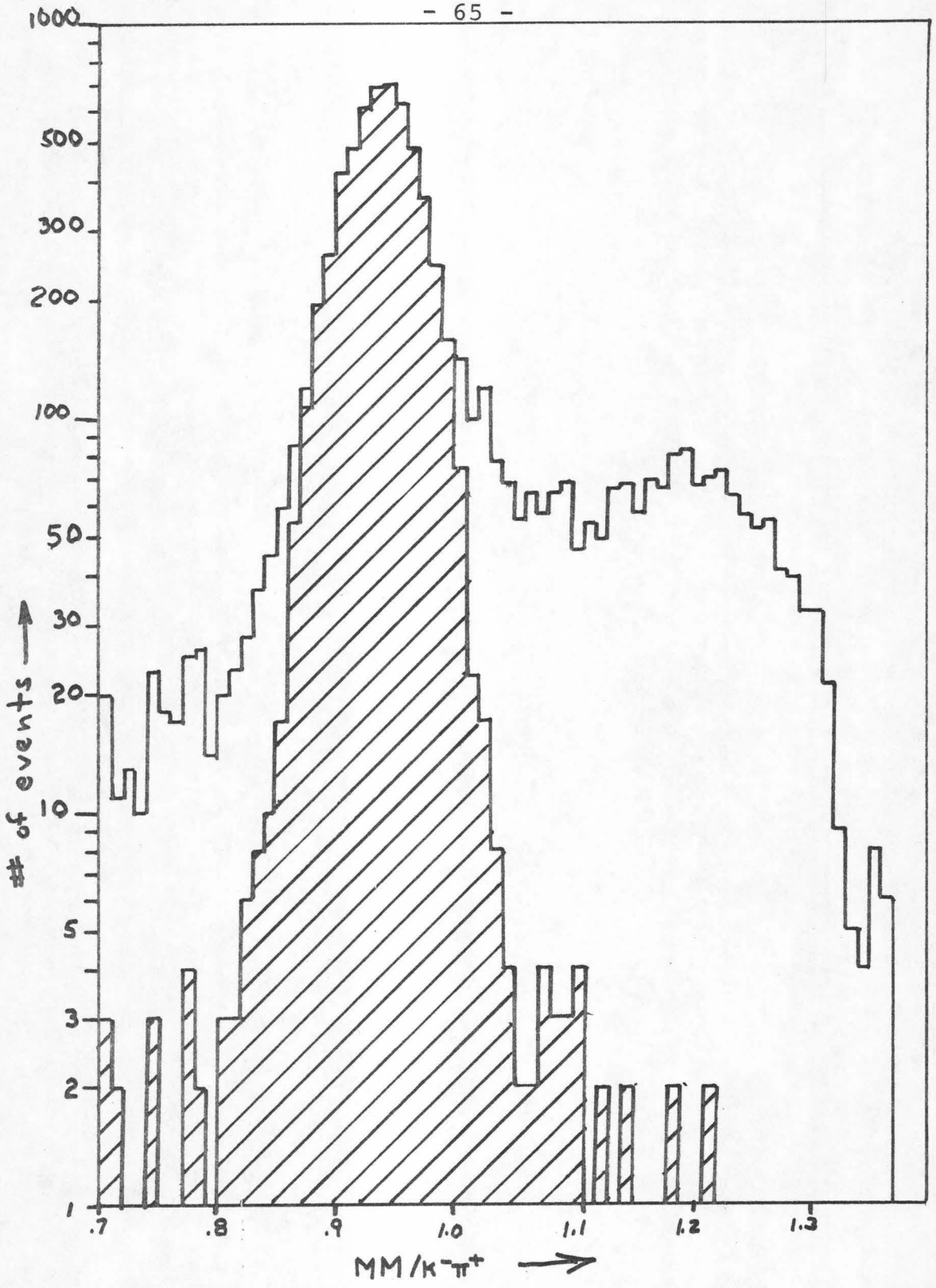

Figure III-5. Missing mass above $K^-\pi^+$ with the chi-square selection ($\chi^2<7$ is cross hatched, other curve is all events).

B. Background From Λ^0 and K^0 Events with Neutral Decays

At the beginning of this experiment, the major sources of background were expected to be reactions having approximately the same final state kinetic energy as the reaction of interest, $K^-p \to K^-\pi^+n$. These reactions fall into three classes:

$$K^-p \to \pi^-\pi^+ + (\Lambda + \ldots) \qquad A$$
$$\to \pi^-p + (\bar{K}^0 + \ldots) \qquad B$$
$$\to K^-p + (\pi^0 + \ldots) \qquad C$$

When these reactions are improperly interpreted as $K^-p \to K^-\pi^+n$, they all tend to give a neutral missing mass peak at approximately the neutron mass. In Figure III-6, the missing mass above $K^-\pi^+$ is plotted for the two-prong-Vee events measured in this experiment. There is a clear peak at 1 GeV/c^2 due to improper identification of the charged tracks. It is thus necessary to supplement the missing mass formation with a more direct measurement of these background sources.

When the Λ^0 or K^0 reactions are accompanied by a neutral decay, they appear as background in our $K^-p \to K^-\pi^+n$ data[ii].

[ii] Table II-1 indicates that $\pi^-\pi^+\Sigma^0$ and $\pi^-\pi^+\Lambda^0\pi^0$ are as significant cross sections as $\pi^-\pi^+\Lambda^0$. These events also contaminate our sample. Our methods treat such events as part of the Λ^0 sample.

Figure III-6. Missing mass above $K^-\pi^+$ for our two-prong-Vee sample.

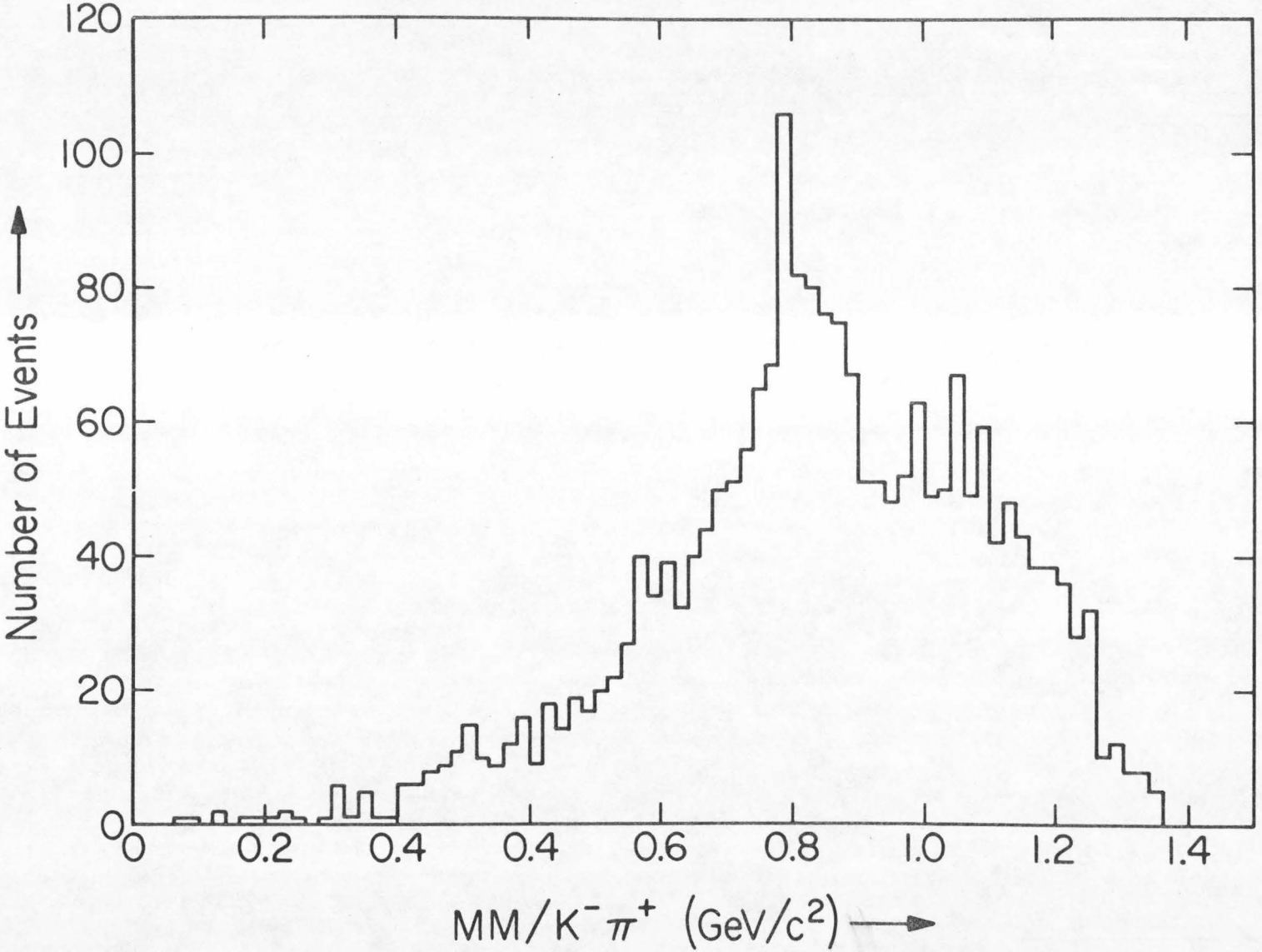
120
100
80
60
40
20
0
0
0.2
0.4
0.4
0.6
0.8
1.0
1.2
1.4
Number of Events
MM/K⁻π⁺ (GeV/c²)

However, when they decay via charged modes, they are included in the two-prong-Vee sample described in section II-C and summarized in Table III-2.

Since the branching ratio for charged decays is independent of the production dynamics, a sample of two-prong-Vee events gives an unbiased estimate of the contamination from these sources. Because the K^0's and the Λ's have different neutral to charged branching ratios, they must be treated separately. Figures III-7 and III-8 are Chew-Low plots for the two-prong-Vee events which contain a K^0 or Λ^0 and fit $K^-p \to K^-\pi^+n$ with $\chi^2<7$. Both samples exhibit a more or less uniform distribution in the $K^-\pi^+n$ Chew-Low plane. The effective cross sections calculated from these events appear in Table III-3. This table shows that K^0 and Λ backgrounds are negligible in the low t - K* region ($|t| < 0.5$, $0.84 < m_{K\pi} < 0.94$).

The background due to reaction C cannot be studied in a similar manner. However, its similarity to reaction B -- expecially the fact that in both reactions the only source of contamination comes from events with a fast forward going proton for which the cross section is known to be small -- leads to the conclusion that background from this reaction can be neglected as well.

The two-prong-Vee events (of Figures III-7 and III-8 were also used to examine the usefulness of a separate ionization pass, in which the expected ionization deduced

Table III-2. The Two-Prong-Vee Sample

	Total	Number of Events Passing $K^-\pi^+n$ Hypothesis with $\chi^2 < 7$	Fraction of Events Which Have $\chi^2 < 7$ for $K^-\pi^+n$ Hypothesis
unambiguous Λ events	1370	362	0.26
unambiguous K^0 events	309	35	0.11
ambiguous Vee events	481	113	0.24
Total	2160	510	

Classification of the 113 ambiguous Vee events based upon production vertex fits

unambiguous Λ events	77
unambiguous K^0 events	8
events with good production vertex fits for both K^0 and Λ reactions	2
no production vertex fits	26

Table III-3. Effective K^0 and Λ Cross Sections As Determined From the Two-Prong-Vee Events

	K^0	Λ^0	True Sample
# used as sample	309	1370	---
visible cross section as determined at p_{lab}=1.95 (see Table II-1)	0.84 mb	3.2 mb	2.7±0.5 mb
μbarn equivalent size of sample (≡f)	2.73μb/ev	2.33μb/ev	0.16μb/ev
Require all events to fit $K^-p \to K^-\pi^+n$ with $\chi^2<7$			
# of events $\lvert t\rvert<0.5$ and $0.84<m_{K\pi}<0.94$	1	6	4360
# of events $\lvert t\rvert<0.5$	12	47	8742
all events	35	362	19881
Convert to cross sections with f and correct for visible/ invisible decay			
$\sigma\{\lvert t\rvert<0.5, 0.84<m_{K\pi}<0.94\}$	5±5μb	7±3μb	(0.7±0.1 mb)
$\sigma\{\lvert t\rvert<0.5\}$	65±9μb	55±8μb	(1.4±0.1 mb)
all events	190±32μb	420±22μb	(3.2±0.3 mb)

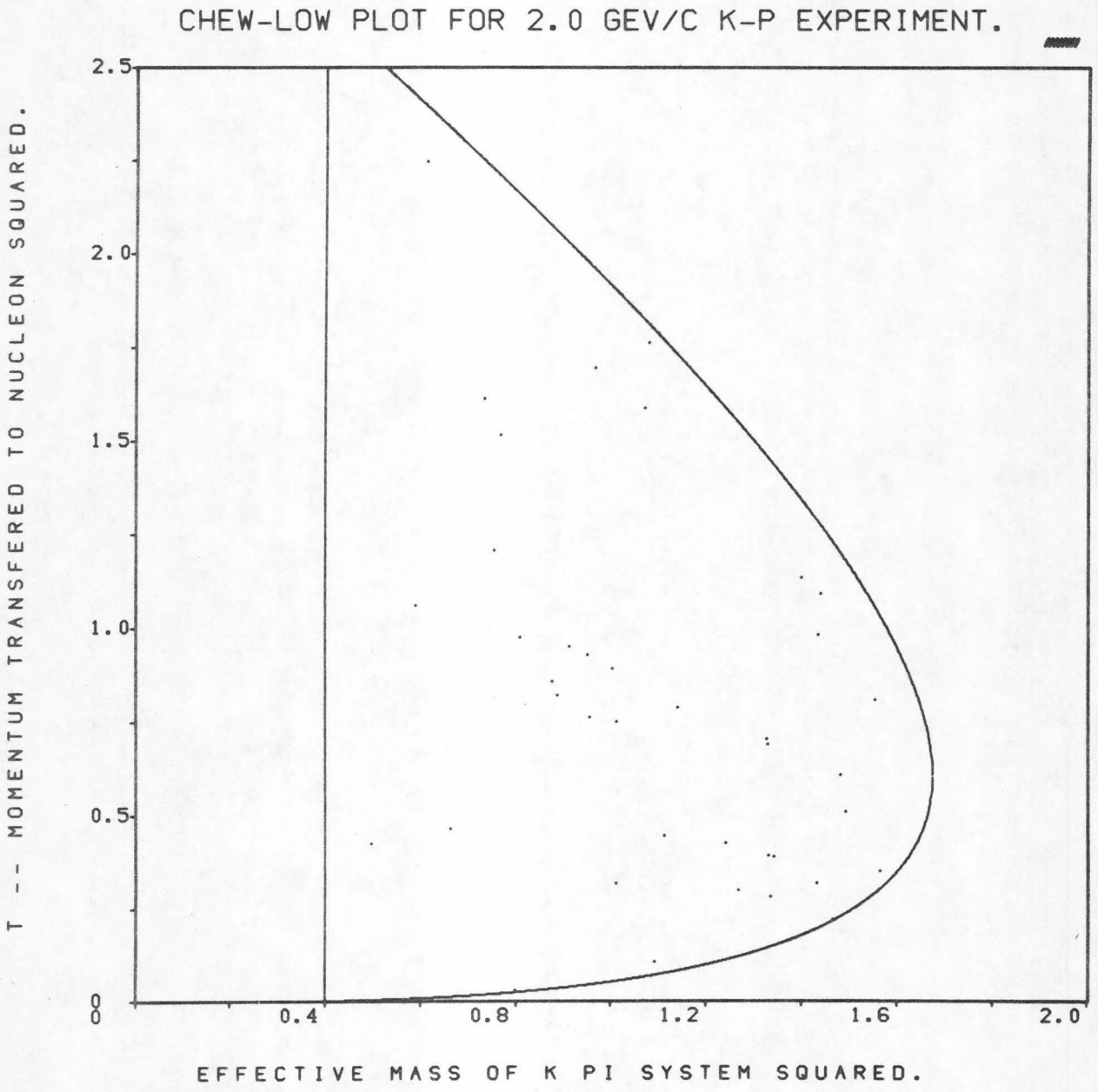

Figure III-7. The Chew-Low plot of the two-prong-Vee sample with a kinematically identifiable K^{o}.

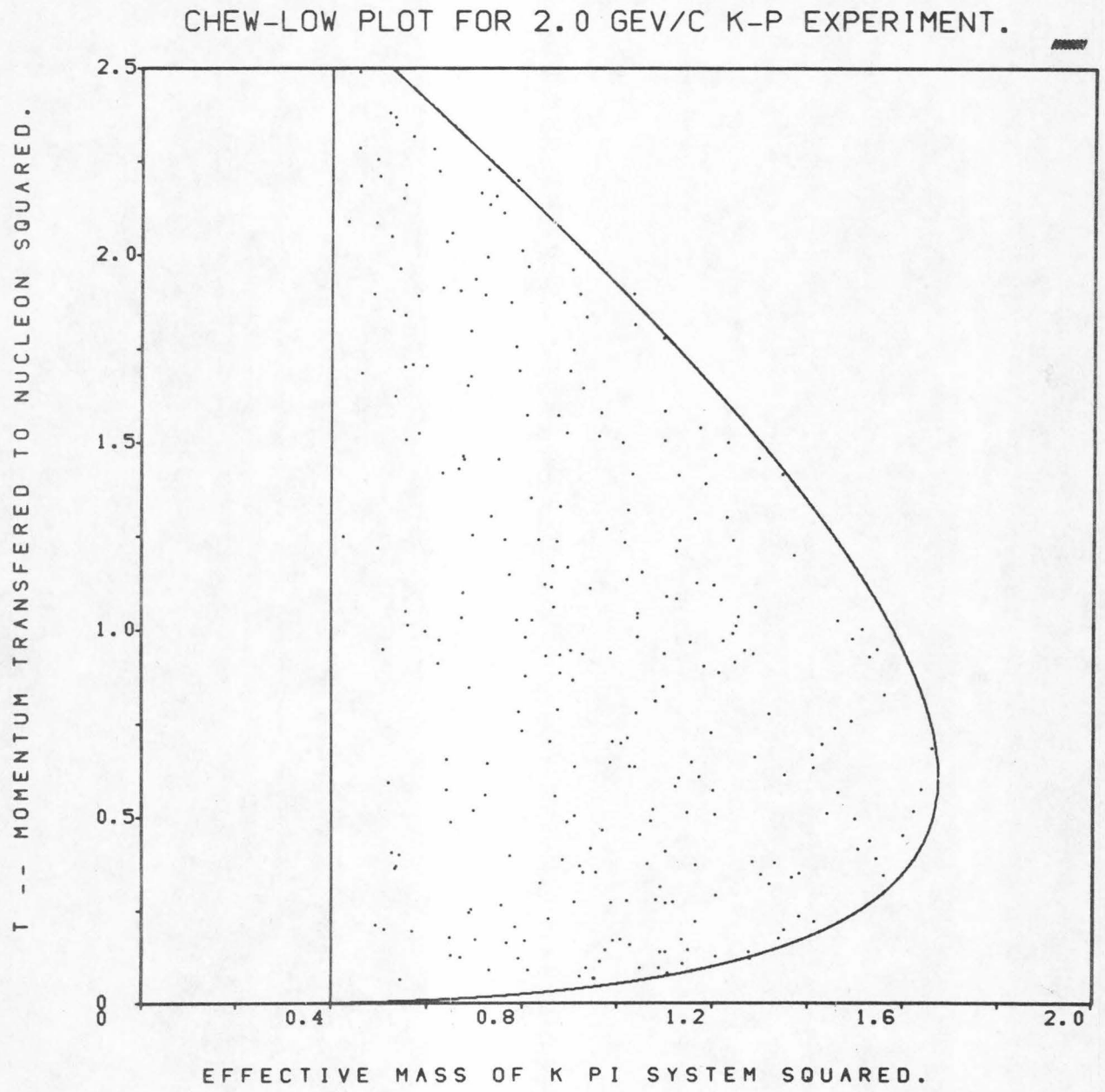

Figure III-8. The Chew-Low plot of the two-prong-Vee sample with a kinematically identifiable Λ^{o}.

from the kinematic fit could be applied to further exclude background due to proton events. A study was made to distinguish between reactions of the type:

$$K^- p \rightarrow \pi^- p\, K^0 \quad (K^0 \hookrightarrow \pi^- \pi^+)$$

$$K^- p \rightarrow \pi^- \pi^+ \Lambda \quad (\Lambda \hookrightarrow \pi^- p)$$

by assigning the proton on the basis of bubble density to either the production or decay vertex. Since, in this case, one of the two particles must be a proton, this is an easy problem compared to that encountered in identifying the protons in our sample of two prongs. Nevertheless, for the sample studied, in 80% of the events the proton could not be identified[iii]. This implies that an ionization pass could not significantly improve our sample.

[iii] This problem is partially due to the darker than normal tracks in our film (Dauber 1966).

C. The Scanning Efficiency

The scanning efficiency was determined by three independent studies. The results of these studies are tabulated in Table III-4.

The first study was performed by having two rolls of film measured by all of the scanners. These measurements were obtained to test the reproduceability of the measurement process and the scanning efficiency. A detailed description of the results of this study appears in Appendix I.

The second and third studies were performed by using two independent sets of previously measured events as sources of random events which should have been found during our experiment.

One set of events originated from a pilot project conducted as part of the feasibility study for this experiment. In this project, all the two prong events in twelve rolls of film were measured and processed (Malamud 1968). Our final DST was checked against this sample to determine whether these events had been found. The events not found were then examined to determine if they were actually good events. The results of this procedure are summarized in Table III-5.

Since a large fraction of the "not found" sample were judged as bad events, it is important to determine that

Table III-4. Scanning Efficiency*

Sample	Efficiency (%)
two roll	85 ± 5%
pilot project	84 ± 2
⊕ $m_{K\pi}$ = .89 ± .05	82 ± 3
⊕ t < 0.5	83 ± 3
Backward Pi	83 ± 2
⊕ $m_{K\pi}$ = .89 ± .05	85 ± 2
⊕ t < 0.5	84 ± 2

*The errors are the statistical errors of the sample in question only.

TABLE III-5. Summary of Scanning Efficiency Check Using Pilot Project Data

Sample	Total	# Found	# Not Found	Ambiguous Or Good	Bad	Scanning Inefficiency (%)
$\chi^2(K^-\pi^+n)<7$	892	596	296	117	179	16 ± 2
⊕ $0.84<m_{K\pi}<0.94$	322	228	94	50	44	18 ± 3
⊕ $\|t\|<0.5$	201	146	55	29	26	17 ± 3

(b). Detailed List of Reasons for Missing Events

			Bad				
Sample	Good	Ambiguous	No Event*	Outside Fiducial Volume	Proton	Two Prong V**	Kink or Close Scatter
$\chi^2(K^-\pi^+n)<7$	71	46	9	66	39	49	16
⊕ $.84<m_{K\pi}<.94$	39	11	2	17	10	8	7
⊕ $\|t\|$ 0.5	21	8	1	13	9	0	3

*Events erroneously identified as to roll and frame on the pilot DST.

**The two prong V's are events which were measured as 22's in the pilot project but have an associated V.

similar events which were found have not biased our calculated efficiency. The following discussion will show that the bad events exhibit a different Chew-Low distribution and therefore the close agreement of the efficiencies for different $K\pi$ mass and t selections implies that the bias of bad events which were measured both times cannot be significant.

In Figure III-9, the $K^-\pi^+$ mass is plotted for the events in this sample and the subset missed in our scan show a K* peak indicating the loss of good events. The events judged bad have been divided into subsamples based upon the reason for considering them as bad events. Only the Outside Fiducial Volume (OFV) and Close Scatter samples exhibit K* peaks indicating that only these two samples contain significant numbers of good events. The CS events represent a loss of good events; however, since they comprise 2% of this sample, they do not represent a large enough effect to influence our results.

That the missing events represent an unbiased loss of events in t, the momentum transfer, is seen in Figure III-10. The t distribution of events is plotted for the total sample and for events missed in the production pass. There is no significant difference, so we conclude that this study indicates that the event loss is random.

Figure III-9. The $K\pi$ effective mass plots for the pilot project scanning efficiency study.

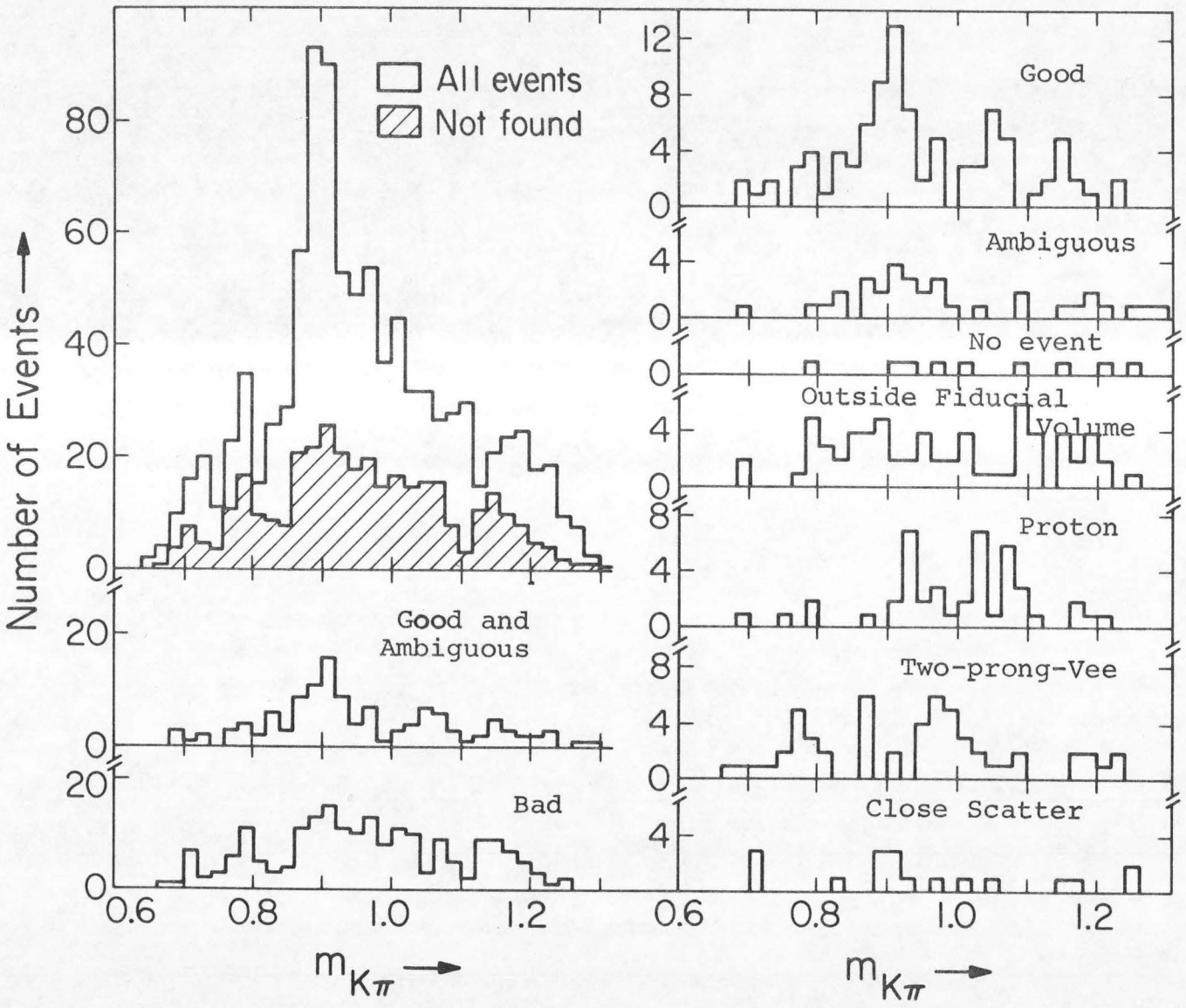
All events
Not found
Number of Events
Good and Ambiguous
Bad
Good
Ambiguous
No event
Outside Fiducial Volume
Proton
Two-prong-Vee
Close Scatter
$m_{K\pi}$
$m_{K\pi}$

Figure III-10. The t distribution for the K^* events in the pilot project scanning efficiency study.

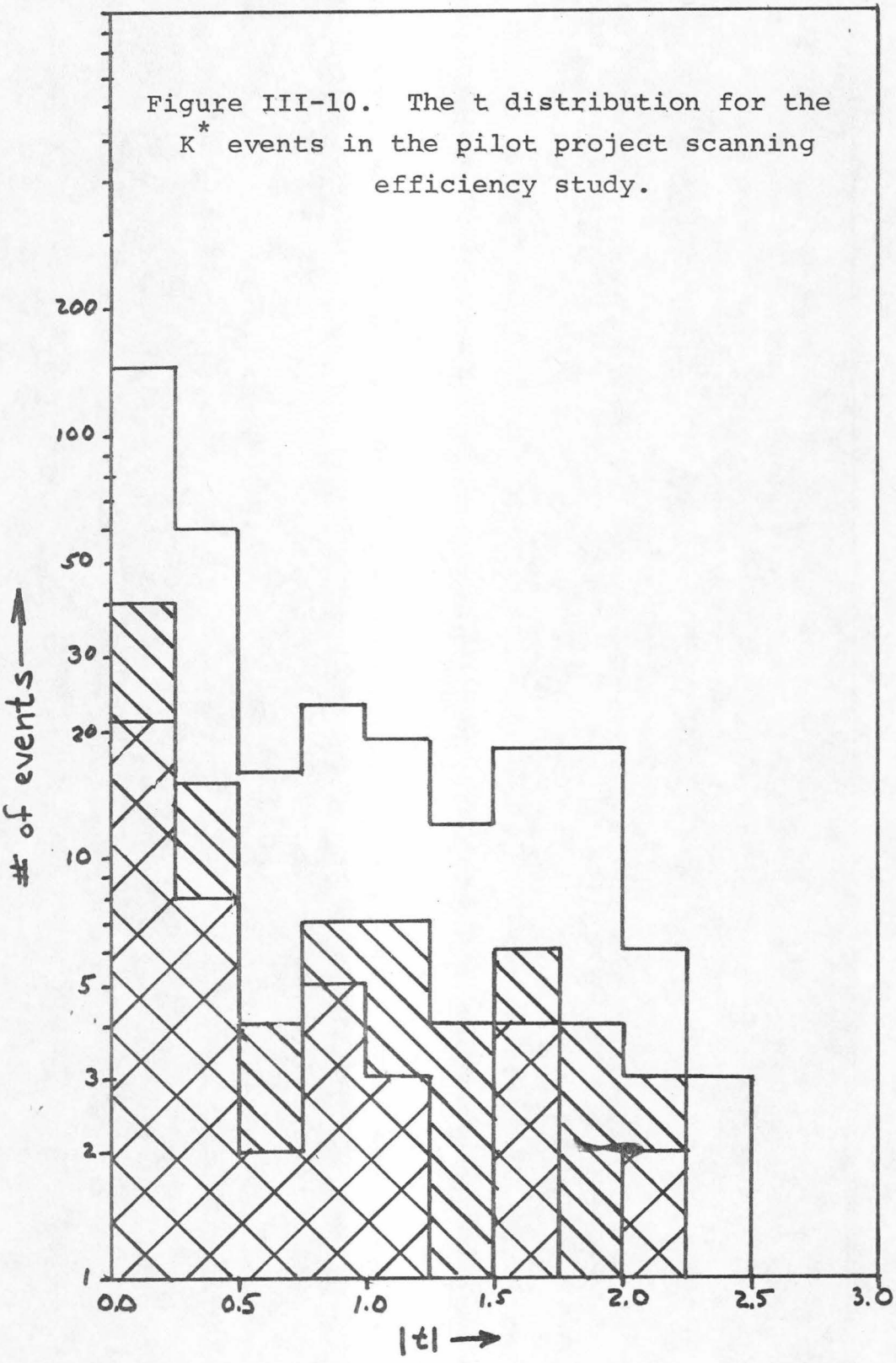

A second sample of events was available as a source of random events distributed throughout the film. All events with a backward π^+ had been measured in about two thirds of the film. This provides us with a set of events not biased by roll number but which is kinematically biased. Such a sample is useable as a source of random events since the missed events can be compared to the sample's overall distribution.

In this study, the events were examined before the computer check of the final DST was made to remove any possible bias of bad events which were measured both times. The results of this check scan and the comparison with our DST appear in Table III-6. In part (b) of this table are the reasons for rejection of the events judged to be bad in the rescan.

In Figure III-11, the t distribution for the missed events is displayed. This distribution shows a significant enhancement at large t. However this bias is also exhibited by the total sample. Therefore we conclude that this bias arises from the non-random selection of the Backward-π sample and not a bias in our scanning efficiency.

The errors in Table III-4 are due only to statistics. However, since the three samples were independent and give the same results, we conclude that our scanning efficiency is 84±2%.

TABLE III-6. Scanning Efficiency as Determined by Using the Backward Pi Sample

Sample	Good		Bad		Scanning
	Found	Not Found	Found	Not Found	Inefficiency (%)
$\chi^2(K^-\pi^+n)<3$	780	159	29	81	17 ± 2
Θ $M_{K\pi}$ = .89 ± .05	363	66	12	33	15 ± 2
$\Theta\|t\|<0.5$	198	36	7	16	16 ± 2

(b). Detailed List of Reasons for Rejection

Sample		Good	Ambig.	No Event	Outside Fiducial Volume	Two Prong V	Close Scatter	Off Beam
$\chi^2<3$	Found	757	23	3	2	6	13	5
	Not Found	148	11	39	6	6	26	4
$\oplus$ $M_{K\pi}$ = .89 ± .05	Found	352	11	1	1	2	4	4
	Not Found	62	4	18	2	3	8	1
$\oplus\|t\|<0.5$	Found	191	8	1	0	2	2	2
	Not Found	32	4	11	1	0	3	1

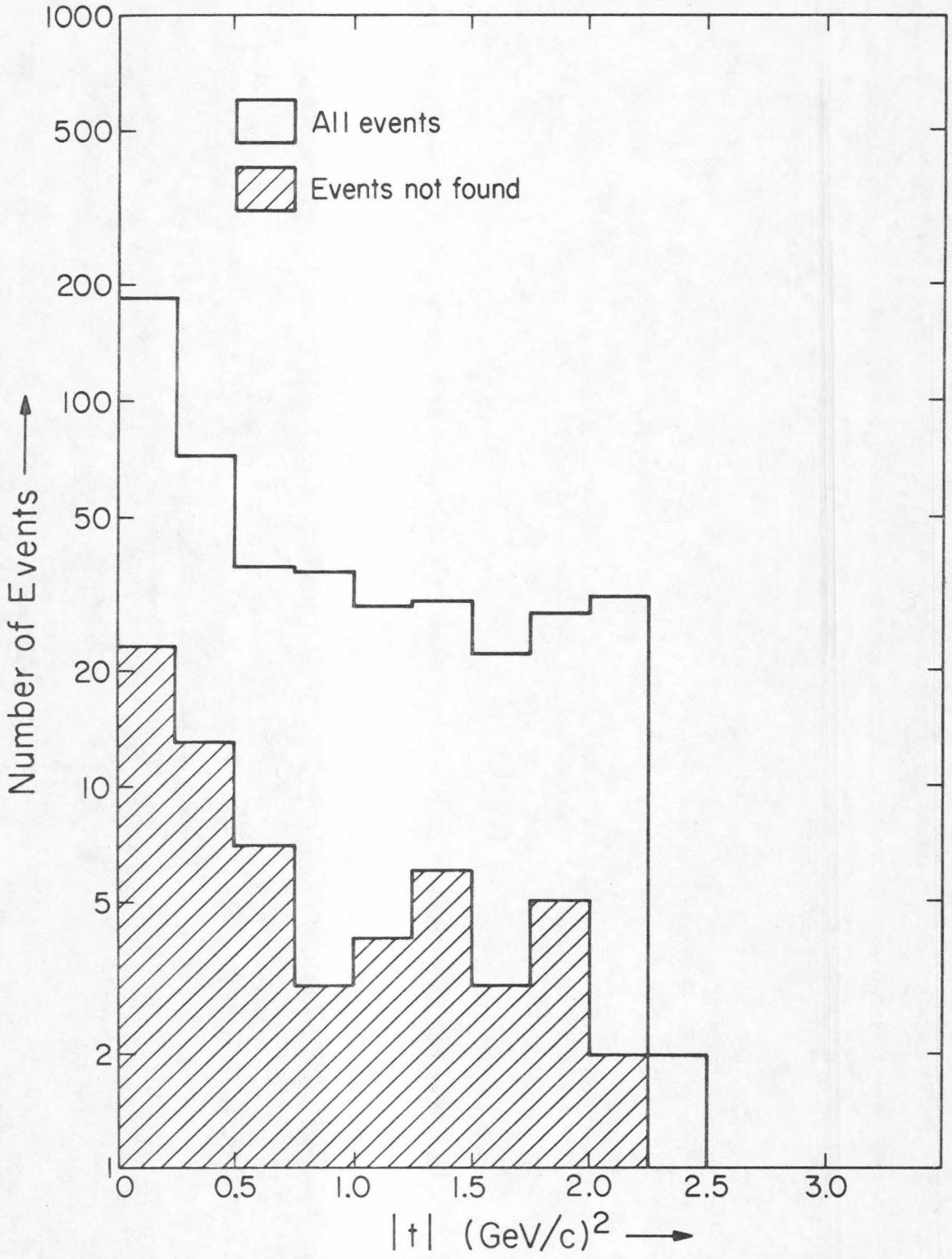

Figure III-11. The t distribution for the K^* events in the "backward pi" scanning efficiency study.

D. Cross Section Determination

19,881 events fit $K^-\pi^+n$ with a $\chi^2<7$. In order to convert this number into a cross section, it is necessary to know the size of the exposure (i.e. the total K^- track length in the fiducial volume used) and the necessary correction factors for background, losses due to scanning errors, and losses due to kinematics program failures. From previous measurement of the τ^- decays, the total track length is known to be 2142±56 km using the fiducial volume and beam momentum interval given here:

$$1.9 < p_{beam} < 2.1 \text{ GeV/c swum to } y = 0$$

$$-13.5 < x_{int} < +14 \text{ cm}$$

$$-73 < y_{int} < +62 \text{ cm}$$

$$+12 < z_{int} < +42 \text{ cm}$$

$$-2^0 < \text{dip} < +2^0$$

$$80^0 < \phi < 86^0$$

This track length is equivalent to 7.48 ± 0.2 ev/μbarn. The fiducial volume used for our experiment was the same except for the y coordinate which was reduced to $-73<y_{int}<42$ cm to correspond to the smaller scanning volume used. A scanning cutoff at rake 11 was used instead of rake 15 in order to lengthen the average length of the secondary tracks to improve the measurement resolution. The corrected exposure size was 6.6±0.2 ev/μbarn. (This includes a 4% effect due

to the decrease in the beam intensity caused by decays and interactions). The total cross section for the reaction is determined to be 3.2 ± 0.3 mb, after correction for:

(i) the scanning efficiency: (84±2)% (see Section III-C)

(ii) the program efficiency: (95±5)% (see Section II-D)

(iii) the background contamination in the total final sample: (80±5)% (see Section III-A)

Chapter IV. General Features of the Data

A. Resonance Production in $K^-p \to K^-\pi^+n$

Quasi-two body production of the K*(890) is the dominant process seen in our data. This process accounts for about 50% of all the events observed. However two other resonances are also present. These are baryon resonances which decay into π^+n; they are the $\Delta^+(1236)$ and the N*(1688). These resonances appear as bands in the Dalitz plot shown in Figure IV-1.

The Dalitz plot is constructed with effective mass squares (rather than masses) to yield a scatter plot in which the phase space per unit area is constant (see Appendix IX). Therefore all non-uniformities in the density of events are due to differences in the magnitude of the matrix elements. The phase space curves drawn through the projections are normalized to the data. The estimated cross section of each resonance appears in Table IV-1. Due to the presence of interference, discussed below, these numbers are only approximate.

In a later section we will remove the effect of the Δ^+ and N* upon the K* angular distribution by means of a solid angle cut. The reason we cannot merely perform a subtraction is that there are interference effects present. Such

Table IV-1. Effective Cross Section for Resonance Production

	Mass^2 Selection	No Background Subtraction	With Background Subtraction
K*(890)	.75 - .84	1.35 $\pm$ 0.03 mb	1.03 $\pm$ 0.06 mb
Δ*(1236)	1.48 - 1.68	0.61 $\pm$ 0.02 mb	0.18 $\pm$ 0.03 mb
N*(1688)	2.64 - 3.06	0.51 $\pm$ 0.06 mb	0.14 $\pm$ 0.03 mb

Figure IV-1. The Dalitz plot, which shows the presence of three prominent resonances in our data.

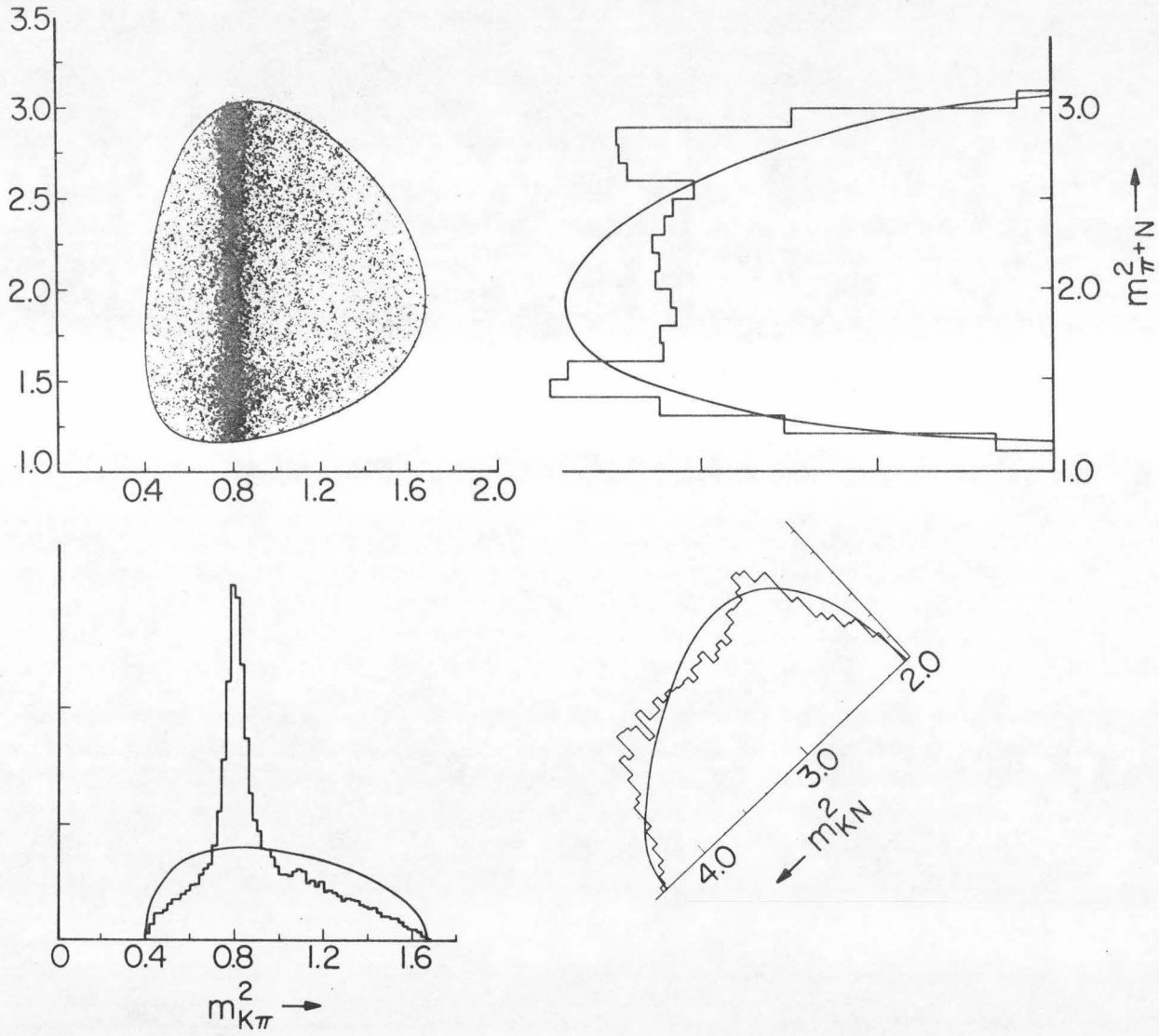
3.5
3.0
2.5
2.0
1.5
1.0
0.4
0.8
1.2
1.6
2.0
3.0
2.0
1.0
$m^2_{\pi^+N}$
0
0.4
0.8
1.2
1.6
$m^2_{K\pi}$
2.0
3.0
4.0
m^2_{KN}

effects have been seen previously in $K^+p \to K^0\pi^+p$ (Bland 1966) and are expected from elementary quantum mechanics. We present below a heuristic analysis which makes plausible the presence at a significant level of such effects in our data.

Figure IV-2 shows the π^+n effective mass squared distributions for different selections on $m_{K\pi}$. The curves are the phase space predictions normalized to the number of events with π^+n mass in the non-resonant region 1.3 to 1.55 GeV/c^2.

In Table IV-2, the $\Delta^+(1236)$ and N*(1688) enhancements are summarized. The ratios of these enhancements to the phase space show peaks in the K* band ($m_{K\pi}^2$ = 0.76 to 0.84 GeV^2/c^4). This suggests that there are substantial interference effects.

This conclusion is complicated to prove because of the expected anisotropy of the K* decay. However qualitatively one can see that this does not affect the conclusion in the Δ^+ case by the following argument.

Since the K* is spin 1, the K* decay amplitude must be of the form: $A^x(\bar{\theta},\bar{\phi}) = a_1+a_2 \cos\bar{\theta}$ in some frame. The s-channel helicity frame must be related to this frame by some rotation $\beta=\beta(m_{K\pi},t)$. Therefore the amplitude can be written as:

$$A^s(\theta,\phi) = a_1+a_2 (\cos\theta \cos\beta - \sin\theta \sin\beta \cos\phi).$$

Table IV-2. Events Above Phase Space in Dalitz Plot

$m^2_{K\pi}$	Δ^+	N*	$\Delta^+/_{p.s.}$ $(\frac{10^3 \text{ events}}{GeV^2/c^4})$	N*/p.s. $(\frac{10^3 \text{ events}}{GeV^2/c^4})$
0.40 - 0.62	123 ± 21	1 ± 9	.56 ± .1	.00 ± .04
0.62 - 0.72	144 ± 19	1 ± 16	1.4 ± .2	.0 ± .2
0.72 - 0.76	78 ± 17	10 ± 15	2.0 ± .4	.2 ± .4
0.76 - 0.80	174 ± 24	117 ± 23	4.4 ± .6	2.9 ± .6
0.80 - 0.84	162 ± 23	136 ± 22	4.0 ± .6	3.4 ± .6
0.84 - 0.90	94 ± 20	154 ± 21	1.6 ± .3	2.6 ± .3
0.90 - 1.00	68 ± 19	84 ± 20	.68 ± .2	.84 ± .2
1.00 - 1.14	108 ± 20	64 ± 19	.77 ± .1	.46 ± .1
1.14 - 1.32	106 ± 21	154 ± 21	.59 ± .1	.86 ± .1
1.32 - 2.00	0 ± 19	28 ± 8	.0 ± .3	.04 ± .1

Figure IV-2. Sections of the Dalitz plot showing the behavior of the baryon resonance peaks as a function of $M_{K\pi}$.

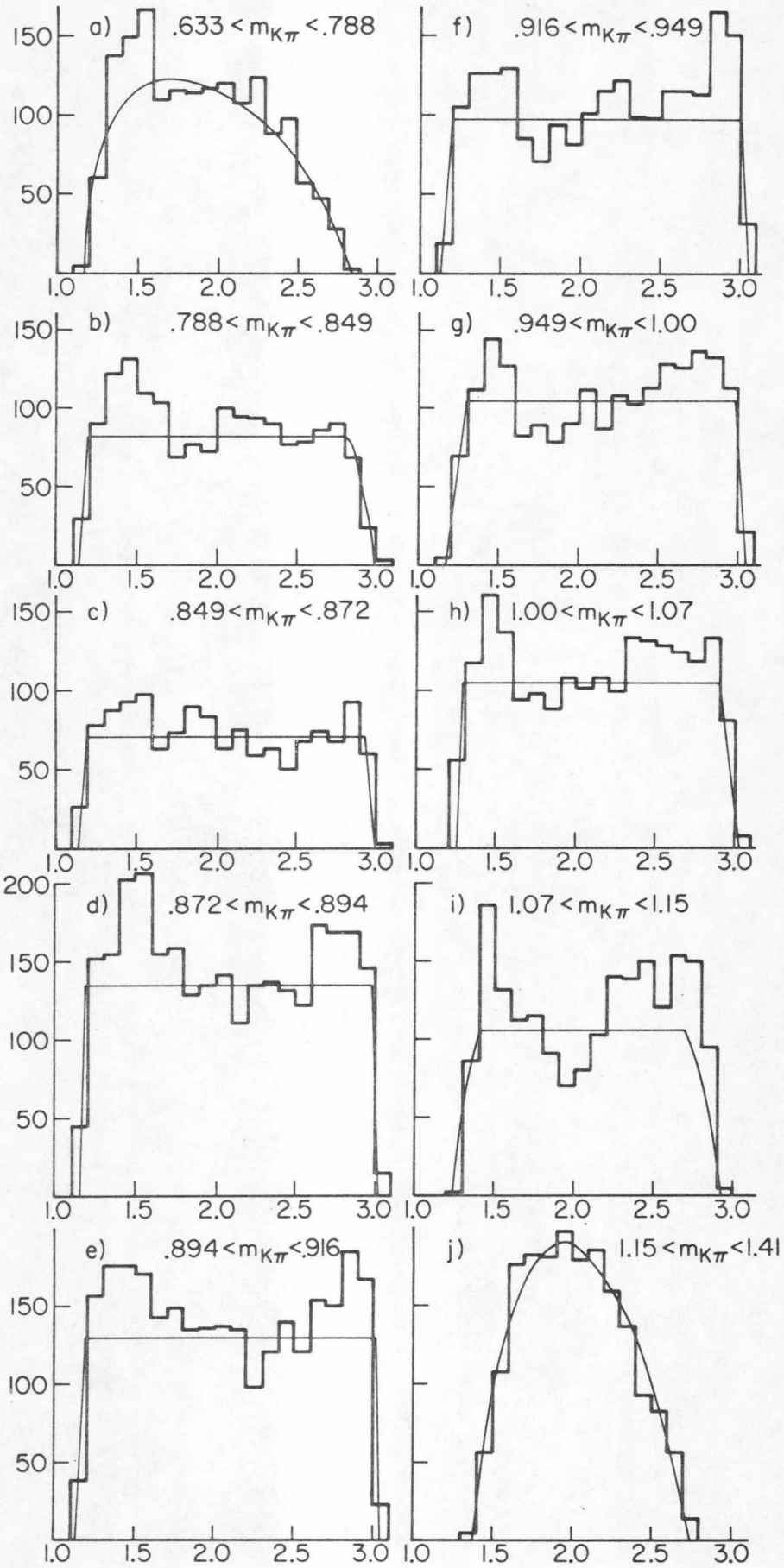
a) .633 < $m_{K\pi}$ < .788
b) .788 < $m_{K\pi}$ < .849
c) .849 < $m_{K\pi}$ < .872
d) .872 < $m_{K\pi}$ < .894
e) .894 < $m_{K\pi}$ < .916
f) .916 < $m_{K\pi}$ < .949
g) .949 < $m_{K\pi}$ < 1.00
h) 1.00 < $m_{K\pi}$ < 1.07
i) 1.07 < $m_{K\pi}$ < 1.15
j) 1.15 < $m_{K\pi}$ < 1.41
50
100
150
200
1.0
1.5
2.0
2.5
3.0

Then the decay distribution must be of the form:

$$|A|^2 = |a_1|^2 + |a_2|^2 \quad (\cos^2\theta \cos^2\beta + \sin^2\theta \sin^2\beta \cos^2\phi - 2 \sin\theta \cos\theta \sin\beta \cos\beta \cos\phi) + 2 \text{ Re } a_1^* a_2 \quad (\cos\theta \cos\beta - \sin\theta \sin\beta \cos\phi)$$

integrating over ϕ, reduces this distribution to:

$$|A|^2 = |a_1|^2 + |a_2|^2 (\cos^2\theta \cos^2\beta + \tfrac{1}{2} \sin^2\theta \sin^2\beta) + 2 \text{ Re } a_1^* a_2 \quad (\cos\theta \cos\beta).$$

This is a polynomial of order 2 in cos θ and so has only a single minimum or maximum.

For the s-channel helicity frame, cos θ is linearly related to $m^2_{\pi^+n}$, the effective π^+n mass squared (see Appendix IV), so that the distributions in Figure IV-2 can exhibit only one extremum. Clearly in Figure IV-2d (for example) that extremum is a minimum. Therefore the lack of about 100 events in the interval $m^2_{\pi^+n}$ = 1.2 to 1.4 in this figure indicates that very little of the bump at $m^2_{\pi^+n}$ = 1.5 GeV^2/c^4 can be ascribed to the K* decay anisotropy. The same argument cannot be applied to the N*(1688) because it occurs too close to the phase space boundary.

This indicates that the simple classical non-interfering resonance model cannot hope to describe the data. This effect has also been observed in the reaction $K^+p \to K^0\pi^+p$ at 1.2 GeV/c (Bland 1966). We will again discuss this effect

when we deal with it as a background affecting the evaluation of the $K\pi$ moments.

B. Dependence of the Cross Section Upon Momentum Transfer

The dominant process in the reaction $K^- p \to K^- \pi^+ n$ is the quasi-two body production of the K*(890). Thus we shall investigate the dependences of the K* cross section on energy, and the K* differential cross section on momentum transfer. The first of these is discussed in Section V-A, where our results are compared to experiments at different energies. Here we discuss the momentum dependence. This is the only dynamical variable for a quasi-two body scattering process at fixed energy, if spins are neglected. (The momentum transfer is defined as $t = (\vec{p}_n - \vec{p}_p)^2$).

Figure IV-3 is the Chew-Low plot (t vs $m_{K\pi}^2$) for the events in this experiment. For fixed $m_{K\pi}^2$, the phase space is uniform in t. Thus the enhancement at small t is dynamical in origin. This effect is referred to as peripheralism, because of the interpretation that large impact parameter interactions dominate such high energy processes.

Since Δ^+ and N* production also contribute to the data, it is interesting to examine the corresponding plot for baryon resonance formation. Figure IV-4 is the Chew-Low plot ($t_{Kin,Kout}$ vs $m^2_{\pi^+ n}$) for all events, and Figure IV-5 is the same plot for non-K* events (not in the mass range 890 ± 50 MeV). For the Δ^+ there is an enhancement at small $t_{Kin,Kout}$ like the one in the K* plot. This indicates that

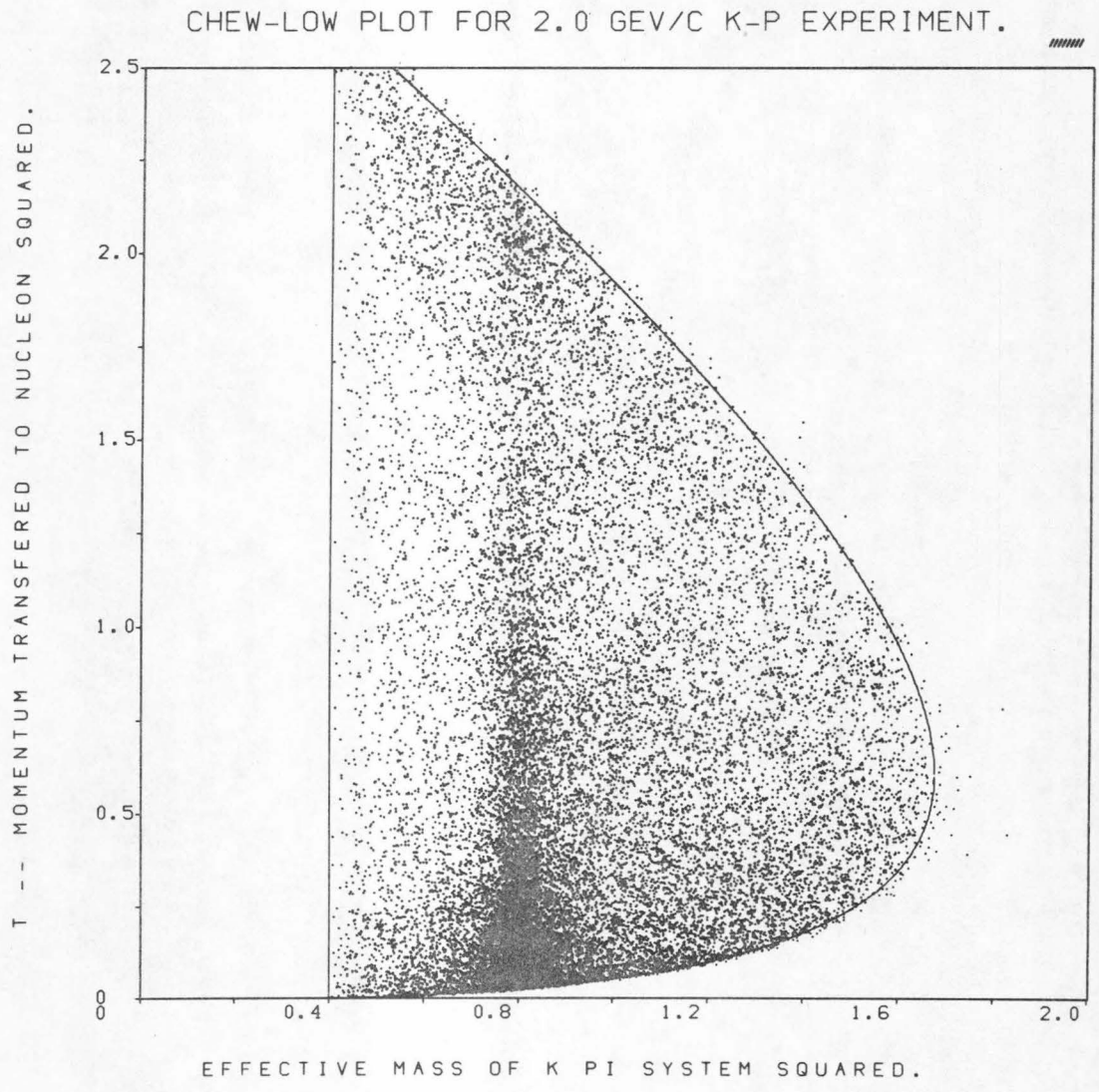

Figure IV-3. Chew-Low plot -- assuming K^* production

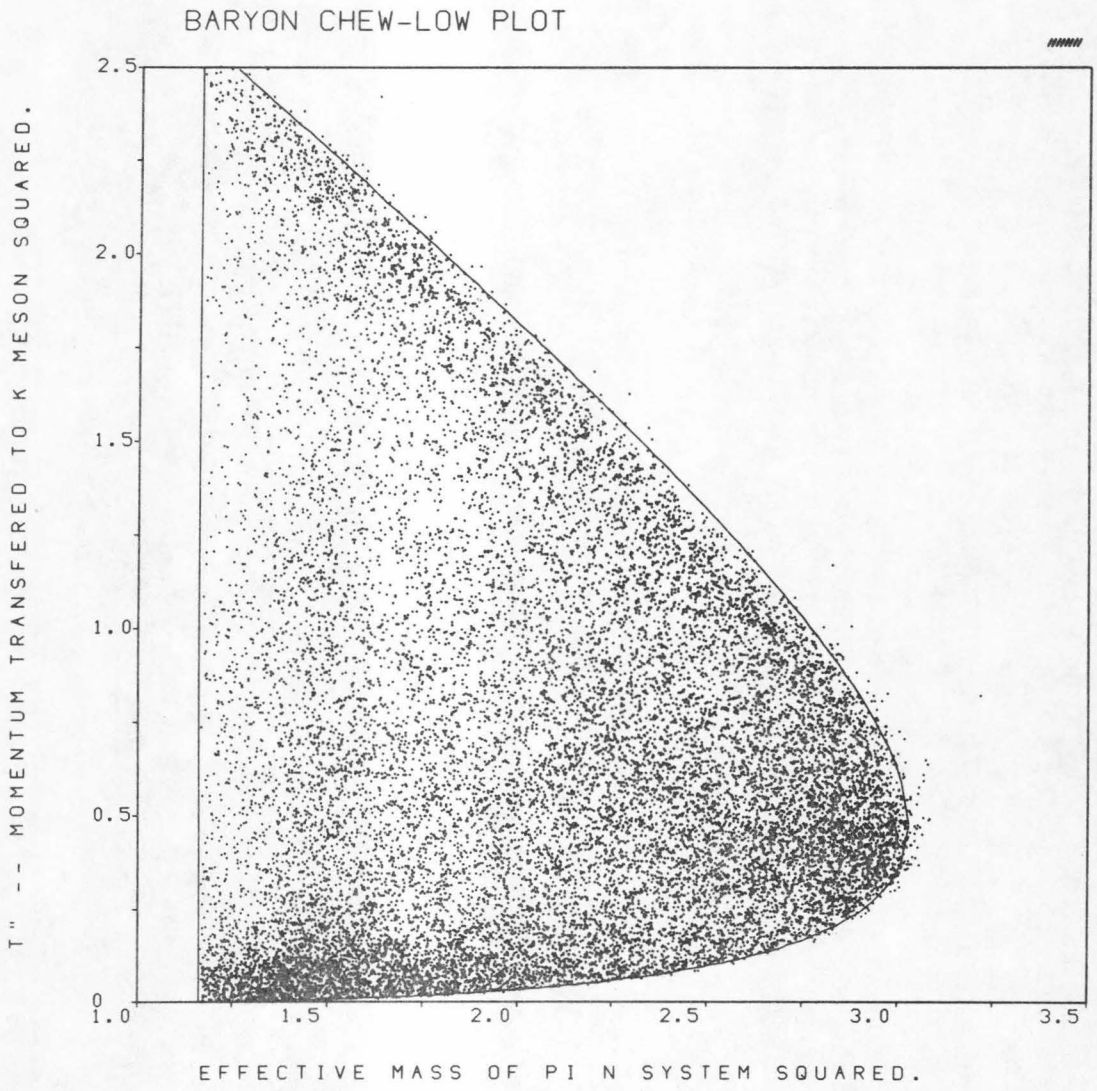

Figure IV-4. Chew-Low plot -- assuming baryon resonance production.

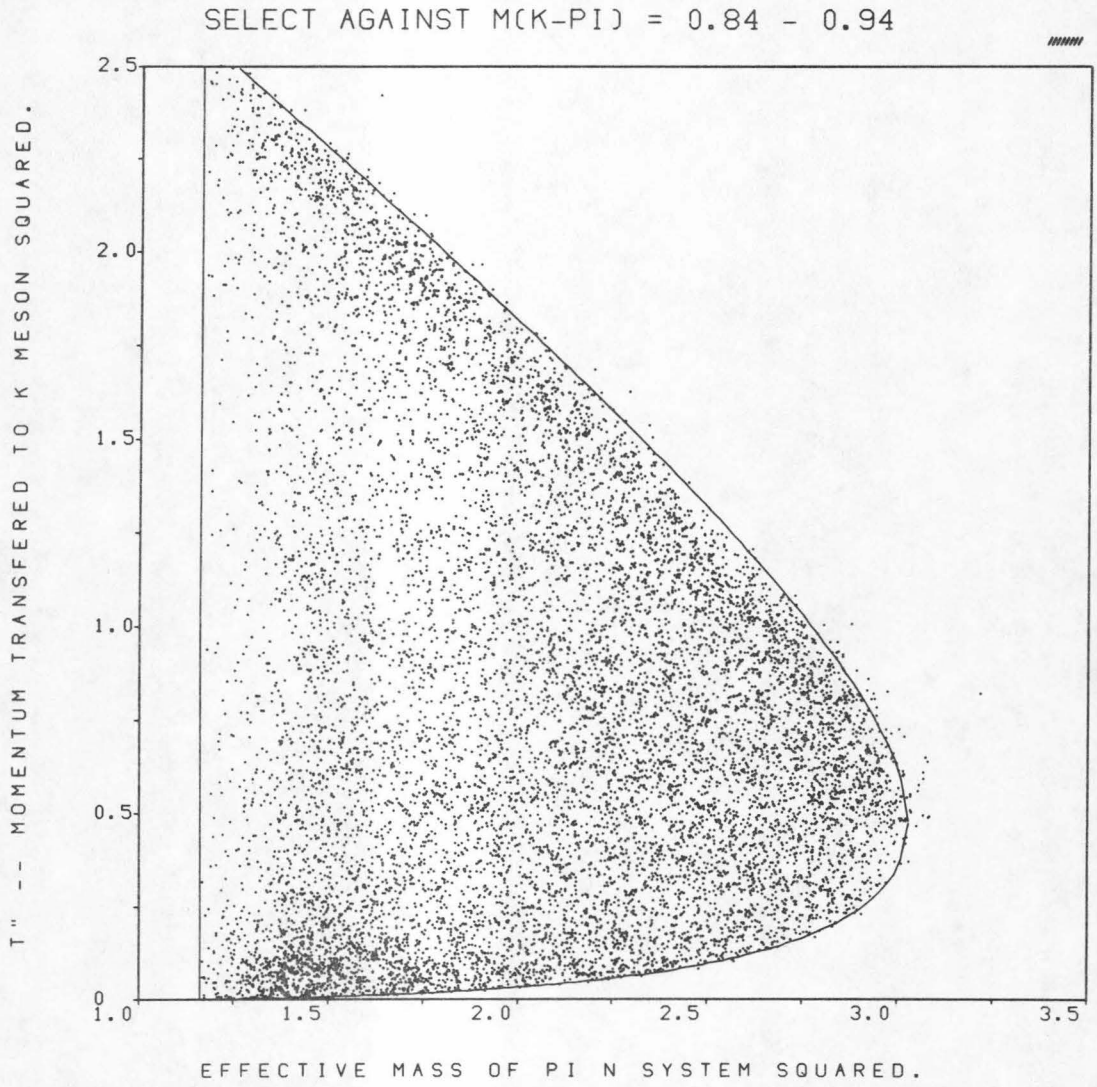

Figure IV-5. Chew-Low plot -- assuming baryon resonance production and removing the $K^{*}(890)$ events.

the Δ^+ is also produced by a peripheral mechanism. Since the N*(1688) occurs at the kinematic limit, the slope of its production angular distribution is not apparent.

Figure IV-6 is the differential cross sections for various regions of $K\pi$ mass in the t range 0.0 to 0.5 GeV^2/c^2. The curves are for the function $t(t+\mu^2)^{-2}$ normalized to the data (the significance of this form which is the simple pion-exchange pole equation, is discussed in Chapter V), and are used here only to provide a convenient way of comparing the shape of the t dependence at different $m_{K\pi}$ values. The similarity of the shapes of the different $m_{K\pi}$ selections implies that there is little difference in the t dependence of the "true K*" events and the non-resonant background beneath the K*.

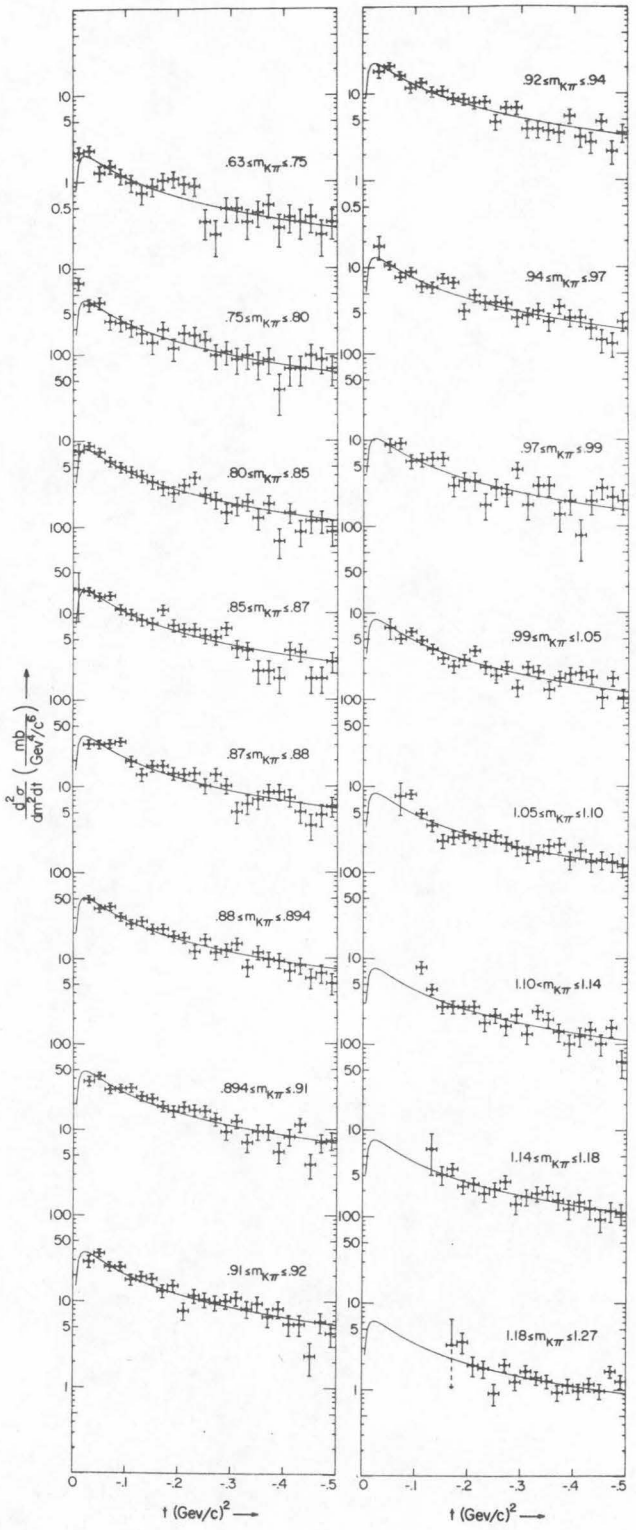

Figure IV-6. The t - distribution of our data.

C. Angular Correlations in the Kπ Rest Frame

Besides the dependence of the differential cross section upon characteristic masses, and the momentum transfer; one also measures the dependence of the cross section (and thus the amplitude) upon the kinematic variables which describe the angular distribution of the K (and π) in the Kπ rest frame. This distribution exhibits many energy independent and reaction independent features (as will be shown in Chapter V). These features are presumed to reflect the angular distribution of Kπ elastic scattering. For purposes of the analyses to be described in Chapter V, the data have been binned in t and $m_{K\pi}$ and the spherical harmonic moments extracted independently for each bin. The reason for extracting the moments is to decrease the data handling problem.

For low effective Kπ masses, only low partial waves interact and have significant phase shifts. Assuming a range of 1 fermi, only partial waves with $J<2$ are significant[(i)] for our mass interval. The effective range envelop for this assumed range is shown in Figure IV-7. If the maximum interacting partial wave is J_M, the only moments

---

[(i)] Assuming $j \leqslant kr$ is required for an interaction to occur.

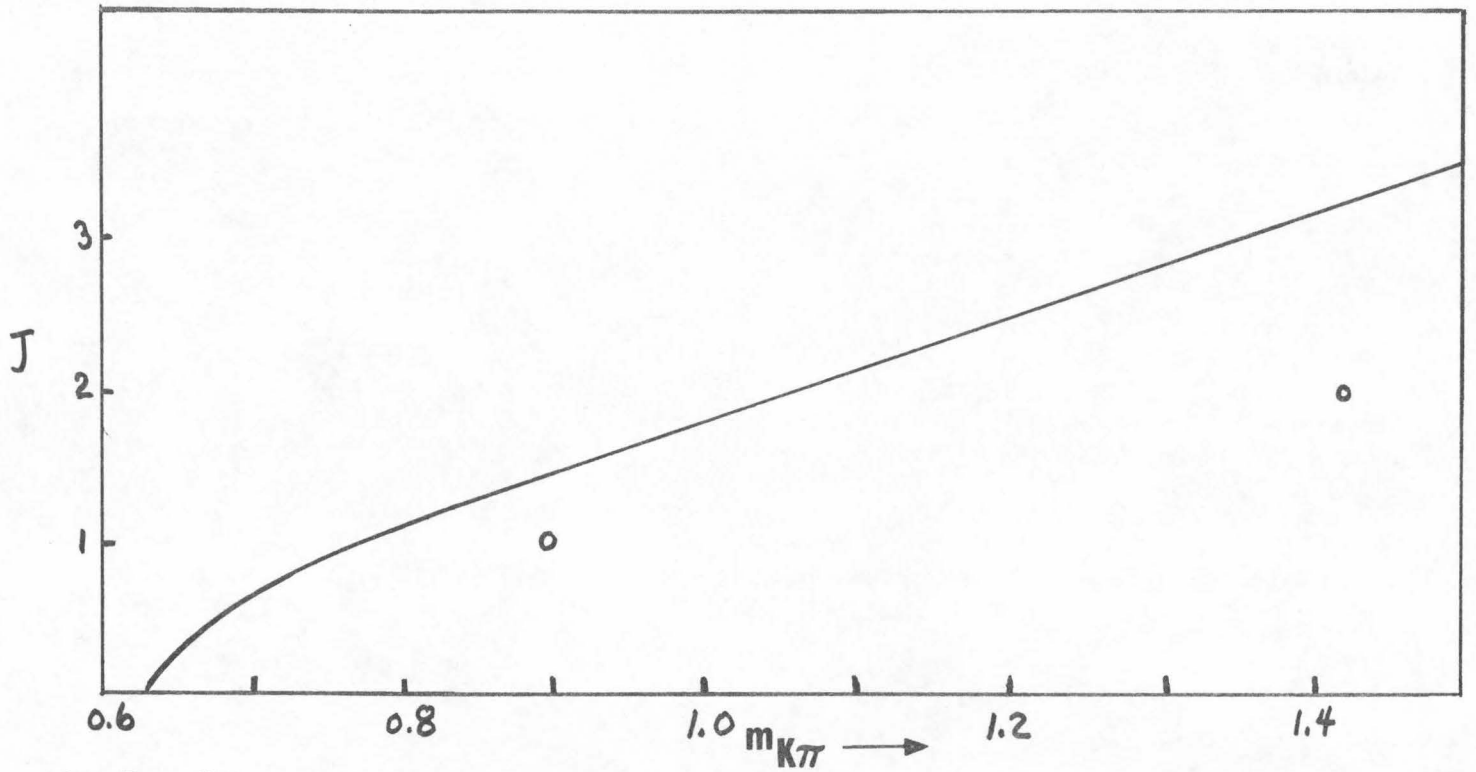

Figure IV-7. "The effective range" envelope for Kπ scattering; which delineates the region where each partial wave can matter. ($j_{max} = \frac{R_o}{hc}\left[\frac{(s-(m_1+m_2)^2)\ (s-(m_1-m_2)^2)}{4s}\right]^{\frac{1}{2}}$, R_o = 1 fermi, and $S = m_{K\pi}{}^2$).

with $L<2J_M$ are non-zero. Experimentally, in our data no moments with $L>2$ are statistically different from zero.

The standard method for evaluating the moments of an angular distribution with uniform 4π acceptance is to average $Y_{lm}(\theta,\phi)$ over all events:

$$\bar{a}_{lm} = \frac{\sum_{i = \text{all events}}^{N} Y_{lm}(\theta_i,\phi_i)}{N}$$

Due to the orthonormal properties of the Y_{lm}'s, this has the effect of extracting the coefficient a_{lm} in the expansion:

$$\frac{d\sigma}{d\Omega} = \sigma_T \sum_{lm} a_{lm} Y_{lm}(\theta,\phi) \quad (ii)$$

(where $a_{00} = \frac{1}{\sqrt{4\pi}}$).

Because there are theoretical questions as to which coordinate frame to use, the moments have been calculated for the following two coordinate frames (see Figure IV-8): the helicity or s-channel frame (polar axis chosen along the K* line of flight in the center of mass), and the Gottfried-Jackson or t-channel frame (polar axis chosen along the beam direction as seen in the K* rest frame). For each

---

(ii) Strictly speaking $\lim_{N\to\infty} \bar{a}_{lm} = a_{lm}$

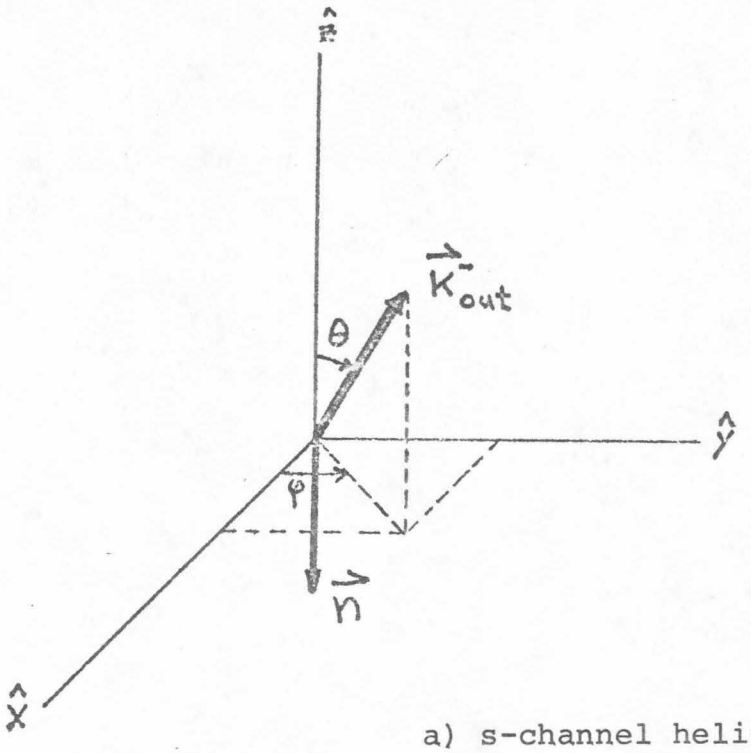

a) s-channel helicity frame.

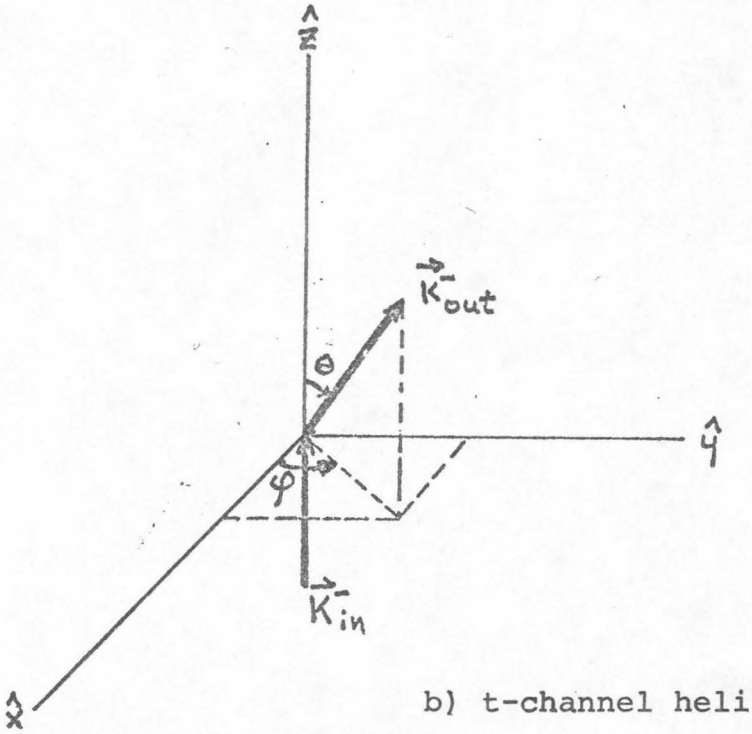

b) t-channel helicity frame.

Figure IV-8. Kπ - coordinate frames.

event, the rotation angle (crossing angle) is well defined. However, since the data are binned in t and $m_{K\pi}$ (instead of being at a unique t - $m_{K\pi}$ point) and the crossing angle varies rapidly with t (see Figure IV-9), the resulting sets of moments are not simply related.

In evaluating the $K\pi$ moments, the background due to $\Delta(1236)$ and N*(1688) can be removed by excluding all events in the Δ^+ and N* mass regions and correcting for this cut by acceptance corrections (see Appendix IV). This is necessary in our situation because the lack of a detailed understanding of the behavior of the K* - Δ^+ interference makes a subtraction impossible. This change in method yields the second set of moments in Figure IV-10[iii] (the first set of moments is generated by the standard method of averaging the moments over events). There are slight differences, but they do not appear to be statistically significant.

The two most noticeable features of our moments are the size of $a_{2,0}$ and the rapidly changing value of $a_{1,0}$.

[iii] This method has a limitation in that a maximum 1 must be assumed to generate the fit. Since this limitation exists and the moments in Figure IV-10 agree we shall use the moments generated by the first method in Chapter V.

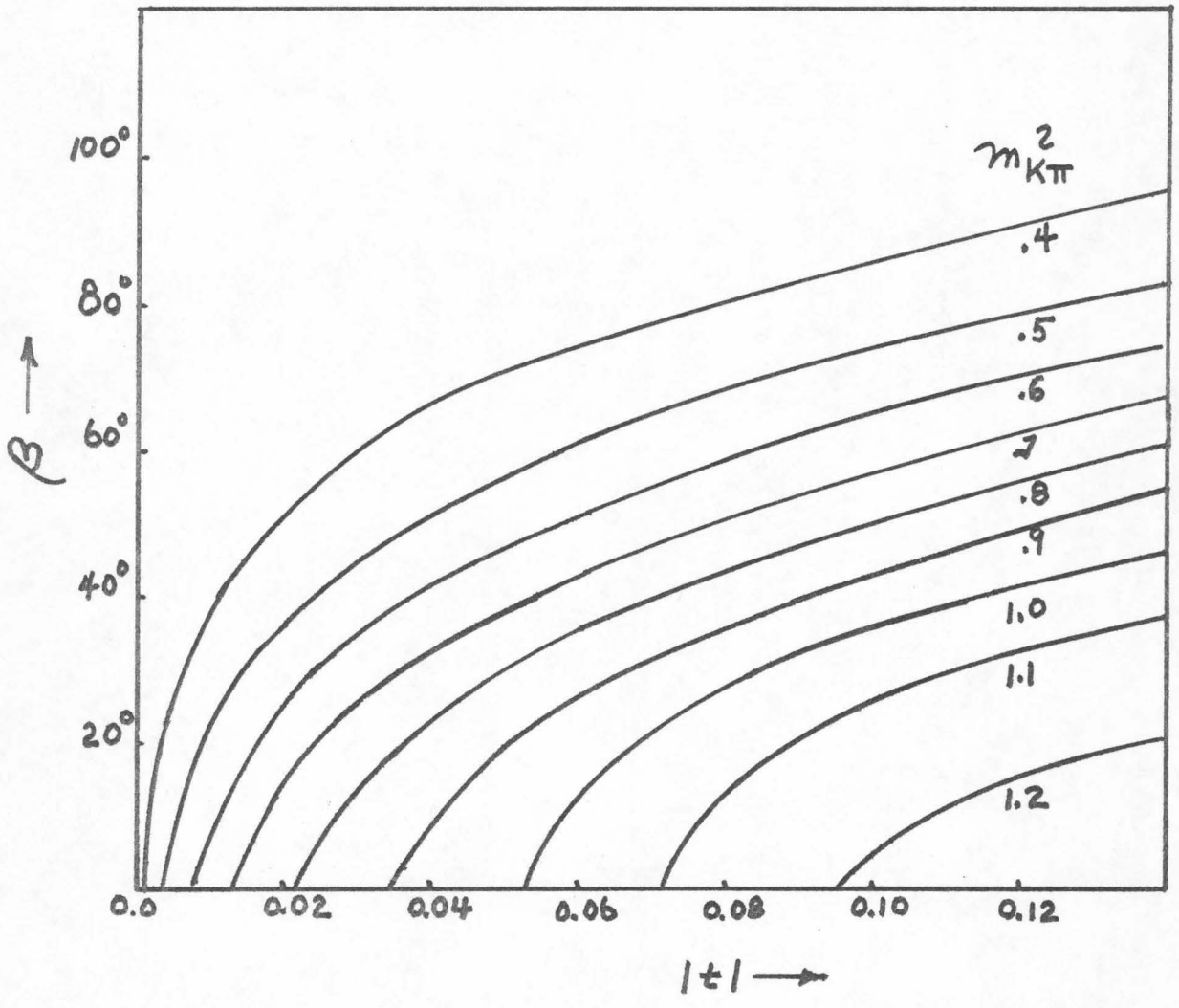

Figure IV-9. The crossing angle between the s- and t-channel helicity frames for P_{lab} = 2.0 Gev/c in $K^- p \to K^- \pi^+ n$.

Figure IV-10. The spherical harmonic moments of our data ($+ < 0.5$) in the s- and t-channel frames using both the method of moments (□) and the maximum likelihood method (△).

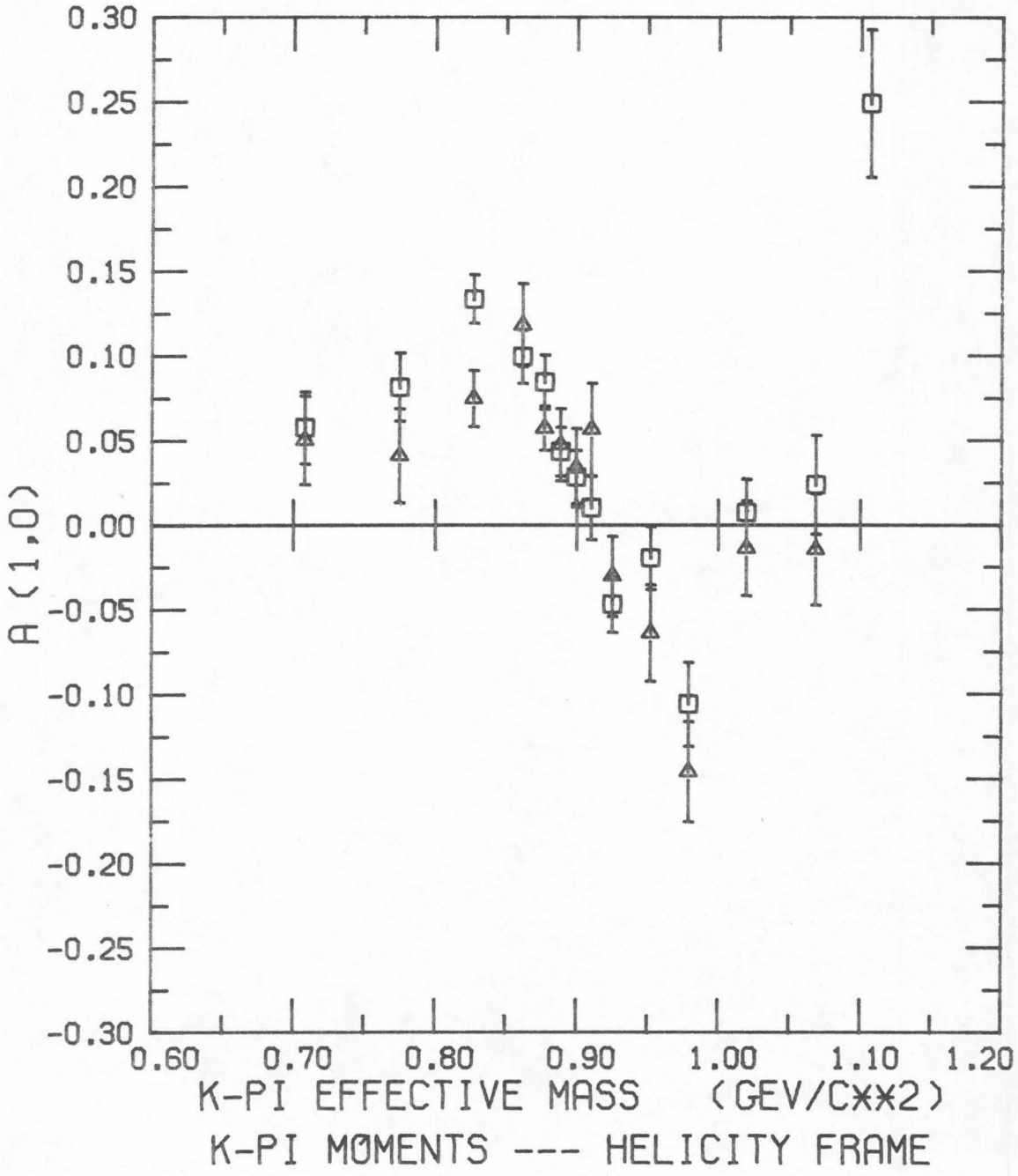
0.30
0.25
0.20
0.15
0.10
0.05
0.00
-0.05
-0.10
-0.15
-0.20
-0.25
-0.30
A(1,0)
0.60
0.70
0.80
0.90
1.00
1.10
1.20
K-PI EFFECTIVE MASS (GEV/C**2)
K-PI MOMENTS --- HELICITY FRAME

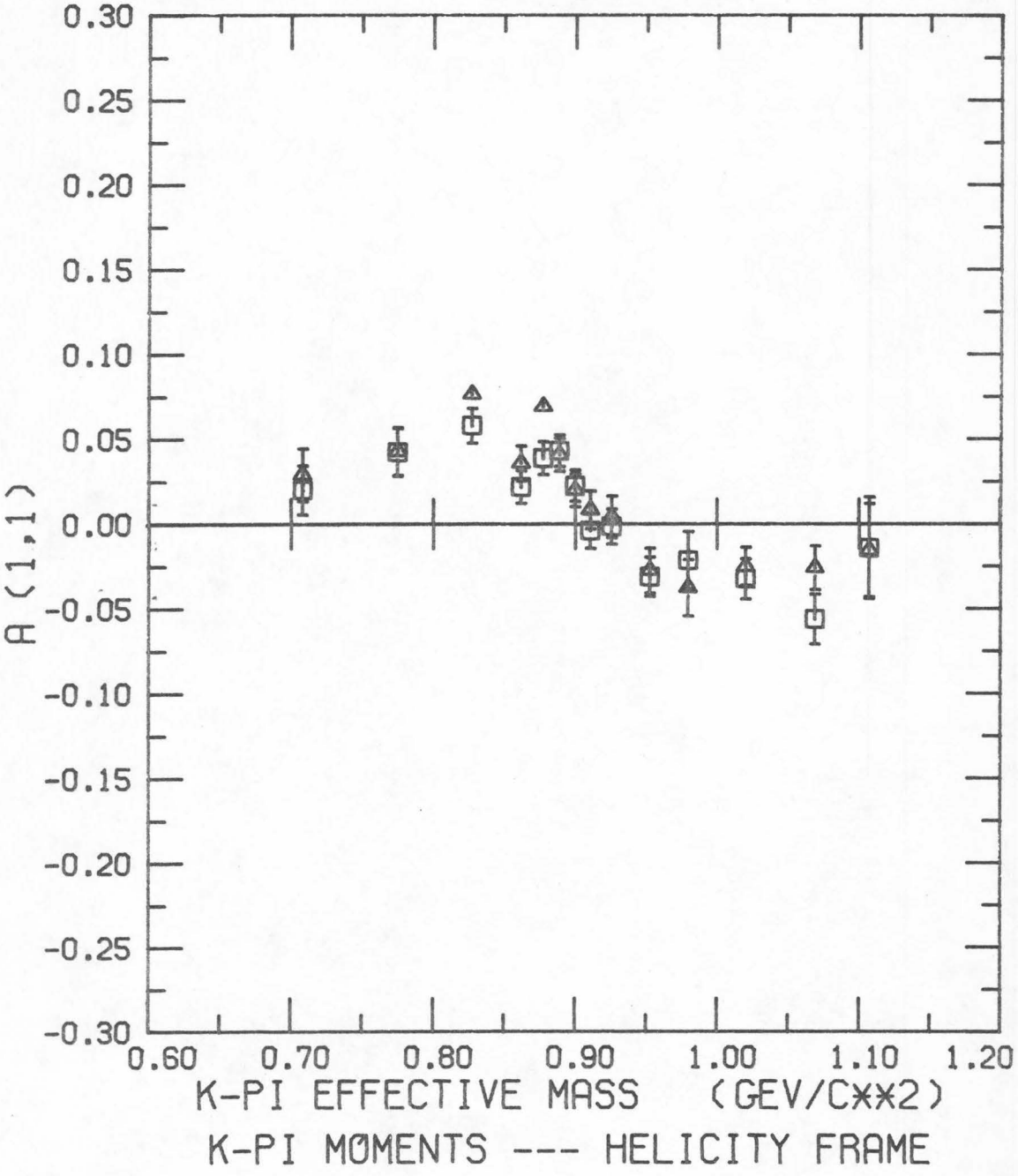
0.30
0.25
0.20
0.15
0.10
0.05
0.00
-0.05
-0.10
-0.15
-0.20
-0.25
-0.30
A(1,1)
0.60
0.70
0.80
0.90
1.00
1.10
1.20
K-PI EFFECTIVE MASS (GEV/C**2)
K-PI MOMENTS --- HELICITY FRAME

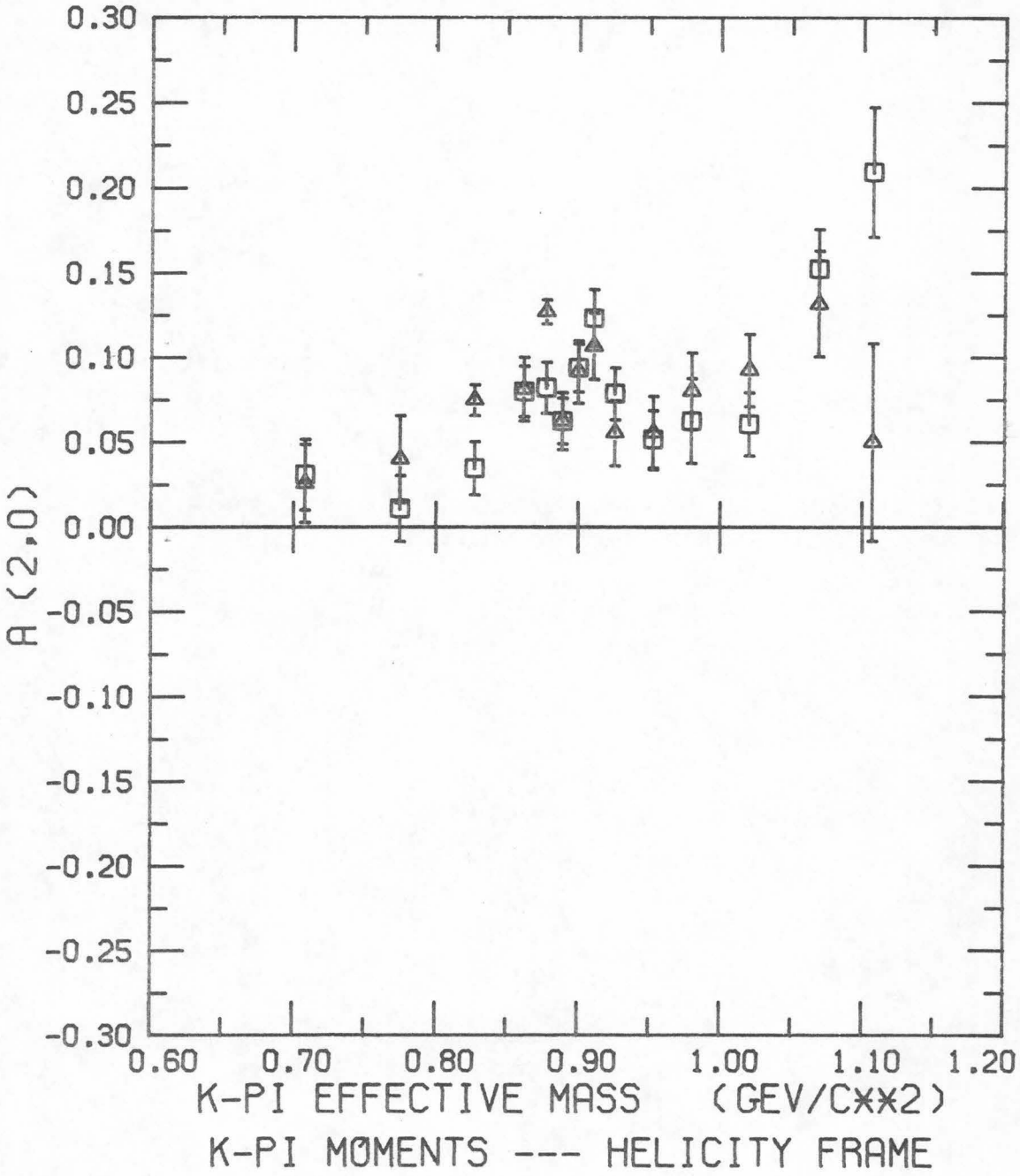
0.30
0.25
0.20
0.15
0.10
0.05
0.00
-0.05
-0.10
-0.15
-0.20
-0.25
-0.30
A(2,0)
0.60
0.70
0.80
0.90
1.00
1.10
1.20
K-PI EFFECTIVE MASS (GEV/C**2)
K-PI MOMENTS --- HELICITY FRAME

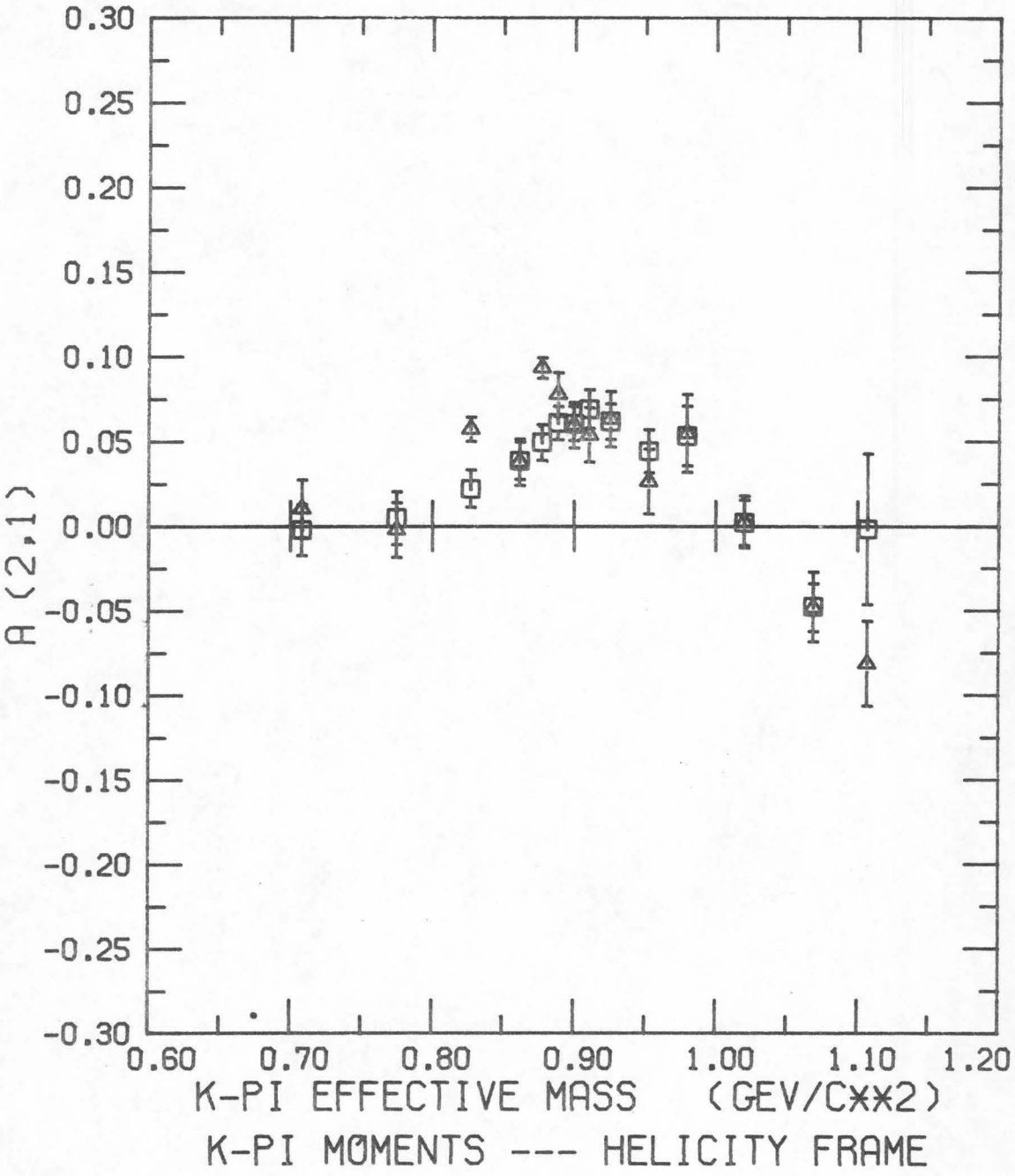
0.30
0.25
0.20
0.15
0.10
0.05
0.00
-0.05
-0.10
-0.15
-0.20
-0.25
-0.30
A(2,1)
0.60
0.70
0.80
0.90
1.00
1.10
1.20
K-PI EFFECTIVE MASS (GEV/C**2)
K-PI MOMENTS --- HELICITY FRAME

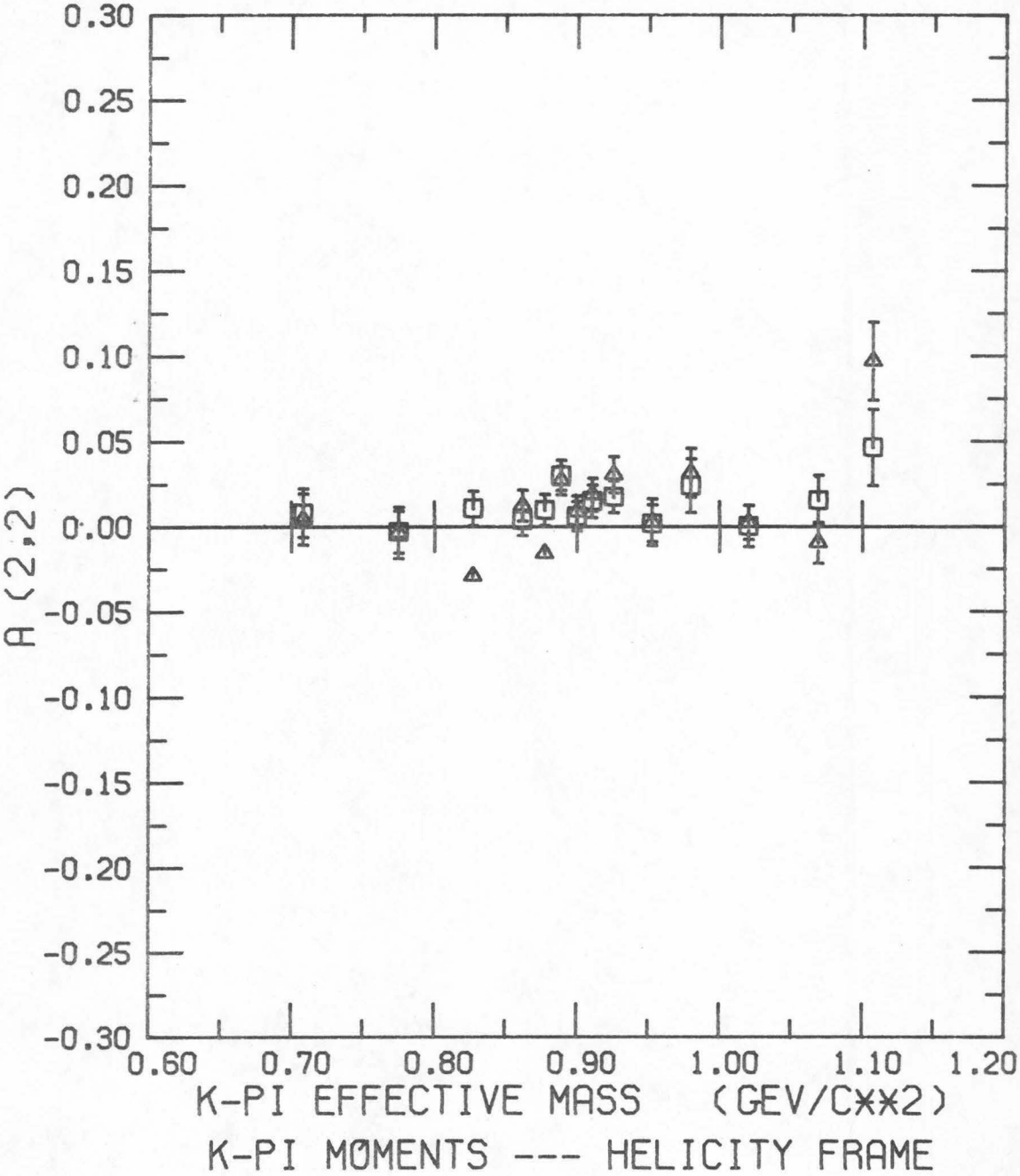
0.30
0.25
0.20
0.15
0.10
0.05
0.00
-0.05
-0.10
-0.15
-0.20
-0.25
-0.30
A(2,2)
0.60
0.70
0.80
0.90
1.00
1.10
1.20
K-PI EFFECTIVE MASS (GEV/C**2)
K-PI MOMENTS --- HELICITY FRAME

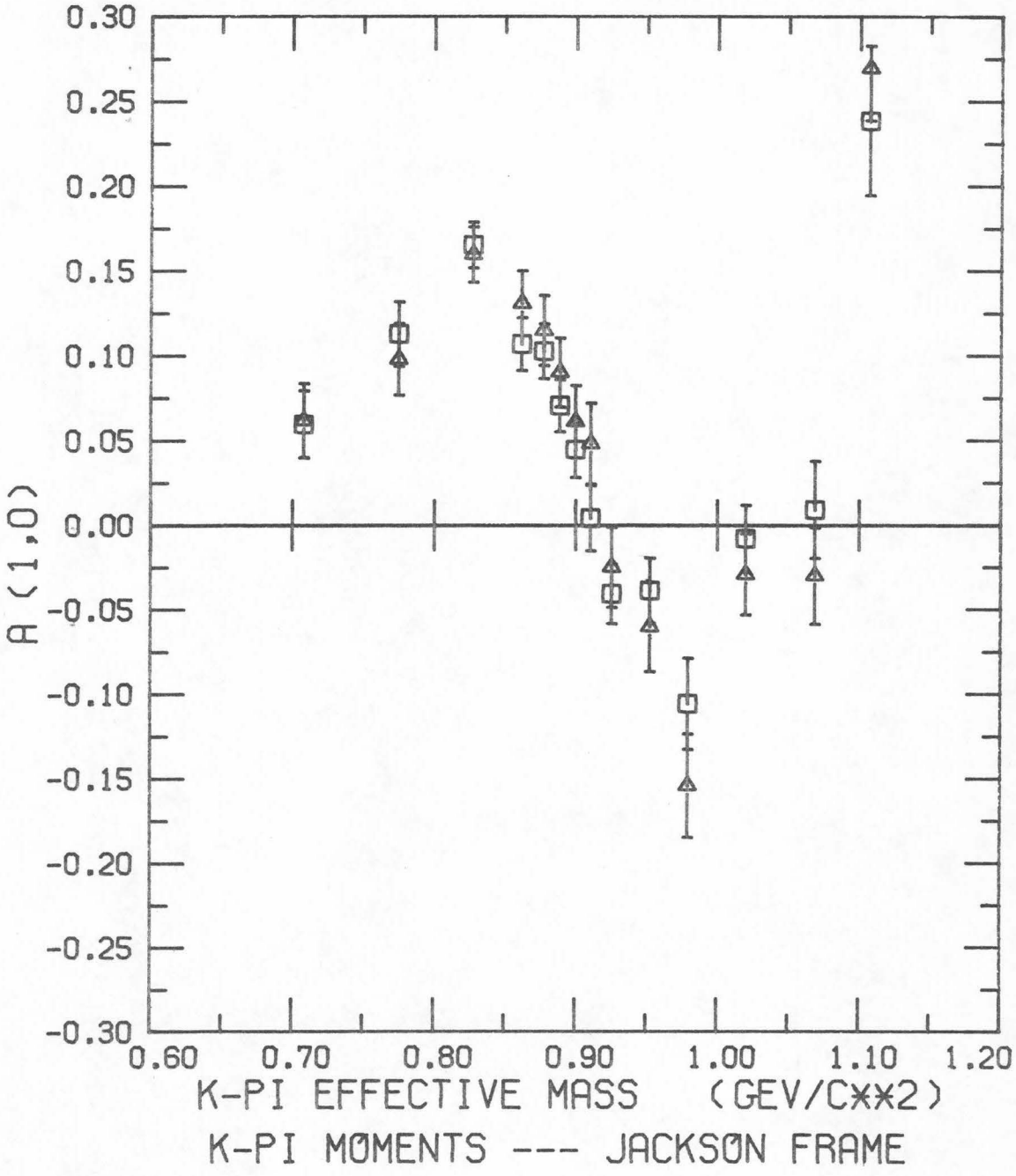
0.30
0.25
0.20
0.15
0.10
0.05
0.00
-0.05
-0.10
-0.15
-0.20
-0.25
-0.30
A(1,0)
0.60
0.70
0.80
0.90
1.00
1.10
1.20
K-PI EFFECTIVE MASS (GEV/C**2)
K-PI MOMENTS --- JACKSON FRAME

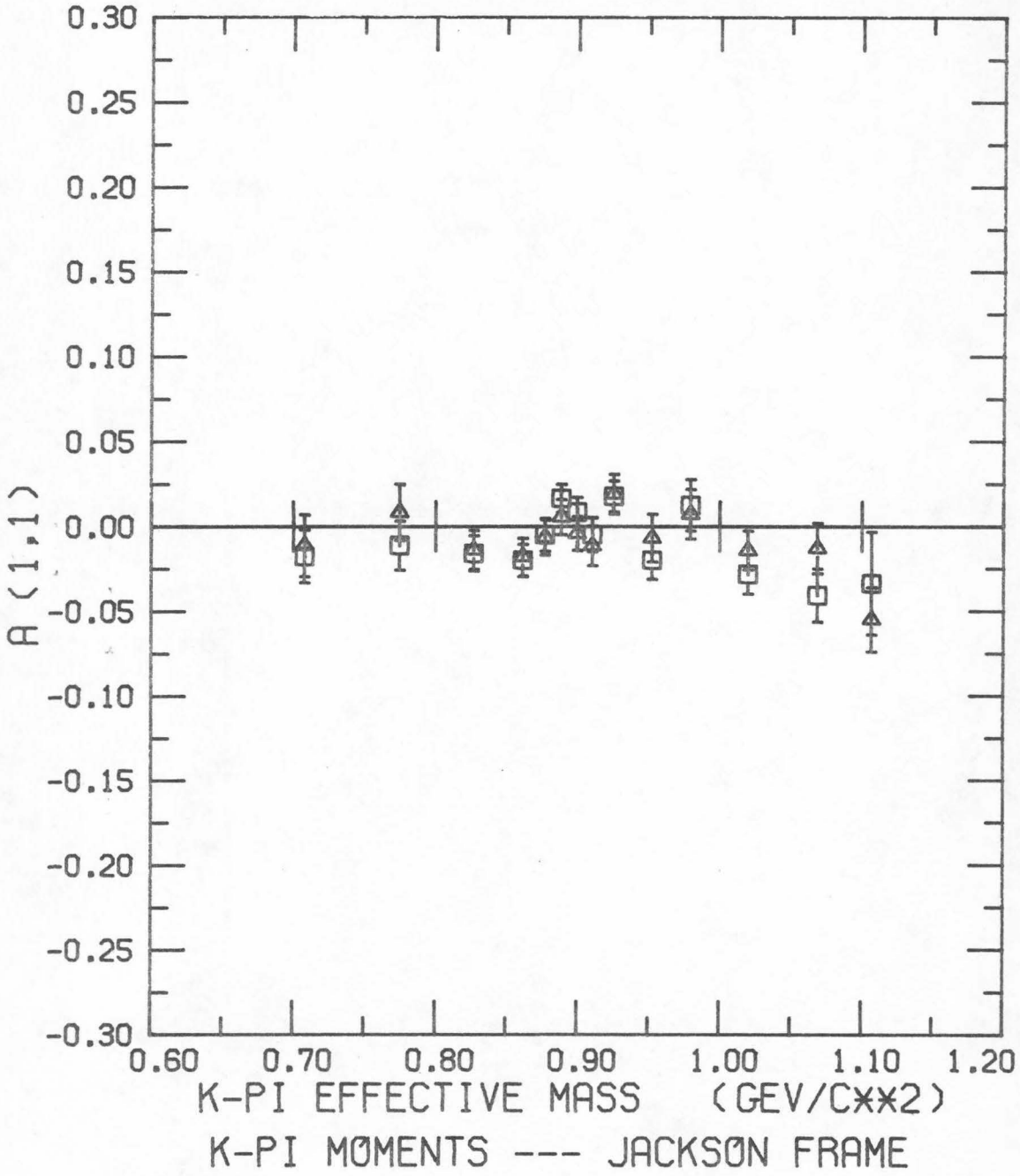
0.30
0.25
0.20
0.15
0.10
0.05
0.00
-0.05
-0.10
-0.15
-0.20
-0.25
-0.30
A(1,1)
0.60
0.70
0.80
0.90
1.00
1.10
1.20
K-PI EFFECTIVE MASS (GEV/C**2)
K-PI MOMENTS --- JACKSON FRAME

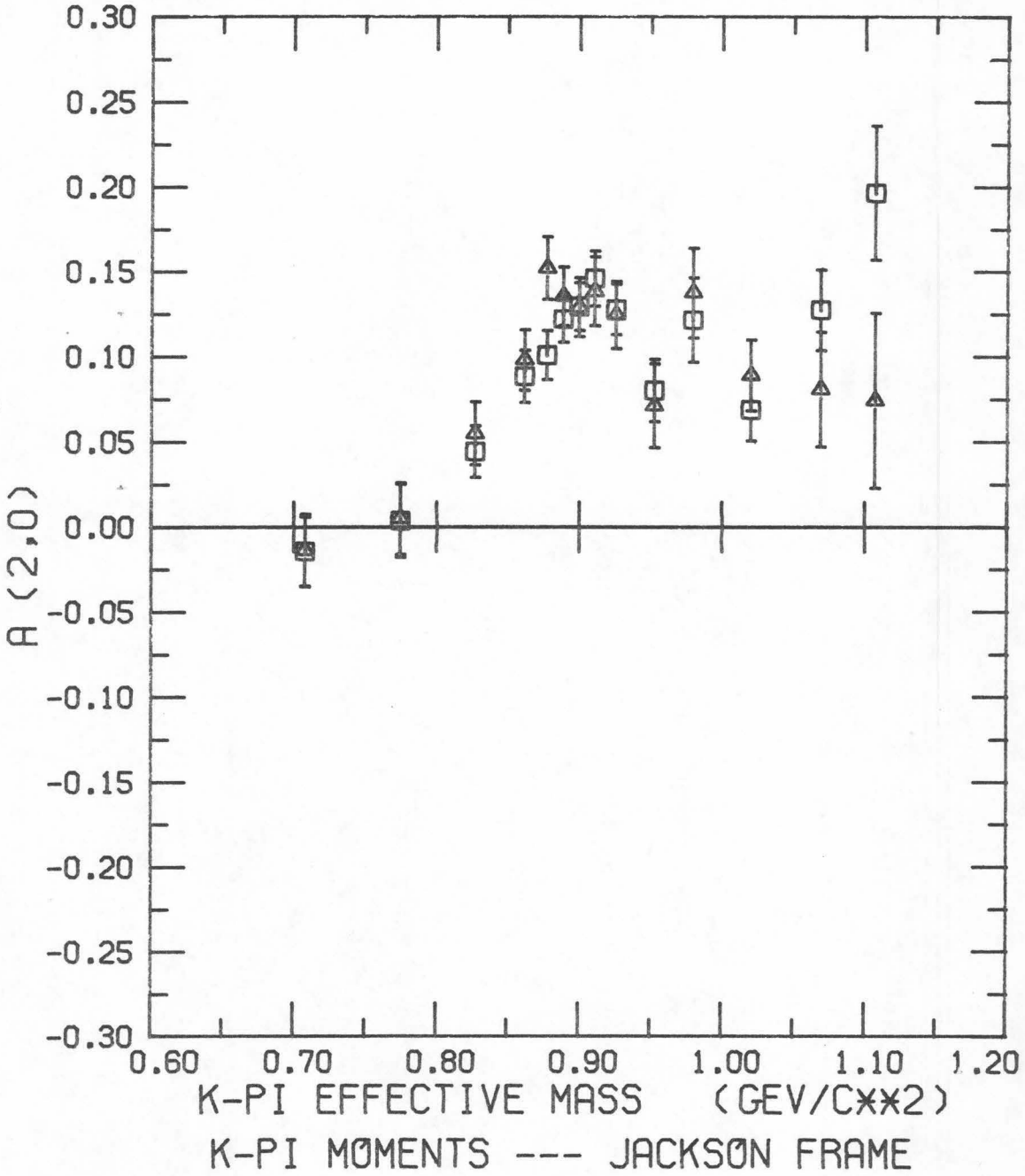
0.30
0.25
0.20
0.15
0.10
0.05
0.00
-0.05
-0.10
-0.15
-0.20
-0.25
-0.30
A(2,0)
0.60
0.70
0.80
0.90
1.00
1.10
1.20
K-PI EFFECTIVE MASS (GEV/C**2)
K-PI MOMENTS --- JACKSON FRAME

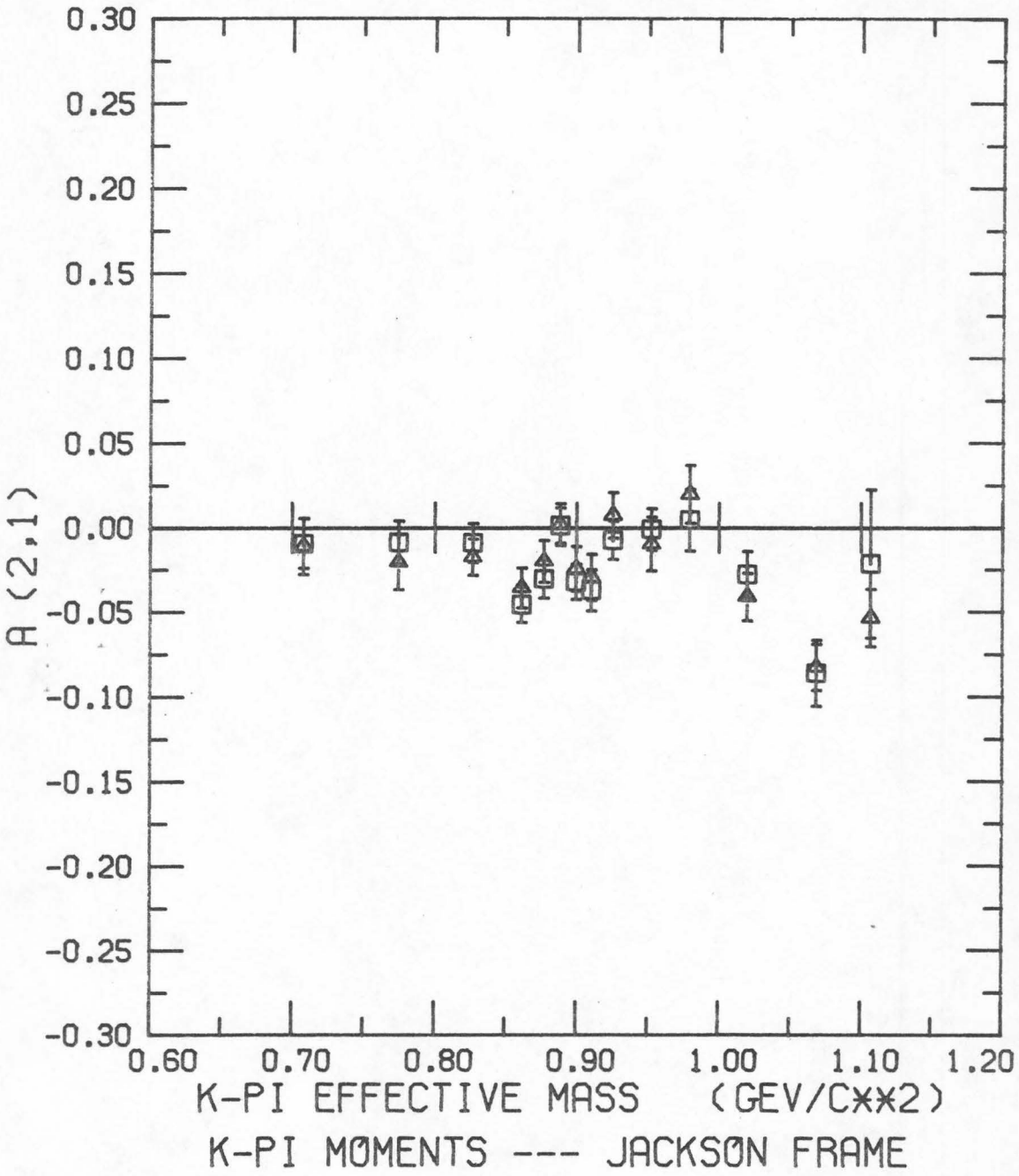
0.30
0.25
0.20
0.15
0.10
0.05
0.00
-0.05
-0.10
-0.15
-0.20
-0.25
-0.30
A(2,1)
0.60
0.70
0.80
0.90
1.00
1.10
1.20
K-PI EFFECTIVE MASS (GEV/C**2)
K-PI MOMENTS --- JACKSON FRAME

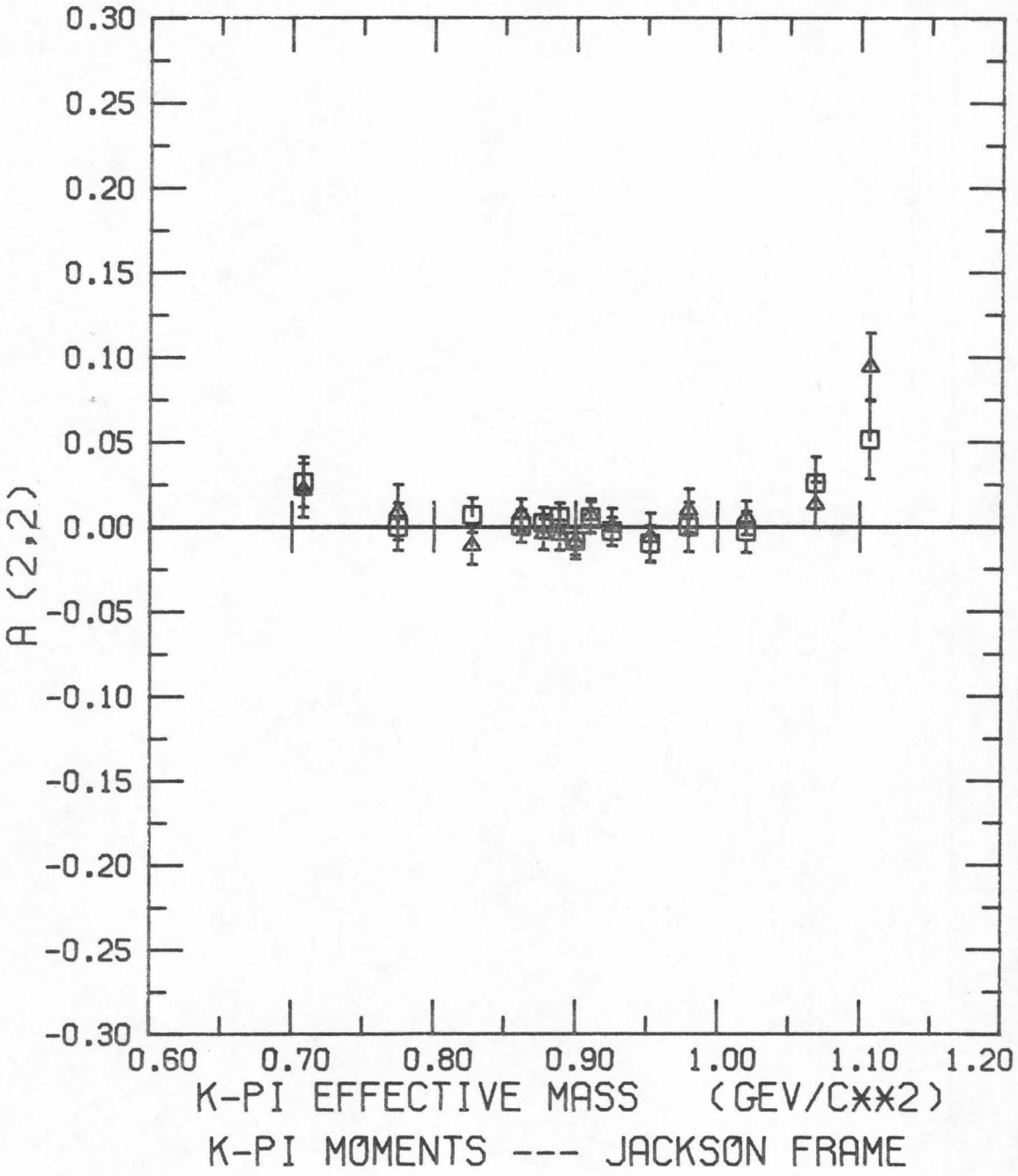
0.30
0.25
0.20
0.15
0.10
0.05
0.00
-0.05
-0.10
-0.15
-0.20
-0.25
-0.30
A(2,2)
0.60
0.70
0.80
0.90
1.00
1.10
1.20
K-PI EFFECTIVE MASS (GEV/C**2)
K-PI MOMENTS --- JACKSON FRAME

These features of our data appear to be quite similar to those observed in other experiments at other energies in both K^+ and K^-. Detailed comparisons will be discussed in Chapter V.

D. An Anomalous Backward Peak

As part of the analysis of our data, we have found an anomalous backward peak. This peak appears in Figure IV-5 as the enhancement along the upper diagonal edge. In Figure IV-11, the t_{p,K^-} distribution is plotted for various m_{π^+n} mass selections. The effect is clearly beyond statistics. To explain such a peak requires either an exotic baryon exchange or a significant two particle exchange amplitude, both of which are theoretically highly unattractive. It is therefore of great interest to discover if there is any other possible explanation for this peak.

The first explanation to consider is that it might result from some asymmetry of the K*(890) decay, since about 50% of the events in our sample arise from this source. In Figure IV-11, the solid distributions correspond to the non-K* events (not in the interval $m_{K\pi}$ = .84 to .94 GeV/c^2). Since the peak is as prominent in the non-K* events as in the total sample, we conclude that the peak is not the result of a K* decay asymmetry.

A second possible explanation for the peak is that it is due to a background reaction. This is seen to be impossible in Figure IV-12, where the chi-square distributions are plotted for the various 1-C mass hypotheses. The only tenable hypothesis is that of our reaction and it seems to show a nice shape. That no other hypothesis is plausible

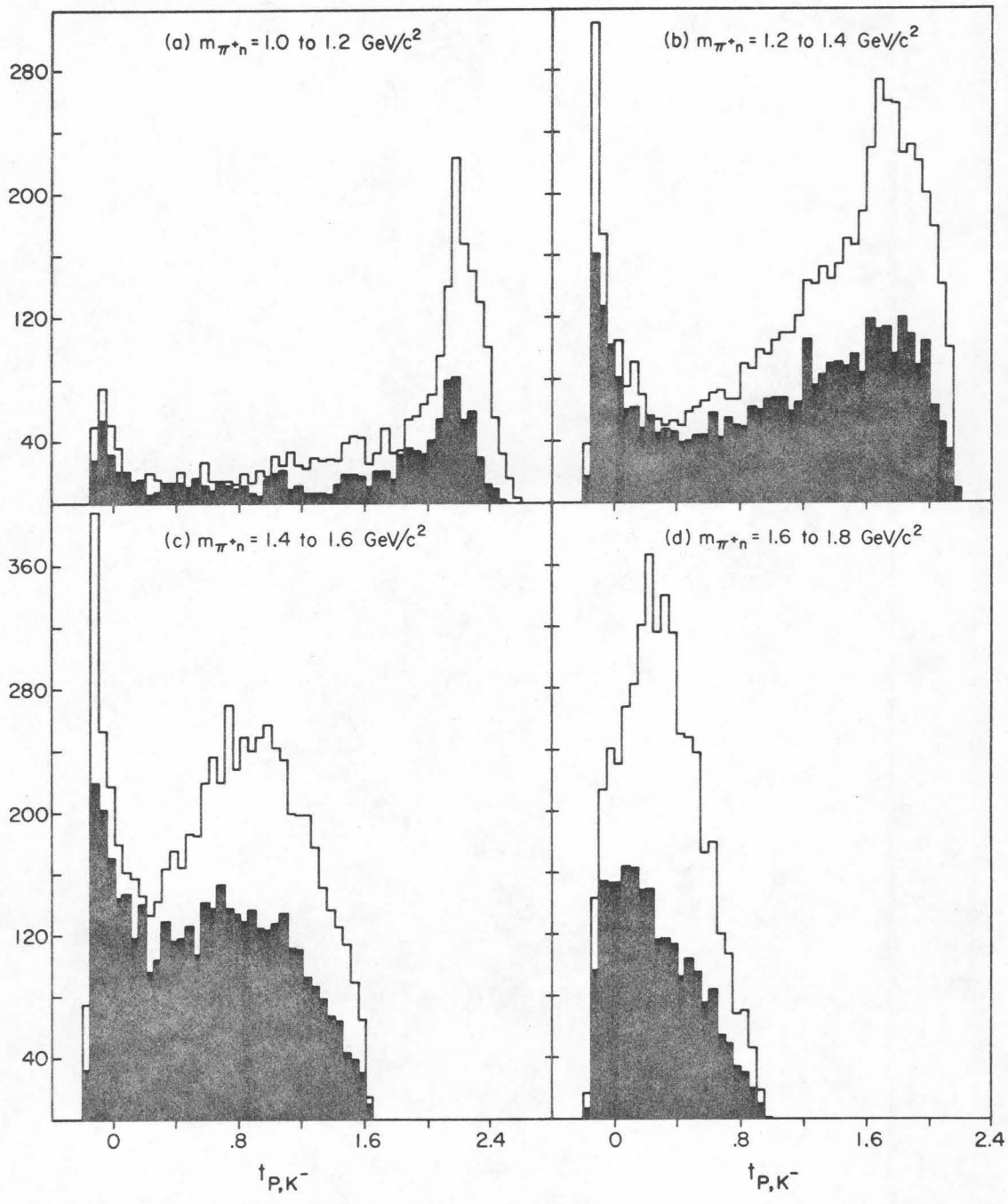

Figure IV-11. The distribution of events by momentum transfer between the incident proton and the outgoing K^-; showing the anomalous backward peak.

Figure IV-12. The chi-square distributions for the backward peak events for the various 1-constraint hypotheses.

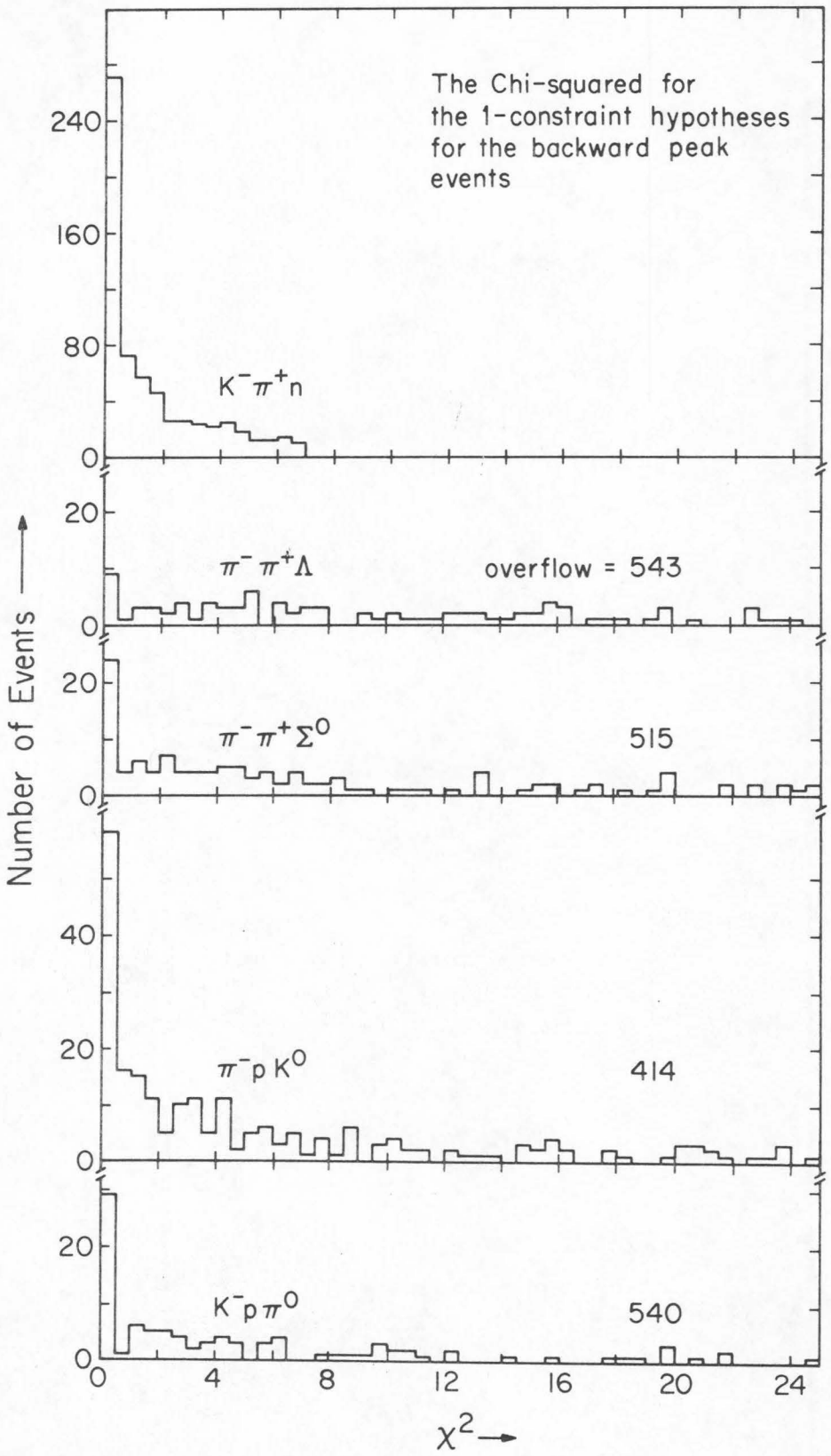
The Chi-squared for the 1-constraint hypotheses for the backward peak events
$K^-\pi^+n$
$\pi^-\pi^+\Lambda$
overflow = 543
$\pi^-\pi^+\Sigma^0$
515
$\pi^-p\,K^0$
414
$K^-p\pi^0$
540
Number of Events
χ^2
0
4
8
12
16
20
24
240
160
80
40

can also be seen in Figure IV-13 where the missing mass squared plots of our peak subsample for the various possible choices of charged tracks is plotted. Again there is no other possible mass hypothesis.

The next alternative we must consider is that the peak consists of events that are correctly identified, but result from a two body resonance's mass peak or decay asymmetry. In Figure IV-14 is displayed the Dalitz plot for the events with $t_{p,K^-} < 0$. There is no peak. In Figure IV-15, the K^-n mass for the events with $t_{p,K^-} < 0$ and $m_{\pi^+n} < 1.35$ are plotted with the corresponding distribution for all events and the phase space curve.

However one possible (rather tenuous) explanation remains which cannot be ruled out with our data. There exists a resonance ($\Sigma(2250)$) seen only in the total cross section and K^-p elastic scattering at this energy. To conclusively determine if this is indeed the explanation for our peak, the energy dependence of the peak must be examined. If the behavior with energy is rapid, then it is indeed a s-channel effect. If not, then the resonance explanation must be incorrect.

We note an interesting feature of this effect. If one examines the π^+n mass distributions shown in Figure IV-16 for fixed low t_{p,K^-}, the $\Delta^+(1236)$ peak is absent. From this we conclude that the π^+ and n are in an $I=\frac{1}{2}$ state.

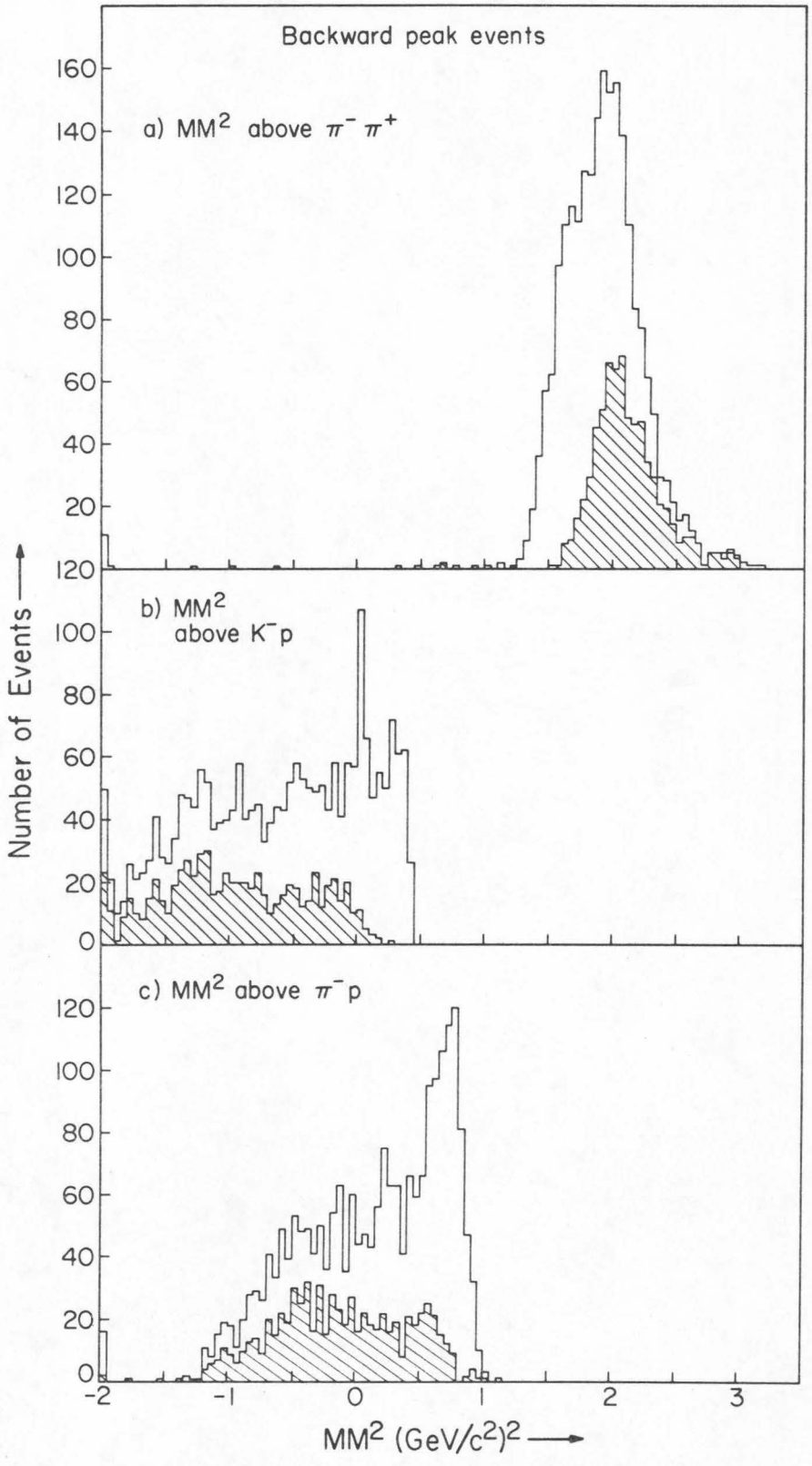

Figure IV-13. Missing mass squared above the various track hypotheses for the backward sample.

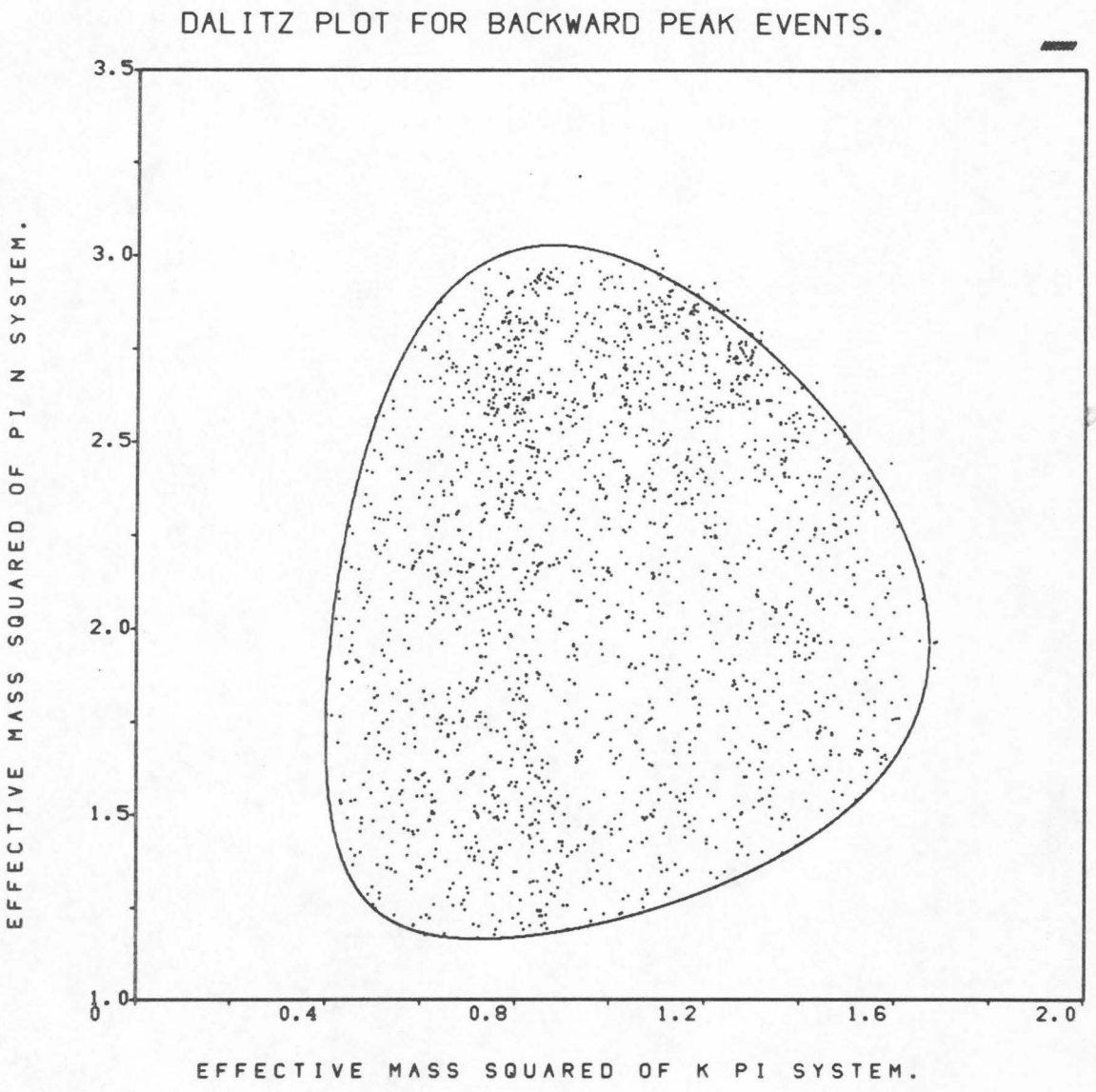

Figure IV-14. Dalitz plot for the anomalous peak sample.

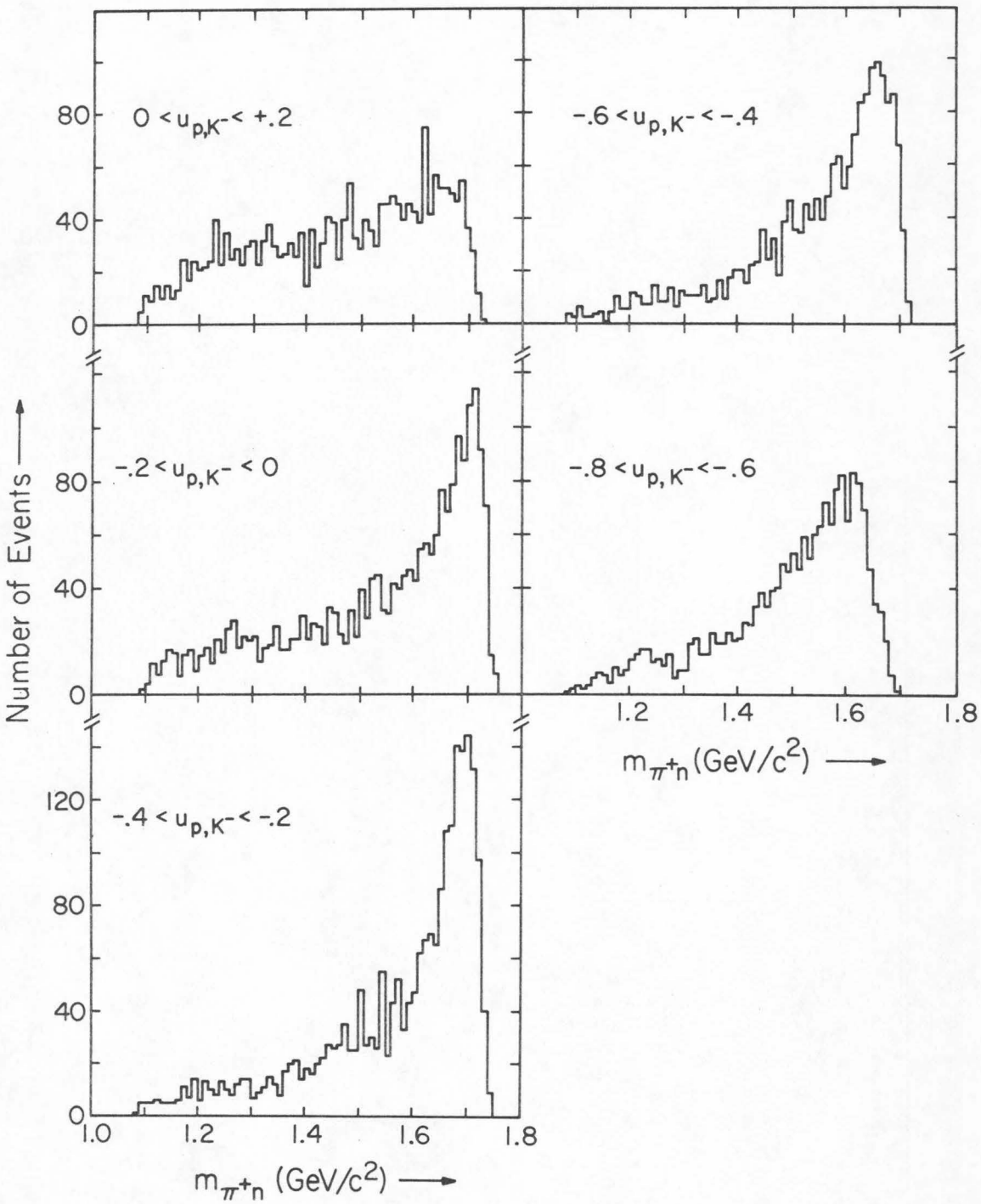

Figure IV-15. Mass distributions for various selections on t_{p,K^-}.

Chapter V. Analysis

A. Comparison of Our Differential Cross Section and Moments With Other Kπ Production Reactions

Because of the great interest in strange baryon production in the past, a relatively large number of K^-p exposures have been run in bubble chambers. In many of these exposures, the two prongs have been recently measured and analyzed. The wide variety of beam momenta represented by these exposures makes it fruitful to study the energy dependence of our reaction. The energy dependence just below our beam energy is of particular interest because in this interval the transition from the dominance of s-channel resonances to t-channel exchange poles occurs. At higher energies the s-dependence can be interpreted in terms of a Regge exchange.

In particular, to study the OPE hypothesis and its application to Kπ scattering, it is necessary for us to show that our data possess, first, the general characteristics of a t-channel exchange dominated process, and second, the specific features which characterize OPE. (The question of t-channel exchange dominance is a serious question in this experiment because of the relatively low beam momentum.)

The characteristics of a t-channel exchange mechanism are: (1) a smooth dependence of $\sigma_{K^*}(E)$ upon energy, and (2) pole-like (peripheral) behavior of $\frac{d\sigma}{dt}$ (see Section IV-A).

Figure V-1 displays the total cross section for production of K*(890) as a function of beam momentum (the straight line is p_{lab}^{-2}). The smooth linear dependence appears to extend down to $p_{lab} \sim 1.8$ GeV/c[i]. At first sight this is somewhat surprising since the many Y* resonances should be expected to affect the cross section at low energy. However, it should not have been totally unexpected as most hadronic reactions are quite smooth around 2 GeV/c. For instance the production cross section for $K^- p \to \bar{K}^0 n$ has been recently measured very accurately and shows imperceptible structure around 2 GeV/c (Bricman 1970).

In Figure V-2, the differential cross sections for several different energies have been plotted together after removing the p_{lab}^{-2} dependence. The different experimental curves agree to the degree expected from the statistical and systematic accuracy of the data. This indicates that the mechanism which dominates at 5 - 10 GeV/c already dominates

---

[i] The 3.9 and 4.6 GeV/c BNL data is statistically highly accurate, however a Breit-Wigner fitting method was used to extract the K* cross section. This may be expected to introduce systematic differences in the results from the results of all other experiments, since everyone else uses a simple mass cut.

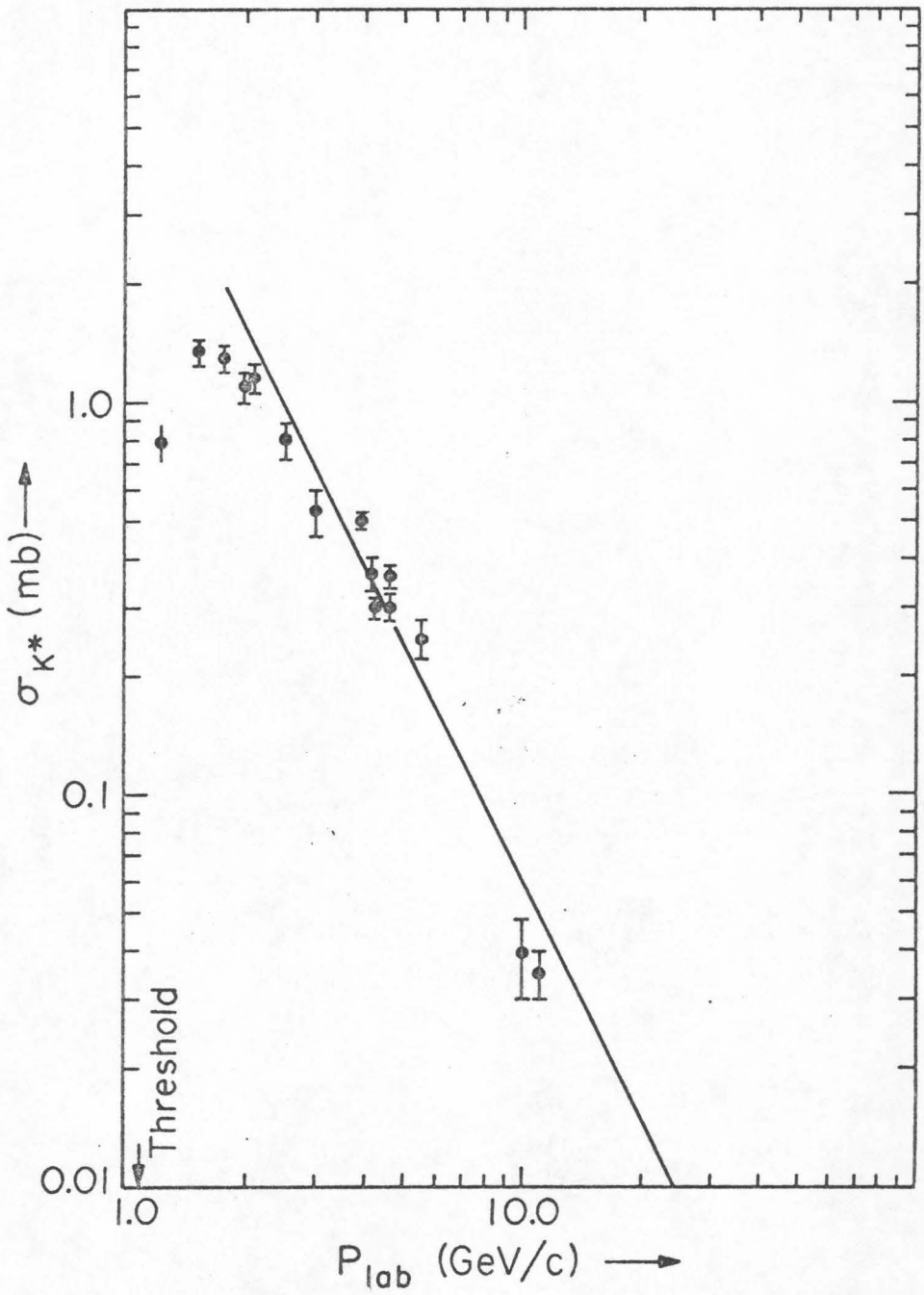

Figure V-1. The total K^* production cross section, which shows that the transition from s-channel to t-channel dominance occurs at about 1.8 GeV/c.

at 2 GeV/c. Therefore we conclude that our data are truly dominated by a t-channel exchange process. We also conclude from Figure V-2, that there is no other significant energy dependence (such as "shrinkage") left in the differential cross section. This implies that there is no need for any other s dependence to fit such data. This behavior explains why various phenomenologists have been able to claim good fits at many energies with relatively simple, albeit theoretically implausible, formulas (Wolf 1969, Gottfried 1964).

The characteristic signs of OPE are: (1) t-channel dominance, (2) a p_{lab}^{-2} dependence of the differential cross section (see Appendix X), (3) a zero in the differential cross section at t=0, and (4) a flat Treiman-Yang angle distribution. We can see that the first two of these conditions are satisfied by our reaction from the data presented above. The third characteristic of vanishing at t=0 cannot be really determined since this point lies outside the physical region. However in Figure V-2, the differential cross section does appear to turn over at small t.

The fourth condition is an easy one to examine and is generally regarded as the most characteristic sign of OPE. We have examined the Treiman-Yang angle distribution and it appears statistically consistent with isotropy. However a physically more precise way to examine this test is to look

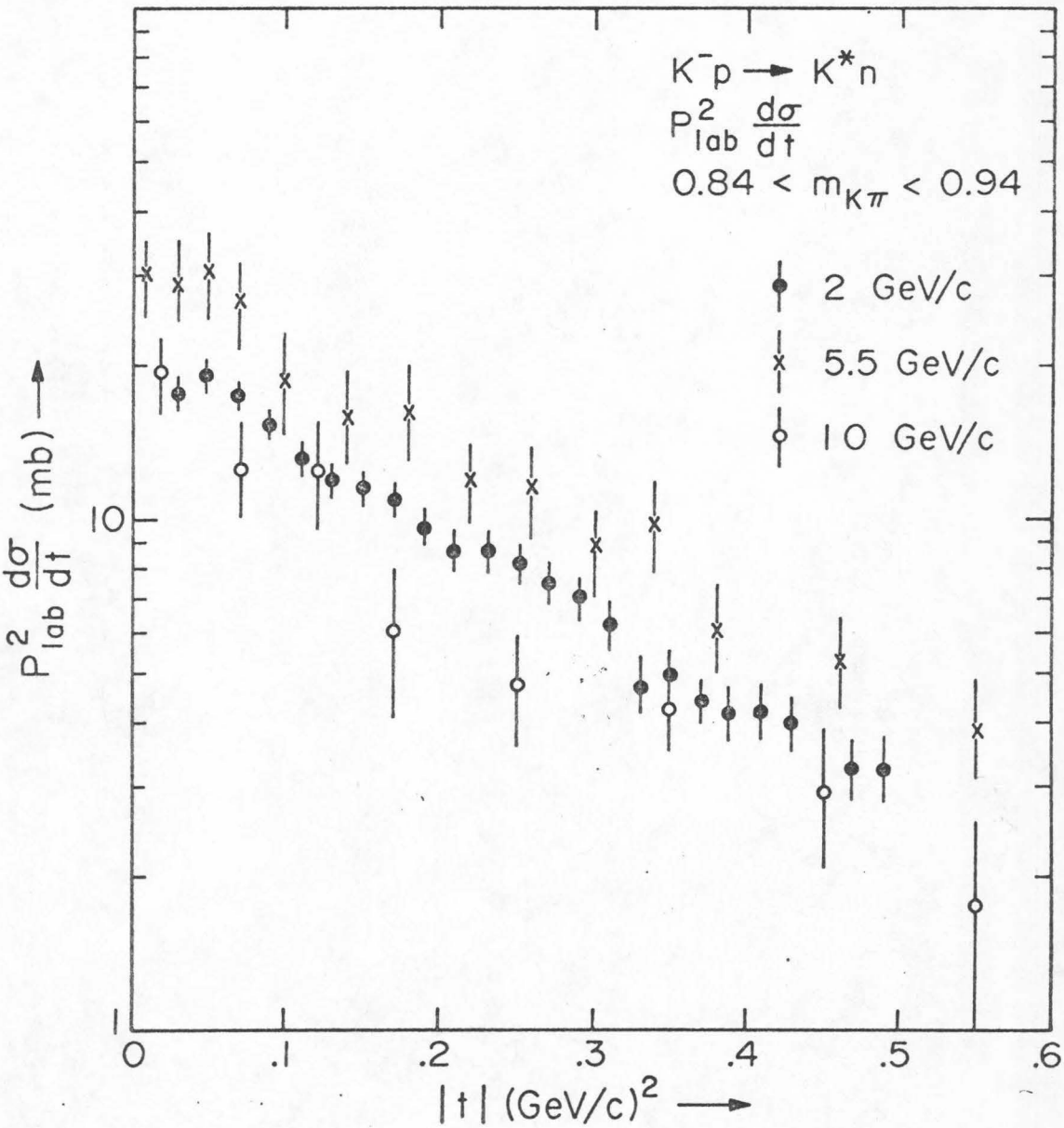

Figure V-2. The differential cross section as a function of beam momentum after removing the P_{lab}^{-2} dependence.

at the $m \neq 0$ moments of the $K\pi$ decay angular distribution. In Figure IV-10, we see that these moments are close to zero but show statistically significant, small deviations from zero. Because these deviations are small and there is no even marginally plausible theory which describes these effects, we will treat them as minor perturbations in our further analysis.

These spherical harmonic moments of the decay distribution are an almost universally computed form of information which can be compared between experiments. In Figure V-3, the $a_{1,0}$ and $a_{2,0}$ decay moments of our experiment are shown. Superimposed are the moments obtained in the 5.5 GeV/c ANL exposure (Fox 1971). There is quite good agreement, indicating that the beam momentum does not affect the angular distribution. Thus the moments like the differential cross section seem to exhibit an exceptionally simple behavior with energy, in agreement with the t-channel exchange model's prediction. The dependence of the moments upon meson-meson mass is a more complex question which will be discussed later.

In the light of the simple energy dependence of $K^-p \rightarrow K^*n$, it is interesting to compare this reaction to the reaction $K^+n \rightarrow K^*p$, which can differ from the first only if the OPE hypothesis breaks down and there is more than one significant exchange mechanism (see Appendix X) or if s-channel effects (such as absorption) are to be significant

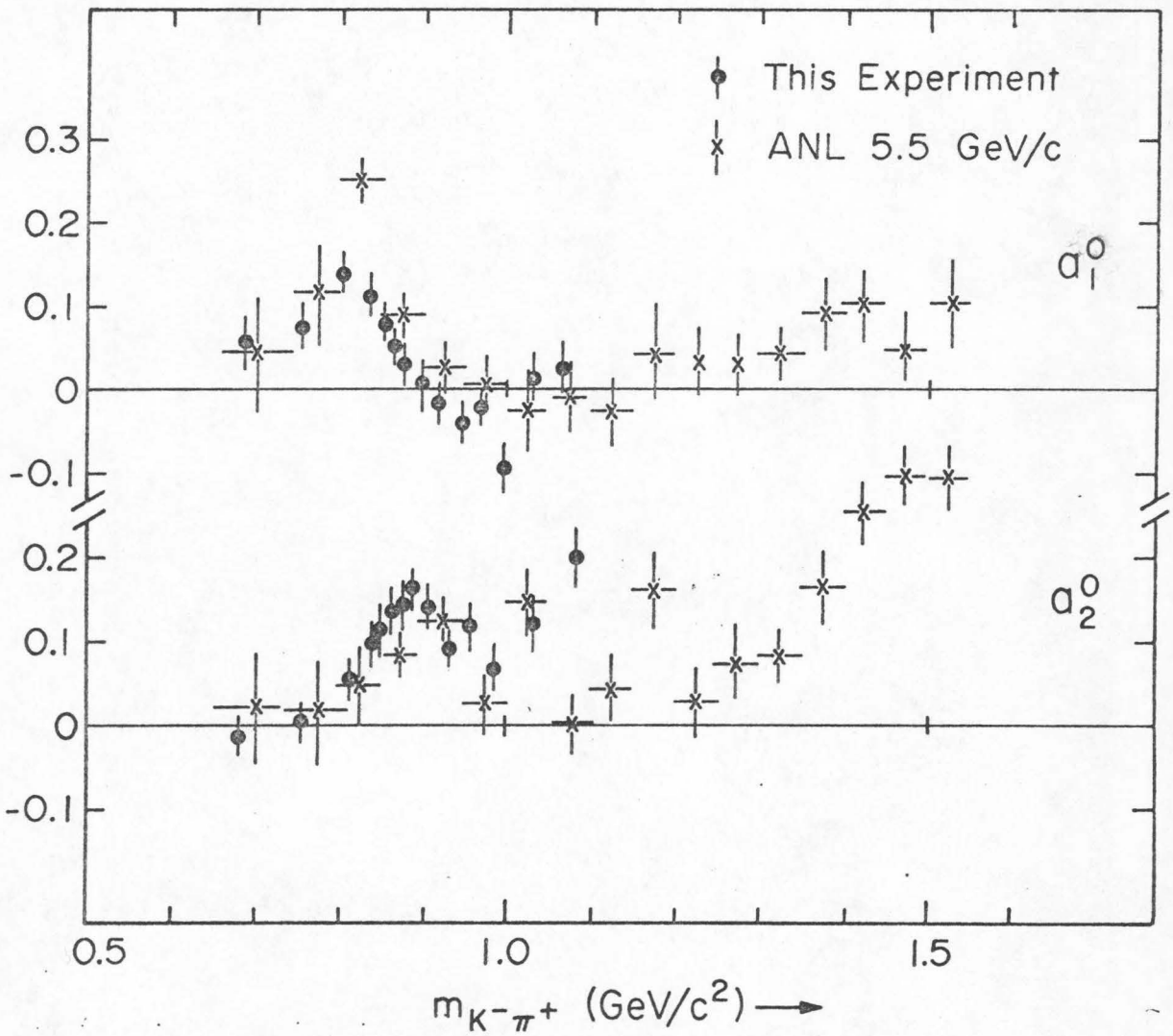

Figure V-3. Comparison of the m = 0 moments of the 5.5 GeV/c ANL K^-p experiment with our data.

at all energies (since we have seen that the shape of the cross section does not change between 2 and 10 GeV/c in K^-p where the absorption is expected to be present). In Figure V-4, the K^+n and K^-p differential cross sections at 2 GeV/c are superimposed. The two sets of data appear to be quite different. (This result will be made more quantitative in the next section.) In Figure V-5, the helicity frame moments for events with $|t| \leq 0.12$ of K^-p and K^+n are superimposed. Here, unlike in the differential cross section, there is good agreement. Note however that for larger t's the two sets of moments begin to disagree. The consequences of this phenomenon will be discussed further in Section V-E.

From these qualitative comparisons, we conclude that $K^-p \rightarrow K^*n$ has a very simple energy dependence and that it is closely, but not simply related to the reaction $K^+n \rightarrow K^*p$. These conclusions will be examined further in the following sections.

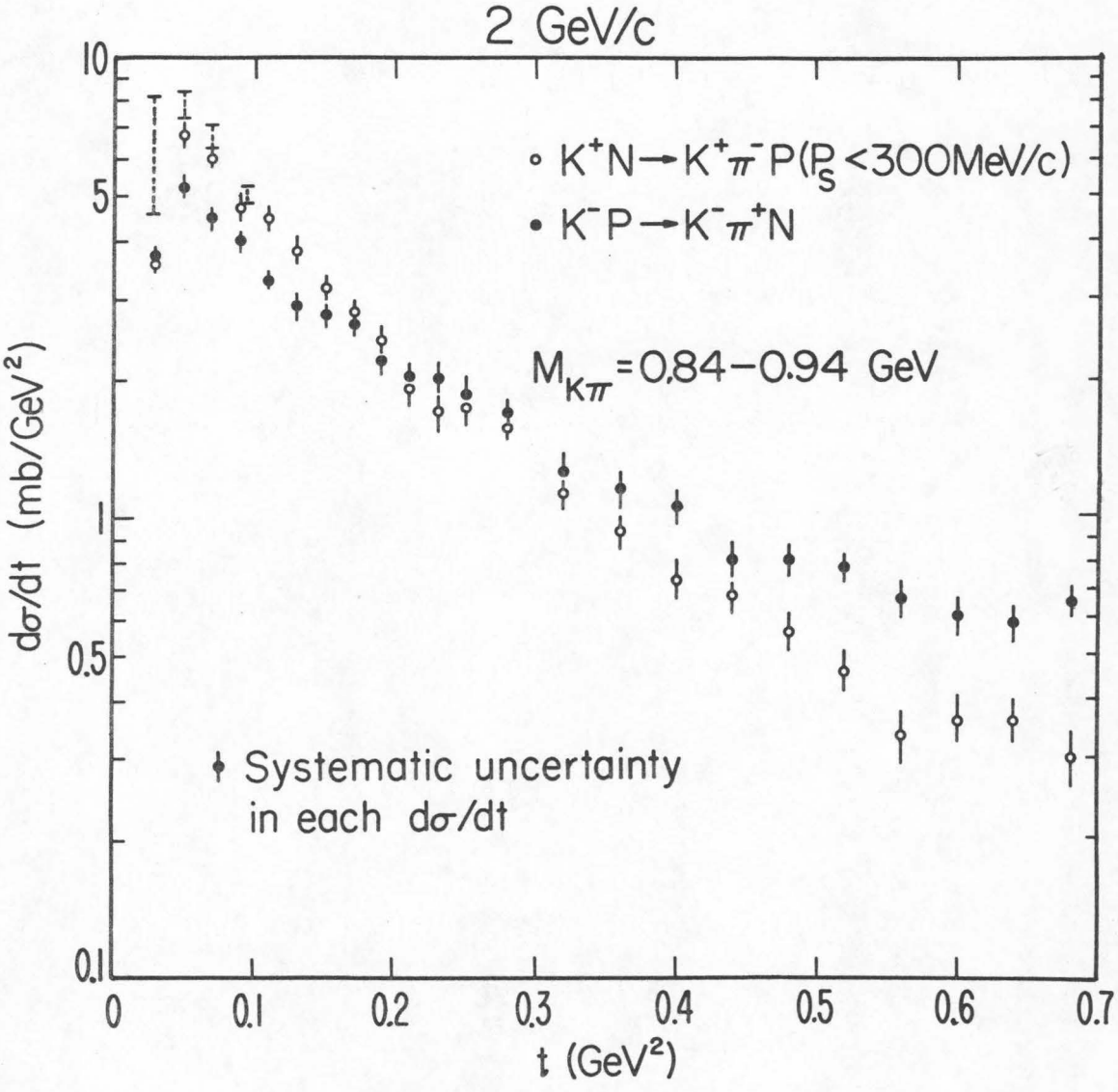

Figure V-4. Comparison of the differential cross section for $K^- p \to K^{*} n$ and $K^+ n \to K^{*} p$ at 2 GeV/c.

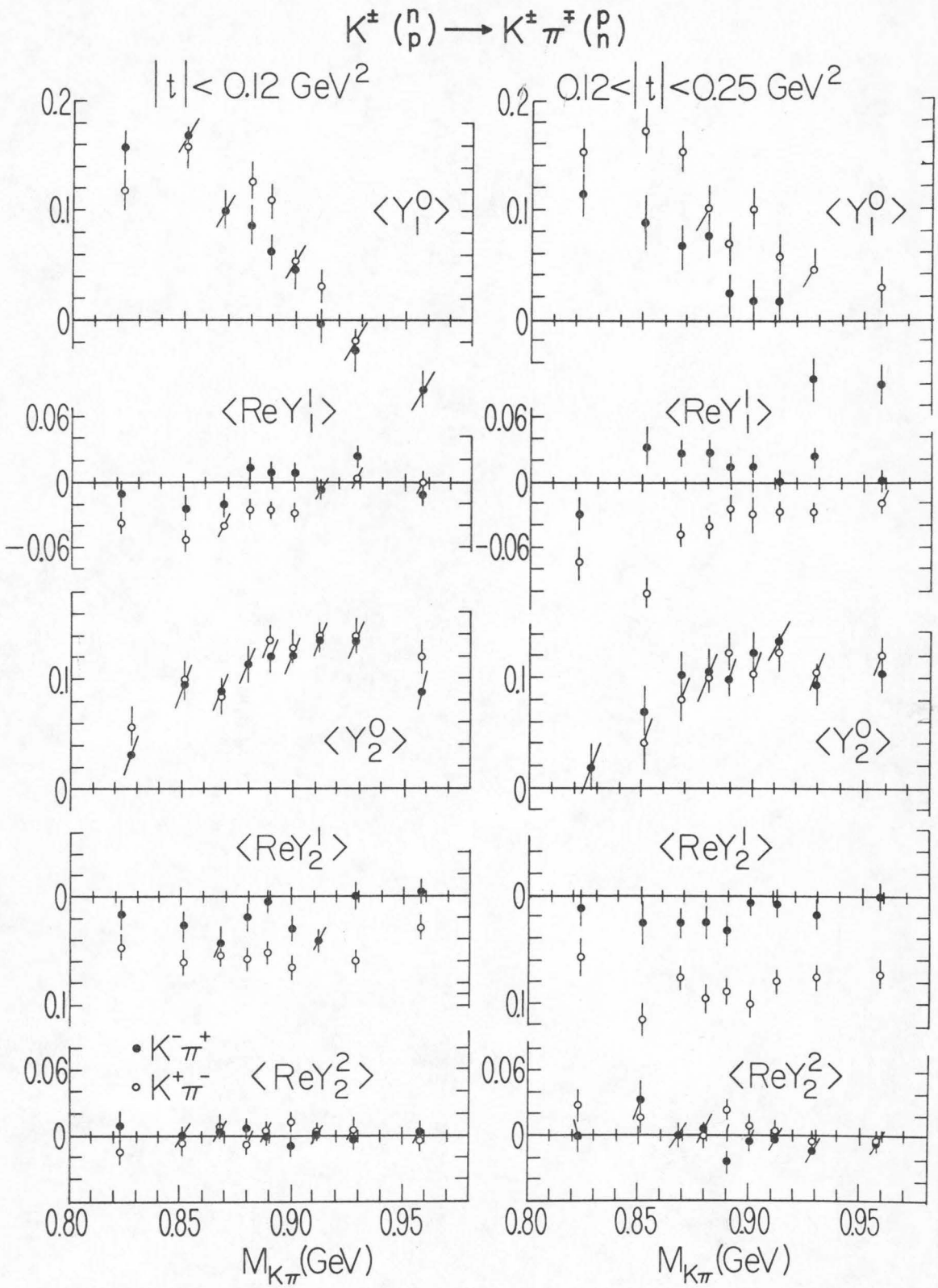

Figure V-5. Comparison of the moments for $K^-p \to K^*n$ and $K^+n \to K^*p$ at 2 GeV/c.

B. Parameterizations of the Differential Cross Section

In order to quantitatively examine our data and to compare them to other measurements, we have resorted to several independent parameterizations. In this section we shall discuss two fits to the differential cross section alone.

To study the general shape and the absolute magnitude of the forward peak, an exponential fit to the differential cross section was employed. The results of our fits are tabulated in Table V-1. Because of the shift in the physical low t limit toward lower values at higher beam momentum, the kinematic region which determines the fitted parameters can change. Therefore all fits were restricted to the interval 0.05 to 0.50 $(GeV/c)^2$. (For the data at the lowest momenta, the endpoints were excluded if they represented abrupt changes from the general shape of the differential cross section at that particular energy.)

From these fits we conclude that $\lim_{t\to 0} \frac{d\sigma}{dt}$ rises from p_{lab} = 1.2 to 1.8 GeV/c and then falls off smoothly from there to above 5.5 GeV/c. The shape parameter shows no significant change between 1.2 and 10 GeV/c. Initially, this result seemed quite surprising since we expected threshold effects to modify the shape of the differential cross section at the lowest energies. However, this was found to be an insignificant effect.

Table V-1. Exponential Parameters $(\frac{d\sigma}{dt} = e^{A+Bt})^{\dagger}$

	P_{lab}	Source	A	B	$A + 2 \ln P_{lab}$
K^-	1.22	LRL*	1.61 ± .16	3.70 ± .68	2.00 ± .16
	1.51	LRL*	2.11 ± .06	4.08 ± .26	2.94 ± .06
	1.76	LRL*	1.70 ± .06	3.69 ± .26	2.83 ± .06
	1.83	LRL*	1.94 ± .07	4.63 ± .32	3.15 ± .07
	2.00	Caltech-UCLA	2.00 ± .03	4.66 ± .15	3.38 ± .03
	2.02	LRL*	1.90 ± .06	4.95 ± .29	3.31 ± .06
	1.95	LRL*(1)	1.99 ± .11	5.29 ± .46	3.33 ± .11
	2.10	LRL*	1.52 ± .11	3.90 ± .45	3.01 ± .11
	2.54	LRL*	1.54 ± .07	4.97 ± .30	3.40 ± .07
	3.0	Saclay	0.66 ± .19	4.28 ± .64	2.86 ± .19
	3.9	BNL‡	1.12 ± .05	4.40 ± .22	3.84 ± .05
	4.2	NA	0.36 ± .05	4.8 ± .4	3.23 ± .05
	4.6	BNL‡	1.18 ± .07	5.24 ± .29	4.23 ± .07
	5.5	ANL	- .05 ± .11	4.08 ± .40	3.36 ± .11
	10.0	ABCLV	-1.76 ± .20	4.22 ± .69	2.84 ± .20
K^+	2.0	UCLA-Caltech‡‡	2.43 ± .06	7.09 ± .27	3.81 ± .06
	3.0	Saclay	1.68 ± .07	7.48 ± .41	3.87 ± .07
	12.0	LRL	-1.50 ± .12	-7.02 ± .60	3.47 ± .12

†Fit to points with $0.05 < |t| < 0.50$, $0.84 < m_{K\pi} < 0.94$; unless otherwise denoted.

*The LRL points are composites, data collected over a range of energy. The 2.02 GeV/c point is divided because of its nearness to our energy.

‡The differential cross section is extracted by fitting a Breit Wigner + background to each t bin.

Table V-1 (cont.)

‡‡ Preliminary results

(1) A 29% pion contamination of the beam probably makes these data unreliable.

For contrast we have also fit the available $K^+n \to K^*p$ data, and these fits show a large difference from K^-p; a difference not permitted in any simple one particle exchange model. This point will be discussed further when we discuss more complex fits.

In summary, these fits lead us to conclude that our reaction has a $p_{lab}^{-2}\, e^{5t}$ dependence between 1.8 and 10 GeV/c and that there is no other significant dependence. But that $K^+n \to K^*p$ exhibits a markedly different behavior.

A widely used method of fitting pion exchange data is in terms of the Benecke-Durr (BD) or Durr-Pilkun (DP) parameters (Durr 1965, Benecke 1968). These formalisms are convenient frameworks to describe data with a small number of parameters, but we do not consider them as serious theoretical models. They have an advantage over the exponential in that they incorporate a second order t dependence which is closer to that of the experimental cross section. Our attitude toward these parameterizations is that while they may be theoretically unsound, they provide a common basis for comparing our data to others since they are widely used.

The BD prescription is:

(1)

$$\frac{d^2\sigma}{dm^2dt} = \frac{1}{4\pi^3 p^{*2} s}\left[mq \sum_{l=0}^{\infty} \frac{U_l(R_l^K q_t)}{U_l(R_l^K q)}\, \sigma_{K\pi}^{\,l}(m)\right] \frac{|t|}{(t-\mu^2)^2}\, \pi^2 g^2 \frac{(1+R_N^2 Q^2)}{(1+R_N^2 Q_t^2)}$$

If we neglect all Kπ partial waves but $\ell=1$, then the sum over ℓ reduces to a form in which, ideally, all parameters can be found. A full description of the various parameters appears in Appendix VI. It suffices for our purposes to know that the free parameters in the fit are the normalization ($\sigma_{K\pi}^{1}$) and the two effective radii $R_K(=R_1^K)$ and R_N which determine the shape of the differential cross section. As is explained in Appendix VI, the two "radial" parameters are actually superfluous. Only one parameter is needed to determine the shape since they both have roughly the same effect upon the theoretical differential cross section. Assuming the value $R_N=2.3$ $(GeV/c)^{-1}$ as known (Trippe 1968), we obtain a fit of $\chi^2 = 596$ for 358 degrees of freedom for a value of $R_K = 0.6$ $(GeV/c)^{-1}$ which corresponds to a Kπ radius of 0.26 fermis, an unphysically low value (a value of about 1 fermi being expected).

While fitting our distributions with the BD formula for one pion exchange, we discovered that we could fit our data with the original Chew-Low formula which is equation (1) with all kinematic form factors eliminated:

$$\frac{d^2\sigma}{dm^2dt} = \frac{1}{4\pi^3 p^{*2} s} \; g^2\pi^2 \; \frac{|t|}{(t-\mu^2)^2} \; mq \; \sigma_{K\pi}(m^2)$$

where q is the on-mass-shell Kπ center of mass 3 momentum and m is the Kπ effective mass. This formula fits our data

with a chi-square of 486 for 360 degrees of freedom. This equation was used to generate the curves in Figure IV-7. Notice that only the m dependence is a part of the fit and the t dependence is fixed. While 486 is a high chi-square for 360 degrees of freedom, we see from Figure IV-6, that it is an extremely good fit to the general slope.

The Chew-Low theory claims that the normalization of the fitted theoretical curves ($\sigma_{K\pi}$) is the $K\pi$ elastic cross section. For the fits in question, we obtain the $K\pi$ elastic cross sections shown in Figure V-6 with peak values of $\sim$50 mb at the K*(890).[ii] This is to be compared with the value of 80 - 90 mb predicted by unitarity. Since the P wave is almost certainly unitary at $m_{K\pi}$ = 890 MeV/c^2, this represents a clear failure of the idea of a pole extrapolation.

One might argue that these discrepancies might be due to our experiment being too low in energy for t-channel processes to dominate. However it is evident from Table V-1 that all other $K^-p \rightarrow K^*n$ experiments will have similiar results. From this we conclude that our results are an intrinsic property of the reaction and not of our beam momentum.

[ii] The curve with $R_K = R_N = 0$ is the curve given by the unadorned pole equation.

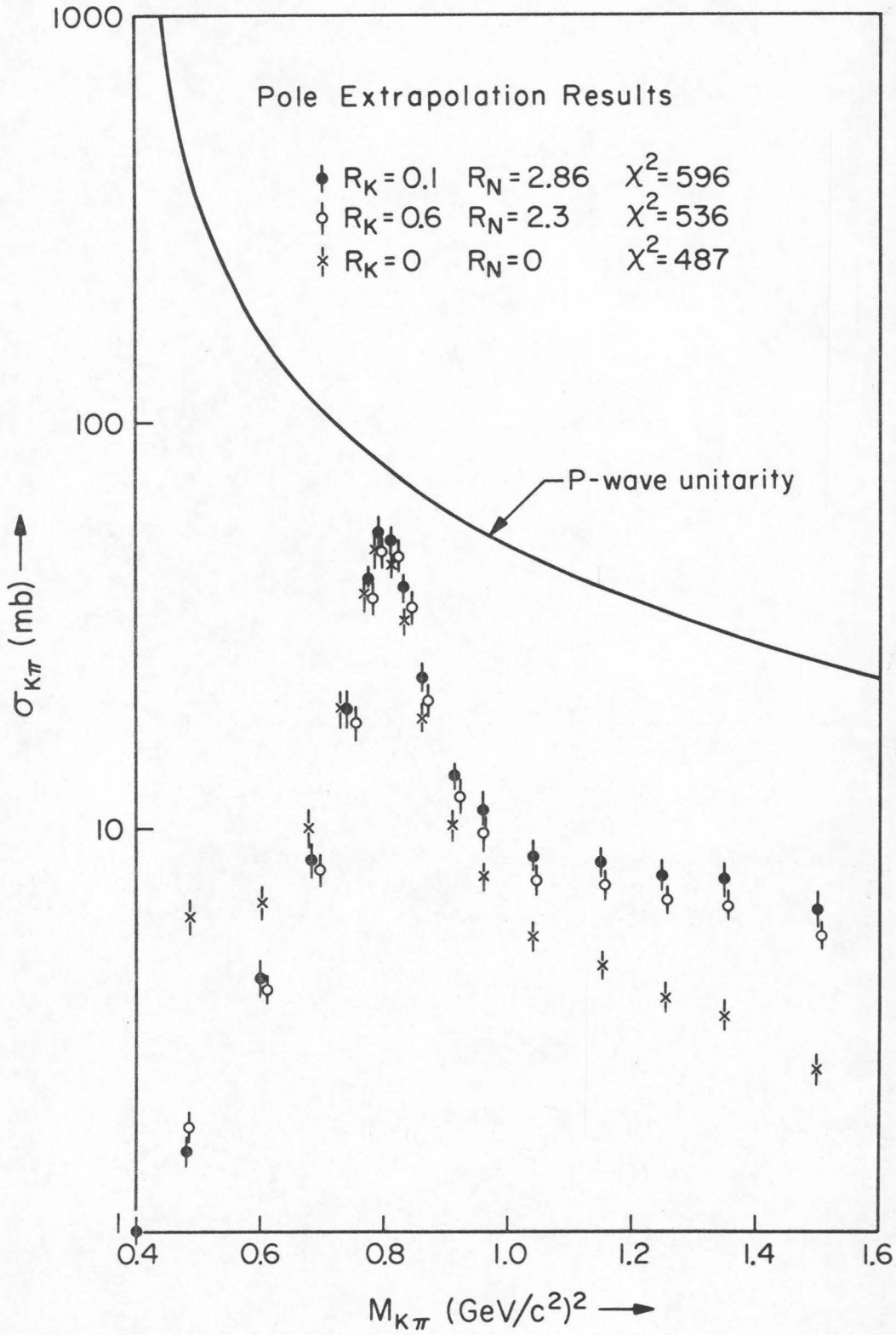

Figure V-6. The pole extrapolation results which show the disagreement between our extrapolated values and the prediction of P-wave anitarity.

We have learned that in a study of the reaction $K^-n \to K^-\pi^-p$, it has been found that the original Chew-Low equation also fits this reaction (Cho 1970). This fit was used to extract the (unknown) $K^-\pi^-$ cross section. As this method yielded the wrong extrapolated $K^-\pi^+ \to K^-\pi^+$ cross sections for our data, we conclude that the $K^-\pi^- \to K^-\pi^-$ cross section cannot be reliably determined this way, as yet, and that the quoted results may be wrong by up to a factor of 2. (This being the discrepancy in our data.) However the agreement of these two experimental cross sections with the t-dependencies of the original Chew-Low equation constitute an important experimental fact which is as yet unexplained. The original Chew-Low hypothesis cannot be considered as explaining this fit since this theory predicts a fit to $K^+n \to K^+\pi^-p$ and $\pi^-p \to \pi^-\pi^+n$ as well -- further in $K^-p \to K^-\pi^+n$ the normalization is fixed theoretically at a value which we showed above disagrees with our data.

C. A Model Independent Amplitude Decomposition Scheme

In order to examine the behavior of the moments in a quantitative manner without excessive formalism, a prescription for decomposing the moments suggested by G. C. Fox was employed. If we assume that the process can be characterized as the production of a quasi-stable $K\pi$ state, then the amplitude for our reaction can be written as $T_{ij}^{lm}(\bar{s},t)$; where i and j represent the initial and final state nucleon helicities, l and m are the $K\pi$ spin and helicity, $\bar{s}$ is the $K\pi$ mass squared, and t is the four-momentum transfered squared. Then the scattering amplitude is of the form:

$$A_{ij}(\theta,\phi,\bar{s},t) = \sum_{l=0}^{\infty} \sum_{m=-l}^{l} T_{ij}^{lm}(\bar{s},t)\ Y_{lm}(\theta,\phi)$$

This implies that the probability distribution can be written as:

$$P(\theta,\phi,\bar{s},t) = \sum_{\substack{lm \\ l'm'}} \sum_{i=-\frac{1}{2}}^{\frac{1}{2}} \sum_{j=-\frac{1}{2}}^{\frac{1}{2}} T_{ij}^{l'm'}(\bar{s},t)^{*}\, T_{ij}^{lm}(\bar{s},t)\, Y^{*}_{l'm'}(\theta,\phi)\, Y_{lm}(\theta,\phi)$$

where we have summed and averaged over the nucleon helicities. Rewriting this in terms of single Y_{lm}'s yields:

$$P = \sum_{\substack{\ell m \\ \ell' m'}} \sum_{k=|\ell-\ell'|}^{(\ell+\ell')} \tfrac{1}{2} \sum_{ij} T_{ij}^{\ell' m'}(\bar{s},t)^{*}\, T_{ij}^{\ell m}(s,t)\,(-\ell)^{m'}$$

$$\left[\frac{(2\ell+1)(2\ell'+1)}{4\pi(2k+1)}\right]^{\frac{1}{2}} \langle \ell,\ell';o,o|k,o\rangle\langle \ell,\ell';m,-m'|k,s\rangle Y_{ks}(\theta,\phi)$$

where $s = m-m'$ and $\langle j_1,j_2;m_1,m_2|j,m\rangle$ is the usual C-G coefficient[iii]. Extracting the expectation values of the various moments yields[iv]:

$$a_{ks} = \sum_{\substack{\ell m \\ \ell' m'}} T_{ij}^{\ell' m'}(\bar{s},t)^{*}\, T_{ij}^{\ell m}(\bar{s},t)\,(-1)^{m'} \langle \ell,\ell';oo|k,o\rangle\langle \ell,\ell';m,-m'|k,s\rangle$$

For our purposes we can neglect all terms with $\ell,\ell'>1$ since only the S and P waves can be significant in our mass range. Neglecting the non-flip and double flip amplitudes, there are only six non-zero amplitudes which are pairwise equal from parity; they are $T_{+-}^{00} = T_{-+}^{00}$, $T_{+-}^{10} = T_{-+}^{10}$, and $T_{+-}^{11} = T_{-+}^{1-1}$. The summation over nucleon helicities therefore consists of the

---

[iii] The sign conventions are adopted from Edmonds 1960.

[iv] This assumption is ture if either (1) only one nucleon spin amplitude is significant, (2) after summing over spins there exists an "average scattering amplitude", or that (3) the virtual meson's wave function does not depend upon nucleon spin.

sum of pairwise equal terms. So the sum can be reduced to:

$$a_{ks} = \sum_{\substack{l m \\ l' m'}} T_{+-}^{l'm'}(\bar{s},t) T_{+-}^{lm}(\bar{s},t) (-1)^{m'} \langle l,l';m,-m'|ks\rangle\langle l,l';o,o|ko\rangle$$

Then letting $T_{+-}^{00} = A, T_{+-}^{10} = B_0 e^{i\delta_0}, T_{+-}^{11} = B_1 e^{i\delta_1}$, yields the following formulas:

$$A^2 + B_0^2 + B_1^2 = 1$$

$$AB_0 \cos\delta_0 = \sqrt{\pi}\, a_{1,0}$$

$$AB_1 \cos\delta_1 = \sqrt{\pi}\, a_{1,1}$$

$$B_0^2 - \tfrac{1}{2}B_1^2 = \sqrt{5\pi}\, a_{2,0}$$

$$B_0 B_1 \cos(\delta_0 - \delta_1) = \sqrt{5\pi/3}\, a_{2,1}$$

Since there are five unknowns and five equations, (the normalization being fixed by the first equation), the solution is exactly determined and there are neither extra constraints nor undefined parameters. Fitting this set of equations to our data (with $t<0.12$) yields the results shown in Figure V-7.

The first feature we note is the insignificance of the P-wave helicity one amplitude (B_1). This wave is small in the vicinity of the $K^*(890)$ and becomes significantly non-zero only at the ends of our sensitive range where the phase space cutoff and possible backgrounds could be expected to distort the results. This behavior implies that there is

Figure V-7. The results of the Fox Amplitude Decomposition.

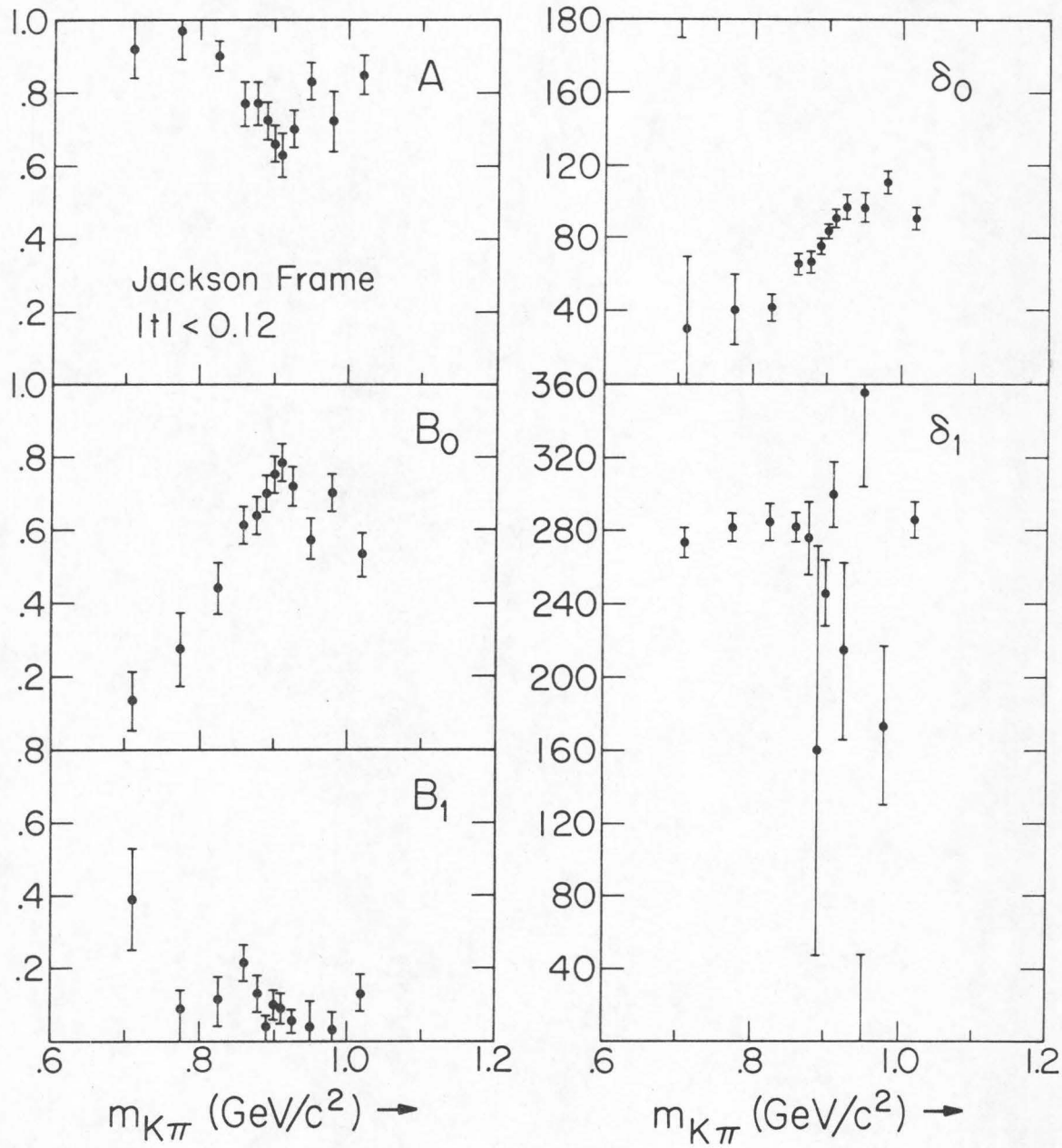
A
Jackson Frame
|t| < 0.12
B_0
B_1
δ_0
δ_1
$m_{K\pi}$ (GeV/c^2) →
$m_{K\pi}$ (GeV/c^2) →

little K^* production by vector exchange. Therefore we do not need to include ρ or A_2 contributions in more detailed phase shift schemes.

A second important feature to notice is that the maximum magnitude of B_0 is 0.78±0.05. If we assume that the S and P waves are unitary and that the I = 3/2 amplitudes are negligible, then $B_0=\left[\frac{3\sin^2\delta_p}{\sin^2\delta_s+3\sin^2\delta_p}\right]^{\frac{1}{2}}$ which implies that $0.87<B_0<1$ at the $K^*(890)$. Since B_0 is never as large as 0.87 and 0.87 is only possible if the S wave is also resonant at 890 MeV/c^2, we conclude that the absolute magnitude of the moments is unreliable, although the qualitative features are intrinsic to the t-channel as we have seen in Section V-2. We attribute this feature to the presence of an extraneous non-resonant S wave background.

The third feature we note is that the P-wave helicity zero remains large above the $K^*(890)$ and does not vanish as it would for a true P-wave Breit-Wigner. In particular if there were a S-wave resonance above the $K^*(890)$ as some authors claim (Trippe 1968), then we would see a large decrease in the P-wave fraction at $\sim$1.0 GeV/c^2. We shall discuss this question again in the next section when we apply a more sophisticated analysis scheme.

Finally, from this fit we conclude that the relative phase between the S and P waves at $m_{K\pi}$=.89 GeV/c^2 is

$70^{\circ} \pm 10^{\circ}$. Since the P-wave phase shift is 90° at the K^{*}, this implies that the S-wave phase shift is $\sim 20 \pm 10^{\circ}$.

D. The Schlein-Malamud Method

The problem discussed in the previous section of an obviously unitary P-wave resonance exhibiting a too small $a_{2,0}$ moment has also been encountered in attempts to extract the $\pi\pi$ elastic cross section in the region of the $\rho(765)$ from the reaction $\pi^- p \to \pi^- \pi^+ n$. A plausible explanation proposed by Schlein and Malamud (Schlein 1967) and applied by them (Malamud 1967) to this reaction ($\pi^- p \to \pi^- \pi^+ n$) has yielded promising results. We have applied their procedure to our data in order to extract the corresponding $K\pi$ elastic cross section and the model's nucleon factors, and thus to extend the test of their model.

The Schlein-Malamud method assumes that the absolute magnitudes of the moments are unreliable but that they have the correct meson-meson mass ($\bar{s}$) dependence. The discrepancy is ascribed to the summation over nucleon spin amplitudes for which the correction factors are assumed to be $\bar{s}$ independent[(v)]. Then in order to set the scale, the P-wave amplitude is assumed to be a unitary Breit-Wigner. (For a more complete explanation see Appendix XI.) In Figure V-8, the results of a fit to our data using the

---

[(v)] Strictly speaking, the nucleon spin amplitudes should be expected to have some slowly varying $m_{K\pi}$ dependence. However, because of the limited statistics, it is not practical to attempt a fit with such a $m_{K\pi}$ dependence.

Figure V-8. The S-wave phase shifts as determined by the Schlein-Malamud method.

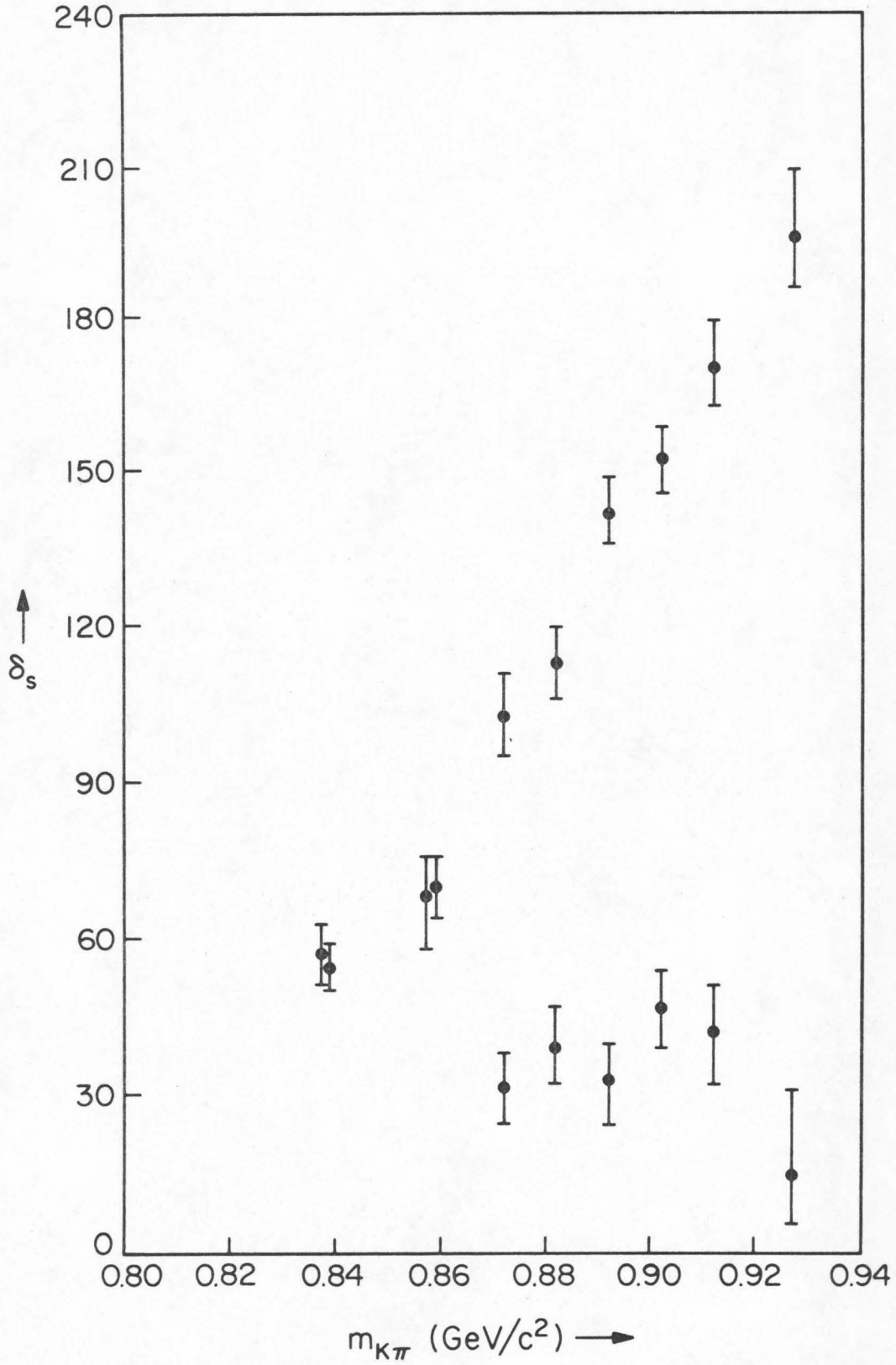
240
210
180
150
120
90
60
30
0
δ_s
0.80
0.82
0.84
0.86
0.88
0.90
0.92
0.94
$m_{K\pi}$ (GeV/c^2) ⟶

Schlein-Malamud method are shown. Both the helicity frame and the Jackson frame moments have been used, since it is not a priori clear which frame is better.

The helicity frame moments were used to make it possible for us to compare the nucleon factors obtained in our fit with those obtained in the $\pi\pi$ case. If the model is correct, then the nucleon parameters should be the same in $\pi^- p \to \pi^- \pi^+ n$ and $K^- p \to K^- \pi^+ n$.

The chi-squares obtained for the various fits are shown in Table V-2 and are reasonably good. However from the behavior of the moments, shown in Figure V-9, we conclude that the goodness of the fits may be artificial. It is possible that the data exhibits a small enough variation and the functional form being fitted is flexible enough to give a good chi-square purely by accident. Such behavior is also exhibited by other experiments. In Figure V-10, a fit to an experiment on $K^+ p \to K^+ \pi^- \Delta^{++}$ at p_{lab}=7.3 GeV/c (Trippe 1968) is displayed while the chi-square for this fit was quite good, the discrepancies above the K^* in the $a_{2,0}$ moment seem highly artificial.

As can be observed (in Table V-2), the comparison of the nucleon factors is not particularly good. These discrepancies are a sensitive measure of the errors in the factorization assumption.

Table V-2. S + M Parameters

t Range	Solu.	$\lvert\bar{s}\rvert^2$	$\Sigma\lvert\bar{P}_i\rvert^2$	$\bar{P}o.\bar{S}$	$P\bar{o}^2-\frac{1}{2}(\lvert\bar{P}_1\rvert^2+\lvert\bar{P}_{-1}\rvert^2)$	$\frac{\lvert\bar{P}_1\rvert^2+\lvert P_{-1}\rvert^2}{\lvert\bar{P}o\rvert^2}$	χ^2
$\lvert t\rvert<0.06$	Up	22±2	106±11	39±4	52±5	.52±.05	44
	Down	29±3	100±10	45±4	54±5	.43±.04	39
$0.06<\lvert t\rvert<0.12$	Up	15±2	149±15	26±3	40±4	.95±.10	33
	Down	16±2	145±15	27±3	40±4	.94±.10	33
$\pi\pi$ helicity $\lvert t\rvert<0.175$		76±5	226±5	110±4	129±4	.40±.03	

Figure V-9. Comparison of the theoretical fit and the experimental moments for the Schlein-Malamud method.

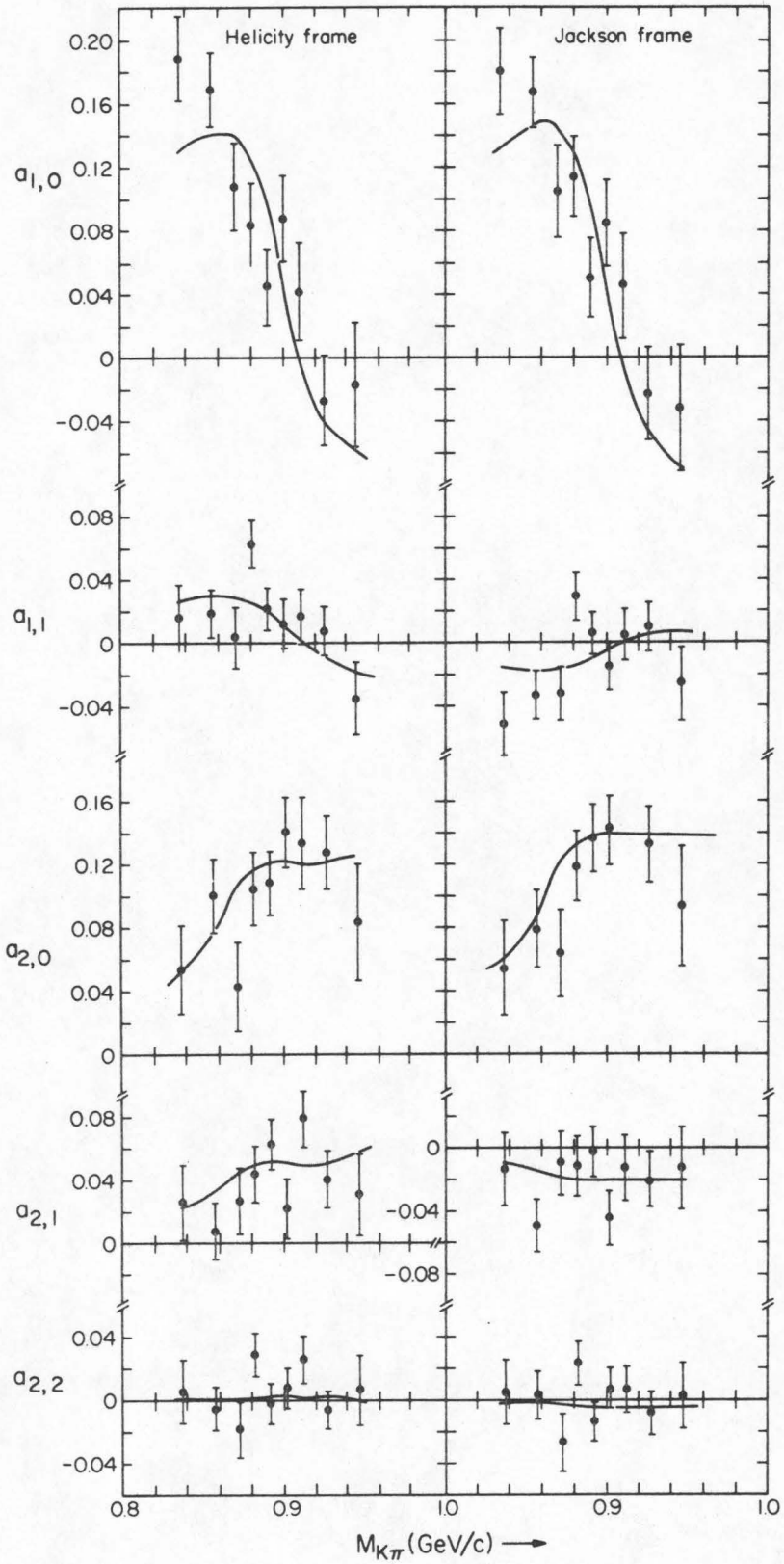
Helicity frame
Jackson frame
$a_{1,0}$
$a_{1,1}$
$a_{2,0}$
$a_{2,1}$
$a_{2,2}$
0.20
0.16
0.12
0.08
0.04
0
-0.04
-0.08
0.8
0.9
1.0
$M_{K\pi}$ (GeV/c) ⟶

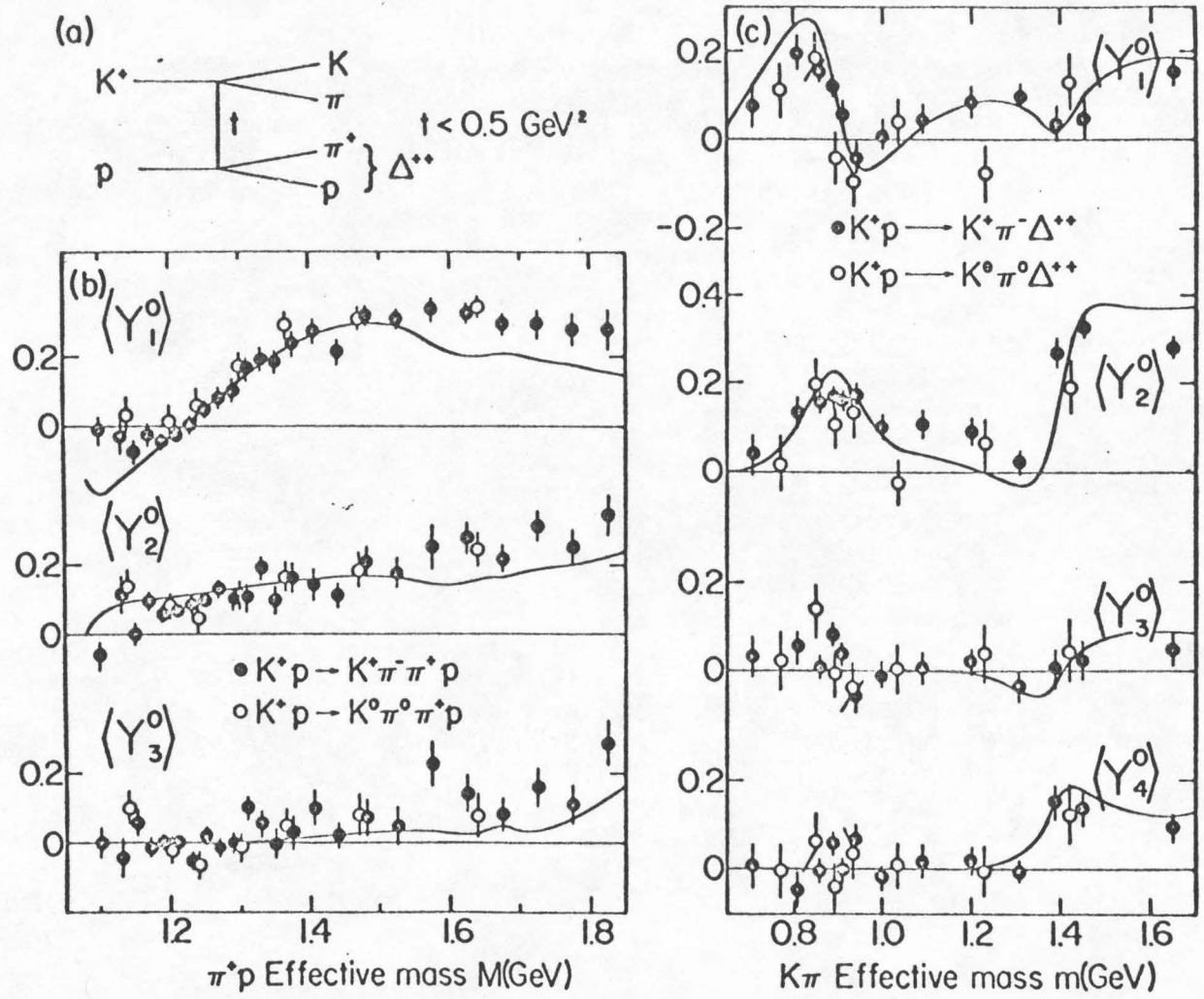

Figure V-10. The results of an experiment on $K^+p \to K^+\pi^-\Delta^{++}$ at $p_{lab} = 7.3$ (reproduced from Trippe 1968).

E. The Froggatt and Morgan Hypothesis

An analysis (Marateck 1969) of $\pi^- p \to \pi^- \pi^+ n$ indicated that the extrapolated production cross section in this reaction does not vanish at t=0 as is required for pure "one pion exchange". C. D. Froggatt and D. Morgan have proposed a new model for this phenomenon (Froggatt 1969) in which the spin and di-pion mass dependences of the background are simply parameterized; thus suggesting a new prescription for performing a non-evasive Chew-Low extrapolation[vi]. This formalism has been applied to the reaction $\pi^- p \to \pi^- \pi^+ n$ (Scharenguivel 1970) and the resulting fits show a significant non-evasive contribution to the overall amplitude in $\pi^- p \to \pi^- \pi^+ n$. Since this mechanism provides a method by which the $K^+ n$ and $K^- p$ cross sections can differ, we have undertaken a study to determine whether the differences between our data and the related reaction $K^+ n \to K^+ \pi^- p$ can be understood in terms of this parameterization. (An explanation of the parameters appears in Appendix XII.)

[vi] The word non-evasive is used to imply that the scattering amplitude is not required to vanish at t=0.

For the purposes of our analysis in this section we have also used data collected by R. Poster on the reaction $K^+D \to K^+\pi^-pp$ at p_{lab}= 2 GeV/c (Poster to be published). Figure V-11 illustrates the differences between this reaction and our reaction. The curves shown in this figure are the result of a simultaneous fit to the K^+ and K^- data, employing added ad hoc t dependence[vii]. This fit shows that this formalism can generate the differences between the two reactions and provide an adequate description of their t dependence.

To extract the S-wave phase shift's mass dependence, the data were divided into finer $m_{K\pi}$ bins and coarser t bins. The results of a fit to our data in these new bins appears in Table V-3 and the corresponding Kπ S-wave phase shifts are plotted in Figure V-12. These phase shifts show the two solutions found by the World Kπ collaboration (Bingham 1971). The first of these is a smooth non-resonant solution rising from $\sim 0^\circ$ at threshold to $\sim 30^\circ$ below the $K^*(890)$ and reaching $\sim 50^\circ$ at $m_{K\pi}$= 1.0 GeV/c^2 with a slight dip at .890. The second solution appears just like the first except that at $m_{K\pi}$ = 0.870 GeV/c^2 the solution rises by 180° in 0.030 GeV/c^2, so that at and above the K^* the solution equals

---

[vii] Averaged over the Kπ mass range 0.84 to 0.94 GeV/c^2, the two phase shift solutions of the world K^π collaboration both have $|A_s|^2$=0.13, $|A_p|^2$=0.24, and Re $A_s^* A_p$ = 0.09.

Table V-3. Parameters Obtained From Froggatt-Morgan Fit.

			K^+N				K^-P			
$m_{K\pi}$	χ^2	$\delta^2_{1/2}$	Γ^0_0	Γ^1_0	Γ^1_1	α	Γ^0_0	Γ^1_0	Γ^1_1	α
.675	26	12	- .07	.73	.37	0.6	.29	.19	.75	- 5.3
.725	42	17	- .04	.06	.08	2.6	- .08	.00	- .07	3.3
.725	45	5	- .89	- .17	.22	-0.2	- .53	- .52	- .49	- 2.3
.725	42	176	- .29	.69	-.39	-3.5	- .59	.38	.24	- 1.8
.775	33	22	.29	.20	.19	-2.6	- .13	.15	.00	0.0
.775	33	18	- .16	- .04	.19	-0.5	- .30	.08	.00	- 0.9
.825	85	32	.00	.01	.15	-0.4	- .10	.19	.05	- 1.0
.825	78	48	.16	.18	.13	-2.1	.25	.06	.04	- 3.3
.862	86	89	.11	.10	.13	-1.6	.16	.30	.08	- 3.4
.862	93	26	- .09	- .03	.17	-1.4	.01	.23	.14	- 1.8
.888	63	24	.01	.05	.14	-0.9	- .09	.19	.12	- 1.3
.888	64	143	.05	.08	.13	-0.9	- .06	.22	.11	- 1.5
.913	35	34	- .14	- .08	.17	-1.7	- .11	.16	.12	- 0.2
.913	35	2	- .20	- .12	.19	-2.1	.45	.13	.14	- 0.2
.938	107	22	-1.33	.33	.00	-0.6	- .90	.27	.00	- 0.7
.938	57	13	.22	- .20	.21	-2.1	- .14	.19	.16	0.4
.975	31	9	- .30	- .08	.24	0.1	-5.43	.12	- .00	- 1.7
.975	24	49	.18	.07	.12	0.7	.13	.19	- .00	0.2
1.025	44	6	12.76	1.21	.00	-4.4	-11.15	.03	.00	- 4.0
1.025	40	56	.13	1.00	.00	-1.3	.15	.20	- .02	- 0.8
1.075	93	73	.46	1.34	.44	-2.0	.50	-1.14	.74	- 7.6
1.075	96	7	-9.41	.80	.00	0.9	.49	-1.05	.76	- 6.2
1.075	95	65	.50	1.46	.51	-2.6	.15	- .63	.39	- 4.6
1.125	34	10	.14	- .01	-.17	7.8	.61	-1.71	.69	- 5.1
1.125	33	6	2.41	- .07	.16	7.0	-1.41	-1.67	.67	- 5.0
1.125	34	102	.87	-1.52	.38	-4.3	.61	-1.77	.51	- 5.6
1.175	10	49	.99	.68	.06	18.8	.42	3.03	.66	- 1.4
1.175	11	6	-1.91	- .54	-.52	1.3	.59	.68	- .09	20.8
1.175	10	95	.88	.80	-.02	26.0	.43	-3.28	-1.32	- 7.8

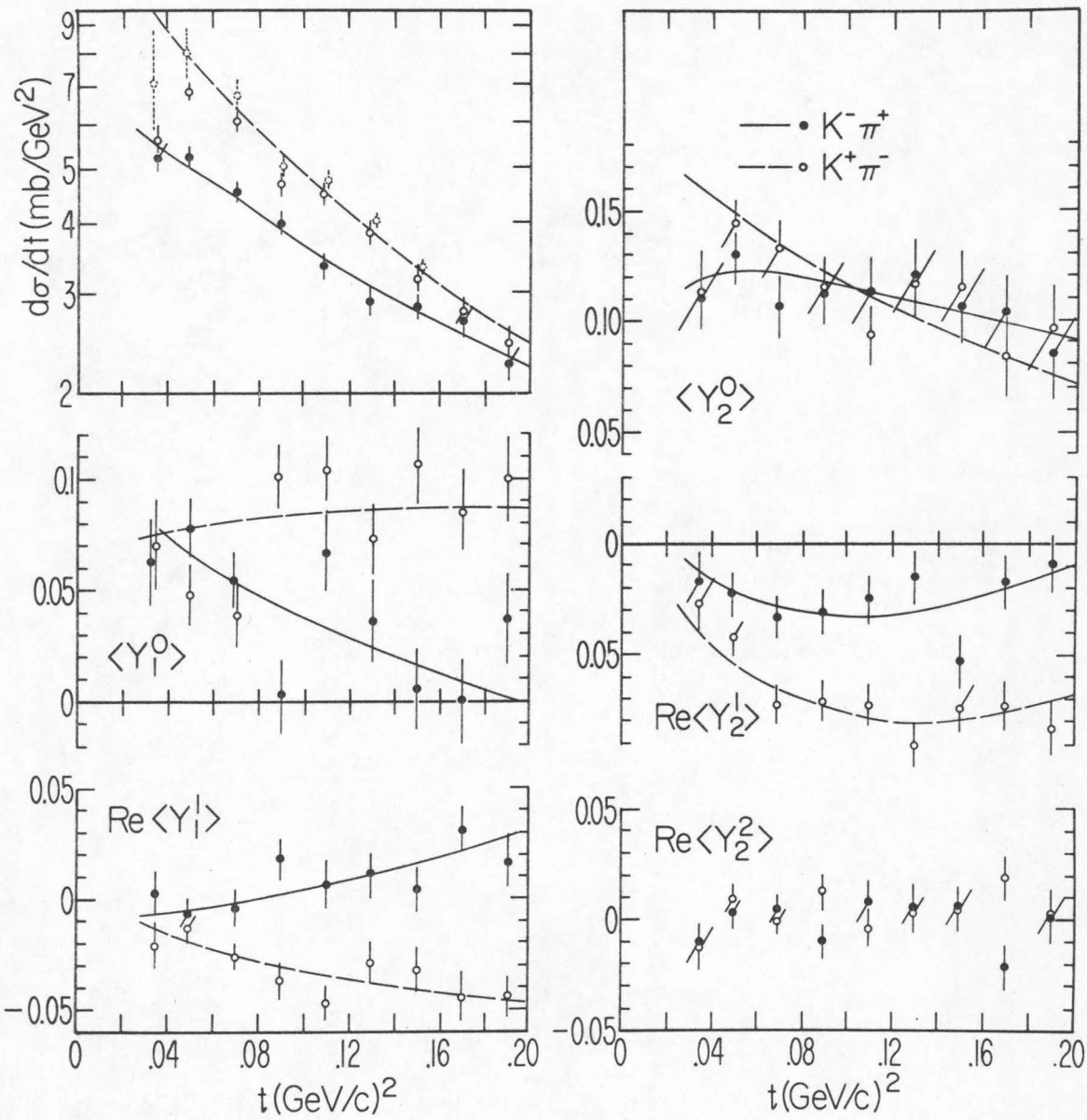

Figure V-11. Comparison of the theoretical fit and the experimental values for a Froggatt and Morgan fit to the data of the Caltech-UCLA collaboration integrated over the K^* region ($m_{K\pi}$ = .84 to .94).

Figure V-12. The S-wave phase shifts as determined by the Froggatt-Morgan method.

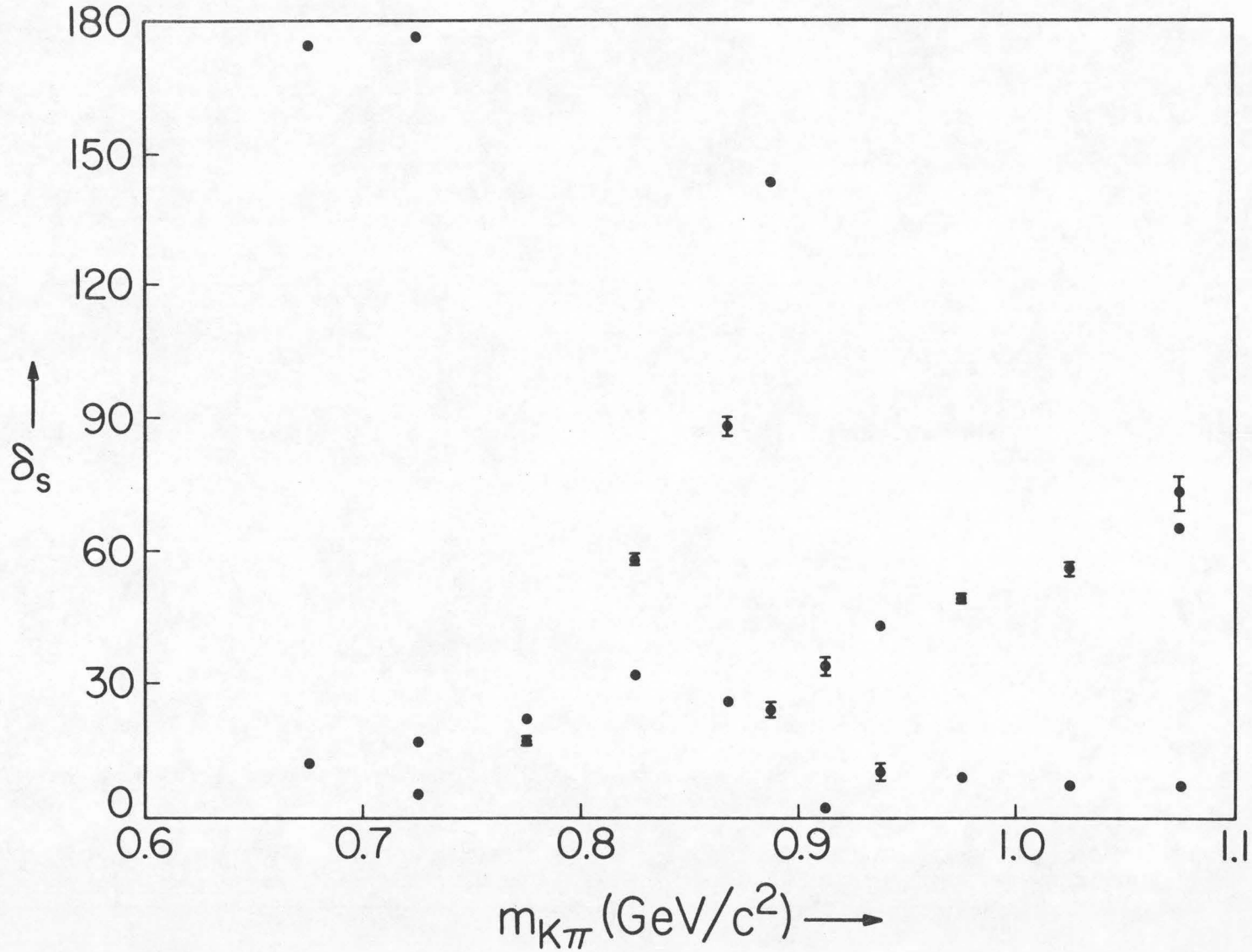
180
150
120
90
60
30
0
δ_s
0.6
0.7
0.8
0.9
1.0
1.1
$m_{K\pi}$ (GeV/c^2) ⟶

solution 1 + 180°. These results are consistent with those obtained by the World DST collaboration and cannot discrimi= nate between the two solutions. However during our analysis several points have been raised which shed light on the issue.

The structure of the theory is such that the S-wave phase shift is mainly determined by the value of $a_{1,0}$. Since the theoretical value of $a_{1,0}$, defined as $f_{1,0} = K(\delta_S,\delta_P)(\cos(\delta_S-\delta_P) \sin \delta_S \sin \delta_P)$, is periodic in δ_S there are, in general, for fixed δ_P and $a_{1,0}$, two values of δ_S which satisfy this equation. However there exists one situation in which δ_S is unique. This condition arises when $f_{1,0}-a_{1,0} \sim (\delta_S - \delta_S^0)^2$ near the solution δ_S^0. This implies that $\frac{df}{d\delta_S}1,0(\delta_S^0) = 0$. As an example, assume that K is constant then $\frac{df}{d\delta_S}1,0 = 0$ implies that $2\ \delta_S-\delta_P = 90^\circ$ would be the required condition. In general this is not exactly true since K is dependent upon δ_S so the position of the unique solution is shifted (for our data such a point occurs at $m_{K\pi}$=0.80 where $\delta_P \sim 15^\circ$ and $\delta_S \sim 25^\circ$). Note however that the condition is a constraint upon both δ_S and δ_P and is not a special point for either. Therefore we expect smooth behavior of δ_S at this point and we should only consider solutions which cross through such points and not solutions which shift branches.

At threshold, the P-wave phase shift rises slower than the S-wave from the expected $p^{2\ell+1}$ behavior. Therefore below the crossing point we choose the upper solution of $10 - 20^{o}$. Therefore the argument above strongly favors the non-resonant solution above the crossing point.

A second feature to realize is how the true solution gives rise to its "ghost". The equation we are solving is $c(\delta_P)a_{1,0} = \cos(\delta_S - \delta_P)\ \sin\delta_S\sin\delta_P$ neglecting the $\sin\delta_P$ and expanding the cosine yields: $c(\delta_P)a_{1,0} = \cos\delta_S\sin\delta_S \cos\delta_P+\sin^2\delta_S\sin\delta_P$. In the region below the K^*, δ_P changes from 0 to 90^{o}, while the $a_{1,0}$ moment decreases slightly. Thus we can see from Figure V-13, how a real non-resonant slowly-changing solution will generate a fast-moving resonant solution and a "fast" solution will have a partner which could be either "fast" or slowly changing. So if either the "slow" or the "fast" solution is correct, then we expect another solution as a "ghost". Therefore we conclude that a fast solution is not unexpected, but we must consider independently the question of whether such a sharp S-wave resonance is to be expected. The answer is clearly no.

Examining the effect such an S wave resonance would have on the total cross section, shown in Figure V-14, makes it even less plausible. However, we have been informed that one can manipulate the parameters to give agreement to within the statistical accuracy of our experiment.

Figure V-13. A schematic view of how the two solutions arise and why one of the solutions changes rapidly.

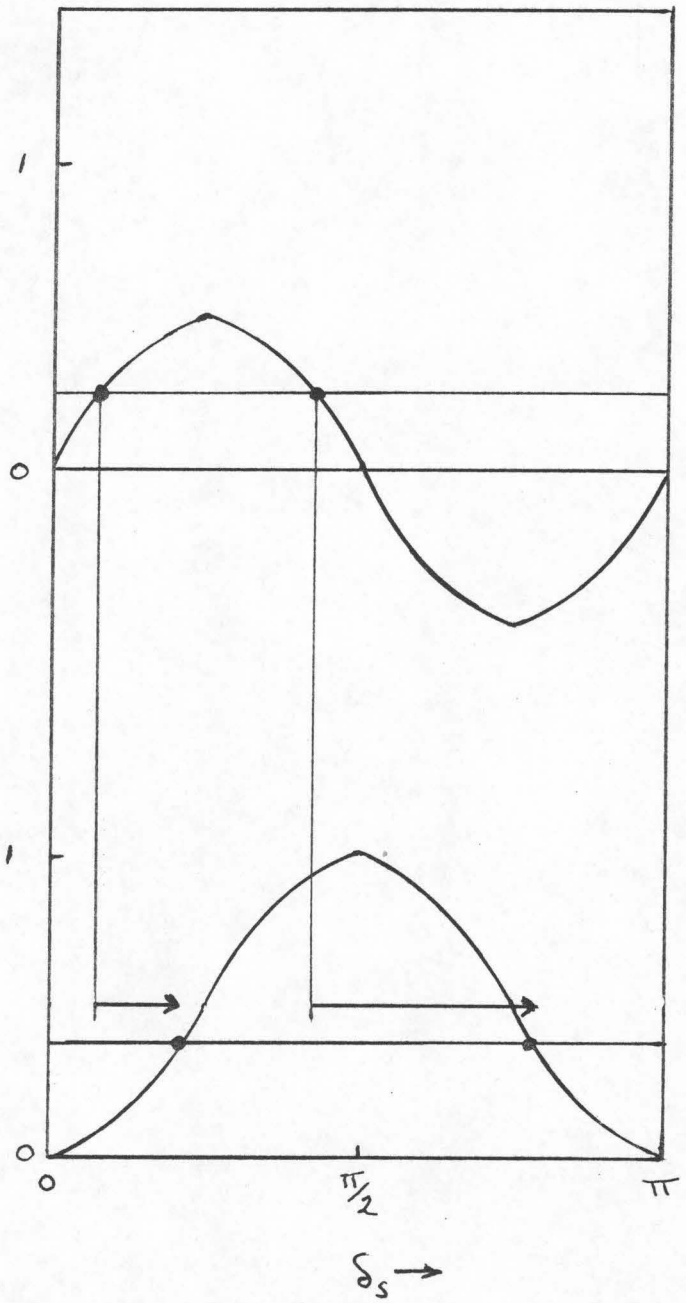

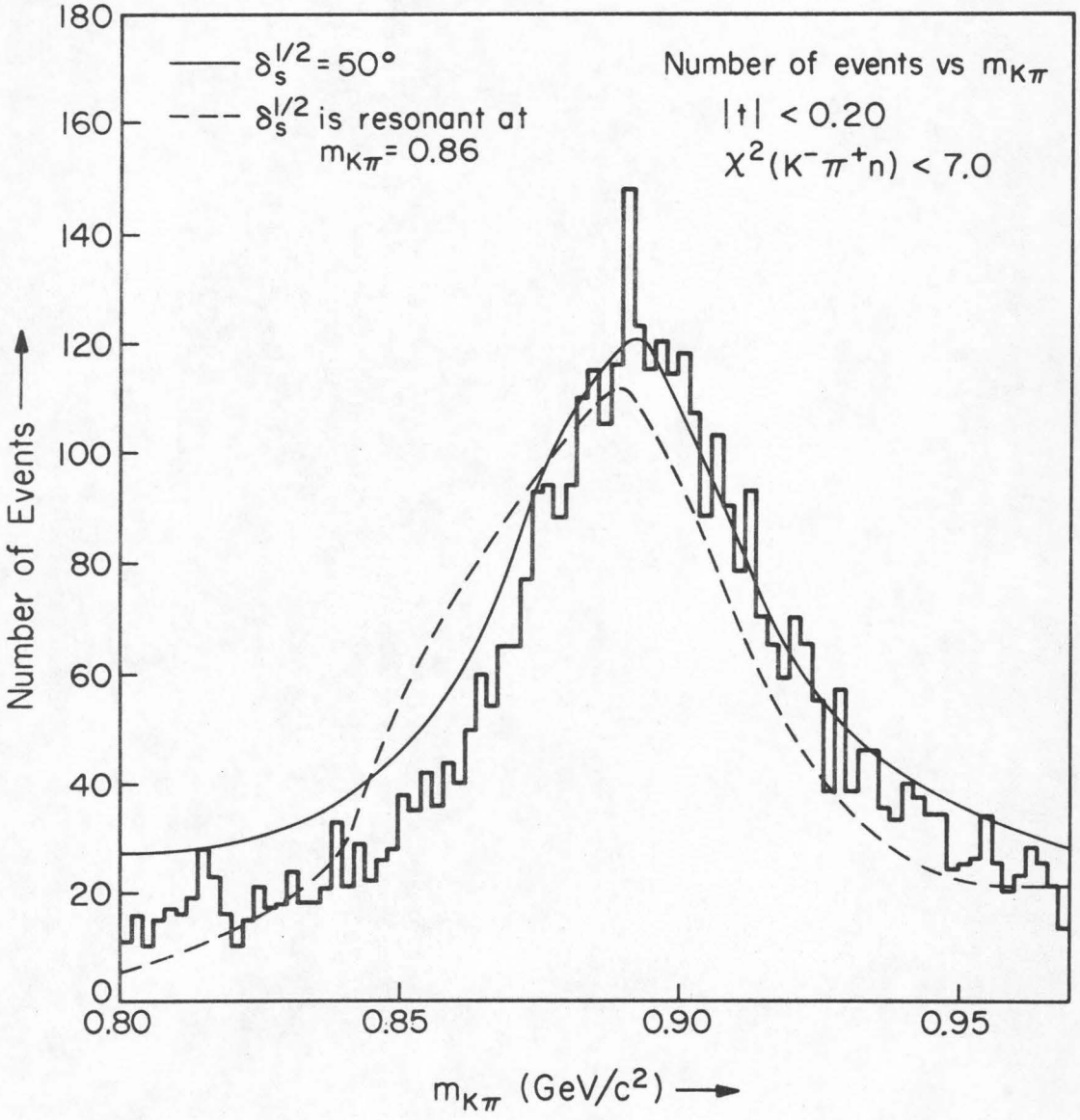

Figure V-14. The effect of an S-wave resonance on the cross section.

In conclusion, these points cast serious doubt upon the existence of a $J^P = 0^+$ S-wave resonance at $m_{K\pi} = 0.86$ GeV/c^2.

F. OPE, Moments, and the Kπ S Wave Phase Shift: An Evaluation

From these rather speculative fits to the differential cross section and the moments, what can we extract that we should believe and what should we regard as model-dependent, artificial constructs? We will attempt in this section to summarize what we have learned and estimate the degree of confidence which we can assign to these conclusions.

We have found regularities in the behavior of the moments which are independent of beam momentum, similiar in different but related reactions (for small $t < 0.12$), and agree qualitatively with theoretical expectations. Yet the deviations exhibited by the data from the predictions of the simplest models (such as the quantitative discrepancy of $a_{2,0}$ from the value expected from unitarity at the $K^*(890)$) argues that such models are not completely adequate descriptions of the actual situation. Thus the interpretation of the data is not nearly as obvious as many people have claimed. So we conclude that such analyses have great promise but that one must, at present, view any results from such studies with a degree of skepticism.

If we assume that the theory is approximately correct and that the methods are reasonable, then we can examine the data and ask whether the real Kπ cross section exhibits such features.

The $a_{2,0}$ moment does rise from zero at threshold to a maximum at the K^*, as would be expected of real $K\pi$ scattering. However it does not rise as far as the unitarity prediction. Therefore the quantitative values are suspect and almost certainly wrong. Such an effect could be caused by extraneous background, an incompletely polarized state, or a relative enhancement of the S wave by "kinematic factors", etc. Until the source of this discrepancy is correctly identified, truly valid quantitative fits are impossible.

The $a_{1,0}$ moment shows a sign change at $m_{K\pi}=0.92 GeV/c^2$ which is probably a feature of the real $K\pi$ interaction. However, the absolute magnitude of the moment is suspect since we already know that the absolute magnitude of the $a_{2,0}$ moment is incorrect. This zero in $a_{1,0}$ implies that the relative phase at $m_{K\pi}=0.92$ GeV/c^2 is 90^o. Since the P wave is 135^o (assuming a unitary Breit-Wigner) at this point, the S wave phase shift is 45 ± 20^o at this point. The great uncertainty in this value is due to the rapid change in the P wave phase shift in this region.

The $m\neq 0$ moments are small, but significantly non-zero - indicative of effects neglected in the simplest theoretical formulations. They constitute incompletely understood limitations to the present lines of analysis. The S-M and F-M methods are clearly not completely satisfactory treatments of such effects. However it is not clear in which

direction further improvements should be made on such models.

Finally, based upon the fits we have found, we conclude that the S wave $K\pi$ resonance at $m_{K\pi} = 0.86$ GeV/c^2 is almost certainly an artifact of the fit employed by the world $K\pi$ collaboration. We expect a large dip in $a_{2,0}$ at $m_{K\pi}=0.86$ if such a resonance exists. A slight dip does exist, but not nearly as prominent as would be expected. The character of $a_{1,0}$ should change abruptly. Above the K^*, the $a_{1,0}$ moment should increase as the P wave approaches 180°. Instead we see a minimum[viii]. The real behavior of the S wave is, with many theoretical reservations, a smooth rise from small values at threshold to $20 - 40^\circ$ at the K^* and beyond.

[viii] Also if there is such a 0^+ resonance, where are its SU(3) partners?

Chapter VI. Discussion

From our experiment, we conclude that the reaction $K^- p \to K^{*o} n$ is far from being understood. Although many people have published fairly good fits to the differential cross section and the moments of the decay angular distribution, these fits have contributed little, if anything, to the theory of the strong interaction. It is clearly necessary to either measure the cross section much more precisely so as to distinguish between theories or to perform a universal fit -- to fit all measureable reactions simultaneously. Any other course of action can clearly never yield satisfactory results because of the obvious uniqueness problems.

The difference in the behavior of the differential cross section can be explained by absorption effects, by significant amplitudes for the exchange of other particles (e.g. ρ, A_2, B), or by significant contributions from multi-particle exchange (i.e. Regge cuts). Explanations (a la Jackson) involving absorption effects alone seem to be quite dubious, since the primary effect of absorption is expected to be the alteration of only the low energy

behavior of K^-p reactions[(i)]; instead, $K^-p \to K^{*o}n$ seems to be very simply behaved between 2 and 10 GeV/c (and presumably thereafter). This is shown in Section IV-B. Also it is to be noted that naive absorption models (i.e. before experiment) predict that the differential cross section for the absorbed reaction (K^-p) will have a steeper slope than the differential cross section for the unabsorbed reaction (K^+n), which is the opposite of the experimental observations. More sophisticated absorption models suffer from the flaw that some cross sections before absorption either rise with t or become constant. This implies that the absorption is controlling the shape at large t in all reactions; a physically unattractive situation.

Explanations invoking different exchanges or of multi-particle exchange are all unsatisfactory in practice since they all contain far too many unknown parameters to give unique fits or reasonable predictions.

The large difference between $\lim_{t\to 0} \frac{d\sigma}{dt}$ for $K^+n \to K^*p$ and $K^-p \to K^*n$ leads us to question the validity of all pole extrapolations, including those of $\pi^-p \to \pi^-\pi^+n$ and $pp \to pp\pi^+\pi^-$ since there is no a priori reason within the model to suspect these reactions to yield better results

---

(i) This is a result of the suppression of the lower partial waves due to competition from other channels.

than the two kaon reactions and if only one kaon reaction had been measured, then the present models would have been flexible enough to accomodate even these results. (Although the K^- pole extrapolation still would not have worked without other terms.) Thus we can only view the $\pi\pi$ results as an interesting coincidence or as a doubtful check of the method (that in this case the cross section does reach the unitarity limit at the ρ) rather than as a confirmation of a rather speculative theory. A similiar discrepancy has been found in the reactions $K^+p \to K^{*o}\Delta^{++}$ and $K^-n \to K^{*o}\Delta^+$ (Henri 1971).

On the other hand, the quantitative similiarity of the moments (for $t \tilde{\sim} 0.06$) for these two reactions both in absolute magnitude and in $m_{K\pi}$ dependence imply that this form of information is apparently independent of the S-channel state; thus implying that the fundamental assertion of the Chew-Low hypothesis is indeed correct. This argues strongly for a relatively simple picture of the interaction amplitude, since it implies that some form of factorization of the S matrix is indeed possible.

The validity of extracting the properties of meson-meson scattering is therefore left in an ambiguous state. It is clear that the simplistic statements made by many of the present workers in the field is over optimistic. Yet there do exist some indications that the decay moments of our reaction do reflect the behavior of the $K\pi$ interaction.

For instance, it is clear that the P wave is dominated by a resonance -- the $K^{*}(890)$.

Appendix I. Comments on the Scanning-Measuring Technique Used in This Experiment

The SMP operators simultaneously scanned for and measured the events of interest in the film. There were two different phases in the measurement.

In the first part of the measurement both the two prong V events and the two prongs were measured. During this phase, the standard UCLA scan-measuring control program was used. This program produces a card for every frame examined. Based upon the number of these scan cards, 22 K, the calculated fraction of the experiment that the two prong V events represent was (11 ± 2)%. During the second phase of the experiment, the following were no longer measured: the two-prong-V events, the events with a kink within 10 cm of the vertex[i], and events the positive track could be identified as a proton. The SMP control program was also

---

[i] The events with kinks tend to be Σ^- or Ξ^- events which are produced copiously at our energy. The true K^-'s do not decay significantly in the 10 centimeters. (see Figure A-1). An added advantage is that even the real events with a <10 cm track will have a large momentum measurement error and thus be ambiguous.

changed. The new program required the scanners to positively utilize the semi-automatic frame advance since the latter had led a large rate of frame misidentification.

In order to estimate the scanning efficiency, the SMP operators all scanned and measured the same two rolls. The results of the study of this sample are presented in Table A-1. While these numbers are an indication of the scanning efficiency, they are not completely unbiased. The events missed by the better scanners are ones in which the proton criteria were slightly misinterpreted. Such slight shifts cannot influence our results. The poor scanners tended to miss events almost at random, which again is unbiased.

TABLE A-1. Scanning Efficiency

Operator #	% Missed	% Incorrectly Rejected
40	3.7	1.6
42	16.1*	7.7*
48	10.9*	0.
49	5.8	5.6
71	8.4	3.1

*Adjusted for incomplete measurements

Figure A-1. Apparent lifetime in centimeters in hydrogen as a function of initial momentum*.

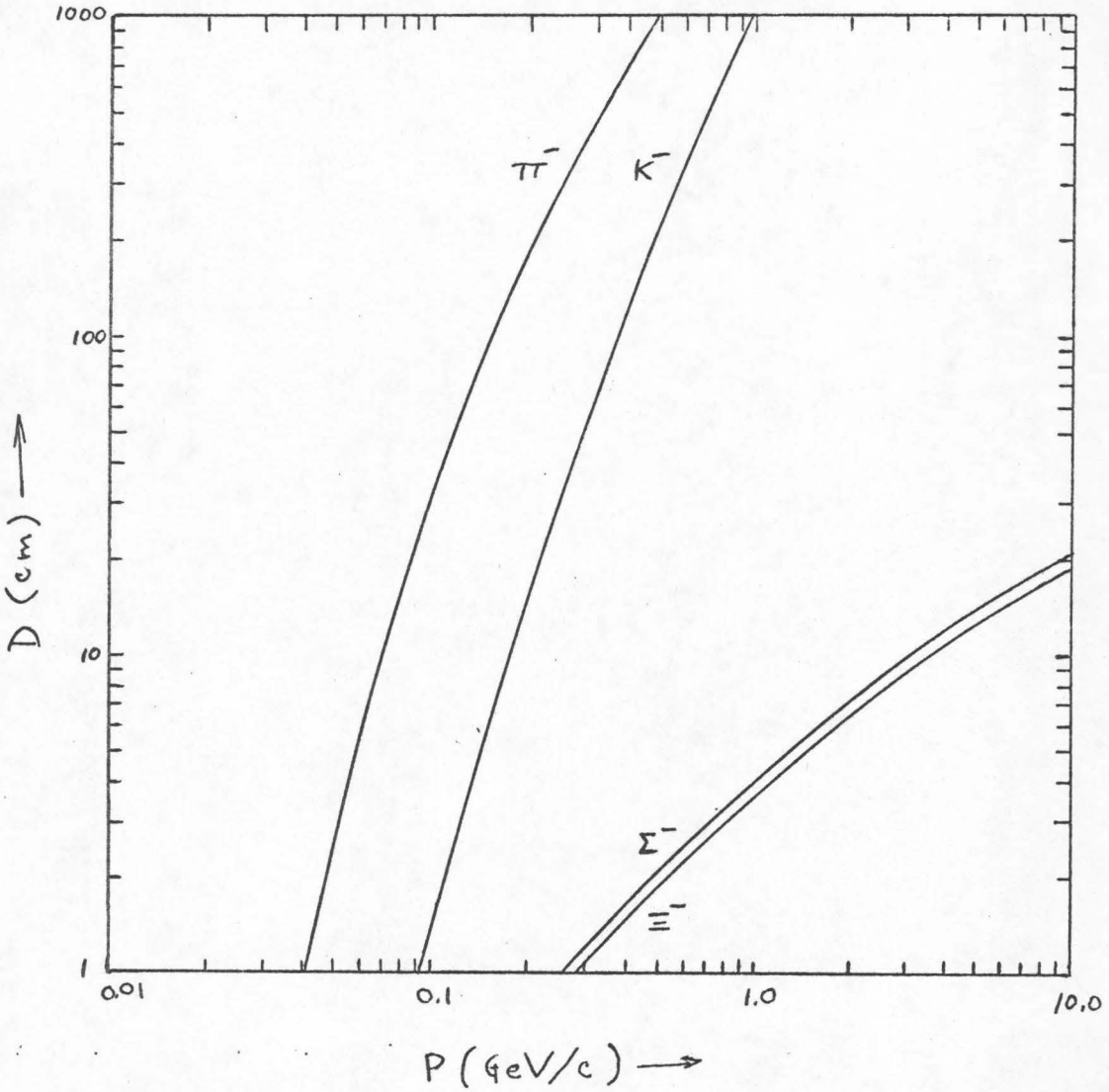

* dE/dx loss is calculated from a formula obtained from *The Quantum Theory of Radiation*, Heitler, P. 368.

Appendix II: Beam Averaging

Since our film had been used for a previous experiment, the beam average had already been determined (Trippe 1965). However it was decided that it would be useful for it to be redetermined in the new data to verify the old results.

The standard method is to average the fitted momenta of a sample of highly constrained events. For example the previous determination in our film used the $K^-p \rightarrow \Xi^-K^+$ and $K^-p \rightarrow \Xi^-K^o\pi^+$ reactions. Since our data contained only two-prong Vees, no easily identifiable $\geq$4c fit was available. It was decided to use the K^-p elastic events. It was guessed that the greater statistics would compensate for the possibility of mis-identified events which might give spurious results.

The exposure was divided into two samples due to a retuning of the beam during the running. This fact was discovered in the earlier determination.

Figure A-2a is a histogram of the fitted beam momenta for the events in the early data used for the previous determination. Figures A-2b and A-2c are the same histogram for the samples used in this determination. The conclusions appear in Table A-2. The method used to determine the average and the width was to find the median and the ¼

Table A-2

	Early Data		Later Data	
	Old Value	New Value	Old Value	New Value
P(y=0)	1960 ± 5	1953 ± 3	2000 ± 5	2000 ± 3
$\sigma_{measured}$ [2]	36	36.4 ± 5	36	36.6 ± 5
$\sigma_{resolution}$ [2]	20.4	26 ± 5 [1]	20.4	26 ± 5 [1]
σ_{beam} [2]	30	25 ± 10	30	25 ± 10
$\sigma_{nominal}$ [2]	40.0	25	40.0	25

1) This number was computed by taking $\left[(\Sigma(\delta p)^2)/N\right]^{\frac{1}{2}} = \overline{\delta\chi}$ averaged over a sample of the data (where δp is the SQUAW estimate of the error in the beam momentum) and multiplying by the width of the pull quantity for the beam momentum (1.56)

2) $\sigma_{measured}$ = experimental standard deviation

$\sigma_{resolution}$ = calculated width due to measuring errors

σ_{beam} = best estimate of beam width = $\sqrt{\sigma_m^2 - \sigma_r^2}$

$\sigma_{nominal}$ = actual value placed in PBEAM.

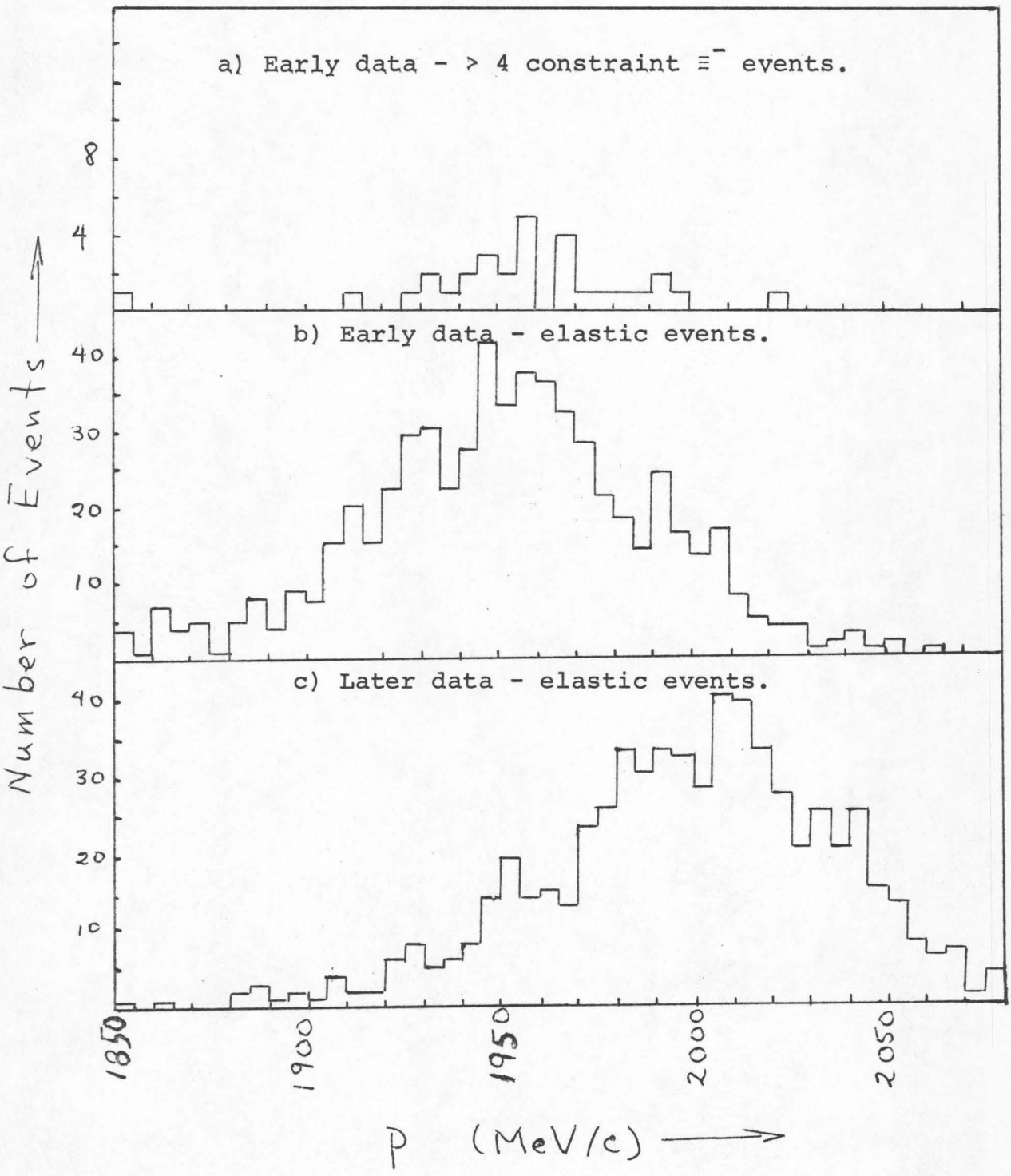

Figure A-2. Beam momentum determination.

integral points and assume that the distribution was a gaussian. This method has the advantage that it, unlike the mean and the second moment, does not depend upon the tails of the distribution which are dominated by spurious nongaussian errors.

After measuring the experimental width, the added width due to measurement errors must be removed. The following procedure was used to minimize the dependence upon a priori estimates of measurement errors. The median of the SQUAW estimated error was multiplied by the factor, 1.56, by which the distribution of the beam momentum pull quantity was wider than the ideal case (pull quantity = $\left|\text{measured value} - \text{fitted value}\right| / \left|\text{estimated error}\right|$). Then the resolution width was assumed to be independent of the beam width so that $\sigma^2\text{beam} = \sigma^2\text{measured} - \sigma^2\text{resolution}$.

Since the majority of errors in TVGP are known to be under-estimated and since this experiment involves a one constraint fit, it was decided that the nominal value used for beam averaging should be an underestimate. This is the opposite conclusion from that arrived at in the earlier determination.

Appendix III: Λ^o vs. K^o Separation

It is a canonical rule that if a Vee can be a lambda, it is a lambda. This statement can be understood in terms of the kinematics. For a Vee, one measures the momenta of the two outgoing tracks. From these vectors and a hypothesis as to these particles masses the neutral particle's mass can be reconstructed. In Figure A-3a and A-3b we have plotted the value of the neutral particle's mass as a function of two relevant quantities: the neutral particle's momentum and its decay angle in the true center of mass. (Only the cases in which a misidentification is made are interesting.) The region of ambiguous events corresponds to the ± 5 MeV/C^2 and ± 50 MeV/c^2 lines in the figures. These widths arise from a study of the experimental widths of the lambda and the kaon that arise from measurement errors. This disparity arises from the difference in the relative amount of kinetic energy in the two processes. When the $\bar{K}^o$ decays to two pions, half its rest mass is converted into momentum; when the Λ^o decays almost all of its energy is represented by the rest mass of the two final state particles. Thus, roughly speaking, the momentum measurements must determine a large quantity in the $\bar{K}^o$ case and a small quantity in the Λ^o case.

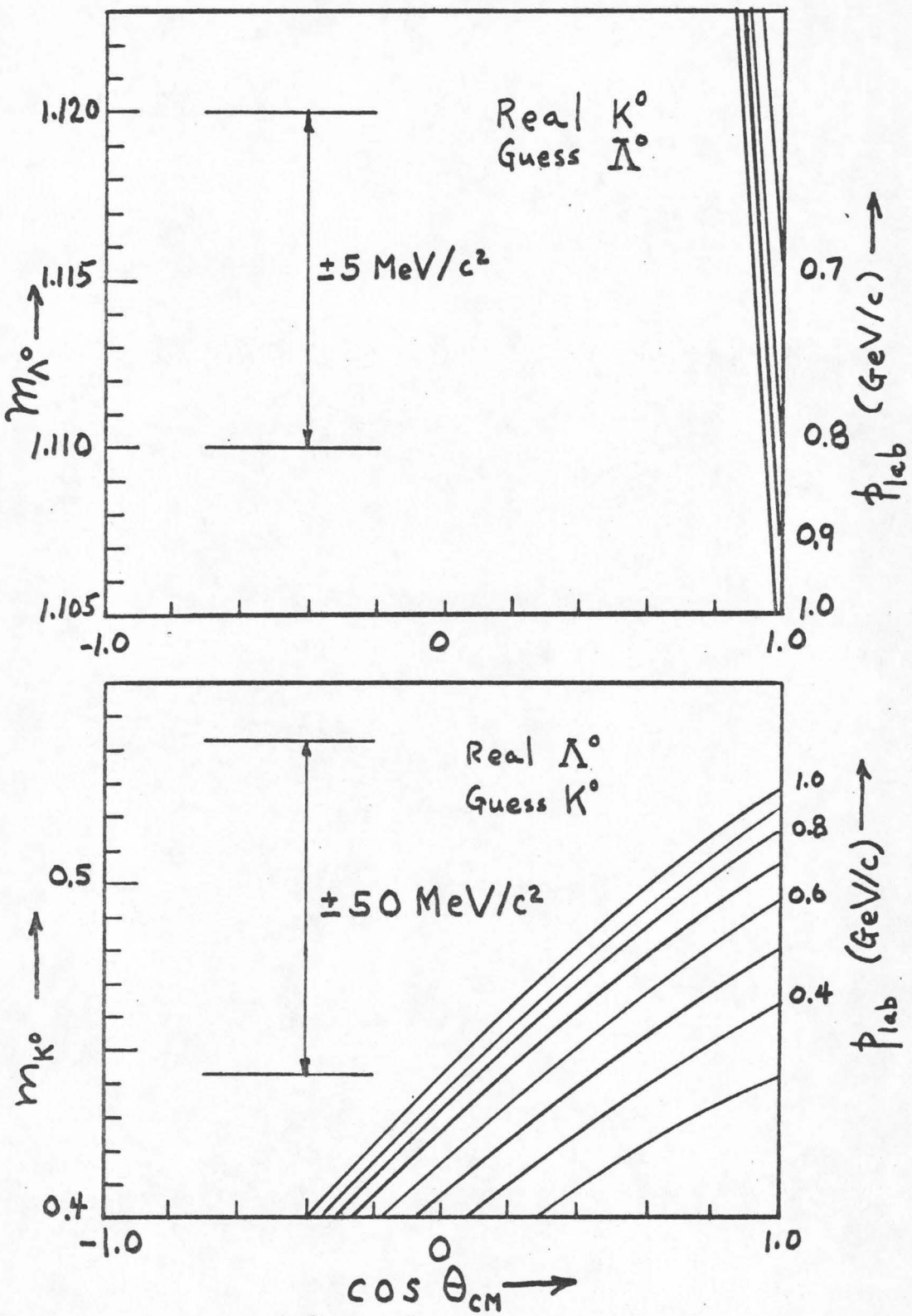

Figure A-3. The K^o vs Λ^o ambiguity problem as a function of the center of mass decay angle.

Assuming that the decay distribution of lambdas is roughly flat in cos θ_{cm} (the kaon decay distribution must be isotropic) then about 5% of the kaons will be ambiguous and ∿30% of the lambdas will be ambiguous. This information is sufficient to determine the ratio of $\bar{K}^o$'s to Λ^o's in our ambiguous sample. If ambiguity and fitting $K^-\pi^+$ are assumed to be independent, the K^o/Λ^o is determined. The motivation behind this assumption is that ambiguity arises from the fit to the Vee while fitting $K^-\pi^+n$ depends only upon the fit to the primary vertex. These two are connected only by the neutral particles momentum. However from Figures A-3a and b we can see that the fit to the Vee is only slightly dependent upon the momentum. Thus the numbers in Table III-2 determine the relative number of Λ^o's and $\bar{K}^o$'s.

Appendix IV: Spherical Harmonic Decomposition and the Geometrical Nature of the Baryon Resonance Correction

In order to represent an angular distribution, a decomposition into spherical harmonics is used. This is to be preferred to the density matrix formalism since no assumption of the maximum relevant l is needed. The fact that the Y_{lm}'s are complex valued merely implies that there is a fixed relationship between coefficients of positive and negative m.

Assume that a distribution is of the form

$$\text{Probability } (\theta,\phi) = \sum_{l=o}^{\infty} \sum_{m=l}^{l} a_{lm}\, Y_{lm}\,(\theta,\phi)$$

where Y_{lm} are the spherical harmonics. The fact that the distribution is real valued, implies that $\alpha_{lm} = \alpha^{*}_{l-m}$. This reduces the sum to

$$P(\theta,\phi) = \frac{1}{4\pi} + \sum_{l=1}^{\infty} \left[a_{lo}\, Y_{lo}(\theta,\phi) + 2 \left\{ \sum_{m=1}^{l} a_{lm}\, \mathrm{Re}\, Y_{lm}(\theta,\phi) + b_{lm}\, \mathrm{Im}\, Y_{lm}(\theta,\phi) \right\} \right]$$

Parity conservation implies that the b_{lm}'s must be identically zero (which is true in our data to the limit of our statistics).

Due to the orthonormal property of the $Y_{\ell m}$'s, to find a coefficient in this sum, given a 4π solid angle acceptance, one need only evaluate:

$$a_{\ell m} = \frac{\sum_{i=1}^{N} Y_{\ell m}(\theta_i, \phi_i)}{N}$$

where N is the total number of events. The error is then

$$\delta a_{\ell m} = \left\{ \frac{\sum_{i=1}^{N} \{\mathrm{Re}\, Y_{\ell m}(\theta_i, \phi_i)\}^2 - \frac{1}{N} \left| \sum_{i=1}^{N} Y_{\ell m}(\theta_i, \phi_i) \right|^2}{N^2} \right\}^{\frac{1}{2}}$$

For the purposes of this experiment, it is necessary to explore further the nature of this decomposition when a solid angle cut is imposed and the acceptance is no longer 4π.

When the events with any given pion-nucleon mass are removed a certain solid angle in the $K\pi$ decay sphere is being removed from the acceptance. It is then necessary to calculate the influence of this cut upon the angular distribution and also upon the $m^2_{K\pi}$ vs t distribution. In the helicity frame the form of the cut is fairly simple. This is due to the fact that in this frame:

$$m^2_{\pi^+ n} = m^2_{\pi} + m^2_{n} + 2\, E_{\pi} E_{n} - 2\, P_{\pi} P_{n} \cos \theta^{\text{helicity}}_{K\pi}$$

where P_π and P_n are totally determined by $m^2_{K\pi}$. This equation is independent of $\phi_{helicity}$ corresponding to the fact that the neutron is aligned along the -z axis. In the Jackson frame such simplicity does not exist. In terms of the Jackson angles

$$m^2_{\pi+n} = m^2_\pi + m^2_n + 2\,E_\pi E_n - 2\,P_\pi P_n \left[\cos\beta\,\cos\theta^{G.J.}_{K\pi} - \sin\beta \right.$$

$$\left. \sin\theta^{G.J.}_{K\pi}\quad \cos\phi^{G.J.}_{K\pi}\right]$$

In order to apply the likelihood method of Appendix V, it is necessary to know the integral of $Y_{\ell m}(\theta,\phi)$ over the permissible region for a given $m^2_{K\pi}$ and t ($C_{\ell m}(\theta,\phi) \equiv \int_{R(m^2,t)} Y_{\ell m}(\theta,\phi)\, d\Omega$). In the helicity frame, this reduces to a simple procedure since the boundary of the region associated with a given πN mass is independent of ϕ and t. This immediately implies that for $m \neq o$ the integral of $Y_{\ell m}(\theta,\phi)$ vanishes. For m = o the integral becomes 2π times the integral of a Legendre polynomial in cos θ which can be done analytically and evaluated at the end points.

For the Jackson frame, the integrals can be related by means of a rotation to the ones in the helicity frame. For each individual event, the angle between the Jackson and helicity frames is a well defined function of $m^2_{K\pi}$ and t.

Since the integral is over $Y_{\ell m}(\theta,\phi)$, the transformation properties of the $C_{\ell m}(\theta,\phi)$'s are the same as that of $Y_{\ell m}(\theta,\phi)$. Therefore $C^{G.J.}_{\ell m}(m^2,t) = d_{mo}(\eta)\, C^{helicity}_{\ell}(m^2)$ where $\eta=\eta(m^2,t)$ is the crossing angle.

The rapidly varying values of $C_\ell(m^2)$ and η make it necessary to evaluate the C's for each event individually. Fortunately this is a simple and rapid process. The values of C_ℓ (for $\ell\leq 2$) appear in Figure A-4 for the region excluding $m^2_{\pi n} = 1.53 \pm 0.15\,(GeV/c^2)^2$ and $m^2_{\pi n} = 2.85 \pm 0.21\,(GeV/c^2)^2$.

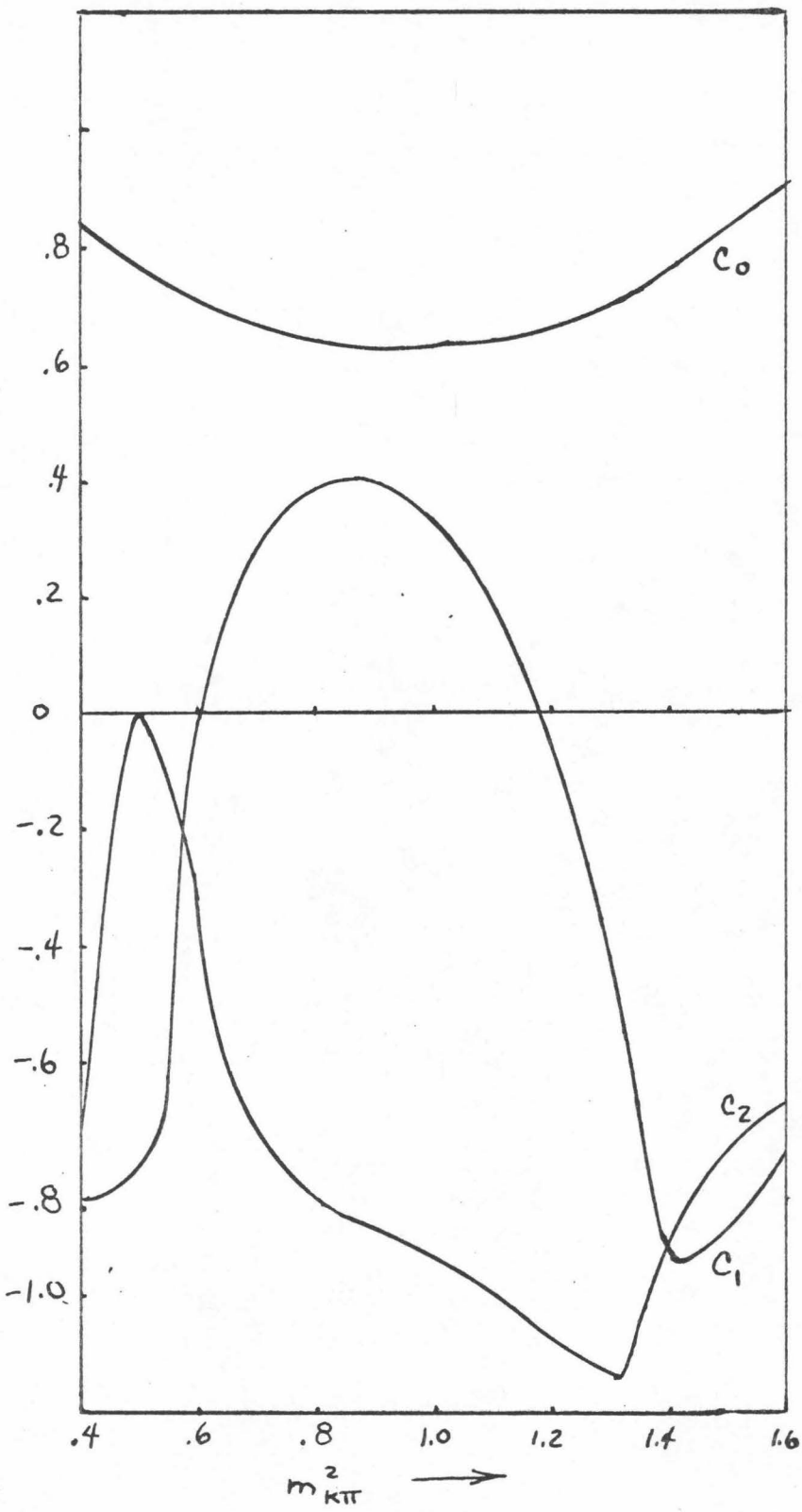

Figure A-4. The 3 spherical harmonic compensation coefficients as a function of $m^2_{K\pi}$.

Appendix V: The Maximum Likelihood Method

In order to fit our angular distributions over regions in which the spherical harmonic functions are a non-orthogonal set, we used the maximum likelihood method. This method possesses a clear advantage over the least squares method in that it does not require the data to be binned, a process which clearly destroys information. However we discovered that the standard prescription sometimes has problems.

The central notion of the procedure is to create a function L, called the likelihood function, which is the probability of our experimental result and is dependent upon the unknown parameters, $\{a_j\}$, and the experimentally measured data, $\{x_i\}$. One then maximizes L as a function of the a_j's. This then gives the best estimate of the true values of the a_j's as a consequence of Bayes'theorem.

The function L can be easily constructed from the probability function for an individual event, $P(x_i, a_j)$. It is

$$L = \prod_{i=1}^{N} P(x_i, a_j)$$

where N is the number of events in the experiment. However it is crucial that the normalization of $P(x_i, a_j)$ be insensitive to the values of the a_j's. Otherwise the maximization procedure will result in a maximizing of the

average value of P. The standard technique (Annis 1953) is given a theoretically meaningful function $Q\ (x_i,a_j)$, is to normalize this function by setting

$$P\ (x_i,a_j) = \frac{Q\ (x_i,a_j)}{\int_R dy\ Q\ (y,a_j)}$$

this will be referred to hereafter as method I.

We have discovered that it is equally valid to define the function P by

$$P\ (x_i,a_j) = Q\ (x_i,a_j) - \frac{\int_R dy\ A\ (y,a_j)}{\int dy} + 1$$

This will be referred to hereafter as method II.

Method II possesses several advantages in certain cases. These advantages arise from the analytic structure of the likelihood function and are illustrated in the following example. Assume that we have an experiment with N measurements $\{x_i\}$ and that we wish to fit this with the function $Q\ (x,\beta) = 1 + \beta x$ where the range of x is (0,1). Then method I gives

$$L_I = \left[\prod_{i=1}^{N} (1 + \beta_I x_i)\right] \left[1 + \frac{\beta}{2}\right]^{-N}$$

as the likelihood function. This function possesses an N^{th}

order pole at $\beta = -2$ [ii]. Thus for $\beta \lesssim -1$ we have structure controlled by the extraneous pole-zero pattern of the probability function. Consider in contrast the analytic structure of the likelihood function given by method II

$$L_{II} = \prod_{i=1}^{N} \left[1 + \beta_{II} \, (x_i - \tfrac{1}{2})\right]$$

This has an N^{th} order pole at infinity. Note however that the resulting parameters in the two methods are different, $\beta_{II} = \beta_I/(1 - \tfrac{1}{2}\beta_I)$. It can also be shown that in this example method I gives a biased estimate of the unknown parameter while method II is unbiased (Yellin 1971).

In this one parameter case we see that the physically meaningful region for β_I is $\beta_I \gtrsim -1$ and can restrict it to that region. However, in the many parameter case such as our spherical harmonic or interference fits, it is not as obvious where the physically meaningful solution must be. We have discovered in fitting our interference terms that quite often method I does not converge but that method II always does.

[ii] It also possesses N zeros in the neighborhood of $\beta = -2$ namely at $\beta_i = -\frac{1}{x_i}$ (where x_i are the data points).

In either case, if we assume that the likelihood function is a gaussian -- which it must be when $N \to \infty$ -- we estimate the error in $a_{\ell m}^{max}$ as

$$\delta\, a_{\ell m}^{max} = - \frac{d^2\, \ell n\, L\, (\beta)}{(d\, a_{\ell m})^2}$$

Appendix VI: Monte Carlo Studies

Any one constraint fit is equivalent, neglecting measurement errors, to a missing mass measurement. In the reaction $K^-p \rightarrow K^-\pi^+n$ there is a missing neutron. Monte Carlo methods can determine the degree of kinematic overlap of reactions such as $K^-p \rightarrow \pi^-\pi^+\Lambda$ or $K^-p \rightarrow \pi^-p\bar{K}^o$. The results of such a study appear in Figures A-5a to c. The calculated "neutron" mass squared is plotted for events generated isotropically in the phase space of the "real" reaction. Notice that there is overlap even in the absence of measurement error. Such an overlap exists because the mistake in particle identification leads to extraneous terms which couple masses and momenta in the neutral mass formula becoming significant.

Figure A-5. Monte Carlo results for events misinterpreted as $K^- p \rightarrow K^- \pi^+ n$ events.

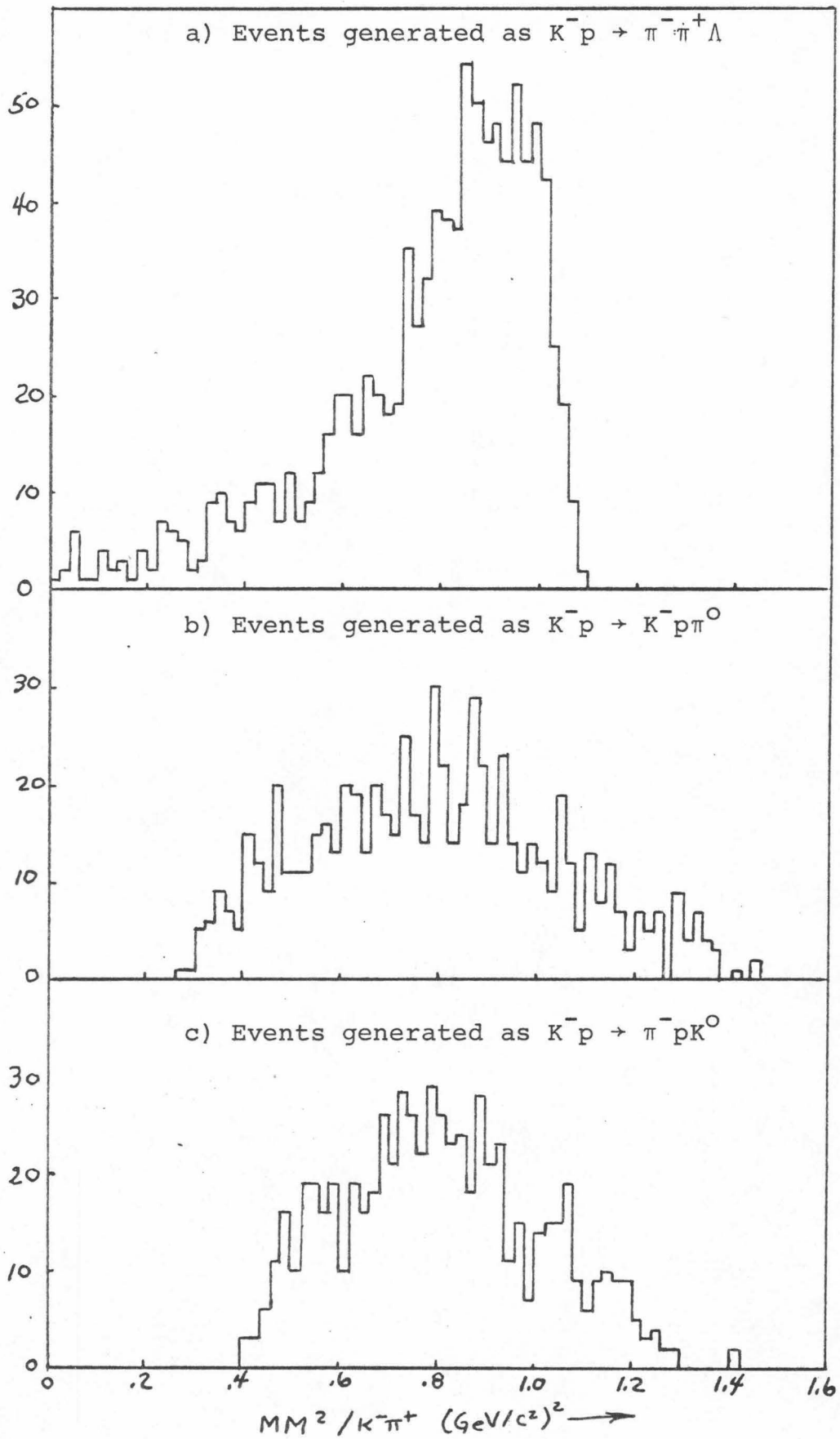
a) Events generated as $K^- p \to \pi^- \pi^+ \Lambda$
b) Events generated as $K^- p \to K^- p \pi^o$
c) Events generated as $K^- p \to \pi^- p K^o$
0
10
20
30
40
50
.2
.4
.6
.8
1.0
1.2
1.4
1.6
$MM^2 / K^- \pi^+$ $(GeV/c^2)^2 \longrightarrow$

Appendix VII. Kinematic Form Factors

The simple one pion exchange hypothesis correctly predicts the energy dependence and the "decay" distribution for reactions such as $\pi^- p \to \pi^- \pi^+ n$. However it does not predict the correct shape for the production distribution $\frac{d\sigma}{dt}$. Several remedies have been suggested to correct this situation; all of which involve several a priori unknown parameters. One reasonable proposal is the Dürr-Pilkun or Benecke-Dürr kinematic form factor hypothesis.

The nature of the parameters is motivated by classical arguments about the off-shell behavior of the angular momentum barrier. This line of reasoning has serious troubles when one realizes that the shapes of the differential cross sections for the two reactions $K^- p \to K^* n$ and $K^+ n \to K^* p$ are very different, and that this difference is not permitted in the Dürr-Pilkun framework. Nevertheless, it does prove interesting to fit our data to this equation and thus provide an analytic description of our data in a formalism that is commonly used.

Simple field theory prescribes that the amplitude for the process in Figure I-1a must have a pion propagator, a γ^5 for pseudoscalar coupling, and a matrix element at each

Figure A-6. The Kinematic form factors.

a) The Durr-Pilkun factors.

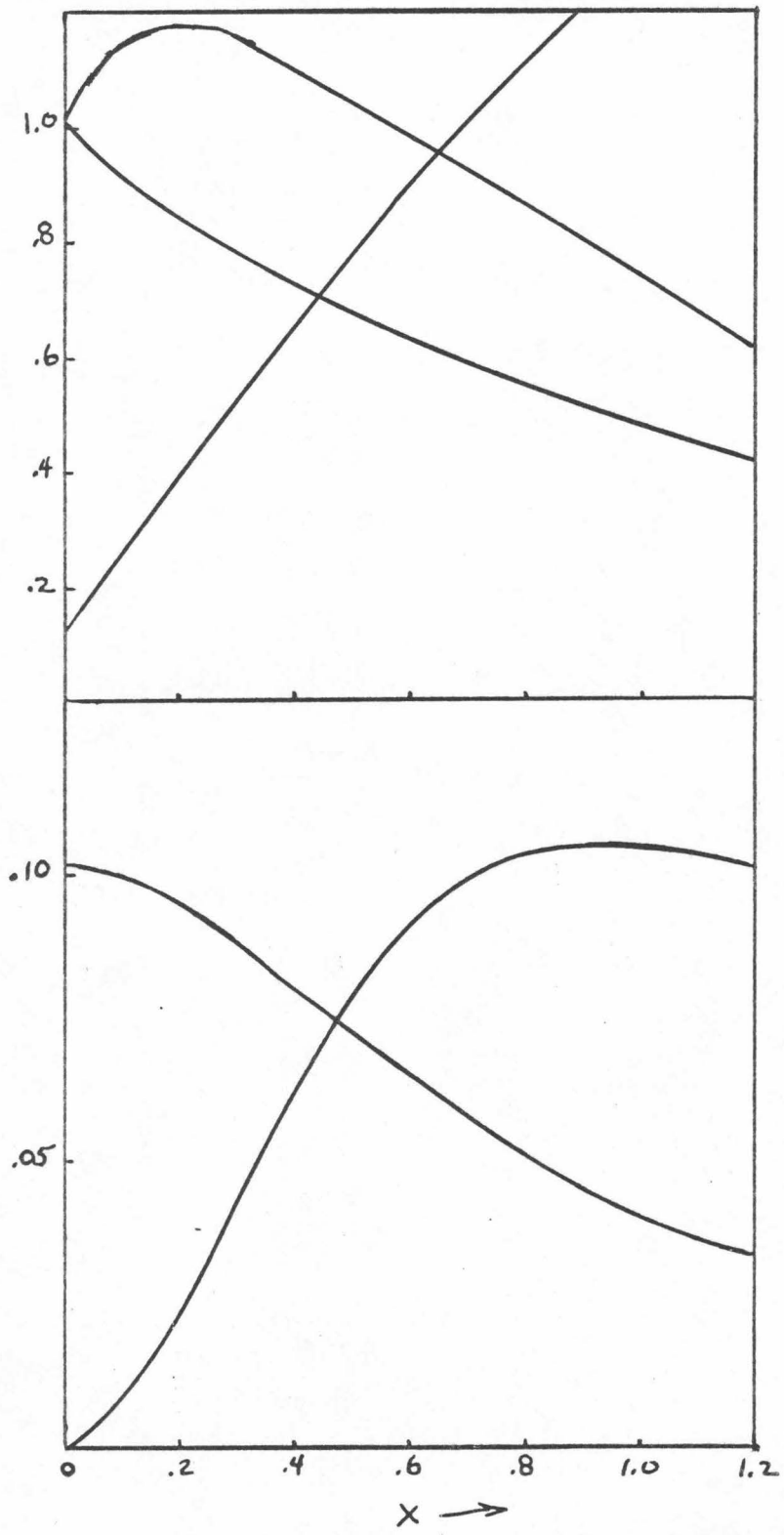

b) The Benecke-Durr factors.

vertex. This gives

$$\frac{d^2\sigma}{dm^2dt} = \frac{1}{4\pi^3 p^{*2} s} |T_{K\pi}(\bar{s},t)|^2 \frac{|-t|}{(t-\mu^2)^2} |T_{np\pi+}(t)|^2$$

where $|T_{K\pi}(\bar{s},t)|^2 = \bar{s}\, q_t\, \sigma_{K\pi}(\bar{s},t)$

and $|T_{np\pi+}|^2 = \pi^2 g^2$

where $g^2=29.2$, and q_t is the virtual pion 3-momentum in the K_π center of mass. One then expands $\sigma_{K\pi}$ as some function with an explicit t dependence. The simplest expansion is

$$\sigma_{K\pi}(\bar{s},t) = \sum_{l=o}^{\infty} \left(\frac{q_t}{q}\right)^{2l} \sigma_{K\pi}^{l}(\bar{s})$$

where $\sigma_K^l(\bar{s})$ is the on-shell $K\pi$ cross section of the l^{th} partial wave, and the $(q_t/q)^2$ is the angular momentum barrier factor. This prescription is referred to as the Born approximation.

The fundamental problem with this form is that the behavior as a function of t is wrong. As $t \to -\infty$, the pion becomes more virtual. In order to keep $\bar{s}$ constant, the pion develops a larger 3-momentum, q_t. The factors of q_t in the numerator then make the differential cross section increase as t increases. In order to remedy this behavior, Benecke, Dürr, and Pilkun proposed (Dürr 1965, Benecke 1968) that one should put in a more complete form of the angular momentum

barrier penetration factors, and so building in the cutoff not provided by the simple Born approximation. According to the Benecke-Dürr prescription (BD), one replaces the off-shell cross section by

$$\sigma_{K\pi}(\bar{s},t) = \frac{q}{qt} \sum_{l=o}^{\infty} \frac{u_l(R_l q_t)}{u_l(R_l q)} \sigma_{K\pi}^{l}(\bar{s})$$

where q (q_t) is the on-shell (off-shell) 3-momentum, R_l are the a priori unknown parameters that represent the radius of interaction of the l^{th} partial wave and the u_l are defined by (see Figure A-6)

$$u_l(x) = \frac{1}{(2x^2)} Q_l\left(1 + \frac{1}{2x^2}\right)$$

where the Q_l are the Legendre functions of the second kind. The functions $u_l(x)$ have the properties that:

$$u_l(x) \sim x^{2l} \text{ for } x << 1$$

$$u_l(x) \sim x^{-2} \ln 4x^2 \text{ for } x >> 1$$

One cannot use a similiar prescription for the baryon vertex since the BD prescription leads to complex valued cross sections. However, as an alternative we can use the Dürr-Pilkun (DP) prescription which is an earlier version of the kinematic form factor model whose major difference is an

incorrect behavior at high t, but which has the same behavior at small t as the BD model.

According to the DP model, one modifies the πNN vertex matrix element by inserting a factor of $(1+R_n^2Q^2)/(1+R_n^2Q_t^2)$ where $Q(Q_t)$ is the on-shell (off-shell) 3-momentum of the virtual pion in the neutron rest frame. The R_n is another parameter which must be determined as part of the fit. Physically it represents the interaction radius of a pion and a neutron in the proton bound state.

We have fit our data with this prescription assuming that the Kπ cross section is predominately P-wave. This leaves us with two phenomenological parameters; one, R_N, to give the effective pion-nucleon P-wave radius; the other, R_K, to give us the effective Kπ P-wave scattering radius.

Permitting both to be free gives us the result seen in Figure A-7. This is a 2-dimensional contour plot of χ^2 for fitting $\frac{d^2\sigma}{dmdt}$ for our data for $|t|<0.5$ binned in 400 bins. The data fit best to a lack of nucleon vertex factor and a Kπ vertex factor of about 2.2 Gev^{-1} which corresponds to an interaction radius of 0.6 fermis. However, from the contour plot it is evident that the fit is not sensitive to a shift of R_K downward and a corresponding shift of R_N upward. If we use a value of $R_n = 2.3\ (Gev/c)^{-1}$ as determined in other experiments (Trippe 1968), we find $R_k=0.60$ represents the best χ^2. This corresponds to a Kπ radius of 0.26 fermis.

Figure A-7. Contour plot of Chi-square as a function of R_K and R_N the DP parameters. Number of degrees of freedom = 386. Innermost contour corresponds to $\chi^2 = 500$, and they are spaced at intervals of 50.

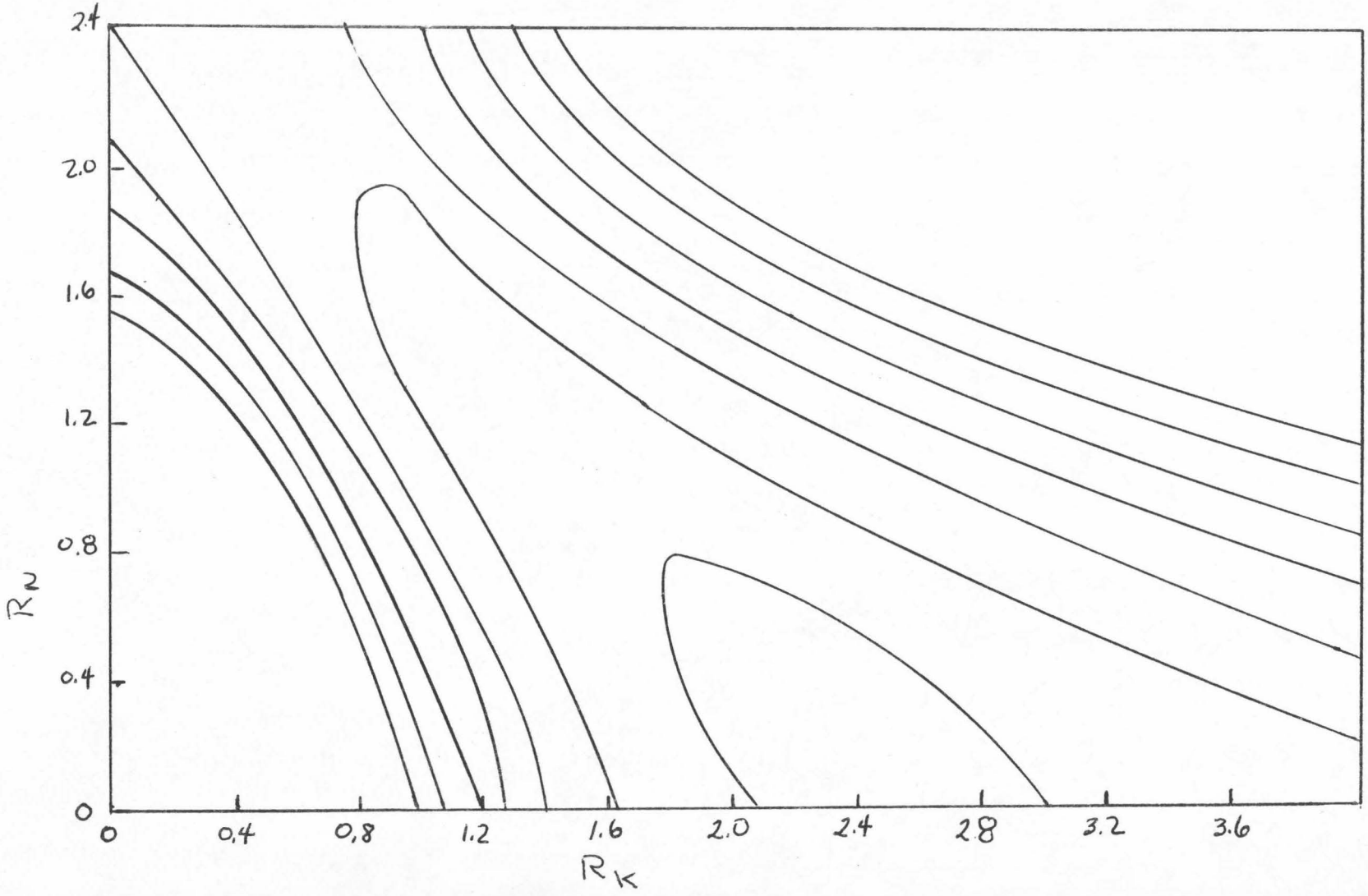
2.4
2.0
1.6
1.2
0.8
0.4
0
R_N
0
0.4
0.8
1.2
1.6
2.0
2.4
2.8
3.2
3.6
R_K

These figures also provide the explanation of why these parameters work so well in fitting experimental data. The curves of Figure A-6 are smoothly varying functions of $R_x \cdot q_x$. Thus both R_K and R_n both primarily change the cross section by changing the slope. Therefore if either parameter is free, it can be chosen to fit the differential cross section. This is indicated by the manner in which the χ^2 is insensitive to shifts along the diagonal.

Appendix VIII. Density Matrix Elements

A commonly used representation of the angular distribution is in terms of the density matrix elements. This formalism is exactly equivalent to a spherical harmonic decomposition. It possesses the disadvantage that the numerical values are dependent upon the assumed maximum significant spin. The density matrix elements possess the advantage that they are more closely related to the dynamics.

The standard form of the density matrix is a representation of definite total spin ℓ, and of mixed polarization m, so that the density matrix is of the form:

$$P_{mm'} = \sum_{mm'} |\ell,m\rangle\langle\ell,m|P|\ell,m'\rangle\langle\ell,m'|$$

However in high energy physics where resonances are broad and sit above large backgrounds in different spin states it is necessary to generalize this formula. Thus the density matrix must be written as:

$$P^{\ell\ell'}_{mm'} = \sum_{\ell\ell'} \sum_{mm'} |\ell,m\rangle\langle\ell,m|P|\ell',m'\rangle\langle\ell',m'|$$

where $P^{\ell\ell'}_{mm'}$ is a tensor of rank 2 over the group SU(2).

The remaining problem is to understand how to evaluate $\langle \ell,m|P|\ell',m'\rangle$ in our particular case. We have a $K\pi$ state of mixed spin and spin orientation which then decays to a K and a π. For any fixed ℓ and m, the amplitude to decay to 2 spinless bosons is proportional to $Y_{\ell m}(\theta,\phi)$ and transforms like $Y_{\ell m}(\theta,\phi)$ (where θ,ϕ are the angles which define the direction of the K in the $K\pi$ rest frame). By the Wigner-Eckart theorm, we can write it as some constant times $Y_{\ell m}(\theta,\phi)$. Therefore the matrix element $\langle \ell m|P|\ell' m'\rangle$ equals the expectation value of $Y_{\ell m}(\theta,\phi)Y^{*}_{\ell m'}(\theta,\phi)$.

In our case, we restrict ℓ to be <1 and then we can invert this expression to yield the angular distribution in terms of the density matrix elements, as follows:

$$W(\theta,\phi)= \frac{1}{4\pi}\Big[1 +(P_{00}-P_{11})(3\cos^2\theta-1)-3\,p_{1,-1}\sin^2\theta\cos^2\phi$$

$$-3\sqrt{2}\,\mathrm{Re}p_{10}\sin 2\theta\cos\phi + 2\sqrt{3}\,P_{0s}\cos\theta - 2\sqrt{6}\,P_{1s}\sin\theta\cos\phi\Big]$$

where

$P_{00} + 2P_{11} + P_{ss}=1$ and $P_{ss} = P^{00}_{00}$, $P_{0s} = P^{10}_{00}$, $P_{1s} = P^{10}_{10}$, and $P_{mm'} = P^{11}_{mm'}$, as is conventional.

Appendix IX. Phase Space

Through the use of a Dalitz plot, one studies the structure of a matrix element through the deviations of an experimental angular distribution from the predictions of pure phase space.

Let $p_i=(E_i,P_i)$ be the four-momenta of the three final state particles in the process $M\to m_1+m_2+m_3$, (where $M^2=s$) in the M center of mass. The differential invariant phase space is

$$d^{12}R(m,m_1,m_2,m_3) = \delta^4(M-\Sigma p_i) \prod_{i=1}^{3} \delta(p_i^2-m_i^2)\, d^4p_i \qquad (1)$$

integrating over the energies (dE_i) yields

$$d^9R = \delta^4(M-\Sigma p_i) \prod_{i=1}^{3} \frac{d^3p_i}{2E_i}$$

next integrating over p_3 reduces the differential to

$$d^6R = \delta(M^o - p_i{}^o)\ \frac{d^3p_1\, d^3p_2}{2E_1 2E_2\ 2E_3} \quad \text{where } E_3 = \sqrt{(\vec{p}_1+\vec{p}_2)^2+m_3^2}$$

Since the three body final state has only four dynamically meaningful variables (neglecting stable particle spins

and the total energy), there remain two dynamically meaningless variables which must still be removed.

Consider a coordinate frame in which the center of mass lies at the origin and particle 1 along the +z axis. Then defining P_2 by the angles ξ and η of Figure A-8, the particle 2 differential becomes $d^3P_2=P_2{}^2\ d\cos\xi\ d\eta\ dP_2$ while the d^3P_1 can be replaced by parameterizing the possible orientations of the production axis $\vec{P}(d^3p_1=P_1{}^2 dP_1\ d\cos\beta\ d\alpha)$.

Substituting these differentials into equation 2 yields

$$d^6R = \delta^4(M^o-\Sigma p_i{}^o)\ \frac{p_1^2p_2^2\ d\cos\xi\ d\eta\ d\cos\beta\ d\alpha\ dp_1\ dp_2}{2E_1\ 2E_2\ 2E_3}$$

Clearly α is not dynamically meaningful, and therefore should be integrated over and set equal to $\pi/2$, yielding

$$d^5R = \delta(M^o-P_i{}^o)\ \frac{2\pi P_1{}^2P_2{}^2\ d\cos\xi\ d\eta\ d\cos\beta\ dp_1\ dp_2}{2E_1\ 2E_2\ 2E_3}$$

We now transform the integral to the variables

$$E_1 = (P_1{}^2 + m_1{}^2)^{\frac{1}{2}}$$

$$E_2 = (P_2{}^2 + m_2{}^2)^{\frac{1}{2}}$$

$$E_3 = (P_1{}^2 + P_2{}^2 + 2P_1P_2\ \cos\xi + m_3)^{\frac{1}{2}}$$

by means of the relation

$$dp_1dp_2\ d\cos\xi = dE_1\ dE_2\ dE_3 \left| \frac{\partial(P_1P_2\ \cos\xi)}{\partial(E_1\ E_2\ E_3)} \right|$$

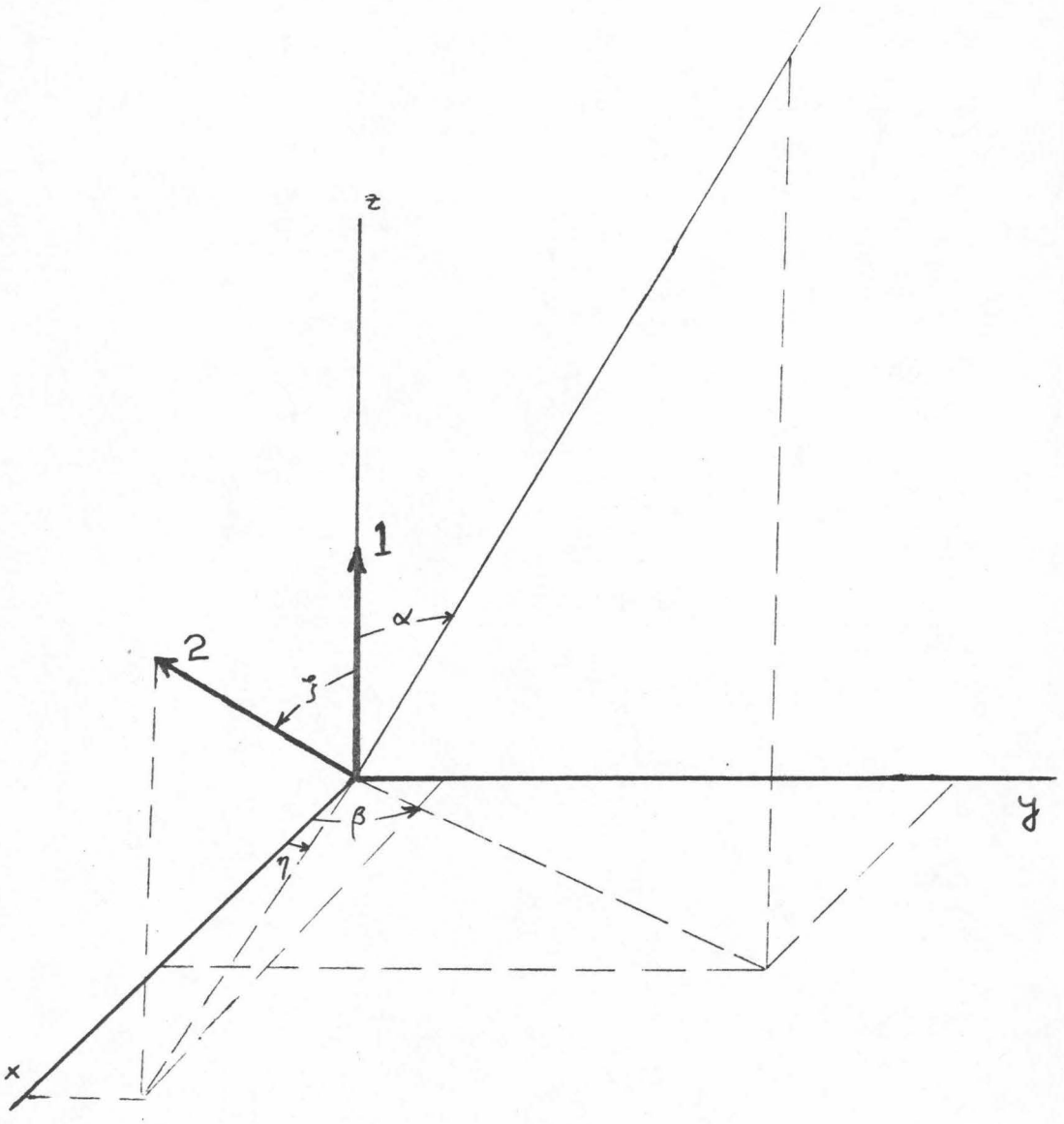

Figure A-8. The general 3-body coordinate system.

The Jacobian is easily found to be

$$\frac{\partial(E_1\ E_2\ E_3)}{\partial(P_1\ P_2\ \cos\xi)} = \begin{bmatrix} P_1/E_1 & 0 & P_1 + P_2\cos\xi \\ 0 & P_2/E_2 & P_2 + P_1\cos\xi \\ 0 & 0 & \frac{P_1\ P_2}{E_3} \end{bmatrix}$$

So that

$$\frac{\partial(P_1\ P_2\ \cos\xi)}{\partial(E_1\ E_2\ E_3)} = \frac{E_1\ E_2\ E_3}{P_1^{\,2}\ P_2^{\,2}}$$

Inserting this into the differential yields

$$d^5R = \delta(M^o - \Sigma P_1{}^o)\ \frac{2\pi}{8}\ dE_1\ dE_2\ dE_3\ d\eta\ d\cos\beta$$

Integrating over E_3 to eliminate the δ-function yields

$$d^4R = \frac{\pi}{4}\ dE_1\ dE_2\ d\eta\ d\cos\beta \qquad (3)$$

which is a form of the irreducible dynamically meaningful differential.

To find the two dimensional differential of the Dalitz plot, we integrate over η and β to yield

$$d^2R = \pi^2\ dE_1\ dE_2$$

To put this in invariant form, we can use the relation

$E_3 = (S + m_3^2 - m_{12}^2)/2\sqrt{S}$

So for fixed s, $dE_3 = dm_{12}^2$ and the matrix element is

$$d^2R = \pi^2 \, dm_{23} \, dm_{13}$$

which is the familiar result that the phase space is uniform on a Dalitz plot.

From formula 3, we can also extract another differential of interest. Since the β dependence is just $d\cos\beta$, the phase space is uniform in β. Note that since $t = (p_0-p_1)^2 = m_0^2+m_1^2-2E_0E_1\cos\beta$ (so $dt = -2E_0E_1 d\cos\beta$), in term of t, the differential is

$$d^4R = \frac{\pi}{4} \, dE_1 \, dE_2 \, \frac{dt}{2E_0E_1} \, d\eta \qquad (4)$$

Now integrating over η and a fixed t interval does not yield a uniform phase space. By integrating over η and E_2 we obtain the following

$$d^2R = \frac{\pi^2}{4E_0} \, \frac{dE_1}{E_1} \, \Delta E_2 \, dt = \frac{\pi^2}{4E_0} \, \frac{\Delta E_2}{(s+m_1^2-m_{23}^2)} \, dm_{23}^2 \, dt$$

which is the unfamiliar phase space of a Chew-Low plot (where

$$\Delta E_2 = \frac{1}{\sqrt{s} \; m_{23}^2} \left[(m_{23}^2-m_2^2-m_3^2)^2-2m_2^2m_3^2\right]^{\frac{1}{2}} \left[(s-m_{23}^2-m_1^2)^2 - 2m_1^2m_{23}^2\right]^{\frac{1}{2}}).$$

Appendix X. t Channel Exchange Mechanisms

Because of Lorentz invariance, the high energy behavior of any process must be describable in terms of the exchange of a spacelike quasi-particle. The analogy with quantum electrodynamics leads one to identify such pseudo-particles with the time-like stable and metastable particles seen in production experiments. It is then natural to select the relevant exchange mechanism by requiring the exchanged object to conserve all possible quantum numbers (Q,S,B, and sometimes P,G, and C).

Since the 4-momentum of the exchanged object is spacelike, the mass squared is negative. Therefore one characteristic of the real particle which must be different for the exchanged object is its mass. A second characteristic which is not simply related is the intrinsic spin of the quasi-particle, since the world line of such an object is fundamentally different from that of a timelike particle.

From perturbation theory, each amplitude has a $(t-m^2)^{-1}$ dependence (where m is the exchanged particle's mass and t, the momentum transfer, is negative in the physical region). Thus only the terms due to particles of lowest mass are significant. Among these some are more significant than

others because of possible differences in coupling constants.

As an example, in the process of interest $K^-P \to K^{*o}N$ (K^* forward) the significant exchanges are the non-strange, charged mesons listed in Table A-3; these being the lowest mass particles for the four possible combinations of P and G. For the related reaction $\pi^-P \to \rho^oN$, G-parity is defined for the mesons and its conservation forbids ρ or B exchange since $G_{exchange} = G_\pi(-) \times G_\rho(+) = -$. No such simplification is possible for the kaonic reaction since the K and K^* do not have a defined G-parity.

The B and A_2 are generally neglected since they are such relatively high mass particles.

ρ(or A_2) exchange can occur only in the P-orbital angular momentum state, which contributes a term to the angular distribution of the form:

$$a \sin^2 \theta + b \sin^2 \theta \cos 2\phi$$

Since a term of this type is not found in our data (see Section V-1) and is present in reactions thought to be due to vector meson exchange, we conclude such terms do not contribute significantly. It is generally believed that this phenomenon is due to the smallness of the ρNN coupling constant.

From the Regge model, a classification of different exchanges by energy dependence has been constructed. The classification is based upon the fact that if the Regge model is correct, then the energy dependence of the differential cross section is

$$\frac{d^2\sigma}{dsdt} \sim f(t)\ s^{2\alpha(t)-2}$$

where $\alpha(t)$ is the Regge trajectory function. This implies that the energy dependence of the forward cross section for the various exchanges is as given in the last column of Table A-3 (assuming all Regge trajectories are straight lines with a slope of 1 $(Gev/c^2)^{-1}$). Thus the s^{-2} dependence of our reaction argues for a pion mechanism.

Table A-3. S=0, I=1 Mesons

Particle	Mass	J^P	G	Energy Dependence
π	140	0^-	-	s^{-2}
ρ	765	1^-	+	$s^{-1.41}$
B	1235	1^+	+	$s^{-3.1}$
A_2	1300	2^+	-	$s^{-1.4}$

Appendix XI. The Schlein-Malamud Factorization Hypothesis

If events with small t are selected in reactions such as $\pi^- p \to \pi^- \pi^+ n$ or $K^- p \to K^- \pi^+ n$, it is commonly believed that the behavior of $\pi\pi$ or $K\pi$ scattering can be extracted from the moments of the decay distribution. However, in these reactions, the $a_{2,0}$ decay moment does not reach the limit predicted by unitarity at the mass of the p or K^*. So, it is necessary to introduce a set of renormalization parameters for the various moments. The Schlein-Malamud method provides a logical prescription for choosing such parameters.

Their model consists of writing the amplitude to reach a final state containing a di-boson system with interval angular momentum ℓ and helicity μ and a nucleon with helicity λ from an initial state with nucleon helicity λ' as $A_\ell^{K\pi}(m,t)\ M_{\ell,\mu}^{\lambda,\lambda'}(s,t)$. Here $A_\ell^{K\pi}$ is the off-shell amplitude for $K\pi$ elastic scattering at momentum transfer t to the $K\pi$ system and with internal orbital angular momentum ℓ. The helicity amplitudes $M_{\ell,\mu}^{\lambda,\lambda'}$ are functions of total cm energy, t and the $K\pi$ invariant mass m. Parity conservation implies $M_{\ell,-\mu}^{-\lambda,-\lambda'} = (-1)^{\mu+\lambda+\lambda'} M_{\ell,\mu}^{\lambda,\lambda'}$.

With this assumption, the differential cross section for the reaction $K^-p \to K^-\pi^+n$ (or $K^+n \to K^+\pi^-p$) may be written as:

$$\frac{d^4\sigma}{dmdt\, d\Omega_{\pi\pi}} = \sum_{\lambda\lambda'} \left| \sum_{l,\mu} A_l^{K\pi} M_{l\mu}^{\lambda\lambda'} Y_l^{\mu}(\Omega_{\pi\pi}) \right|^2 = \frac{d^2\sigma}{dmdt} \sum_{l=0}^{2} \sum_{m=-l}^{+l} \langle Y_l^m \rangle Y_l^m \qquad (1)$$

The observable quantities in equation (1) have the following functional dependence on the $A_l^{K\pi}$ and the helicity amplitudes.

$$\frac{d^2\sigma}{dmdt} = |A_p^{K\pi}|^2 \{|\vec{p}_1|^2 + |\vec{p}_0|^2 + |\vec{p}_{-1}|^2\} \quad |A_s^{K\pi}|^2 \{|\vec{s}|^2\} \qquad (2a)$$

$$\frac{d^2\sigma}{dmdt} \langle Y_1^0 \rangle = \frac{2}{\sqrt{4\pi}} \mathrm{Re}\, (A_s^{K\pi} A_p^{K\pi *}) \{\vec{p}_0 \cdot \vec{s}\} \qquad (2b)$$

$$\frac{d^2\sigma}{dmdt} \langle \mathrm{Re}\, Y_1^1 \rangle = \frac{1}{\sqrt{4\pi}} \mathrm{Re}\, (A_s^{K\pi} A_p^{K\pi *}) \{\vec{s} \cdot (\vec{p}_1 - \vec{p}_{-1})\} \qquad (2c)$$

$$\frac{d^2\sigma}{dmdt} \langle Y_2^0 \rangle = \frac{2}{\sqrt{20\pi}} |A_p^{K\pi}|^2 \{|\vec{p}_0|^2 - \tfrac{1}{2}(|\vec{p}_1|^2 + |\vec{p}_{-1}|^2)\} \qquad (2d)$$

$$\frac{d^2\sigma}{dmdt} \langle \mathrm{Re}\, Y_1^1 \rangle = \sqrt{\frac{3}{20\pi}} |A_p^{K\pi}|^2 \{\vec{p}_0 \cdot (\vec{p}_1 - \vec{p}_{-1})\} \qquad (2e)$$

$$\frac{d^2\sigma}{dmdt} \langle \mathrm{Re}\, Y_2^2 \rangle = \sqrt{\frac{6}{20\pi}} |A_p^{K\pi}|^2 \{-\vec{p}_1 \cdot \vec{p}_{-1}\} \quad . \qquad (2f)$$

In writing equations (2), we have used the convenient two-component vector notation (Schlein 1967) for the helicity amplitudes:

$$\vec{s} = (M^{+\,+}_{0,0}\ ,\ M^{-\,+}_{0,0}) \tag{3a}$$

$$\vec{p}_1 = (M^{+\,+}_{1,1}\ ,\ M^{-\,+}_{1,1}) \tag{3b}$$

$$\vec{p}_0 = (M^{+\,+}_{1,0}\ ,\ M^{-\,+}_{1,0}) \tag{3c}$$

$$\vec{p}_{-1} = (M^{+\,+}_{1,-1},\ M^{-\,+}_{1,-1}) \tag{3d}$$

The $A_l^{K\pi}$'s are defined as

$$A_s^{K\pi}(m,t) = \sqrt{2/3}\ e^{i\delta_0^{1/2}(m)} \sin\delta_0^{1/2}(m) + \sqrt{1/3}\ e^{i f_0^{3/2}(m)} \sin\delta_0^{3/2}(m)$$

$$A_p^{K\pi}(m,t) = \sqrt{2/3}\ e^{i\delta_1^{1/2}(m)} \sin\delta_1^{1/2}(m)$$

(we neglect the T = 3/2 P-wave). The T = 3/2 S-wave is taken from the World DST collaboration paper (Bingham 1971) and the P-wave is assumed to be a unitary Breit-Wigner with a center at 892 Mev and a full width at half maximum = 50 Mev. One assumes the nucleon amplitudes are independent of meson-meson mass and then the S-wave phase shifts and nucleon factors can be found.

Such a prescription has been applied to $\pi^- p \to \pi^- \pi^+ n$ and predicts an S-wave resonance, $\sigma(730)$ (Malamud 1967). In order to further test the model, we have applied it to the reactions $K^- p \to K^- \pi^+ n$ and $K^+ N \to K^+ \pi^- p$. If the factorization hypothesis is correct, this pair of reactions must yield similiar phase shifts. Such a result is expected and found since the decay moments of these two reactions, displayed in Figure V-5, are, within statistics, the same.

For a given reaction and a given $K\pi$ mass bin two solutions for the S-wave phase shift were found. Thus many acceptable solutions to an overall fit to the K^* region are present. However only two solutions are continuous and thus physical. The S+M parameters are insensitive to which of the many S-wave solutions is chosen. The S-wave solutions are given in Figure V-9.

One solution (the up) shows evidence for a S-wave $K\pi$ resonance at ~860 Mev. This ambiguous feature has been found in the reactions $K^+ p \to K^+ \pi^- \Delta^{++}$ and $K^- N \to K^- \pi^+ \Delta^-$ (Bingham 1971).

Appendix XII. The Froggatt-Morgan Method

The fundamental assumption of the Froggatt and Morgan method is to assume that the nucleon helicity factors can be found by fitting the t dependence of the differential cross section and the moments. Thus the data are fitted using the same equations as in the S-M method (they are given in Appendix XI as equations 2a-f). However unlike the S-M method, they do not assume that the nucleon amplitudes are mass independent. Instead a prescription for the nucleon amplitudes is used. In this prescription the non-OPE contributions are parameterized using the Diu-LeBellac helicity amplitude projections (Diu 1968) as follows:

$$\vec{S} = R\left[\frac{\sqrt{t}}{t+\mu^2} + \frac{\Gamma_o^S}{\sqrt{t}}\,,\ \Gamma_o^S\sqrt{\frac{1}{t} - \frac{1}{t_{min}}}\right]$$

$$\vec{P}_o = \sqrt{3}\ R\left[\frac{\sqrt{t}}{t+\mu^2} + \frac{\Gamma_o^P}{\sqrt{t}}\,,\ \Gamma_o^P\sqrt{\frac{1}{t} - \frac{1}{t_{min}}}\right]$$

$$\vec{P}_1 = \sqrt{3}\ R\left[\frac{\Gamma_1^P}{\sqrt{t}}\right]\left[\sqrt{\frac{t}{t_{min}} - 1}\,,\ \sqrt{\frac{t}{t_{min}} - 1}\right]$$

$$\vec{P}_{-1} = \sqrt{3}\ R\ \frac{\Gamma_1^P}{\sqrt{t}}\left[-\sqrt{\frac{t}{t_{min}}-1}\ ,\ \sqrt{\frac{t}{t_{min}}}\ +1\right]$$

where $R = \left[\frac{1}{m_p P_{lab}}\left(\frac{G^2}{4\pi}\right)^{\frac{1}{2}}\frac{m_{K\pi}}{q^{\frac{1}{2}}}\right]$ and Γ_0^S, Γ_0^P, and Γ_1^P are the a priori unknown parameters which characterize the non-pion exchange contributions. Although in general, they may be complex functions of t and $m_{K\pi}$, the successful highly constrained fits to $\pi^- p \to \pi^-\pi^+ n$ (Scharenguivel 1970) with real constant Γ's suggests that the use of real parameters might be a valid approximation.

The only problem presented by this formalism is its inability to reproduce the sharp t dependence of the differential cross section for $K^+ n \to K^+\pi^- p$ we have therefore added an exponential t dependence to the parameterization $(e^{\alpha(t+\mu^2)})$. Thus the parameters used in Section V-E are: δ_S, Γ_0^{0-}, Γ_0^{1-}, Γ_1^{1-}, α^-, Γ_0^{0+}, Γ_1^{1+}, Γ_1^{1+}, and α^+.

REFERENCES

ABCLV Collaboration 1968, 10 GeV/c K^-P Interactions, *Nucl. Phys. B5*, 67; *Nucl. Phys. B7*, 111.

Alvarez, L.W., 1960, A proposed device for the rapid measurement of bubble chamber film, (unpublished Alvarez group memo 223).

Annis, Cheston, and Primakoff, 1953, On Statistical Estimation in Physics, *Rev. Mod. Phys. 25*, 818.

Bassompierre, et. al., 1970, Production of $K^*(890)$ in K^+N Interactions at 3 GeV/c, *Nucl. Phys. B16*, 125.

Benecke and Durr, 1968, A Relativistic Model for Kinematic Form Factors, *N.C. LVIA*, N.2.

Bingham, H.H., et. al., 1971, A new $K\pi$ phase shift analysis, preprint CERN/D. Ph. II/Phys. 71-22.

Bland, R.W., et. al., 1966, Interference Effects in the Reaction $K^+P \rightarrow K^\pm N+\pi$ at 1.2 GeV/c, *Phys. Rev. Letters 17*, 939.

Bricman, C., 1970, Measurement of the $K^-p \rightarrow \bar{K}^0n$ Cross Section from 1 to 3 GeV/c, *Phys. Letters 31B*, 148.

Chew and Low, 1959, Unstable Particles as Targets in Scattering Experiments, *Phys. Rev. Letters 6*, 113.

Cho, Y., et. al., 1970, Study of $K^-\pi^-$ Scattering using the Reaction $K^-d \rightarrow K\pi pp_s$, *Phys. Letters 32B*, 409.

Colton, 1968, Pion Production in Proton-Proton Interactions at 6.6 GeV/c, UCLA-1025 (unpublished thesis).

Dauber, 1966, A Study of Selected Final States in K^-P Scattering at 2 GeV/c, (unpublished UCLA thesis).

Dauber and Trippe, 1965a, Beam Momentum Determination in 20 GeV/c K-63 Exposure, (unpublished UCLA group memo #23).

Dauber and Trippe, 1965b, Beam Track Length Determination in 2.0 GeV/c K-63 Exposure, (unpublisehd UCLA group memo #24).

Donohue and Hogaasen, 1967, A Dynamic Reference System for Spin Quantization, *Phys. Letters 25B*, 554.

Dürr and Pilkun, 1965, Kinematic Form Factors in the Peripheral Model, *N.C. XLA.N3*.

Edmonds, 1960, Angular Momentum in Quantum Mechanics.

Fox, et. al., 1971, Charge Exchange Production Mechanism for $K^*(890)$, *Phys. Rev. D. 4*, 2647.

Froggatt and Morgan, 1969, Nonevasive Chew-Low Extrapolation for the Study of $\pi\pi$ Elastic Scattering, *Phys. Rev. 187*, 2044.

Goebel, 1958, Determination of the $\pi\pi$ Interaction Strength From π-N Scattering, *Phys. Rev. Letters 9*, 337.

Gottfried and Jackson, 1964, Influence of Absorption due to Competing Processes on Peripheral Reactions, *N.C. 34.N3*.

Gutay, 1969, Review of Experimental Methods of Analysis of $\pi\pi$ Scattering and a Unique Set of δ_0^0, *Proceedings of the Conference on $\pi\pi$ and Kπ Interactions*.

Henri, V.P.: 1971, Kπ Interactions, CERN Preprint: CERN/ D. Ph. II/ Phys. 71-23.

Hubbard, R., Huwe, D.D., Kalbfleisch, G.R., Kirz, J., Miller, D.H., Shafer, J.B., Stork, D.H., Ticho, H.K., and Wohl, C.: 1964, Design of the K-63 beam, *UCRL 10960*, see also Merrill, D., Design of the K-63 beam using an Analog Computer, *Alvarez Group Memo No. 519*.

Malamud and Schlein, 1967, $\pi\pi$ Phase Shift Analysis from 600 to 1000 Mev, *Phys. Rev. Letters 19*, 1056.

Malamud, 1968, K^-P Scan-Measure Project, (unpublished UCLA internal report).

Marateck, et. al., 1969, Study of $\pi\pi$ Elastic Scattering Using the Chew-Low Extrapolation Method, *Phys. Rev. Letters 21*, 1613.

Munson, J.H., 1963, The Scanning and Measuring Projector, Ph.D. thesis, part I., UCRL 11154.

Particle Data Group, 1971, Review of Particle Properties, *RMP Vol. 43*, #2, Part II.

Poster, R., to be published.

Scharenguivel, et. al., 1970, Forward Structure of the Single-Pion-Production Amplitude, *Phys. Rev. Letters 24*, 332.

Schlein, 1967, Method for $\pi\pi$ and $K\pi$ Phase-Shift Analysis, *Phys. Rev. Letters 19*, 1052.

Smith, L.T., 1965, Study of the Final States of K^-P at 1.85, 1.95 GeV/c, (unpublished UCLA thesis); see also Pjerron, G.P., 1965, The decay of the Ξ^-, (unpublished UCLA thesis).

Trieman and Yang, 1961, Tests of the Single Pion Exchange Model, *Phys. Rev. Letters 8*, 140.

Trippe, 1968, The $K\pi$ Interaction in $K^+P \rightarrow K^+\pi^-\pi^+P$ at 7.3 GeV/c, (unpublished UCLA thesis).

Winstein, 1970, The polarization of the recoil proton in eta photoproduction, p81ff, (unpublished Caltech thesis).

Wolf, 1969, Single- and Double-Pion Production by One-Pion Exchange and a Comparison with Experimental Data Between 1.6 and 20 GeV/c, *Phys. Rev. 182*, 1538.

Yellin, S.J.: 1971, Photoproduction of eta mesons from deuterium at 0° and 180° with photon energy from 725 MeV to 1225 MeV (unpublished Caltech thesis).